5-2001

Shear Wave Velocity Profiles at Sites Liquefied by the 1999 Kocaeli, Turkey Earthquake

Brady R. Cox
Utah State University

SHEAR WAVE VELOCITY PROFILES AT SITES LIQUEFIED BY THE 1999 KOCAELI, TURKEY EARTHQUAKE

by

Brady R. Cox

A thesis submitted in partial fulfillment
of the requirements for the degree

of

MASTER OF SCIENCE

in

Civil and Environmental Engineering

Approved:

James A. Bay Major Professor	Loren R. Anderson Committee Member
Marvin W. Halling Committee Member	Thomas L. Kent Dean of Graduate Studies

UTAH STATE UNIVERSITY
Logan, Utah
2001

ABSTRACT

Shear Wave Velocity Profiles at Sites Liquefied by

the 1999 Kocaeli, Turkey Earthquake

by

Brady R. Cox, Master of Science

Utah State University, 2001

Major Professor: Dr. James A. Bay
Department: Civil and Environmental Engineering

This paper presents shear wave velocity profiles for 15 sites liquefied by the 1999 Kocaeli, Turkey earthquake. These profiles are used in order to evaluate each liquefaction site by the simplified shear wave velocity procedure. This procedure allowed for the identification of a potentially liquefiable region within the subsurface at each site. Locating this region at each site allowed for the separation of soils that were too stiff to liquefy from soils that were soft enough to liquefy. Once these soft regions had been identified, they were evaluated to separate granular soils expected to liquefy, from fine-grained soils expected not to liquefy. At sites where actual soil samples were available, this was accomplished by using the Chinese Criteria and the Andrews and Martin Criteria. At sites where only CPT data were available, this was accomplished by developing profiles of soil behavior type index (I_C).

Granular soil layers were located within the liquefiable region at 11 of the liquefaction test sites. It is assumed that these layers were the ones responsible for the

observed liquefaction. The depth and thickness of each of these layers have been identified. However, at four of the liquefaction sites, only soils predicted as not susceptible to liquefaction were encountered. In these cases, the layer coming closest to fulfilling the Chinese Criteria and the Andrews and Martin Criteria was chosen as the one most likely to have liquefied. At each of these four sites, this layer appeared to be primarily made up of non-plastic silts having 2 μm clay contents ranging from 15 - 25%.

(308 pages)

ACKNOWLEDGMENTS

First of all I must acknowledge and give thanks to my major professor, Dr. James A. Bay. This project has been a great learning experience for me, and I am grateful for the opportunity that he gave me to work on an interesting and demanding project. He has encouraged me to work hard, not only to fulfill the requirements of the degree, but also to accomplish something that I can be proud of. His knowledge, insight, and guidance have been invaluable in the development of this thesis.

I am very appreciative of the help provided by my other committee members, Dr. Loren R. Anderson and Dr. Marvin W. Halling. Their various areas of specialty were needed on this project. Dr. Anderson provided valuable guidance into understanding the soil properties and behavior observed at the liquefaction sites, while Dr. Halling lent insight in earthquake mechanics and ground accelerations. Their help in previewing this thesis is also appreciated.

I would like to thank and acknowledge the other researchers, from The University of Texas at Austin, who performed SASW testing with us in Turkey, namely, Dr. Kenneth H. Stokoe, II, Dr. Ellen Rathje, Brent Rosenblad, and Mehmet Darendeli. Without their help and cooperation much of the shear wave velocity profiling would not have been accomplished. Aaron Budge from Utah State University was also a huge help during the testing in Turkey.

I acknowledge and give thanks to the joint group of researchers from the University of California at Berkeley, Brigham Young University, the University of California at Los Angeles, ZETAS Earth Technology Corporation, Middle East Technical

University, and Sakarya University. Their investigations in Turkey included large-scale SPT and CPT testing in addition to detailed site mapping. They have very graciously shared the information from these studies, and without it much of this work would have been impossible. Professor John D. Bray and Rodolfo B. Sancio of the University of California at Berkeley, and Professor T. L. Youd of Brigham Young University have provided particular help and cooperation with liquefaction site details.

I must also thank Cem Ozbey from the Kandili Observatory Earthquake Research Institute. His help in translating and finding our way around in Turkey proved invaluable.

My thanks go out to Ken Jewkes, who helped me to design and build the lightweight aluminum tripod and cart that we took with us to Turkey. His time and skills were invaluable in assuring that our equipment was in working order for two hard weeks of testing.

Last, but certainly not least, I thank my wife, Audrey, for her support and patience throughout this project, and throughout my entire education up to this point. She has been willing to handle all of the other duties in our life, allowing me to focus on accomplishing the task at hand. I could not have done this without her support. Additionally, I give thanks to my parents. Although they have not directly helped me with this project, the principles of hard work, confidence, faith, and integrity that they taught me have guided me throughout my life. My parents-in-law also deserve thanks and appreciation for their support and concern for Audrey and me.

Brady R. Cox

CONTENTS

Page

Page

Page

LIST OF TABLES

Page

Page

Page

LIST OF FIGURES

Page

Page

Page

Page

Page

Page

Page

Page

Page

Page

Page

Page

Page

Page

Page

Page

Page

Page

Page

Page

CHAPTER 1

INTRODUCTION

On August 17, 1999, at 3:02 in the morning, a powerful earthquake ripped through northern Turkey. In the aftermath of the earthquake, the Turkish government reported 17,439 people dead, 43,953 injured, and more than 500,000 left homeless (EERI, 2000). This earthquake was later termed the Kocaeli earthquake (after the name of the providence where the epicenter was located) and was estimated as having a moment magnitude (M_W) of 7.4. The actual epicenter was located on the North Anatolian fault, just southeast of the city of Izmit (about 80 km southeast of Istanbul). From this location, the fault ruptured approximately 90 km to the east and 30 km to the west. The rupture was predominantly right-lateral strike-slip, with ground displacements ranging from 1 - 5.5 meters (EERI, 2000).

The Kocaeli earthquake generated intense interest within the engineering community due to reports of massive ground failures and structural collapse. A reconnaissance team from the Earthquake Engineering Research Institute (EERI) arrived in Turkey just days after the earthquake. This group assisted in organizing the efforts of other reconnaissance teams and private researchers so as to optimize the effort to investigate earthquake damage and plan further research. One of these important groups was the U.S.-Turkey NSF Geotechnical Earthquake Engineering reconnaissance team. This team performed aerial and land surveys directed at investigating ground failures that developed during the earthquake. From these reconnaissance efforts, a number of "representative" case histories were selected for further detailed study. These researchers

found particular interest in liquefaction-related ground failures that occurred throughout the city of Adapazari, and lateral spreading that occurred along the shores of Lake Sapanca and Izmit Bay. A full account of their reconnaissance efforts can by found in EERI (2000).

Post-earthquake research at these ground failure sites was spearheaded by a joint group of researchers from the University of California at Berkeley, Brigham Young University, the University of California at Los Angeles, ZETAS Earth Technology Corporation, Middle East Technical University, and Sakarya University. Their investigations included large-scale SPT and CPT testing, in addition to detailed site mapping (www.eerc.berkeley.edu/turkey/adapazari).

In August of 2000, a joint investigation team comprised of researchers from Utah State University (USU) and The University of Texas at Austin (UT) traveled to Turkey in order to perform spectral-analysis-of-surface-waves (SASW) testing at many of these same sites. The National Science Foundation (NSF) and the Pacific Earthquake Engineering Research Center (PEER) sponsored this research due to the desire for combining accurate shear wave velocity profiles with standard penetration test (SPT) and cone penetration test (CPT) data from the same sites. These three testing methods comprise the current realm of simplified procedures for evaluating earthquake-induced soil liquefaction.

Fifteen different liquefaction sites were tested using the SASW method. Chapter 3 of this paper presents the SASW results and shear wave velocity profiles that were developed for each of these sites. Chapter 3 also contains detailed site information and maps showing the locations of SASW centerlines, SPT boreholes, and CPT soundings.

Chapter IV provides a detailed liquefaction analysis of each site aimed at determining the soil layer/layers most likely to have initiated these ground failures. This was accomplished by delineating a potentially liquefiable region at each site using the simplified shear wave velocity procedure (Andrus et al., 2001). Locating this region at each site allowed for the separation of soils that were too stiff to liquefy from soils that were soft enough to liquefy. Once these soft regions had been identified, they were evaluated to separate granular soils expected to liquefy, from fine-grained soils expected not to liquefy. At sites where actual soil samples were available, this was accomplished by using the Chinese Criteria (Seed and Idriss, 1982) and the Andrews and Martin Criteria (Andrews and Martin, 2000). At sites where only CPT data were available, this was accomplished by developing profiles of soil behavior type index (I_C) (Robertson and Wride, 1998).

Granular soil layers were located within the liquefiable region at 11 of the liquefaction test sites. It was assumed that these layers were the ones responsible for the observed liquefaction. The depth and thickness of each of these layers have been identified. However, at four of the liquefaction sites, only soils predicted as not susceptible to liquefaction were encountered. In these cases, the layer coming closest to fulfilling the Chinese Criteria and the Andrews and Martin Criteria was chosen as the one most likely to have liquefied. At each of these four sites, this layer appeared to be primarily made up of non-plastic silts having 2 μm clay contents ranging from 15 - 25 %.

These findings suggest that largely non-plastic soils, having a high percentage of clay size particles, should not be classified as nonliquefiable simply because they have more than 10 - 15% clay-sized particles.

CHAPTER 2

LITERATURE REVIEW

This literature review will briefly discuss some of the general concepts related to earthquake-induced soil liquefaction and its evaluation. Then, the remainder of this chapter will focus on three main topics: (1) the shear wave velocity (V_S) simplified procedure, (2) criteria used for separating liquefiable from nonliquefiable soils, and (3) obtaining V_S profiles using the spectral-analysis-of-surface-waves (SASW) method.

Earthquake-Induced Soil Liquefaction

The diverse and devastating nature of earthquake-induced soil liquefaction was brought to the attention of civil engineers almost single-handedly through the occurrence of two large earthquakes in 1964, the Good Friday Alaska earthquake and the Niigata, Japan earthquake. In the Good Friday Alaska earthquake, extensive damage was done to a wide variety of bridge foundations as liquefied soils spread laterally toward stream channels. Weakened soils also triggered large landslides in the cities of Anchorage, Seward, and Valdez (Seed and Idriss, 1982). In the Niigata, Japan earthquake, thousands of buildings were damaged when their foundation soils liquefied. Many of these buildings settled more than a meter and tilted severely due to differential movement (Seed and Idriss, 1982). While the outward manifestations of the soil failures were different in both earthquakes, the triggering mechanism (the cyclic buildup of excess pore water pressure) appeared to be the same.

The cyclic loading of an earthquake can cause various degrees of soil liquefaction in saturated, cohesionless soils. These degrees have been referred to as cyclic mobility, limited liquefaction, and flow liquefaction, among others (Robertson, Woeller, and Finn, 1992). In this paper, the term soil liquefaction will hereafter refer in a broad sense to the cyclic buildup of excess pore water pressures. This phenomenon is the triggering mechanism responsible for various degrees of soil liquefaction. Excess pore water pressures are induced in a saturated soil deposit because propagating shear waves from an earthquake tend to shake loose soil particles into a denser configuration. However, this densification cannot take place until the water that occupies the voids between particles is forced out. Earthquake-induced cyclic loading occurs so rapidly that even highly permeable sands and gravels cannot dispel water quick enough to stop the buildup of excess pore water pressures. When the pore water pressure approaches a value equal to the effective overburden pressure, large deformations take place and the soil weakens to a point where it is said to have liquefied (Seed and Idriss, 1982).

During an earthquake, soil liquefaction can cause untold amounts of damage. Problems range from tilted buildings to floating pipes, and from failed dam foundations to lateral spreads. Since all of these failures result in the loss of money and lives, predicting the risk of earthquake-induced soil liquefaction is one of the most important tasks that a civil engineer is faced with in seismically active regions. The predominant method used in the United States and throughout much of the world for predicting the liquefaction susceptibility of soils is termed the "simplified procedure" (Andrus et al., 2001).

The original simplified procedure was developed and published by Seed and Idriss (1971). Its basis is to provide a simplified way of predicting both the earthquake-induced stress, and the natural resisting strength within a particular soil deposit. These two values can then be compared as a way to predict if the soil is likely to liquefy in a given earthquake. Seed and Idriss hypothesized that the earthquake-induced stresses could be predicted using the cyclic stress ratio (CSR):

$$CSR = \frac{\tau_{av}}{\sigma'_{vo}} = 0.65\left(\frac{a_{\max}}{g}\right)\left(\frac{\sigma_{vo}}{\sigma'_{vo}}\right)r_d \qquad \text{(Eq. 2.1)}$$

where: CSR = cyclic stress ratio,
τ_{av} = average shear stress in the soil profile,
a_{max} = peak horizontal ground surface acceleration,
g = acceleration of gravity,
σ_{vo} = initial total vertical overburden stress,
σ'_{vo} = initial effective vertical overburden stress,
r_d = stress reduction coefficient which accounts for the flexibility of the soil profile.

The simplified procedure provides for the evaluation of soil liquefaction resistance by using an empirical chart. This chart was developed primarily by compiling blow count data obtained from the standard penetration test (SPT) at sites that did and did not liquefy in previous earthquakes. A line was then drawn on this chart that visually bound and separated the liquefaction case histories from the nonliquefaction case histories. From this chart it is possible to predict the CSR that will induce liquefaction in a soil deposit by entering the chart with a given SPT blow count. This value has more recently been termed the cyclic resistance ratio (CRR) (Youd and Idriss, 1997; Youd and

Idriss, 2001). Knowing the earthquake induced CSR and the natural CRR of the soil, one can easily predict the factor of safety against soil liquefaction.

Over the years the equation developed by Seed and Idriss (1971) for estimating earthquake-induced CSR's (Eq. 2.1) has remained essentially unchanged. However, the empirical chart used to predict a soils CRR through SPT blow counts has been updated and modified as new data have become available (Youd and Idriss, 2001). In addition, other test methods have been developed with similar empirical charts for estimating CRR's. The two most common liquefaction index tests used presently, in addition to the SPT, are the cone penetration test (CPT) and shear wave velocity measurements (V_S).

In 1996, T. L. Youd and I. M. Idriss thought it appropriate to convene a workshop dedicated to the evaluation of the most recent developments among the SPT, CPT and V_s- based simplified procedures. As part of this workshop (1996 NCEER), 20 experts in the field of soil liquefaction met together with the goal of recommending the most recent and correct standards to be followed when applying simplified procedures. The latest developments for both the SPT and CPT based simplified procedures, as recommended by the 1996 NCEER workshop, can be found in Youd and Idriss (1997). The reader is also referred to a brief summary of the suggestions from this conference, and additional suggestions from the 1998 NCEER workshop, found in Youd and Idriss (2001). Only the simplified shear wave velocity procedure will be discussed further in this paper.

The V_S-Based Simplified Procedure

The simplified shear wave velocity (V_s) procedure requires the calculation of three parameters in order evaluate liquefaction potential (Andrus and Stokoe, 2000): (1)

the level of cyclic loading caused by the earthquake expressed as a CSR, (2) the stiffness of the soil expressed as an overburden corrected shear wave velocity, and (3) the resistance of the soil to liquefaction expressed as a CRR. This section addresses the calculation of each of these parameters.

The cyclic stress ratio

As mentioned above, the original CSR equation given by Seed and Idriss (1971) has remained unchanged. It is held in common by the SPT, CPT, and V_S-based simplified procedures. Seed and Idriss originally determined values of r_d for use in Eq. 2.1 through an analytical process using a variety of earthquake motions and soil conditions. These values are shown in Figure 2.1, along with values plotted from an equation that was developed later by Liao and Whitman (1986) to fit the original data:

$$r_d = 1.0 - 0.00765\ z; \quad \text{for } z < 9.15 \text{ m} \qquad \text{(Eq. 2.2a)}$$

$$r_d = 1.174 - 0.0267\ z; \quad \text{for } 9.15 \text{ m} < z < 23 \text{ m} \qquad \text{(Eq. 2.2b)}$$

where: r_d = stress reduction coefficient which accounts for the flexibility of the soil profile,
z = depth below the ground surface, in meters.

Other r_d values have been proposed but are not recommended by the NCEER workshop participants. Youd and Idriss (2001) do not recommend using simplified procedures to calculate a CSR below a depth of 23 meters due to a lack of case histories to verify the procedure at this depth. With this information, one can easily calculate a CSR by using simple site characteristics like soil unit weights and the depth to the water table.

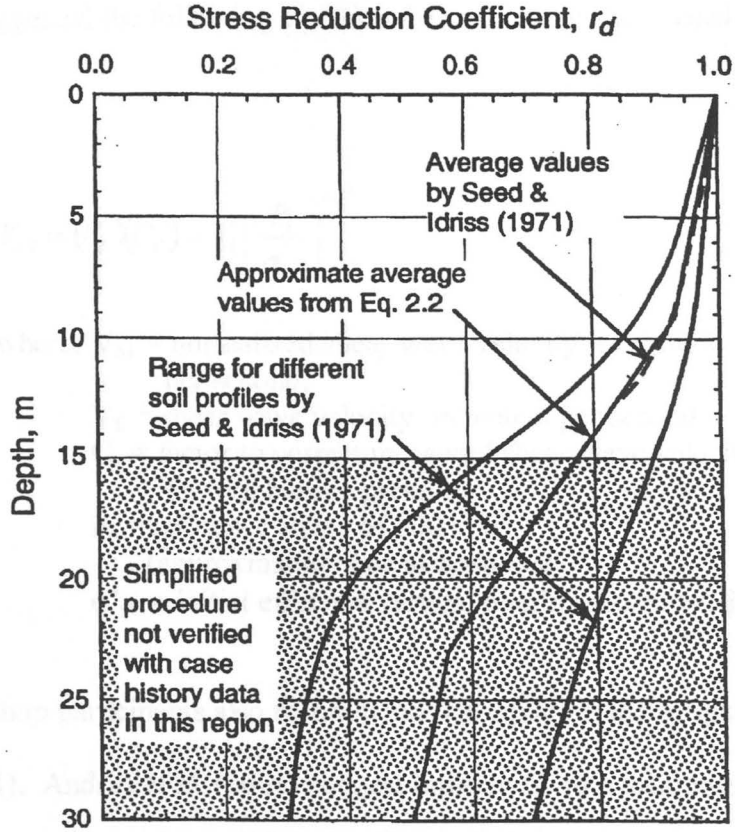

Figure 2.1 Relationship between stress reduction coefficient and depth developed by Seed and Idriss (1971) with approximate average value line from Eq. 2.2 (after Youd and Idriss, 1997).

Corrected shear wave velocities

For a sand of constant void ratio, the shear wave velocity will increase with depth because of the effects of increased effective confining pressure. Hence, it is believed that a correlation between CRR and V_S should be based upon shear wave velocities that have been normalized with respect to effective overburden pressure (Robertson, Woeller, and Finn, 1992). This suggestion is in harmony with the tradition of normalizing penetration-based resistance parameters due to overburden pressure. Robertson, Woeller, and Finn

(1992) have suggested the following equation for calculating the normalized shear wave velocity (V_{S1}):

$$V_{S1} = (V_S)(C_V) = V_S\left(\frac{P_a}{\sigma'_{vo}}\right)^{0.25} \qquad \text{(Eq. 2.3)}$$

where: V_{S1} = normalized shear wave velocity, in meters per second,
V_S = shear wave velocity, in meters per second,
C_v = factor to correct measured shear wave velocity for overburden pressure,
P_a = reference stress of 100 kPa (approximately one atmosphere)
σ'_{vo} = initial effective vertical overburden stress, in kPa.

NCEER Workshop participants also recommend this equation for correcting V_S (Youd and Idriss, 2001). Andrus et al. (2001) suggest limiting C_v to a maximum value of 1.4 at shallow depths. In applying Eq. 2.3 it is implicitly assumed that the initial effective horizontal stress is a constant factor of the initial effective vertical stress. This factor, referred to as K'_o, is assumed to be approximately equal to 0.5 at natural, level-ground sites (Andrus and Stokoe, 2000).

The V_S-based cyclic resistance ratio

The use of shear wave velocity (V_S) in evaluating liquefaction resistance is soundly based. Both V_S and CRR are similarly influenced by soil density, overburden pressure, stress history, geologic age, and soil type and fabric (Robertson et al, 1992; Kayabali, 1996; Yamamoto et al., 2000). V_S is also an actual dynamic soil property which has a clear physical meaning that can be measured both in the laboratory and the

field (Tokimatsu and Uchida, 1990). V_S is directly related to the small-strain shear modulus (G_{max}) by:

$$G_{max} = \rho(V_S)^2 \qquad \text{(Eq. 2.4)}$$

where: G_{max} = small-strain shear modulus,
ρ = mass density of the soil,
V_S = shear wave velocity.

G_{max} is a required soil property in both earthquake site response and soil-structure interaction analyses (Andrus and Stokoe, 2000). Penetration resistance, on the other hand, neither directly measures an actual soil property, nor can be evaluated in the laboratory. Another advantage of using V_S for liquefaction resistance studies is that it can be measured in soils that are hard to sample, such as gravels, and at sites where borings are not permitted, such as landfills (Andrus and Stokoe, 2000).

Andrus et al. (2001) note three concerns about using V_S to evaluate liquefaction resistance. They are: (1) no samples are obtained for soil classification or identification of nonliquefiable clay rich soils, (2) thin layers may not be detected if the measurement interval is too large, and (3) measurements of V_S are made at low strains while excess pore pressure buildup and liquefaction are medium to high-strain phenomena.

Tokimatsu, Kuwayama, and Tamura (1991) list two possible methods for evaluating the liquefaction susceptibility of soils using V_S. The first method is the strain approach, which was developed by Dobry et al. (1982). This method compares the strain expected to be developed in the ground by earthquake shaking to the threshold strain at which excess pore pressures will just begin to develop. The second method is the stress approach, which has been investigated by numerous researchers who will be discussed

later. This method is essentially the simplified procedure correlated with V_S measurements instead of SPT blow counts. Only the stress approach will be considered further herein since it has gained more popularity and acceptance than the strain approach.

V_S liquefaction resistance curves. Andrus et al. (2001) have compiled seven different V_S-based liquefaction resistance curves that were developed by various researchers. These curves are shown in Figure 2.2 and are only appropriate for clean sands shaken by moment magnitude 7.5 earthquakes. The "best fit" curve by Tokimatsu and Uchida (1990) was determined from laboratory cyclic triaxial tests. This curve was fit through the middle of their data set whereas the other curves shown were all drawn to bound the liquefaction case histories. In light of this, Andrus, Stokoe, and Chung (1999) adjusted Tokimatsu and Uchida's "best fit" curve to a "lower bound" curve so as to correlate better with the other investigators method. All of the other curves shown in Figure 2.2 were developed primarily using field performance data. However, the curves by Robertson, Woeller, and Finn (1992), Kayen et al. (1992), and Lodge (1994) are all based on limited data. The curve by Andrus and Stokoe (1997) was developed for the 1996 NCEER workshop by using case histories from 20 earthquakes. Andrus, Stokoe, and Chung (1999) later revised this curve by adding more case histories and correcting a few errors that were found in their original database.

The CRR-V_{S1} curve developed by Andrus, Stokoe, and Chung (1999) is recommended for use in evaluating the liquefaction resistance of soils because it was determined using the largest case history database (26 earthquakes), and it has incorporated suggestions from the two NCEER workshops previously mentioned.

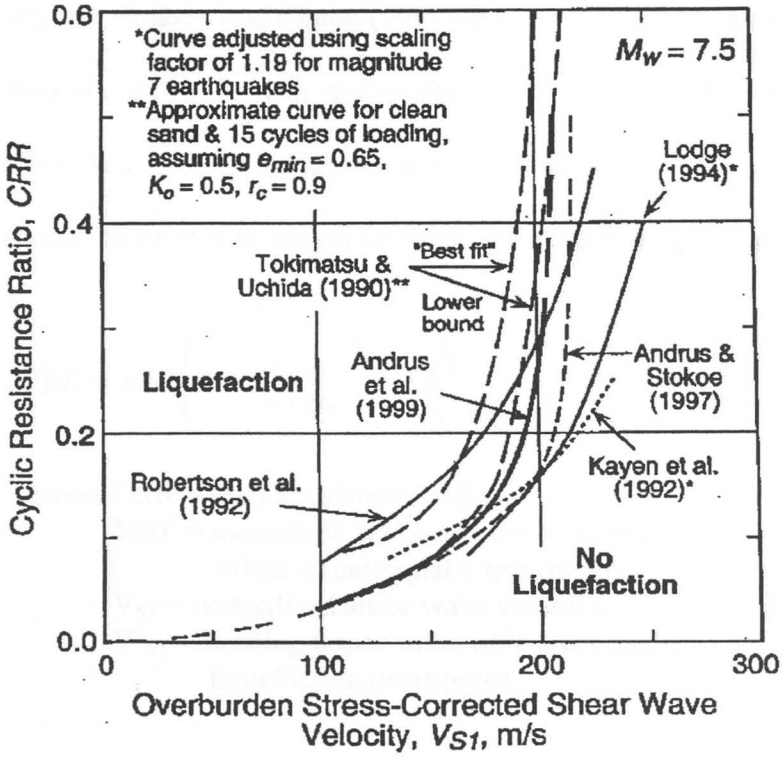

Figure 2.2 Comparison of seven proposed CRR-V_{S1} curves for clean granular soils (after Andrus et al., 2001).

This curve is also the only curve suggested for use by NCEER workshop participants as cited by Youd and Idriss (2001).

The Andrus approach. Ronald Andrus and his colleagues have incorporated exhaustive research into the development of the above recommended V_S-based simplified procedure. A full accounting of their investigations and findings can be found in Andrus and Stokoe (1997), Andrus, Stokoe, and Chung (1999), Andrus and Stokoe (2000), and Andrus et al. (2001). A brief review of their approach to calculating CRR's is given below.

The Andrus, Stokoe, and Chung (1999) curve in Figure 2.2 is only appropriate for uncemented Holocene-age soils with less than 5% fines, shaken by magnitude 7.5

earthquakes. Andrus, Stokoe, and Chung (1999) have developed an equation that can be used to apply their curve to soils with various fines contents shaken by various magnitude earthquakes with various soil ages and cementation conditions. However, the equation shown below should be limited to use on uncemented Holocene-age soils.

$$CRR = MSF\left(0.022\left(\frac{V_{S1}}{100}\right)^2 + 2.8\left(\left(\frac{1}{V_{S1}^* - V_{S1}}\right) - \left(\frac{1}{V_{S1}^*}\right)\right)\right) \qquad \text{(Eq. 2.5)}$$

where: CRR = cyclic resistance ratio,
MSF = magnitude scaling factor to account for the effect of earthquake magnitude,
V_{S1} = normalized shear wave velocity,
V^*_{S1} = limiting upper value of V_{S1} for cyclic liquefaction occurrence.

Figure 2.3 shows three recommended CRR-V_{S1} curves determined for various fines contents and a magnitude 7.5 earthquake using Eq. 2.5. Notice that for a given normalized shear wave velocity, the CRR of the soil increases with increasing fines content.

Numerous researchers have proposed magnitude scaling factors (MSF). A detailed description of these factors, along with the recommended range of MSF from the 1996 NCEER workshop is given in Youd and Idriss (2001). Andrus et al. (2001) comply with this recommended range by suggesting the following equation:

$$MSF = \left(\frac{M_W}{7.5}\right)^{-2.56} \qquad \text{(Eq. 2.6)}$$

where: MSF = magnitude scaling factor,
M_W = moment magnitude of earthquake.

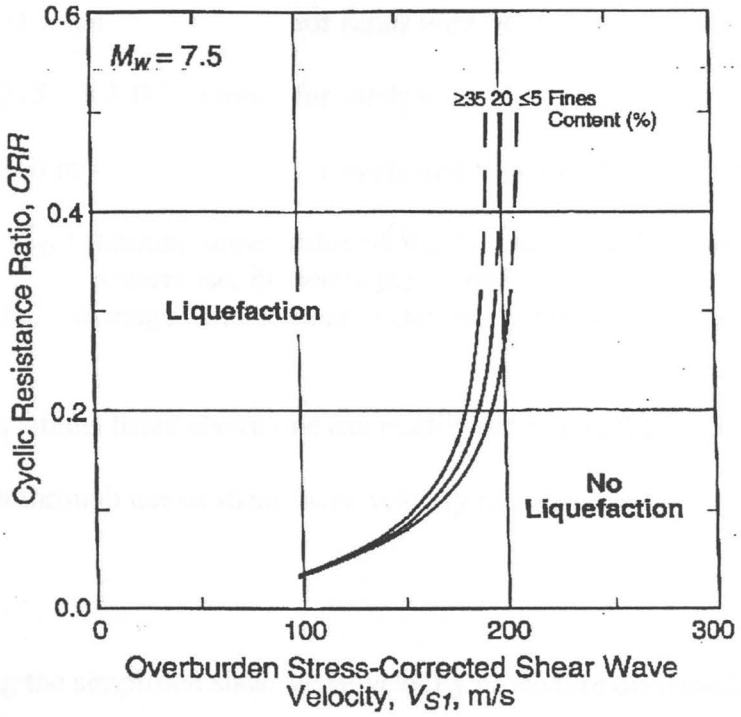

Figure 2.3 Curves with various fines contents recommended for calculation of CRR from V_{S1} (after Andrus, Stokoe, and Chung, 1999).

The assumption of a limiting upper value of V_{S1} is similar to the assumption of a limiting upper value of blow count or tip resistance, for the SPT and CPT tests, respectively. Upper limits for V_{S1} and penetration resistance can be explained partially by the tendency of dense soils to dilate at large strains. This dilative behavior will cause negative pore pressures, which in turn help to increase the effective stress. So it is expected that at some point the corrected shear wave velocity of a soil will be too great to experience liquefaction regardless of the nature of the earthquake-induced cyclic stress ratio. The maximum velocity at which a soil will liquefy seems to decrease with increasing fines content. Andrus et al. (2001) define the maximum liquefiable velocity (V^*_{S1}) as:

$V^*_{S1} = 215$ m/s for sands with FC < 5% (Eq. 2.7a)

$V^*_{S1} = 215 - 0.5(FC-5)$ m/s for sands with 5% < FC < 35% (Eq. 2.7b)

$V^*_{S1} = 200$ m/s for sands and silts with FC > 35% (Eq. 2.7c)

where: V^*_{S1} = limiting upper value of V_{S1} for cyclic liquefaction occurrence, in meters per second,
FC = average fines content of the soil, in percent by mass.

By using the equations listed above one can readily determine the cyclic resistance ratio of a soil deposit through use of shear wave velocity measurements.

Summary

By using the simplified shear wave velocity procedure discussed above, one can readily evaluate the liquefaction potential of a soil deposit. This is done by first calculating the CSR expected to be induced at the site by the design earthquake using Eq. 2.1 and Eq. 2.2. Then a shear wave velocity (V_S) profile of the site must be obtained. This will be discussed in greater detail below. The V_S values should be corrected at each measurement depth for overburden pressure using Eq. 2.3. After this has been done, a CRR can be calculated by using Eq. 2.5, Eq. 2.6, and Eq. 2.7. With a known CSR and CRR, the factor of safety against liquefaction is given by:

$$FS = \left(\frac{CRR}{CSR}\right) \quad \text{(Eq. 2.8)}$$

where: FS = factor of safety against liquefaction,
CRR = cyclic resistance ratio,
CSR = cyclic stress ratio.

However, just because a soil deposit has a higher CSR than CRR does not necessarily mean that it is expected to liquefy. The type of soil and its properties also determine to a large extent the degree of excess pore water pressure buildup. For example, sandy soils are considered as susceptible to liquefaction while clay soils in general are not. Therefore, in order for a soil to be predicted as liquefiable it must: (1) have a higher CSR than CRR, and (2) be a soil type expected to liquefy. One of the drawbacks of the shear wave velocity simplified procedure is that no soil samples are retrieved for the liquefaction evaluation of soils with high fines contents. For this reason, it is always a good idea to perform several SPT or CPT tests in areas where shear wave velocity measurements have been taken in order to obtain information about the subsurface soil types.

Criteria for Separating Liquefiable from Nonliquefiable Soils

Over the years, considerable attention has been devoted by engineers into understanding the liquefaction susceptibility of sands. Substantially less time has been devoted to understanding the liquefaction susceptibility of finer grained silts and clays (Andrews and Martin, 2000; Atukorala, Wijewickreme, and McCammon, 2000; Guo and Prakash, 2000). Because the grain size of silt falls between that of sand and clay, it is often assumed that the liquefaction susceptibility of silts must also fall somewhere between the high susceptibility of sands and the nonsusceptibility of clays (Andrews and Martin, 2000). Yamamuro and Covert (2001) site some of the conflicting results that various researchers have reported from laboratory studies on the liquefaction susceptibility of silty soils. It is clear that the liquefaction susceptibility of silts and silt-

clay mixtures is not fully understood at the present time (Guo and Prakash, 2000). However, several criteria are currently used by engineers to delineate fine-grained soils considered as susceptible to liquefaction from those considered as not susceptible to liquefaction. The most desirable way of making this determination is to obtain soil samples at the site and check these soils against the Chinese Criteria (Seed and Idriss, 1982) or the Andrews and Martin Criteria (Andrews and Martin, 2000). These two criteria lend guidance into what fine-grained soils may or may not be susceptible to liquefaction. CPT data can also be correlated to values that suggest a soils susceptibility to liquefaction. However, these correlations are rough, and when possible actual soil samples should be obtained to verify results. The remainder of this section will focus on evaluating the liquefaction susceptibility of fine-grained soils using the Chinese Criteria, the Andrews and Martin Criteria, and CPT data.

The Chinese Criteria

Chinese researchers observed liquefaction occurrence in silty sand to slightly sandy silts during the 1975 Haicheng, and the 1976 Tangshan, China earthquakes (Andrews and Martin, 2000). Seed and Idriss (1982) presented these findings as a way to determine some sort of criteria to base the prediction of liquefaction in fine-grained soils. These criteria have come to be known as the Chinese Criteria. The Chinese Criteria state that soils with the following characteristics may be vulnerable to severe strength loss during earthquakes:

Clay Content (% finer than 0.005 mm)	<15%
Liquid Limit (LL)	<35
Water Content (W_n)	>(0.9)LL

Clayey soils that fail any of these criteria are considered nonliquefiable.

Andrews and Martin Criteria

Andrews and Martin (2000) have "refined" the Chinese Criteria based primarily on the different definitions of liquid limit and clay content between China and the United States. The liquid limits from the original Chinese data were determined by the fall cone penetrometer, whereas liquid limits in the United States are most typically determined by the Casagrande-type percussion apparatus. Andrews and Martin maintain that a liquid limit of 35 with the fall cone penetrometer corresponds to a liquid limit of 32 with the Casagrande-type apparatus. Also, in China the clay content is defined as particles finer than 0.005 mm while in the United States clay content is defined as particles finer than 0.002 mm. As a result of this difference, Andrews and Martin base their criteria on a clay particle size of 0.002 mm. They also maintain that the liquid limit and clay content are "key" soil parameters while the water content is not. Therefore, water content is not a part of their criteria. Upon this basis, Andrews and Martin have developed the criteria shown in Table 2.1.

CPT correlations

The CPT friction ratio (sleeve resistance divided by cone tip resistance) generally increases with increasing fines content and soil plasticity. This allows for rough estimates of soil type to be determined from CPT data. The chart shown in Figure 2.4

Table 2.1 Andrews and Martin Criteria for evaluation of fine-grained soil liquefaction (after Andrews and Martin, 2000)

	Liquid Limit < 32[1]	Liquid Limit ≥ 32
Clay Content < 10%[2]	Susceptible	Further Studies Required *(Considering plastic non-clay sized grains - such as Mica)*
Clay Content ≥ 10%	Further Studies Required *(Considering non-plastic clay sized grains - such as mine and quarry tailings)*	Not Susceptible

was developed by Robertson (1990) for estimating soil type. The boundaries between soil types 2 - 7 can be approximated by concentric circles (Robertson and Wride, 1998). The radius of these concentric circles, called the soil behavior type index (I_C), can be calculated from the following equation:

$$I_C = \left[(3.47 - Q)^2 + (\log F + 1.22)^2\right]^{0.5} \qquad \text{(Eq. 2.9)}$$

where: I_C = soil behavior type index,
Q = normalized cone penetration resistance (dimensionless),
F = normalized friction ratio, in percent.

The normalized cone penetration resistance is given by the following equation:

$$Q = \left(\frac{q_c - \sigma_{vo}}{P_a}\right)\left(\frac{P_a}{\sigma'_{vo}}\right)^n \qquad \text{(Eq. 2.10)}$$

where: Q = normalized cone penetration resistance (dimensionless),
q_c = measured cone tip penetration resistance, in kPa,
σ_{vo} = total vertical overburden stress, in kPa,
σ'_{vo} = effective vertical overburden stress, in kPa,
P_a = reference stress of 100 kPa,
n = linear stress exponent (varies between 1 - 0.5).

The normalized friction ratio is given by the following equation:

$$F = \left[\frac{f_S}{(q_c - \sigma_{vo})}\right](100) \qquad \text{(Eq. 2.11)}$$

where: F = normalized friction ratio, in percent,
f_S = CPT sleeve friction stress, in kPa,
q_c = measured cone tip penetration resistance, in kPa,
σ_{vo} = total vertical overburden stress, in kPa.

Robertson (1990) developed the chart shown in Figure 2.4 with the normalized cone penetration resistance (Q) having a linear stress exponent (n) equal to one. More recently it has been suggested that n should be varied between 1 and 0.5 in order to get more accurate I_C values for use in the CPT-based simplified procedure (Robertson and Wride, 1998; Youd and Idriss, 2001). In this study, all I_C values were calculated with n = 1 since the original soil classification chart was developed this way. If the calculated I_C value is greater than 2.6, then the soil is considered too clay-rich to liquefy (Youd and Idriss, 2001). A table relating I_C values to soil behavior type is shown in Table 2.2. When no other soil information is available, this provides a reasonable assumption. However, it is strongly recommended that soil samples be retrieved to confirm liquefaction resistance by the Chinese Criteria. I_C values also allow for rough estimates of fines content (FC) according to the following equation:

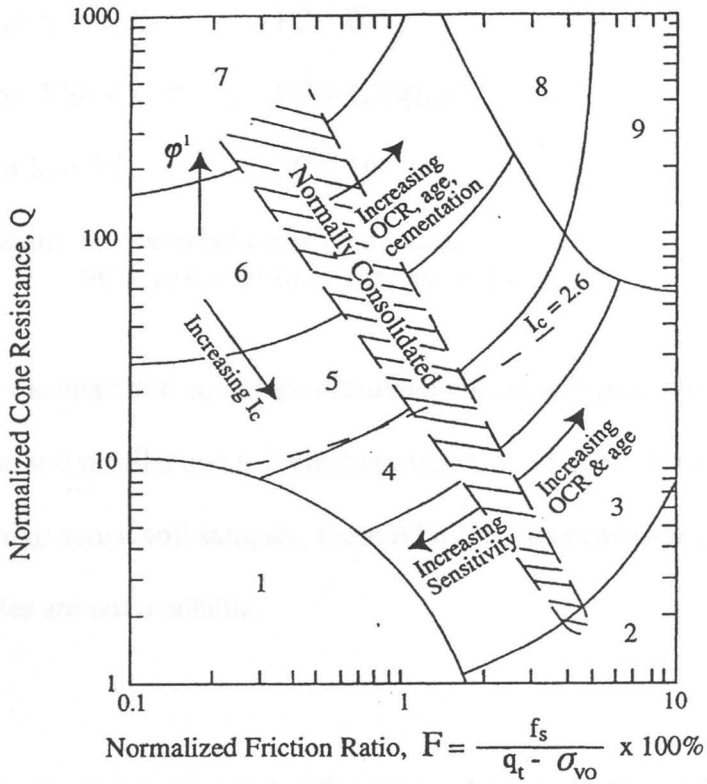

1. Sensitive, fine grained
2. Organic soils - peats
3. Clays - silty clay to clay
4. Silt mixtures - clayey silt to silty clay
5. Sand mixtures - silty sand to sandy silt
6. Sands - clean sand to silty sand
7. Gravelly sand to dense sand
8. Very stiff sand to clayey sand*
9. Very stiff, fine grained*

**Heavily overconsolidated or cemented*

Figure 2.4 CPT-based soil behavior type chart proposed by Robertson (1990). The boundaries separating soil types 2-7 are approximated by the soil behavior type index, I_C.

Table 2.2 Boundaries of soil behavior type (after Robertson 1990)

Soil behavior type index, I_C	Zone	Soil behavior type
$I_C < 1.31$	7	Gravelly sand to dense sand
$1.31 < I_C < 2.05$	6	Sands: clean sand to silty sand
$2.05 < I_C < 2.60$	5	Sand mixtures: silty sand to sandy silt
$2.60 < I_C < 2.95$	4	Silt mixutes: clayey silt to silty clay
$2.95 < I_C < 3.60$	3	Clays: silty clay to clay
$I_C > 3.60$	2	Organic soils: peats

for $I_C < 1.26$; $FC = 0$ (Eq. 2.12a)

for $1.26 < I_C < 3.5$; $FC = 1.75(I_C)^{3.25} - 3.7$ (Eq. 2.12b)

for $I_C > 3.5$; $FC = 100$ (Eq. 2.12c)

where: IC = soil behavior type index,
FC = apparent fines content, in %.

By using the chart and equations discussed above, it is possible to come up with an estimate of the soil profile, and soil characteristics, at a liquefaction site. While not as reliable as obtaining actual soil samples, these relationships provide a good estimate where soil samples are not available.

Summary

The most common current state of practice when evaluating soil liquefaction in silt and silt-clay mixtures is to use the Chinese Criteria. More recently, Andrews and Martin have developed their criteria, which can easily be checked in addition to the Chinese Criteria. When no soil data are available, CPT correlations based on I_c values can be used with caution. It should be noted that the methodologies described above are based solely on index properties and grain size data, and are independent of the intensity and duration of earthquake shaking (Atukorala, Wijewickreme, and McCammon, 2000). This may or may not be a valid approach.

V_S Profiles by the SASW Method

Dynamic methods typically used for obtaining shear wave velocity profiles of near-surface soils are the crosshole, downhole/seismic CPT, suspension logger, and

spectral-analysis-of-surface-waves (SASW). Each method has distinct advantages and disadvantages in relation to the others (Andrus et al., 2001). However, the SASW method is increasing in popularity due to its nonintrusive nature, cost effectiveness, and ability to test hard-to-sample soils.

SASW method

The spectral-analysis-of-surface-waves (SASW) method was initially developed at The University of Texas at Austin, primarily under the direction of Professor Kenneth H. Stokoe, II (Nazarian and Stokoe, 1984). SASW testing can be performed rapidly because both source and receivers are located at the ground surface. The SASW method is not limited to soil testing only, but can be used to evaluate the stiffness of other engineering materials such as concrete and asphalt pavements. The SASW method is used in the field to directly measure the velocity of surface waves of the Rayleigh type. Then, through a forward modeling procedure, these measurements are used to infer a shear wave velocity profile. This procedure is described below.

Rayleigh wave dispersion. In a layered media, the velocity of a propagating surface wave (Rayleigh wave) depends on the frequency (or wavelength) of that wave. This variation of velocity with frequency is called dispersion and is due to the fact that surface waves of different wavelengths disturb different parts of a layered media (Stokoe et al., 1988; Andrus et al., 1998). The Rayleigh wave phase velocity (V_R) depends primarily on the material stiffness of the media within a depth of approximately one wavelength (Brown, Boore, and Stokoe, 2000). This can be seen in Figure 2.5; short wavelength (high frequency) waves propagate only through layer 1, while longer

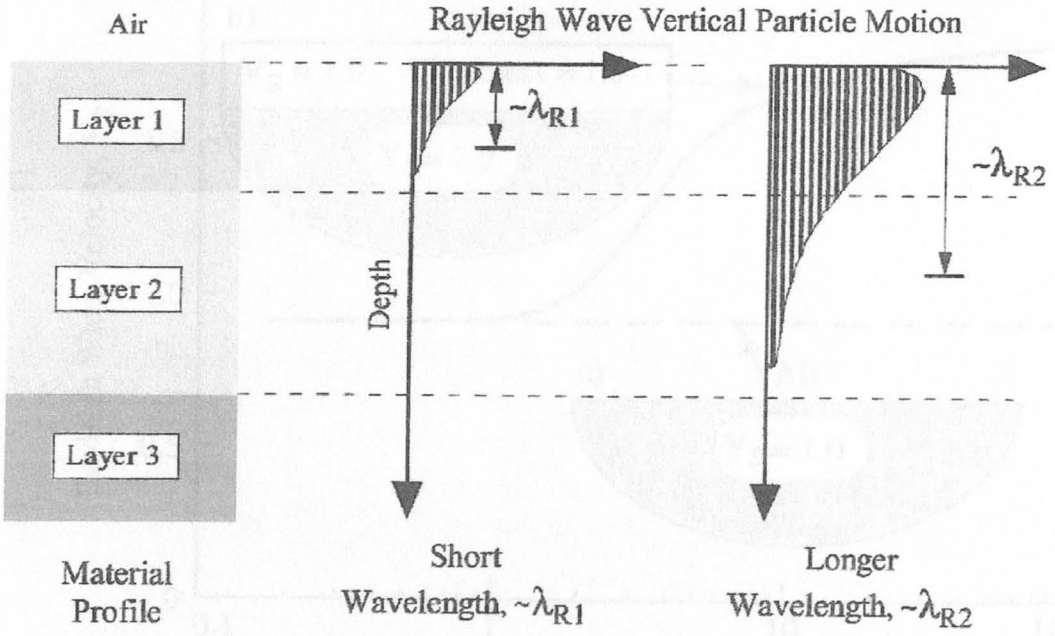

Figure 2.5 Rayleigh waves of different wavelengths that penetrate to different depths, thereby sampling different materials (after Brown, Boore, and Stokoe, 2000).

wavelength (lower frequency) waves propagate through both layer 1 and layer 2. Thus, by using a wide range of surface wave frequencies during testing, one can effectively sample different portions of the layered media.

Rayleigh wave data from a test site are most typically displayed by plotting the Rayleigh wave phase velocity (V_R) versus its corresponding wavelength (λ_R). This type of plot is called a dispersion curve. The variation of velocity with wavelength is related to the variation of the velocity with depth in the media. Two theoretical dispersion curves are shown in Figure 2.6. Figure 2.6a shows that Rayleigh waves propagating in a uniform half-space have a constant velocity (V_R) over every range of wavelengths (λ_R). This velocity will be slightly less than the shear wave velocity (V_S) of the half-space, depending on the value of Poisson's ratio. The dispersion curve for a simple layered

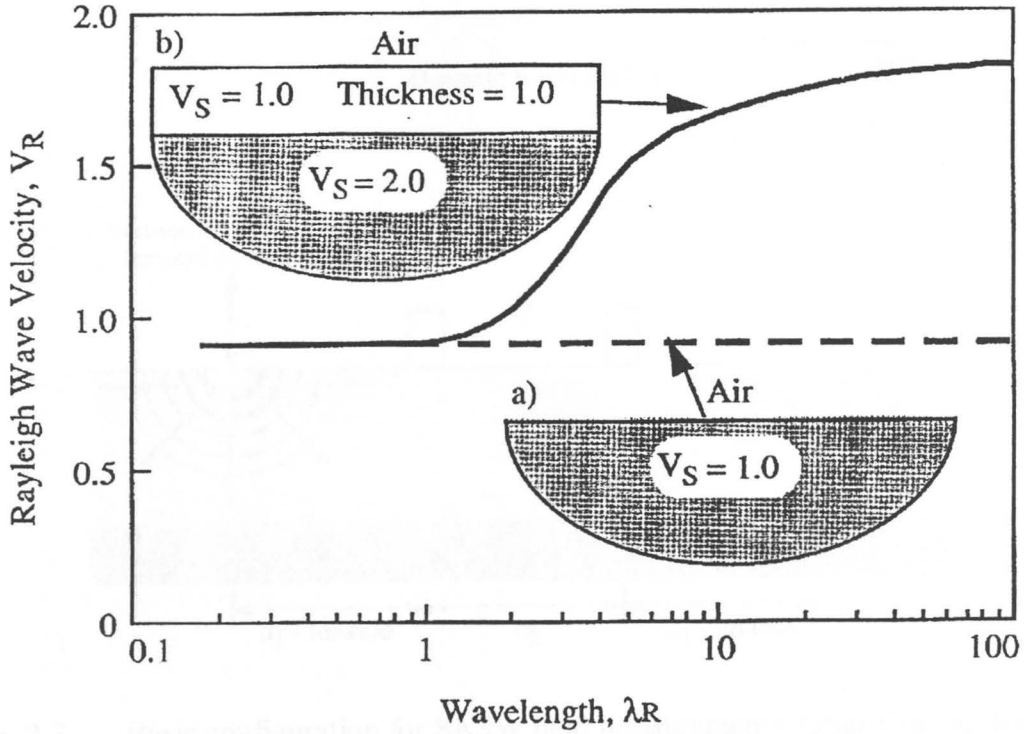

Figure 2.6 Dispersion curves for Rayleigh wave propagations in: a) uniform half-space and b) softer layer over stiffer half-space (after Stokoe et al., 1994).

system, consisting of a softer layer over a stiffer uniform half-space, is shown in Figure 2.6b. For the layered system, V_R varies with wavelength. At wavelengths that are shorter than the thickness of the top layer, V_R is equal to the Rayleigh wave velocity of the top layer. At wavelengths greater than about 30 times the thickness of the top layer, V_R is essentially equal to the Rayleigh wave velocity of the half-space. A transition stage occurs between these wavelengths where V_R is influenced by both layers (Stokoe et al., 1994).

SASW field measurements. Determining a dispersion curve for an actual site requires the measurement of Rayleigh wave velocity (V_R) at various wavelengths (λ_R). Figure 2.7 shows how this is accomplished in the field. A vertical dynamic load is

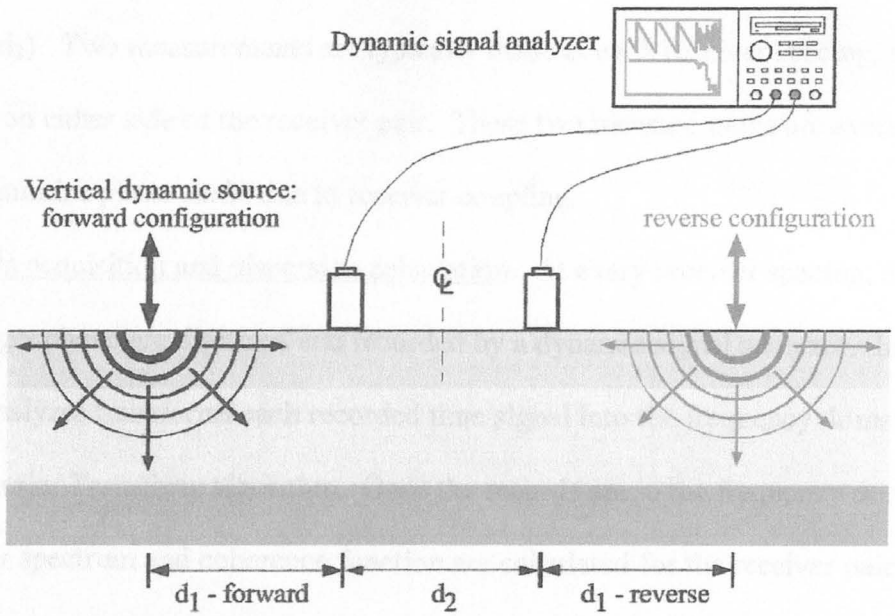

Figure 2.7 Basic configuration for SASW field measurements (after Brown, Boore, and Stokoe, 2000).

applied to the ground surface, which in turn generates a broadband of horizontally propagating Rayleigh waves. Two or more vertically oriented geophones, located on the surface, are used to monitor the passage of these waves. Practical concerns, such as wave attenuation and near-field effects, require the use of several receiver spacings in order to generate the dispersion curve over the range of wavelengths desired (Brown, Boore, and Stokoe, 2000). Typically a constant centerline is maintained and receivers are moved apart to achieve the spacings desired. Handheld hammers are used to generate the small wavelengths needed at close receiver spacings. Drop weights, bulldozers, or vibroseis trucks are used to generate the longer wavelengths required for greater receiver spacings. The distance from the source to the first receiver (d_1) should be greater than one-half of the longest wavelength used from a given receiver spacing in order to minimize near-

field effects. Most often this distance is set equal to the distance separating the two receivers (d_2). Two measurements are typically made at each receiver spacing, one with the source on either side of the receiver pair. These two measurements are averaged in order to minimize phase shifts due to receiver coupling.

Data acquisition and dispersion calculation. At every receiver spacing, the signals from each geophone are digitized and recorded by a dynamic signal analyzer. In real time, the analyzer transforms each recorded time signal into the frequency domain using the Fast Fourier Transform algorithm. Once the records are in the frequency domain, the cross power spectrum and coherence function are calculated for the receiver pair (Stokoe et al., 1994). Typical plots of cross power spectrum phase and coherence are shown in Figure 2.8. The phase of the cross power spectrum represents the phase difference ($\Delta\phi$) between the receivers at each frequency as the wavetrain propagates past. The coherence function represents the signal-to-noise ratio at a given frequency. Coherence values near one represent high-quality data, while values near zero indicate that the data are corrupted by noise. Near-field data (wavelengths longer than twice the receiver spacing) and low coherence data are masked out as shown in Figure 2.8. Once this is accomplished, wavelengths (λ_R) are calculated at each frequency from the unwrapped phase and the distance between receivers by:

$$\lambda_R = \left(\frac{d_2}{\left(\frac{\Delta\phi}{360^\circ} \right)} \right) \qquad \text{(Eq. 2.13)}$$

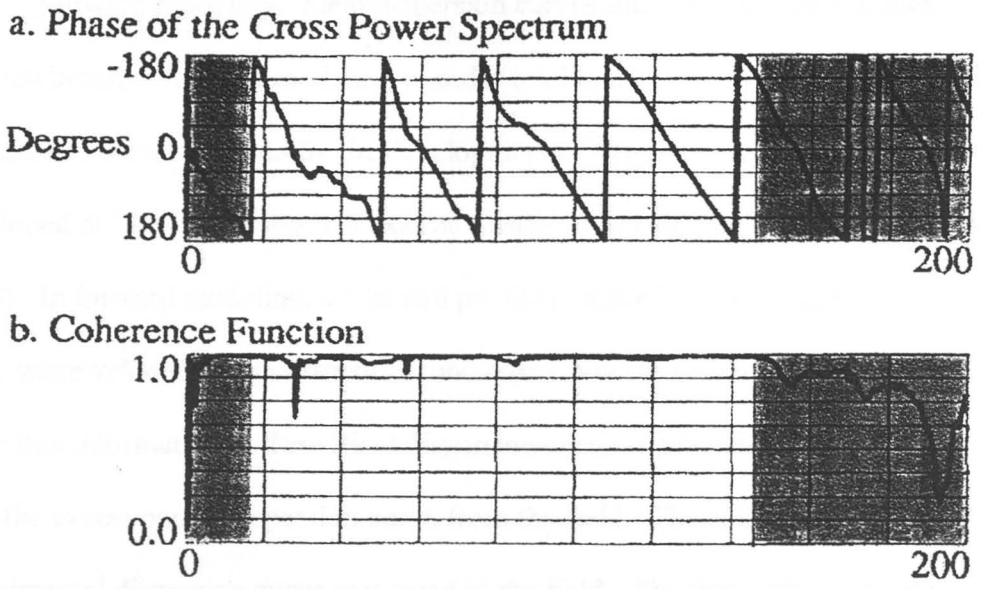

Figure 2.8 a) Wrapped phase of the cross power spectrum and b) coherence function. Shade areas represent near-field and low coherence data that has been masked out (modified from Stokoe et al., 1988).

where: λ_R = Rayleigh wave wavelength,
d_2 = distance between receivers,
$\Delta\phi$ = unwrapped phase of the cross power spectrum, in degrees.

Once λ_R has been determined at each frequency, V_R is easily obtained from the equation:

$$V_R = f(\lambda_R) \qquad \text{(Eq. 2.14)}$$

where: V_R = Rayleigh wave phase velocity,
f = frequency, in cycles per second,
λ_R = Rayleigh wave wavelength

The composite site dispersion curve is obtained by plotting the values of V_R versus λ_R for each set of receiver spacings.

Forward modeling. Field dispersion curves must be reduced and interpreted through iterative forward modeling in order to obtain a shear wave velocity profile. This process has been expedited by the development of WinSASW, a computer program developed at The University of Texas at Austin (Joh, 1992; Brown, Boore, and Stokoe, 2000). In forward modeling, a trial soil profile is made by assuming layer thicknesses, shear wave velocities, mass densities, and either p-wave velocities or Poisson's ratios. From this information, a theoretical dispersion curve is calculated and visually compared with the experimental dispersion curve from the field. The solid line in Figure 2.9 is an experimental dispersion curve measured in the field. The three other curves are theoretical dispersion curves that were generated by assuming soil profiles as mentioned above. This trial-and-error process is used to generate an acceptable match between the experimental and theoretical dispersion curve. In Figure 2.9, Profile 3 is the matching theoretical dispersion curve. The shear wave velocity profile at the site is the final layer thicknesses and shear wave velocities that were assumed to generate the matching theoretical dispersion curve. Figure 2.10 shows the three shear wave velocity profiles that were determined for each of the three trial theoretical dispersion curves in Figure 2.9.

Summary of the SASW method

The SASW method is a powerful nonintrusive test that can be used to evaluate shear wave velocity profiles of various engineering materials. It is reliable and can be performed rapidly, making it very cost effective. Much of the case history data compiled and used by Ron Andrus and colleagues in their shear wave velocity simplified procedure was obtained by the SASW technique (Andrus et al., 2001).

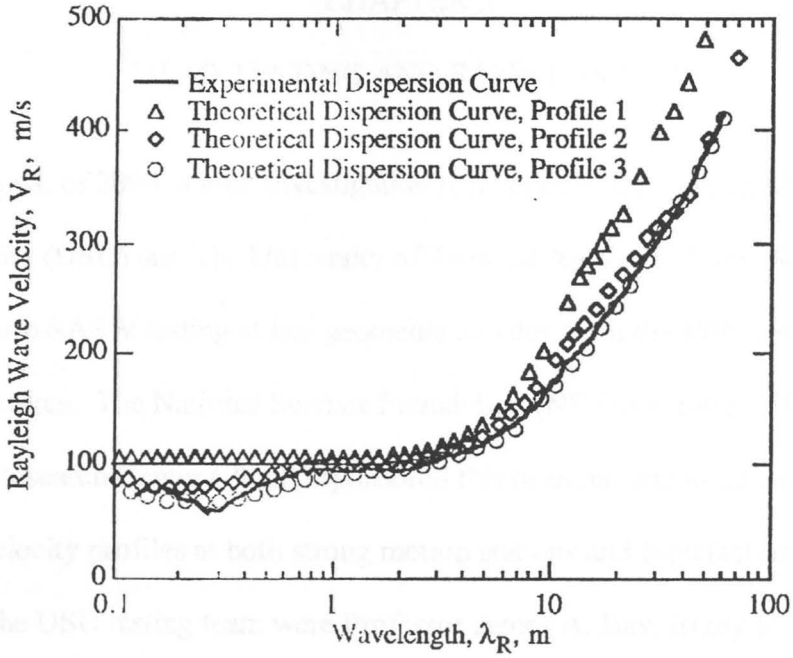

Figure 2.9 Comparison between experimental and assumed theoretical dispersion curves (after Stokoe et al., 1994).

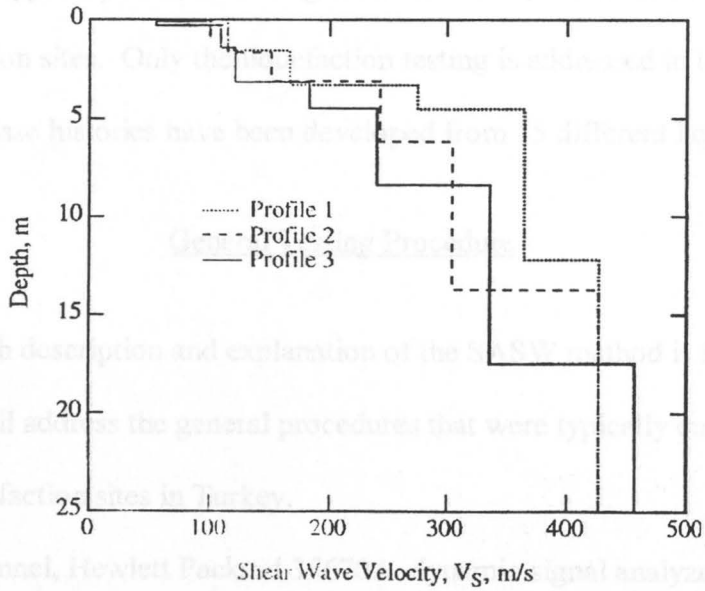

Figure 2.10 Shear wave velocity profiles corresponding to assumed theoretical dispersion curves (after Stokoe et al., 1994).

CHAPTER 3

FIELD TESTING AND SASW RESULTS

In August of 2000, a joint investigation team comprised of researchers from Utah State University (USU) and The University of Texas at Austin (UT) traveled to Turkey in order to perform SASW testing at key geotechnical sites from the 1999 Kocaeli and Duzce earthquakes. The National Science Foundation (NSF) and the Pacific Earthquake Engineering Research Center (PEER) sponsored this research due to the need for accurate shear wave velocity profiles at both strong motion stations and liquefaction sites. Members of the USU testing team were Professor James A. Bay, Brady R. Cox, and Aaron Budge. Members of the UT testing team were Professor Kenneth H. Stokoe, II, Professor Ellen Rathje, Brent Rosenblad, and Mehmet Darendeli. As a division of labor, the team from UT typically tested at strong motion stations, while the team from USU tested at liquefaction sites. Only the liquefaction testing is addressed in this paper. Nineteen SASW case histories have been developed from 15 different liquefaction sites.

General Testing Procedure

An in-depth description and explanation of the SASW method is found in Chapter 2. This section will address the general procedures that were typically employed while testing at the liquefaction sites in Turkey.

A four-channel, Hewlett Packard 35670A, dynamic signal analyzer was used by USU to collect the data at each site. This analyzer allowed for the use of a three-receiver test array as shown in Figure 3.1. The receivers used in Turkey were 1 Hz seismometers

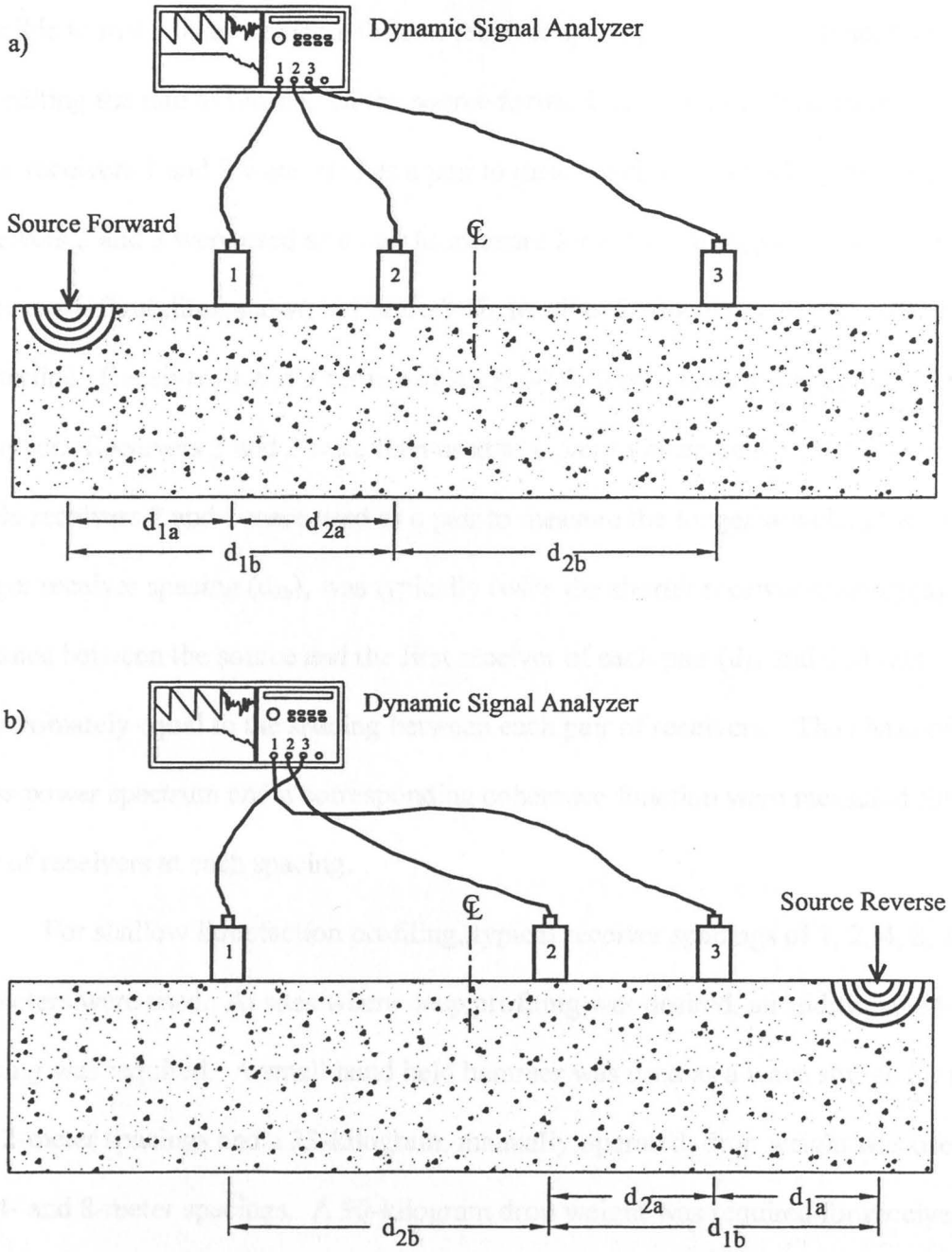

Figure 3.1 SASW testing at liquefaction sites in Turkey facilitated by using a three-receiver array. a) The source forward configuration and b) the source reverse configuration.

(geophones) manufactured by Mark Products. By using a three-receiver test array, it was possible to make measurements for two receiver spacings at the same time, thereby expediting the rate of testing. In the source forward test configuration, shown in Figure 3.1a, receivers 1 and 2 were used as a pair to measure shorter wavelengths, while receivers 2 and 3 were used as a pair to measure longer wavelengths. For the source-reverse configuration, shown in Figure 3.1b, receiver 2 was moved to the other side of the centerline. Receivers 1 and 3 remained static while their cables swapped channels on the analyzer. Receivers 3 and 2 were then used as a pair to measure the shorter wavelengths, while receivers 2 and 1 were used as a pair to measure the longer wavelengths. The longer receiver spacing (d_{2b}), was typically twice the shorter receiver spacing (d_{2a}). The distance between the source and the first receiver of each pair (d_{1a} and d_{1b}) was approximately equal to the spacing between each pair of receivers. The phase of the cross power spectrum and a corresponding coherence function were measured for each pair of receivers at each spacing.

For shallow liquefaction profiling, typical receiver spacings of 1, 2, 4, 8, 16, and 32 meters were used. At sites where deep profiling was desired, an additional 64-meter spacing was required. A small hand held hammer was used as a wave source for the 1- and 2-meter spacings and a 23-kilogram, manually operated, drop weight was used for the 4- and 8-meter spacings. A 90-kilogram drop weight was required for receiver spacings of 16 and 32 meters. This large weight was raised using a lightweight aluminum tripod and winch, and then dropped by triggering a quick release. This system is shown in the photograph in Figure 3.2. Deep liquefaction profiling was performed at two sites. This required the use of a bulldozer as a source (see Figure 3.3).

Figure 3.2 Photograph of the aluminum tripod and 90-kilogram weight used for 16- and 32-meter receiver spacings.

Figure 3.3 Photograph of the bulldozer used as a source at liquefaction sites where deep profiling was desired.

The bulldozer was used as a wave source by positioning it at the appropriate distance, and then having the operator walk it back and forth over a distance of 1 - 2 meters repeatedly. This created sufficient low-frequency energy to generate wavelengths for a 64-meter receiver spacing.

The procedure outlined above was used to perform SASW testing at 15 separate liquefaction sites. Each site will be discussed in detail below.

Liquefaction Sites

A reconnaissance team from the Earthquake Engineering Research Institute (EERI) arrived in Turkey just days after the Kocaeli earthquake. This group assisted in organizing the efforts of other reconnaissance teams and private researchers so as to optimize the effort to investigate earthquake damage and plan further research. One of these important groups was the U.S.-Turkey NSF Geotechnical Earthquake Engineering reconnaissance team. This team performed aerial and land surveys directed at investigating ground failures that developed during the earthquake. From these reconnaissance efforts, a number of "representative" case histories were selected for further detailed study. These researchers found particular interest in liquefaction ground failures that occurred throughout the city of Adapazari, and lateral spreading that occurred along the shores of Lake Sapanca and Izmit Bay. A full account of reconnaissance efforts and participants can by found in EERI (2000).

Additional post-earthquake research at these ground failure sites was spearheaded by a joint group of researchers from the University of California at Berkeley, Brigham Young University, the University of California at Los Angeles, ZETAS Earth

Technology Corporation, Middle East Technical University, and Sakarya University. Their investigations have included large-scale SPT and CPT testing in addition to detailed site mapping. It was desired that SASW testing should be performed at many of the same sites where these investigators were focusing their efforts. Professor Ellen Rathje from UT was able to coordinate efforts with these other researchers to determine at which liquefaction sites shear wave velocity profiles would be most helpful. Therefore, the majority of site maps and pictures for the SASW case histories presented below have been obtained from the above-mentioned researchers at a website detailing all of their efforts (www.eerc.berkeley.edu/turkey/adapazari). Professor John D. Bray and Rodolfo B. Sancio of the University of California at Berkeley, and Professor T. L. Youd of Brigham Young University have since provided particular help and cooperation with liquefaction site details.

Nineteeen SASW centerlines were tested at 15 different liquefaction sites. The locations of these sites are shown on a large-scale map in Figure 3.4. Since the majority of sites are located in the city of Adapazari, a separate map detailing the test locations in this city is shown in Figure 3.5. Full descriptions of each site can be found in EERI (2000). Additional work provided by other researchers at these same sites can also be found at the website listed above. The SASW results from each test are given below.

Adapazari

The city of Adapazari, located approximately 7 km north of the fault rupture, suffered the highest degree of property damage and life loss of any city affected by the

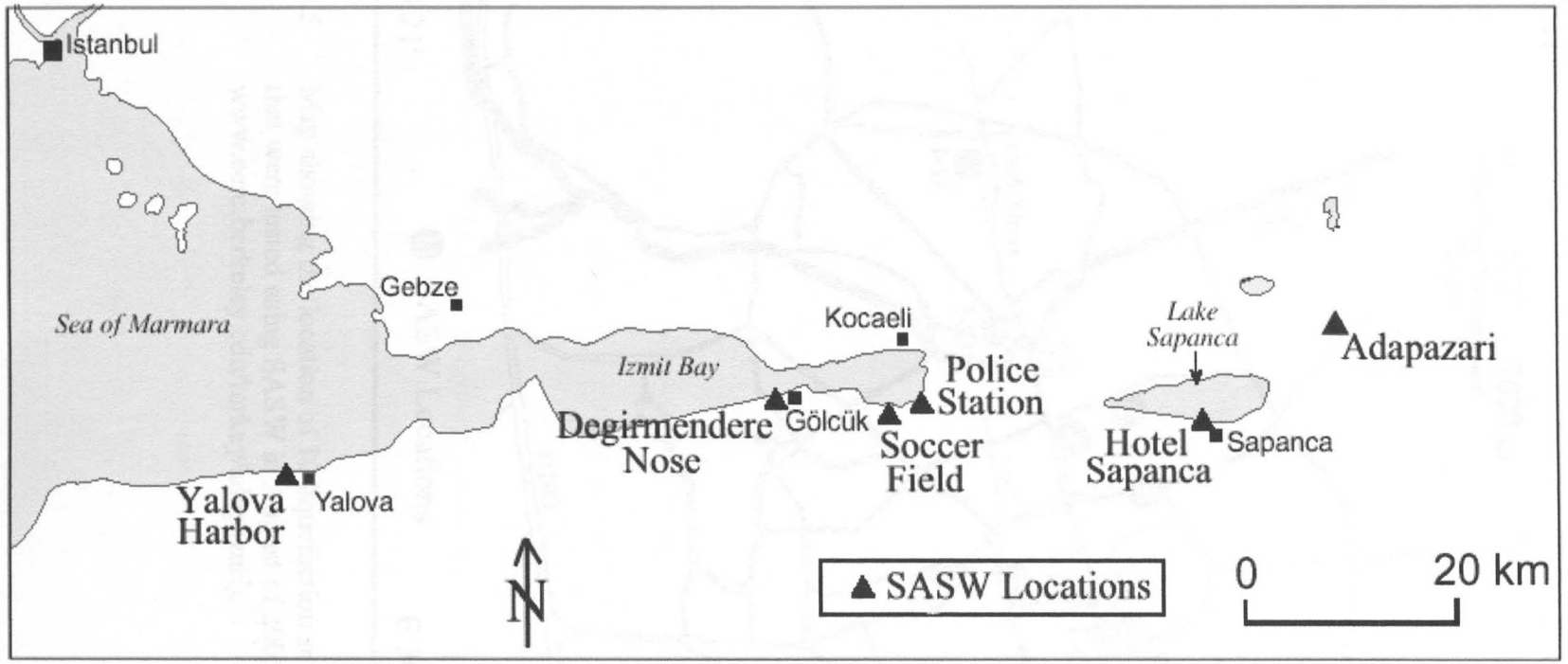

Figure 3.4 Map showing the location of the liquefaction sites that were tested using SASW in August of 2000 (modified from www.eerc.berkeley.edu/turkey/adapazari).

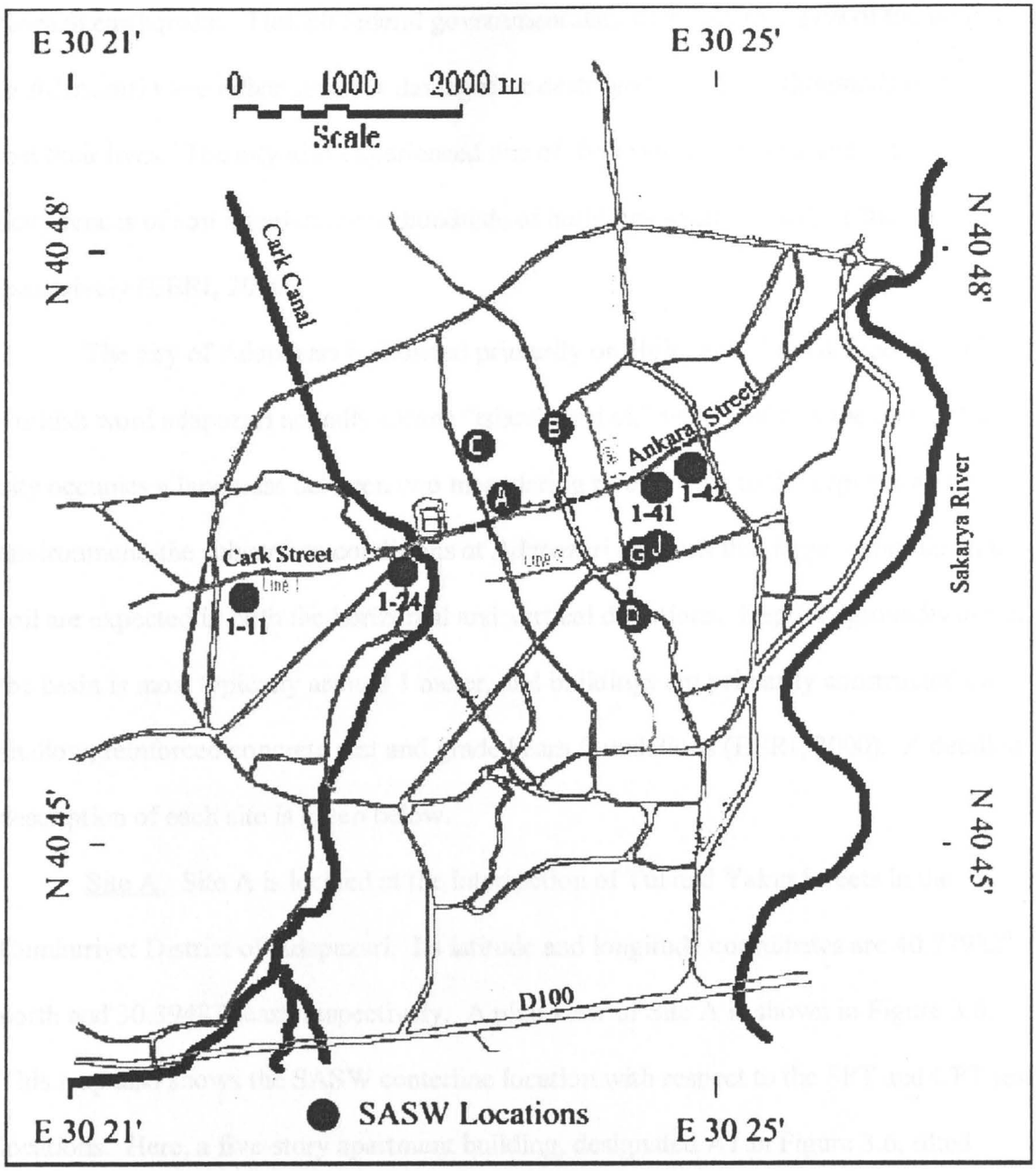

Figure 3.5 Map showing the location of 10 liquefaction sites in the city of Adapazari that were tested using SASW in August of 2000 (modified from www.eerc.berkeley.edu/turkey/adapazari).

Kocaeli earthquake. Turkish federal government data indicates that 27% of the buildings in Adapazari were either severely damaged or destroyed. Literally thousands of people lost their lives. The city also experienced one of the most spectacular and extensive occurrences of soil liquefaction as hundreds of buildings settled, tilted, or translated excessively (EERI, 2000).

The city of Adapazari is founded primarily on Holocene alluvial deposits. The Turkish word adapazari actually means "island market," which reflects the fact that the city occupies a landmass between two meandering rivers. Due to the depositional environment, the subsurface conditions at Adapazari are such that large variations in the soil are expected in both the horizontal and vertical directions. Depth to groundwater in the basin is most typically around 1 meter, and buildings are primarily constructed on shallow, reinforced concrete mat and grade beam foundations (EERI, 2000). A detailed description of each site is given below.

Site A. Site A is located at the intersection of Tul and Yakin Streets in the Cumhuriyet District of Adapazari. Its latitude and longitude coordinates are 40.77922° north and 30.39487° east, respectively. A plan view of Site A is shown in Figure 3.6. This map also shows the SASW centerline location with respect to the SPT and CPT test locations. Here, a five-story apartment building, designated A1 in Figure 3.6, tilted excessively when its northwest corner settled approximately 1.5 meters. A photograph of this building is shown in Figure 3.7. At this same location, another five-story building, designated A2 in Figure 3.6, settled approximately 60 cm. Figure 3.8 shows the experimental dispersion curve measured at Site A. Figure 3.9 shows the comparison

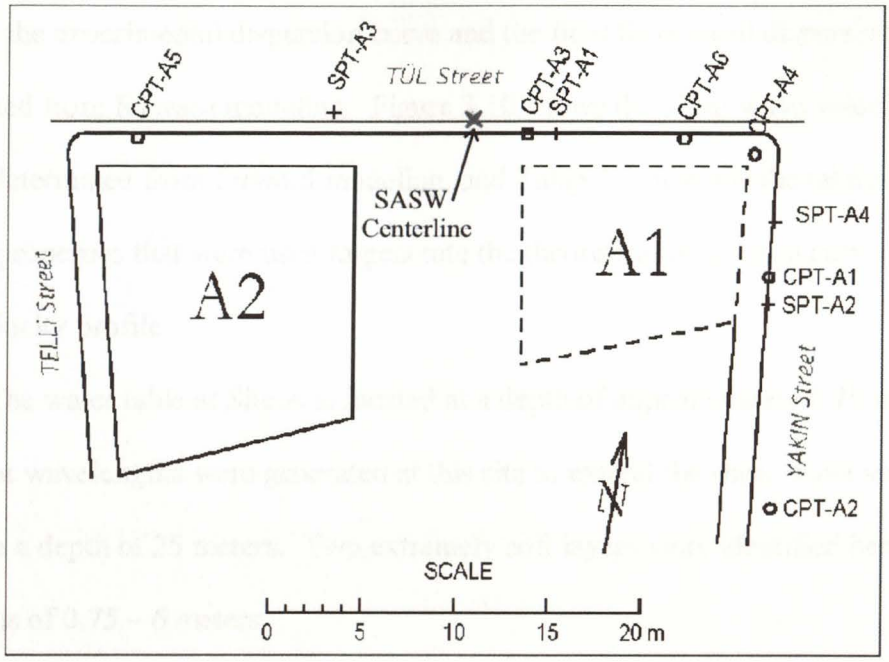

Figure 3.6 Plan view of Site A showing the location of one SASW centerline (modified from www.eerc.berkeley.edu/turkey/adapazari).

Figure 3.7 Photograph of building A1 showing the severe tilting that occurred when its northwest corner settled approximately 1.5 meters (from www.eerc.berkeley.edu/turkey/adapazari).

between the experimental dispersion curve and the final theoretical dispersion curve determined from forward modeling. Figure 3.10 shows the shear wave velocity profile at the site determined from forward modeling, and Table 3.1 presents the tabulated values of layer properties that were used to generate the theoretical dispersion curve and shear wave velocity profile.

The water table at Site A is located at a depth of approximately 0.75 meters. Sufficient wavelengths were generated at this site to extend the shear wave velocity profile to a depth of 25 meters. Two extremely soft layers were identified here between the depths of 0.75 – 6 meters.

Site B. Site B is located at the intersection of Kuyudibi Avenue and Yaprak Street in the Karaosman District of Adapazari. Its latitude and longitude coordinates are 40.78513° north and 30.40024° east, respectively. A plan view of Site B is shown in Figure 3.11. This map also shows the SASW centerline location with respect to the SPT and CPT test locations. Here, liquefaction of foundation soil induced a bearing capacity failure that caused a five-story building, designated B1 in Figure 3.11, to tip over. A photograph of building B1 is shown in Figure 3.12. Figure 3.13 shows the experimental dispersion curve measured at Site B. Figure 3.14 shows the comparison between the experimental dispersion curve and the final theoretical dispersion curve determined from forward modeling. Figure 3.15 shows the shear wave velocity profile at the site determined from forward modeling, and Table 3.2 presents the tabulated values of layer properties that were used to generate the theoretical dispersion curve and shear wave velocity profile.

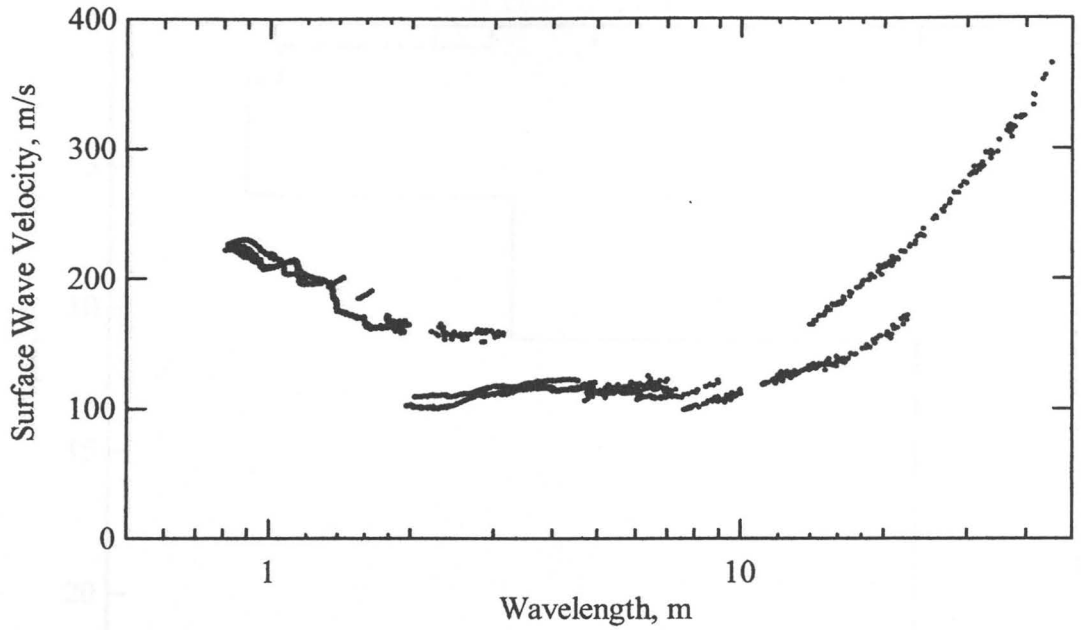

Figure 3.8 Experimental dispersion curve measured at Site A, Aug. 15, 2000, Adapazari, Turkey.

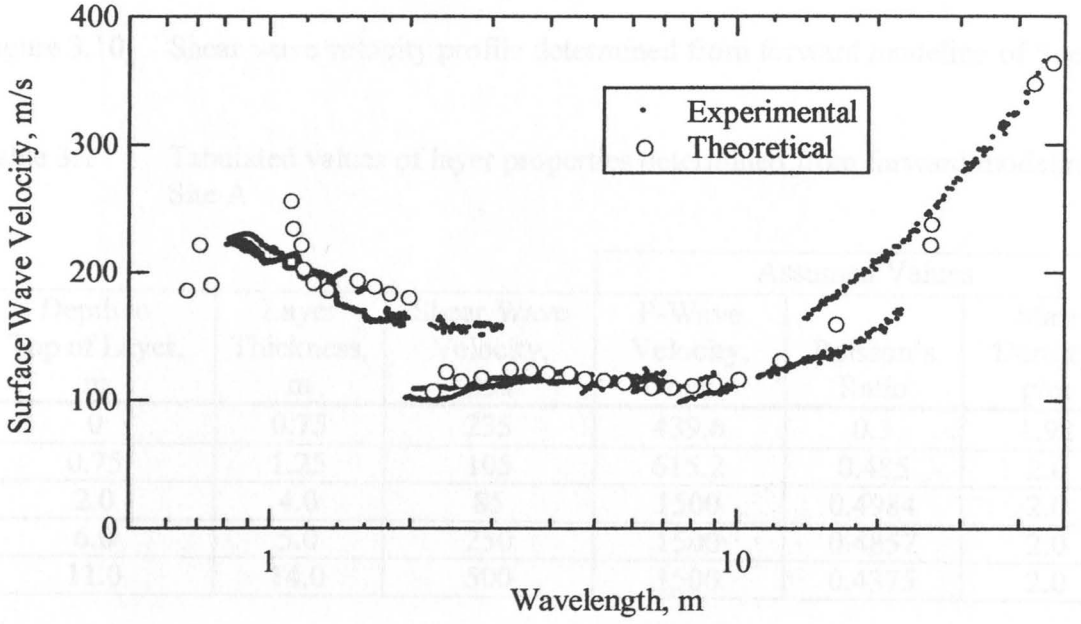

Figure 3.9 Comparison of experimental and theoretical dispersion curves from Site A.

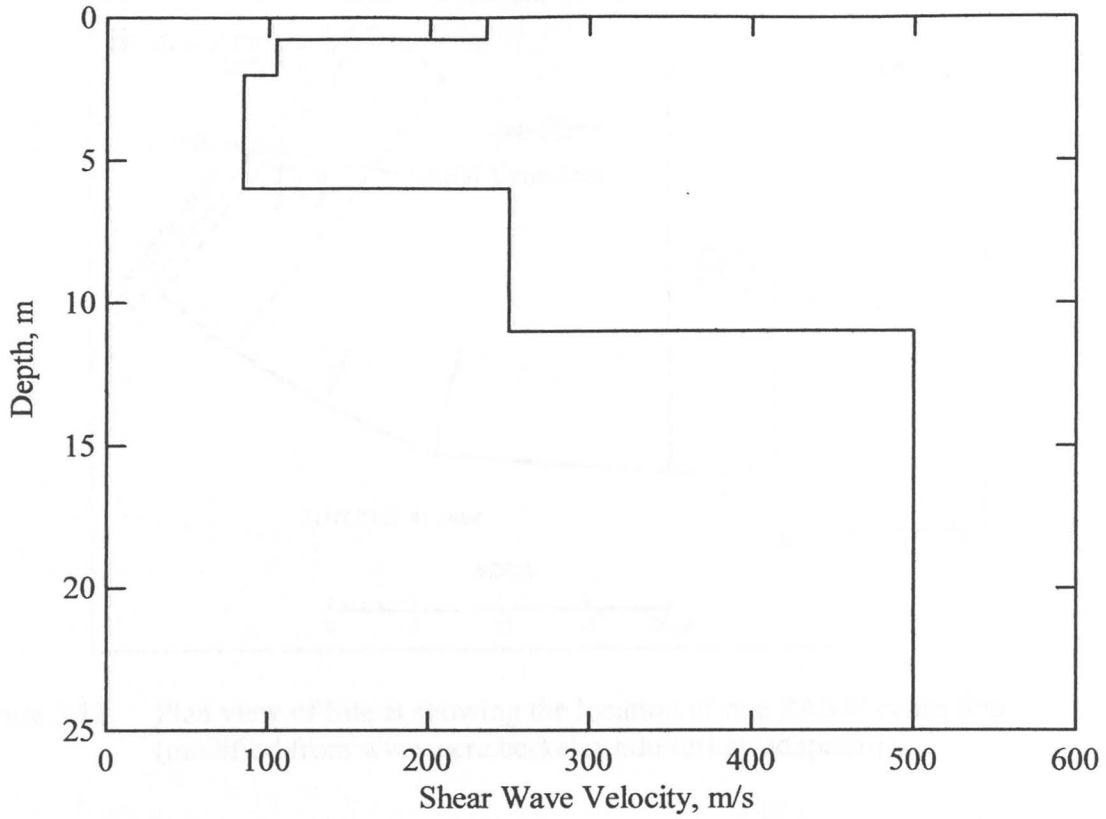

Figure 3.10 Shear wave velocity profile determined from forward modeling of Site A.

Table 3.1 Tabulated values of layer properties determined from forward modeling of Site A

			Assumed Values		
Depth to Top of Layer, m	Layer Thickness, m	Shear Wave Velocity, m/s	P-Wave Velocity, m/s	Poisson's Ratio	Mass Density, g/cc
0	0.75	235	439.6	0.3	1.92
0.75	1.25	105	615.2	0.485	2.0
2.0	4.0	85	1500	0.4984	2.0
6.0	5.0	250	1500	0.4857	2.0
11.0	14.0	500	1500	0.4375	2.0

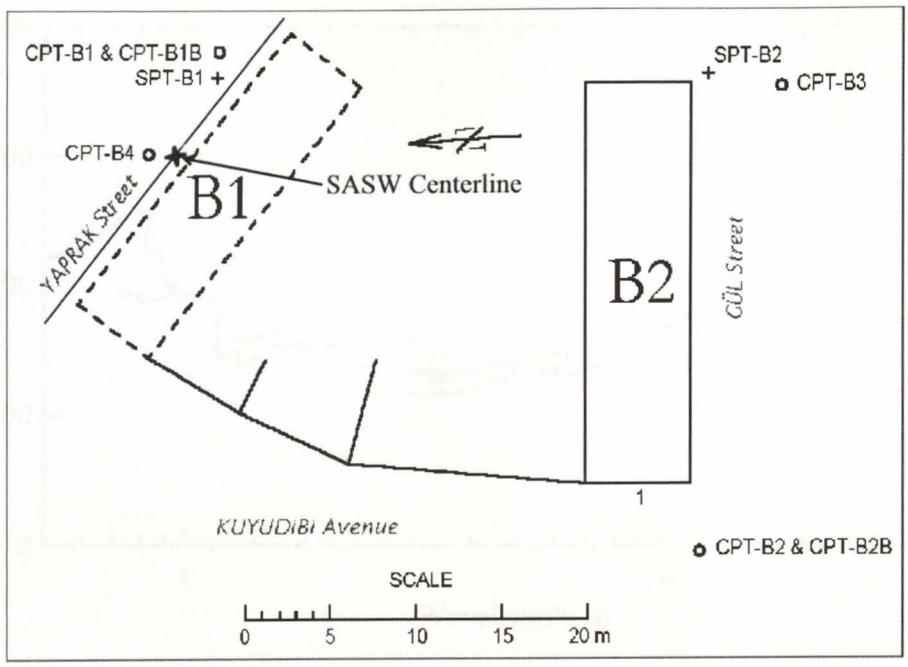

Figure 3.11 Plan view of Site B showing the location of one SASW centerline (modified from www.eerc.berkeley.edu/turkey/adapazari).

Figure 3.12 Photograph showing building B1 after it tipped over due to liquefaction of its foundation soil (from www.eerc.berkeley.edu/turkey/adapazari).

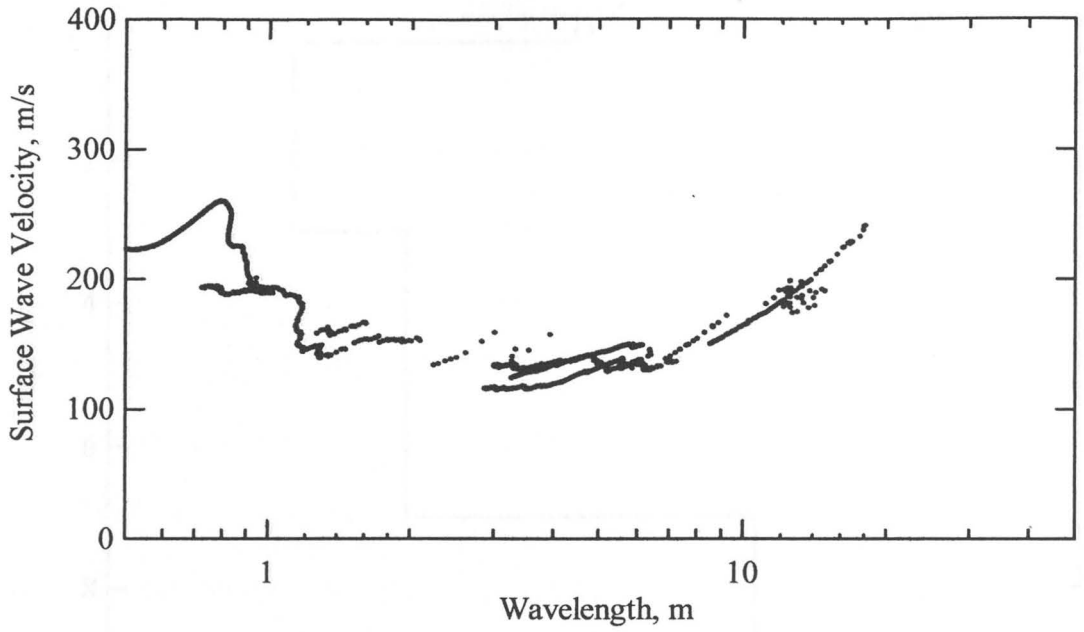

Figure 3.13 Experimental dispersion curve measured at Site B, Aug. 16, 2000, Adapazari, Turkey.

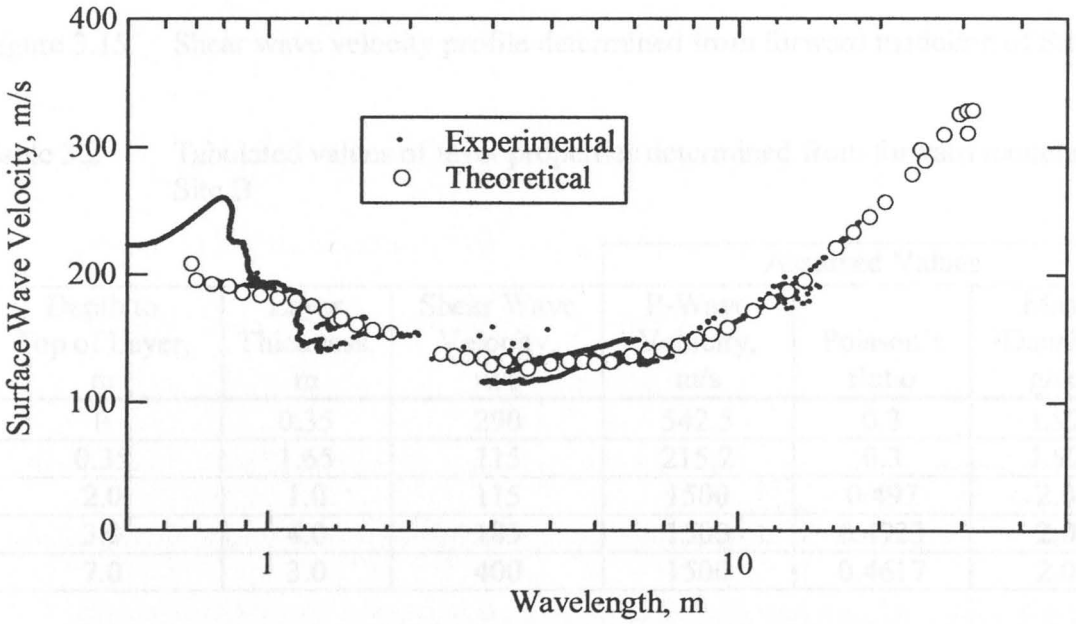

Figure 3.14 Comparison of experimental and theoretical dispersion curves from Site B.

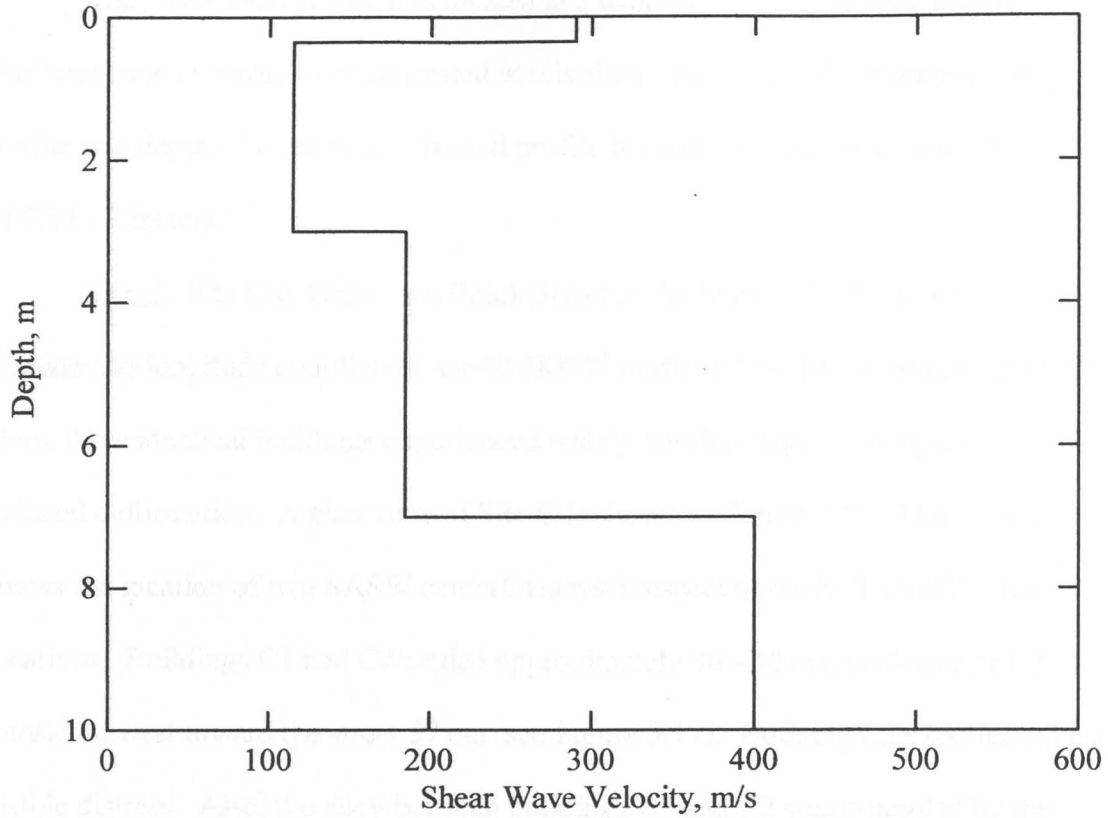

Figure 3.15 Shear wave velocity profile determined from forward modeling of Site B.

Table 3.2 Tabulated values of layer properties determined from forward modeling of Site B

			Assumed Values		
Depth to Top of Layer, m	Layer Thickness, m	Shear Wave Velocity, m/s	P-Wave Velocity, m/s	Poisson's Ratio	Mass Density, g/cc
0	0.35	290	542.5	0.3	1.92
0.35	1.65	115	215.2	0.3	1.92
2.0	1.0	115	1500	0.497	2.0
3.0	4.0	185	1500	0.4923	2.0
7.0	3.0	400	1500	0.4617	2.0

The water table at Site B is located at a depth of approximately 2 meters. Sufficient wavelengths were generated at this site to extend the shear wave velocity profile to a depth of 10 meters. The soil profile is extremely soft here between the depths of 0.35 - 7 meters.

Site C. Site C is located on Boluk Street in the Istikal District of Adapazari. Its latitude and longitude coordinates are 40.78370° north and 30.39221° east, respectively. Here, three identical buildings experienced widely varying degrees of liquefaction-induced deformation. A plan view of Site C is shown in Figure 3.16. This map also shows the location of two SASW centerlines with respect to the SPT and CPT test locations. Buildings C1 and C2 settled approximately 30 - 40 cm, additionally C2 translated west toward the street 57 cm (see Figure 3.17). Building C3 experienced no visible distress. Also, the alley between buildings C1 and C2 was crumpled by the building deformations (see Figure 3.18), but the alley between C2 and C3 was not damaged.

Two SASW tests were performed at Site C to investigate the lateral variability that caused the two northernmost buildings to experience large deformations, while the identical southernmost building experienced no deformation. However, on the day of testing, a bazaar located on the road in front of the buildings necessitated testing in a small area behind the buildings. Due to a lack of space, the southern centerline was positioned much closer to the northern centerline than desired.

Figure 3.19 shows the experimental dispersion curve measured at Site C North Centerline. Figure 3.20 shows the comparison between the experimental dispersion curve and the final theoretical dispersion curve determined from forward modeling of the

north centerline. Figure 3.21 shows the shear wave velocity profile determined from forward modeling, and Table 3.3 presents the tabulated values of layer properties that were used to generate the theoretical dispersion curve and shear wave velocity profile for the North Centerline.

Figure 3.22 shows the experimental dispersion curve measured at Site C South Centerline. Figure 3.23 shows the comparison between the experimental dispersion curve and the final theoretical dispersion curve determined from forward modeling of the south centerline. Figure 3.24 shows the shear wave velocity profile determined from forward modeling, and Table 3.4 presents the tabulated values of layer properties that were used to generate the theoretical dispersion curve and shear wave velocity profile for the south centerline.

The water table at Site C is located at a depth of approximately 1 meter. Sufficient wavelengths were generated at this site to extend the shear wave velocity profile to a depth of 25 meters. Both shear wave velocity profiles show extremely soft soils from the ground surface to a depth of approximately 5 meters.

Site D. Site D is located on Meydan Street in the Cukurahmediye District of Adapazari. Its latitude and longitude coordinates are 40.76929° north and 30.40828° east, respectively. A plan view of Site D is shown in Figure 3.25. This map also shows the SASW centerline location with respect to the SPT and CPT test locations. Here, liquefaction of foundation soil caused a five-story building, designated D1in Figure 3.25, to settle approximately 44 cm, and translate approximately 55 cm to the west and 100 cm to the south. A picture of building D1 is shown in Figure 3.26. Figure 3.27 shows the experimental dispersion curve measured at Site D. Figure 3.28 shows the comparison

between the experimental dispersion curve and the final theoretical dispersion curve determined from forward modeling. Figure 3.29 shows the shear wave velocity profile at the site determined from forward modeling, and Table 3.5 presents the tabulated values of layer properties that were used to generate the theoretical dispersion curve and shear wave velocity profile.

The water table at Site D is located at a depth of approximately 1.5 meters. Sufficient wavelengths were generated at this site to extend the shear wave velocity profile to a depth of 15 meters. The entire soil profile consists of soft soils having shear wave velocities of less than 200 m/s.

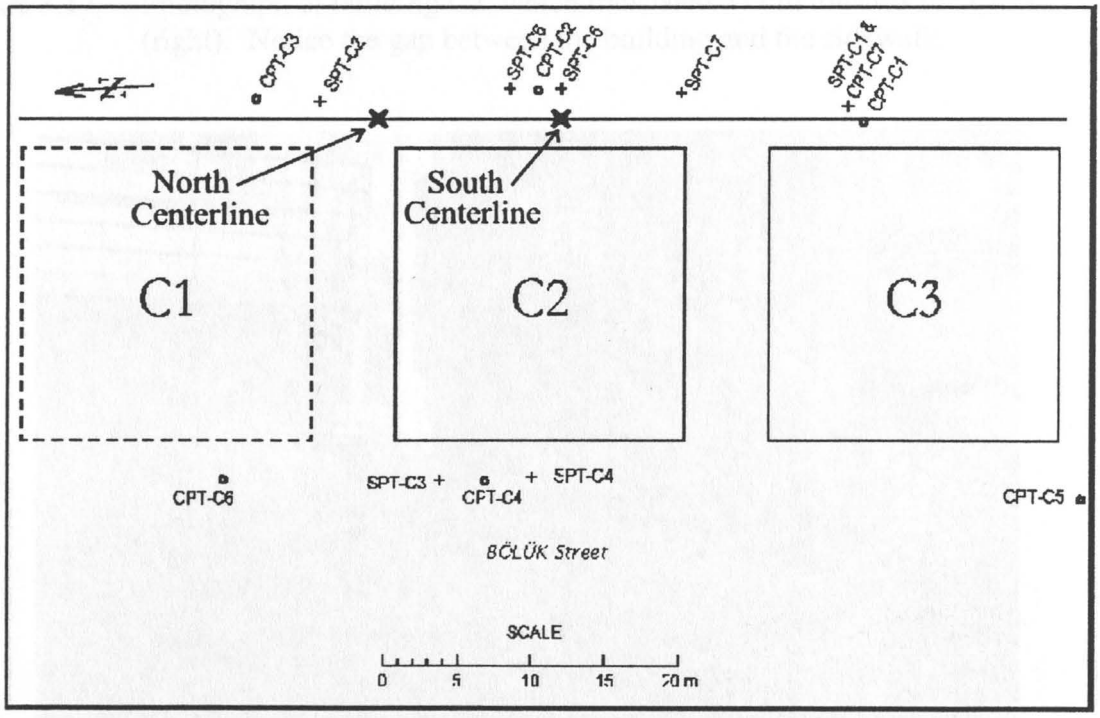

Figure 3.16 Plan view of Site C showing the location of two SASW centerlines (modified from www.eerc.berkeley.edu/turkey/adapazari).

Figure 3.17 Photograph of building C2, which translated 57 cm towards the street (right). Notice the gap between the building and the sidewalk.

Figure 3.18 Photograph of the alley between buildings C1 and C2, which was crumpled by settlement and translation of the buildings (from www.eerc.berkeley.edu/turkey/adapazari).

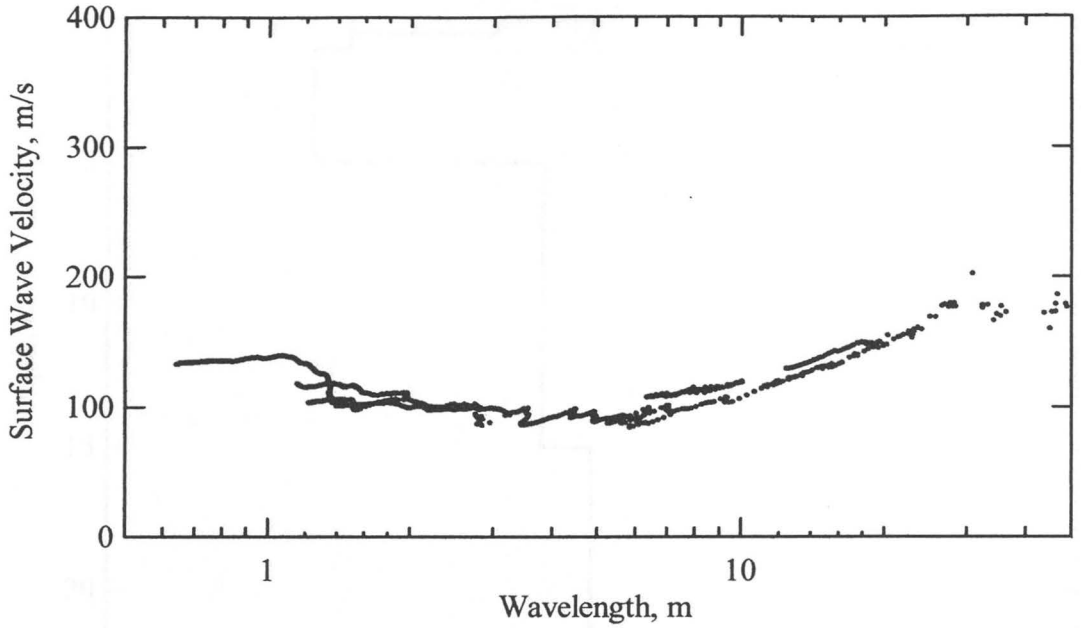

Fig. 3.19 Experimental dispersion curve measured at Site C North Centerline, Aug. 21, 2000, Adapazari, Turkey.

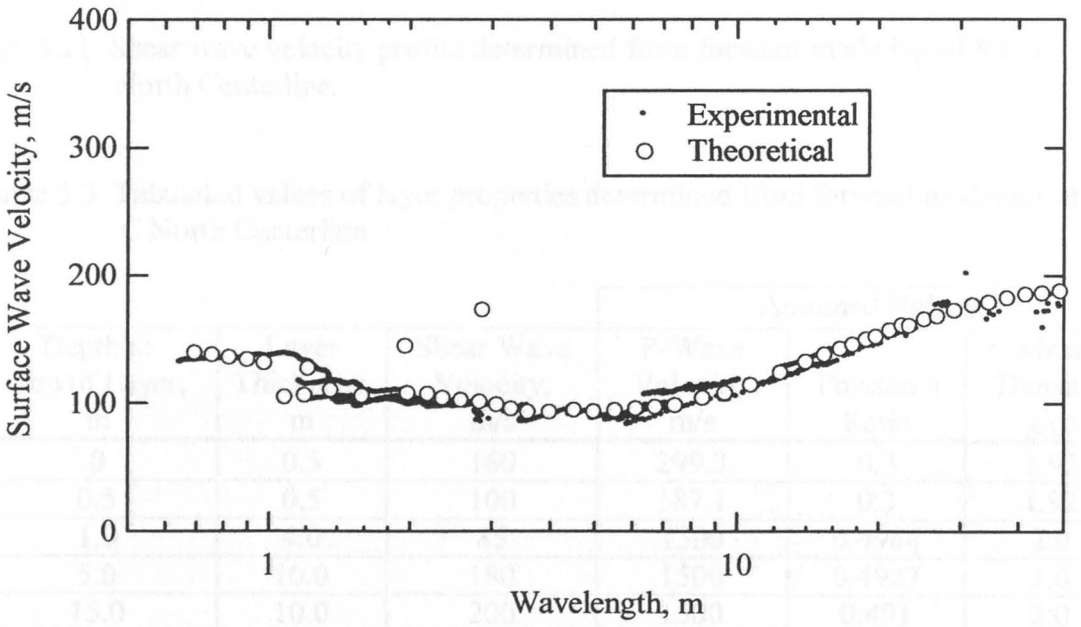

Fig. 3.20 Comparison of experimental and theoretical dispersion curves from Site C North Centerline.

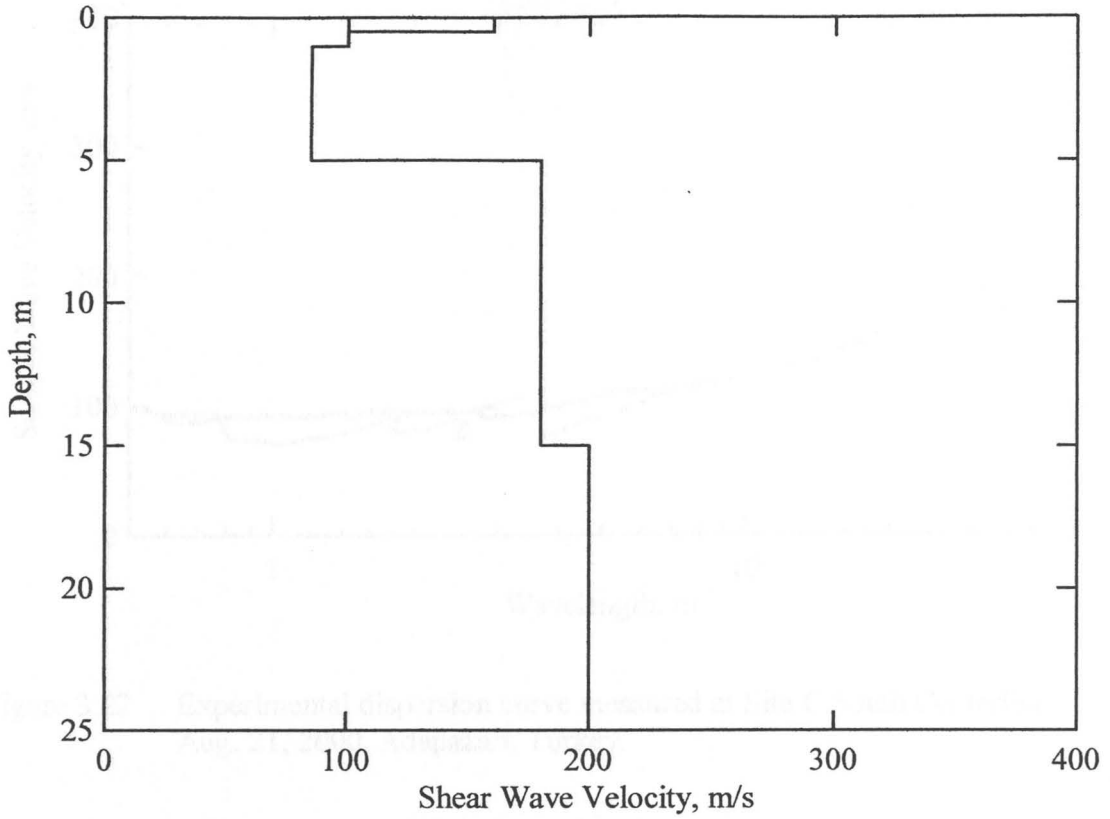

Fig. 3.21 Shear wave velocity profile determined from forward modeling of Site C North Centerline.

Table 3.3 Tabulated values of layer properties determined from forward modeling of Site C North Centerline

			Assumed Values		
Depth to Top of Layer, m	Layer Thickness, m	Shear Wave Velocity, m/s	P-Wave Velocity, m/s	Poisson's Ratio	Mass Density, g/cc
0	0.5	160	299.3	0.3	1.92
0.5	0.5	100	187.1	0.3	1.92
1.0	4.0	85	1500	0.4984	2.0
5.0	10.0	180	1500	0.4927	2.0
15.0	10.0	200	1500	0.491	2.0

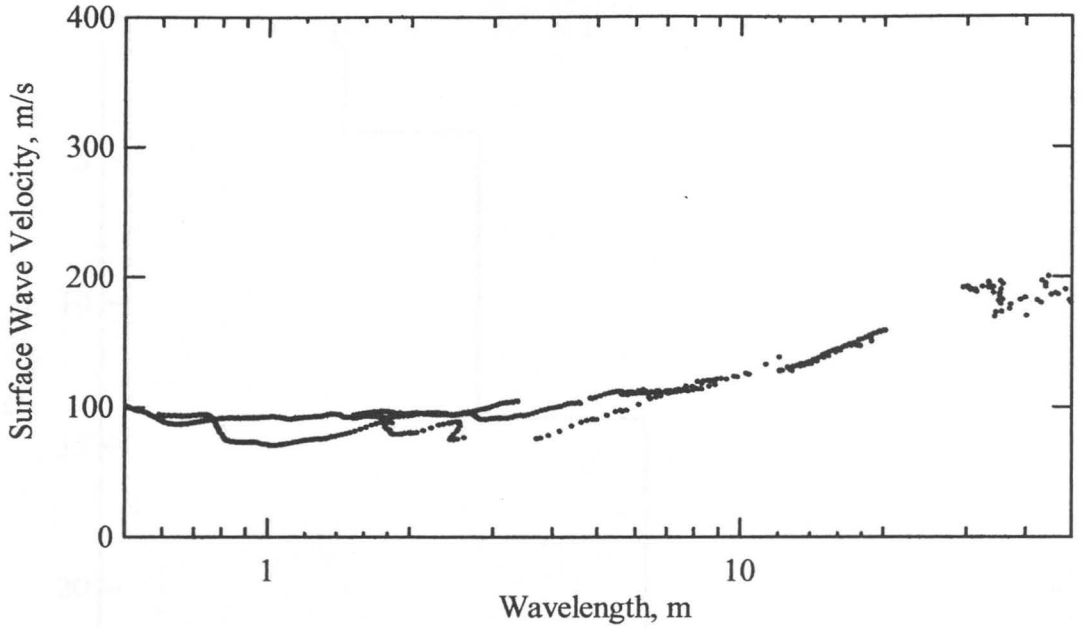

Figure 3.22 Experimental dispersion curve measured at Site C South Centerline, Aug. 21, 2000, Adapazari, Turkey.

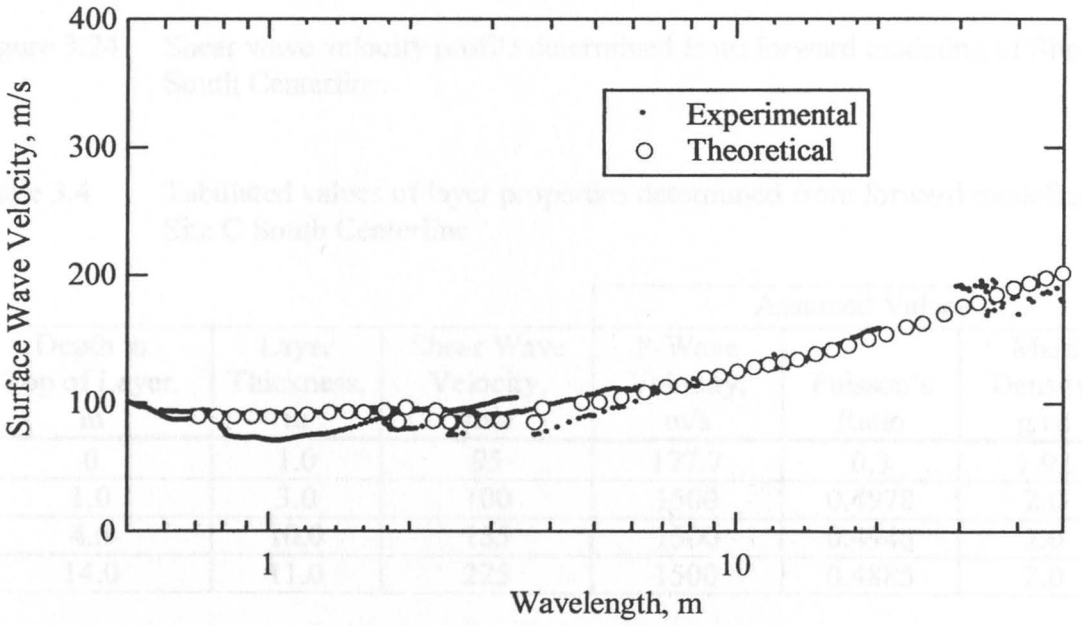

Figure 3.23 Comparison of experimental and theoretical dispersion curves from Site C South Centerline.

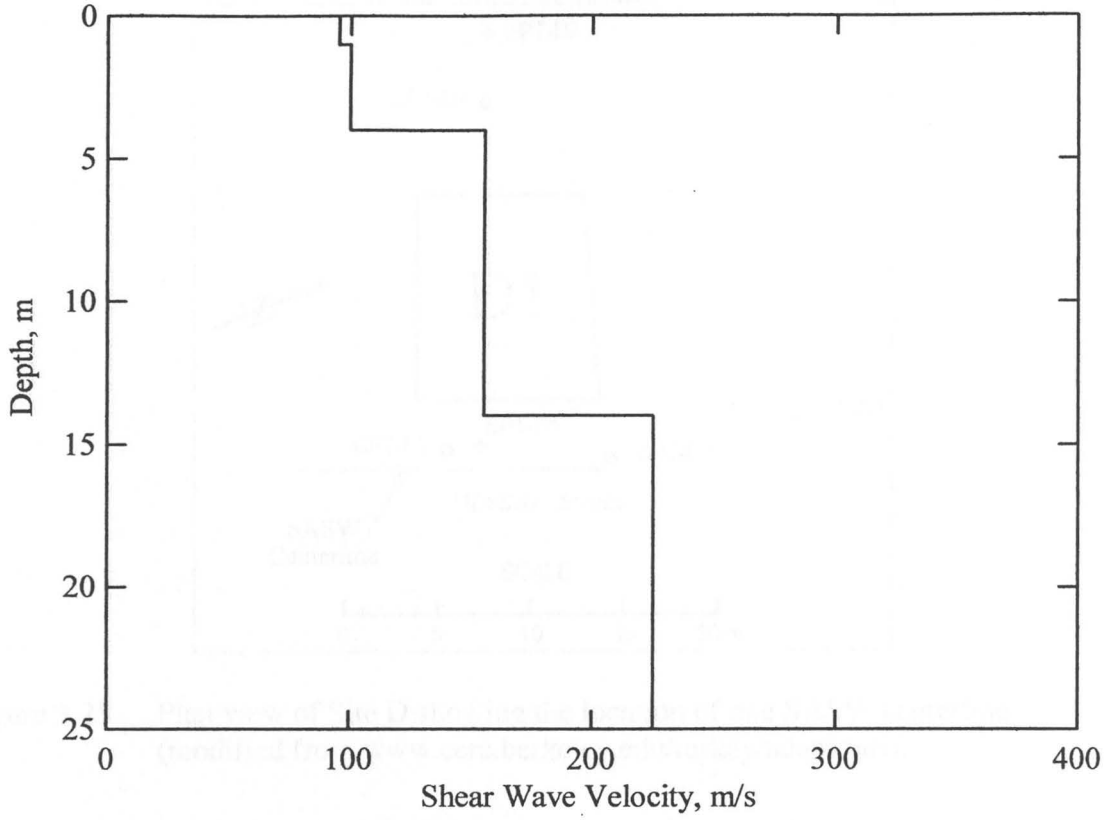

Figure 3.24 Shear wave velocity profile determined from forward modeling of Site C South Centerline.

Table 3.4 Tabulated values of layer properties determined from forward modeling of Site C South Centerline

			Assumed Values		
Depth to Top of Layer, m	Layer Thickness, m	Shear Wave Velocity, m/s	P-Wave Velocity, m/s	Poisson's Ratio	Mass Density, g/cc
0	1.0	95	177.7	0.3	1.92
1.0	3.0	100	1500	0.4978	2.0
4.0	10.0	155	1500	0.4946	2.0
14.0	11.0	225	1500	0.4885	2.0

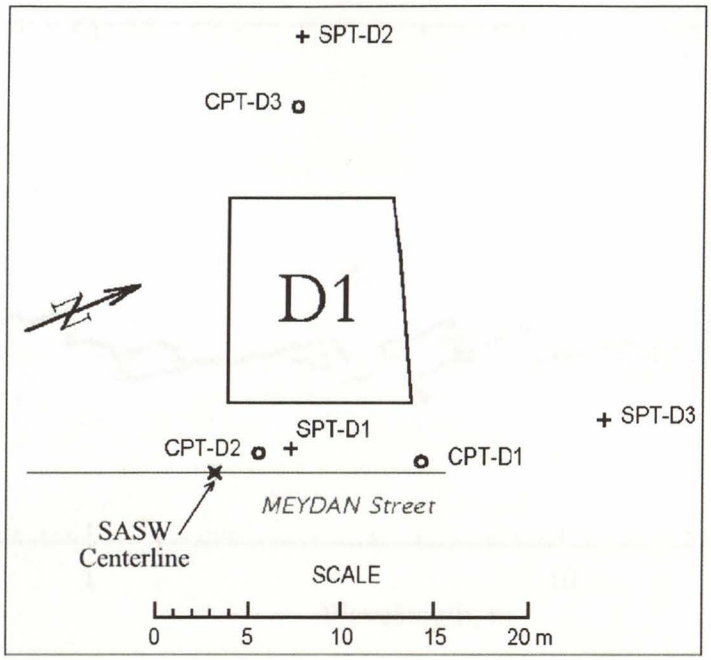

Figure 3.25 Plan view of Site D showing the location of one SASW centerline (modified from www.eerc.berkeley.edu/turkey/adapazari).

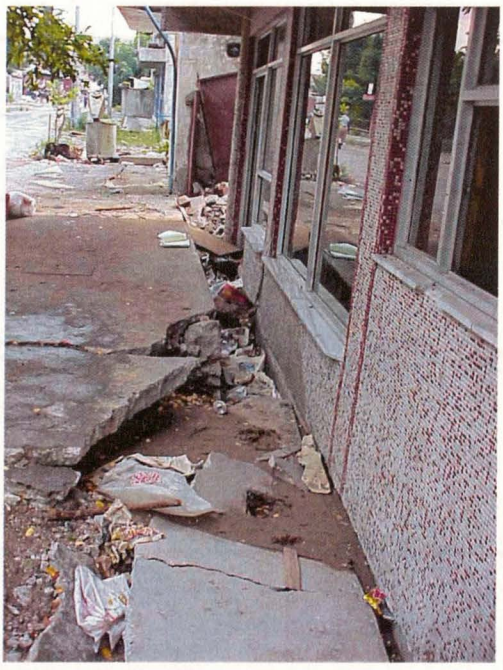

Figure 3.26 Photograph of building D1, which settled and translated during the earthquake. Notice the liquefaction ejecta next to the building (from www.eerc.berkeley.edu/turkey/adapazari).

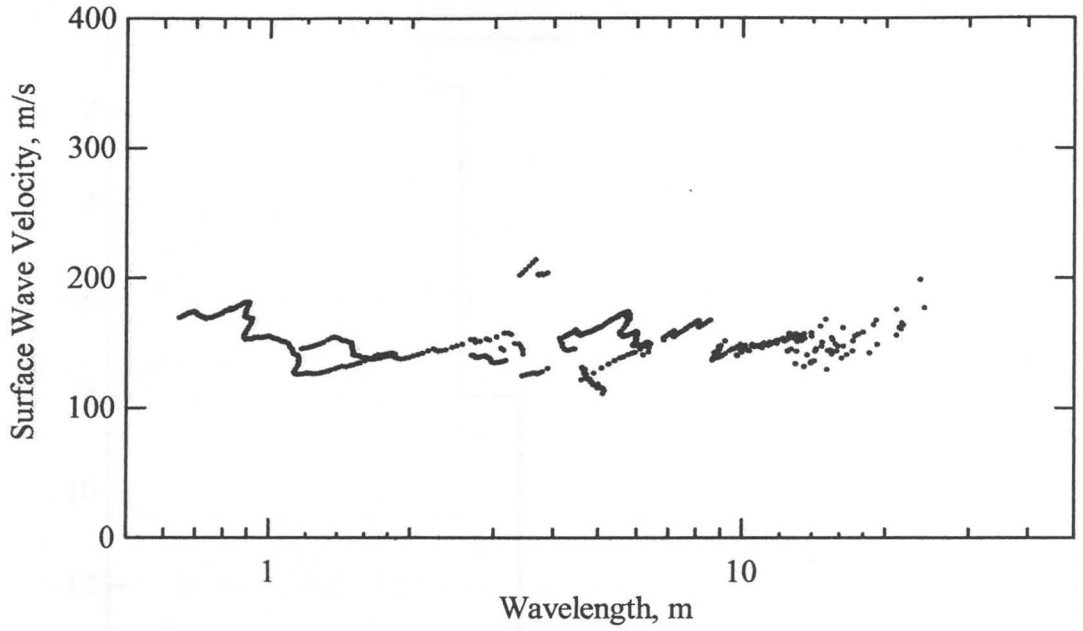

Figure 3.27 Experimental dispersion curve measured at Site D, Aug. 17, 2000, Adapazari, Turkey.

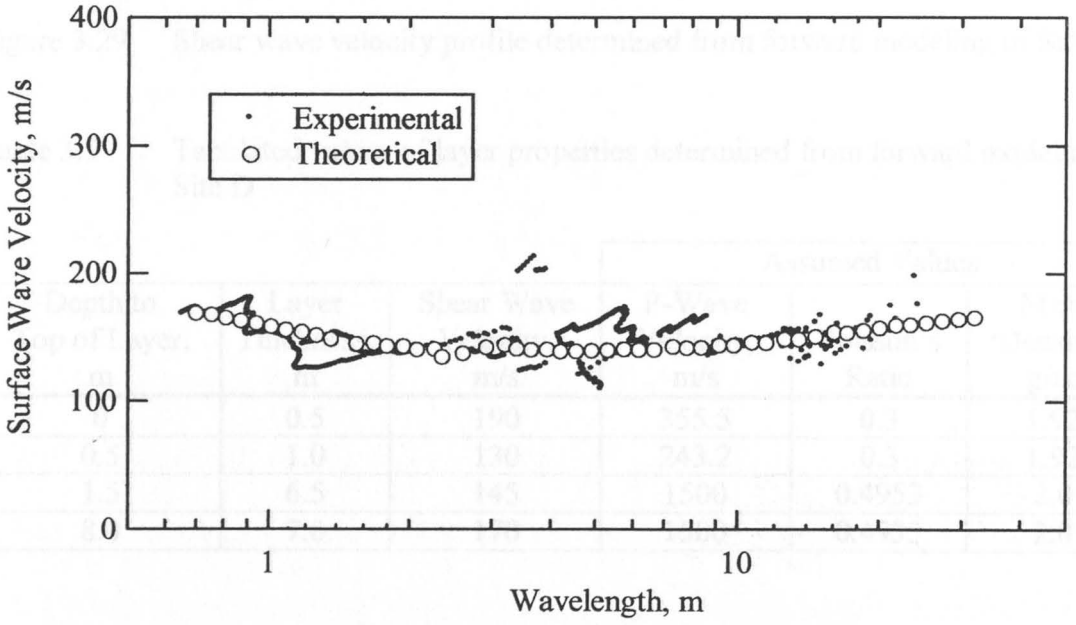

Figure 3.28 Comparison of experimental and theoretical dispersion curves from Site D.

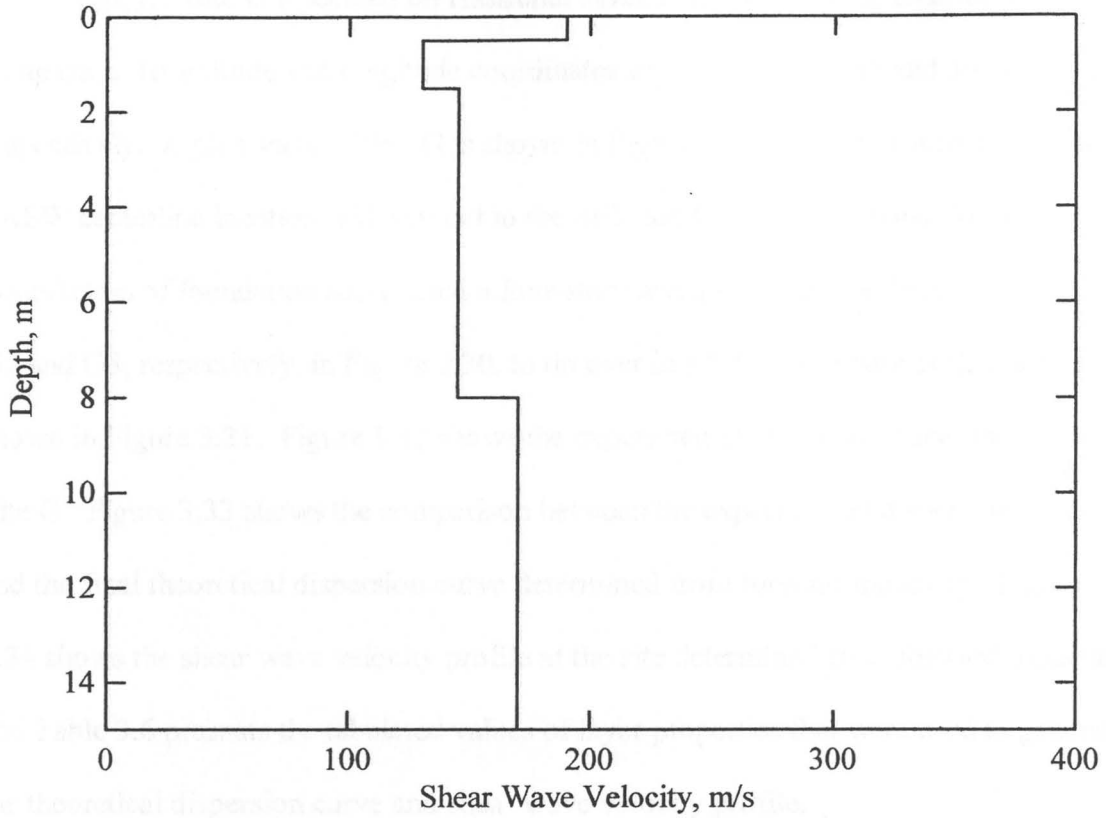

Figure 3.29 Shear wave velocity profile determined from forward modeling of Site D.

Table 3.5 Tabulated values of layer properties determined from forward modeling of Site D

			Assumed Values		
Depth to Top of Layer, m	Layer Thickness, m	Shear Wave Velocity, m/s	P-Wave Velocity, m/s	Poisson's Ratio	Mass Density, g/cc
0	0.5	190	355.5	0.3	1.92
0.5	1.0	130	243.2	0.3	1.92
1.5	6.5	145	1500	0.4953	2.0
8.0	7.0	170	1500	0.4935	2.0

Site G. Site G is located on Hasircilar Avenue in the Yeniqun District of Adapazari. Its latitude and longitude coordinates are 40.77450° north and 30.40896° east, respectively. A plan view of Site G is shown in Figure 3.30. This map also shows the SASW centerline location with respect to the SPT and CPT test locations. Here, liquefaction of foundation soil caused a four-story and a five-story building, designated G2 and G3, respectively, in Figure 3.30, to tip over in a "V". A picture of this failure is shown in Figure 3.31. Figure 3.32 shows the experimental dispersion curve measured at Site G. Figure 3.33 shows the comparison between the experimental dispersion curve and the final theoretical dispersion curve determined from forward modeling. Figure 3.34 shows the shear wave velocity profile at the site determined from forward modeling, and Table 3.6 presents the tabulated values of layer properties that were used to generate the theoretical dispersion curve and shear wave velocity profile.

The water table at Site G is located at a depth of approximately 0.5 meters. Sufficient wavelengths were generated at this site to extend the shear wave velocity profile to a depth of 10 meters. The entire soil profile is extremely soft, having shear wave velocities of less than 200 m/s. The softest soil in the profile is located between the depths of 0.5 – 6 meters.

Site J. Site J is located on Cirak Street in the Yeniqun District of Adapazari. Its latitude and longitude coordinates are 40.77518° north and 30.41077° east, respectively. A plan view of Site J is shown in Figure 3.35. This map also shows the SASW centerline location with respect to the SPT and CPT test locations. Here, liquefaction of foundation soil caused two five-story apartment buildings, designated J1 and J2, respectively, in

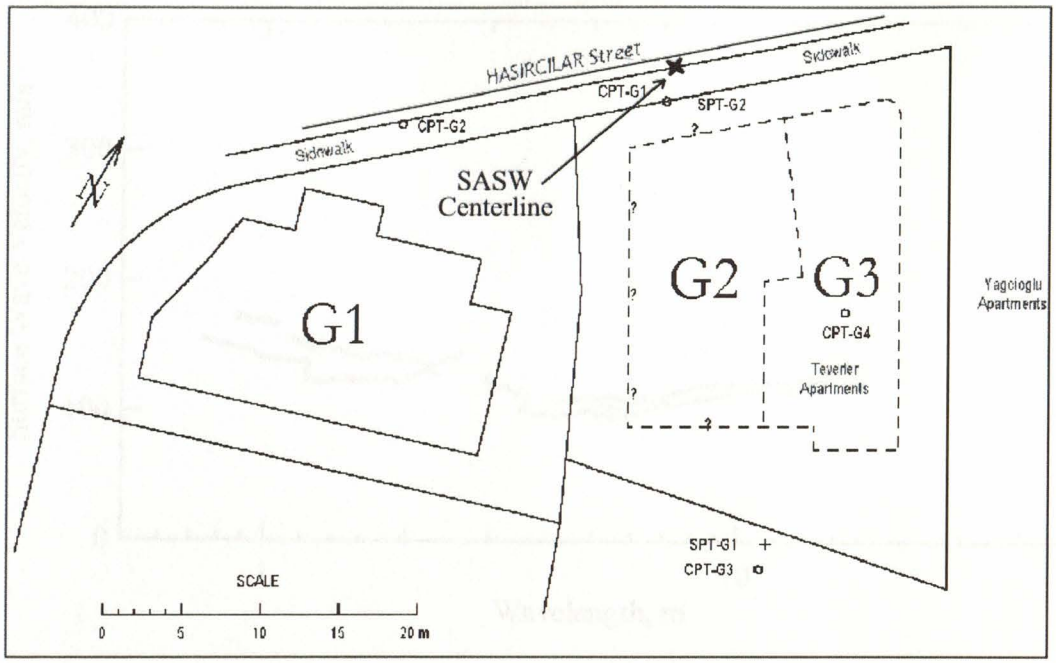

Figure 3.30 Plan view of Site G showing the location of one SASW centerline (modified from www.eerc.berkeley.edu/turkey/adapazari).

Figure 3.31 Photograph of Site G, where liquefaction of foundation soil caused buildings G2 (right) and G3 (left) to tip apart in a "V" (from www.eerc.berkeley.edu/turkey/adapazari).

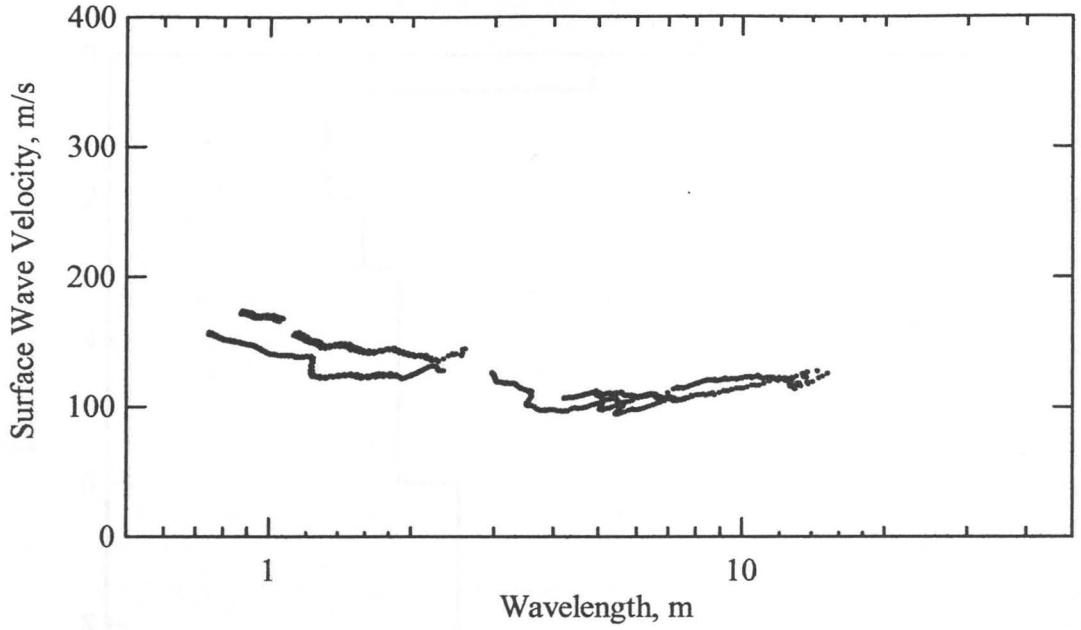

Figure 3.32 Experimental dispersion curve measured at Site G, Aug. 16, 2000, Adapazari, Turkey.

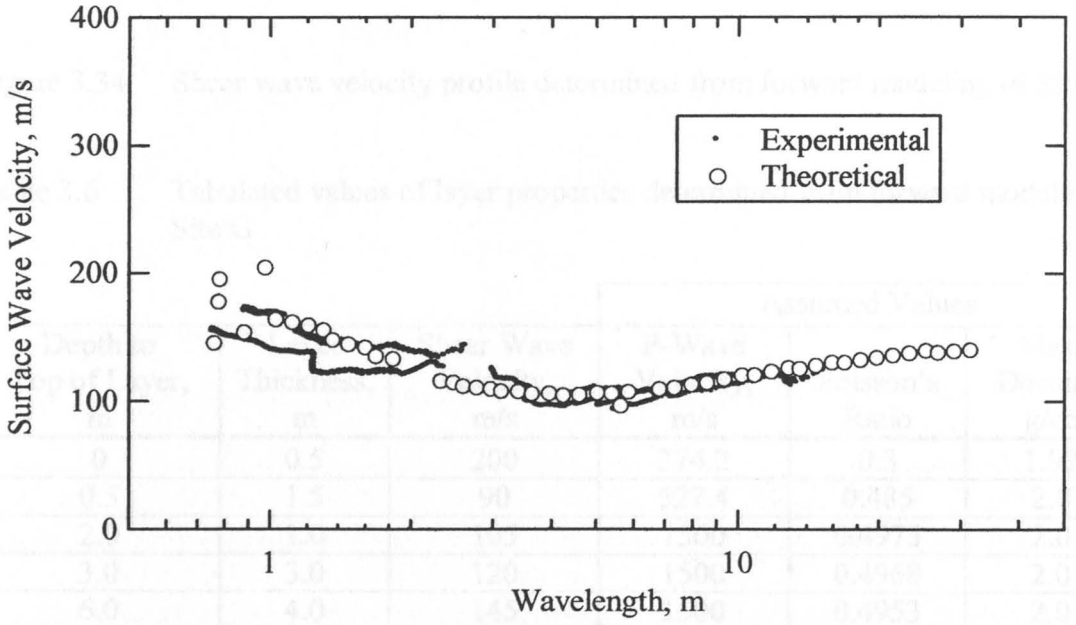

Figure 3.33 Comparison of experimental and theoretical dispersion curves from Site G.

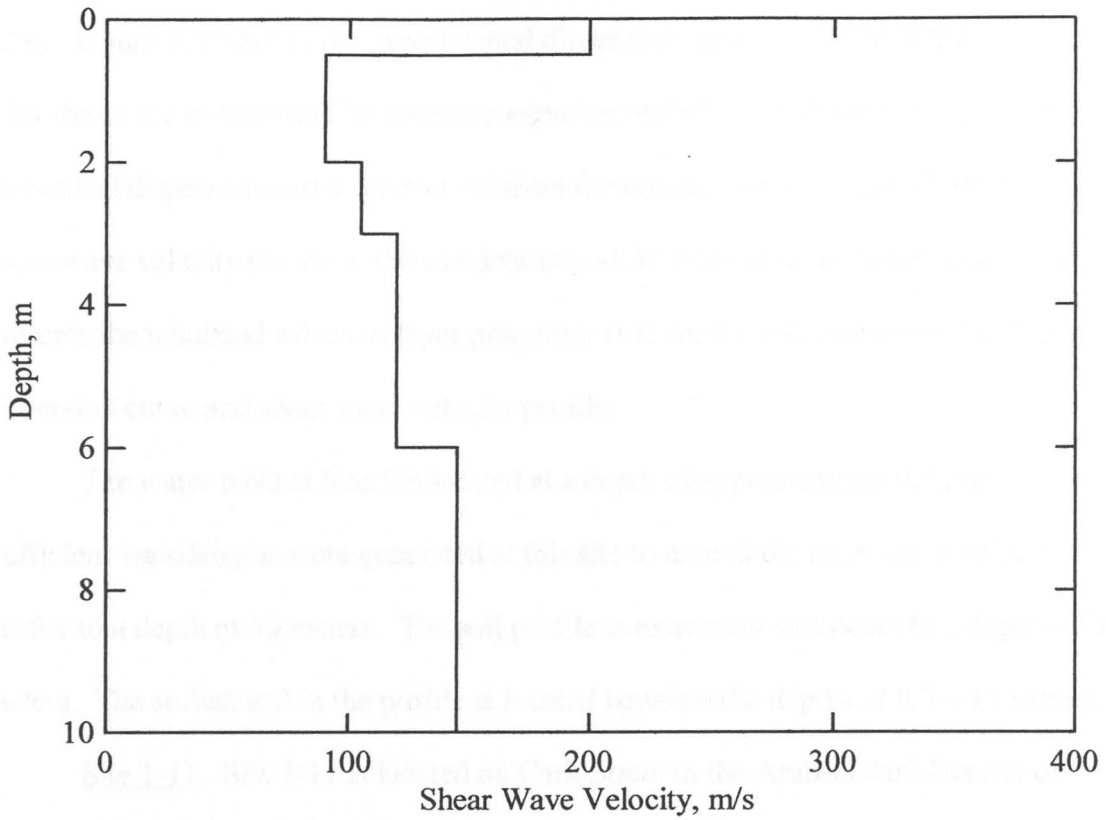

Figure 3.34 Shear wave velocity profile determined from forward modeling of Site G.

Table 3.6 Tabulated values of layer properties determined from forward modeling of Site G

			Assumed Values		
Depth to Top of Layer, m	Layer Thickness, m	Shear Wave Velocity, m/s	P-Wave Velocity, m/s	Poisson's Ratio	Mass Density, g/cc
0	0.5	200	374.2	0.3	1.92
0.5	1.5	90	527.4	0.485	2.0
2.0	1.0	105	1500	0.4975	2.0
3.0	3.0	120	1500	0.4968	2.0
6.0	4.0	145	1500	0.4953	2.0

Figure 3.35, to settle approximately 25 cm. A picture of this failure is shown in Figure 3.36. Figure 3.37 shows the experimental dispersion curve measured at Site J. Figure 3.38 shows the comparison between the experimental dispersion curve and the final theoretical dispersion curve determined from forward modeling. Figure 3.39 shows the shear wave velocity profile at the site determined from forward modeling, and Table 3.7 presents the tabulated values of layer properties that were used to generate the theoretical dispersion curve and shear wave velocity profile.

The water table at Site J is located at a depth of approximately 0.7 meters. Sufficient wavelengths were generated at this site to extend the shear wave velocity profile to a depth of 50 meters. The soil profile is extremely soft down to a depth of 36 meters. The softest soil in the profile is located between the depths of 0.7 – 11 meters.

Site 1-11. Site 1-11 is located on Cark Street in the Arabacialani District of Adapazari. Its latitude and longitude coordinates are 40.77380° north and 30.37207° east, respectively. A plan view of Site 1-11 is shown in Figure 3.40. This map also shows the SASW centerline location with respect to the CPT test locations. Here, liquefaction of foundation soil caused a five-story building, designated N-1 in Figure 3.40, to settle approximately 30 cm. A picture of this failure is shown in Figure 3.41. Figure 3.42 shows the experimental dispersion curve measured at Site 1-11. Figure 3.43 shows the comparison between the experimental dispersion curve and the final theoretical dispersion curve determined from forward modeling. Figure 3.44 shows the shear wave velocity profile at the site determined from forward modeling, and Table 3.8 presents the

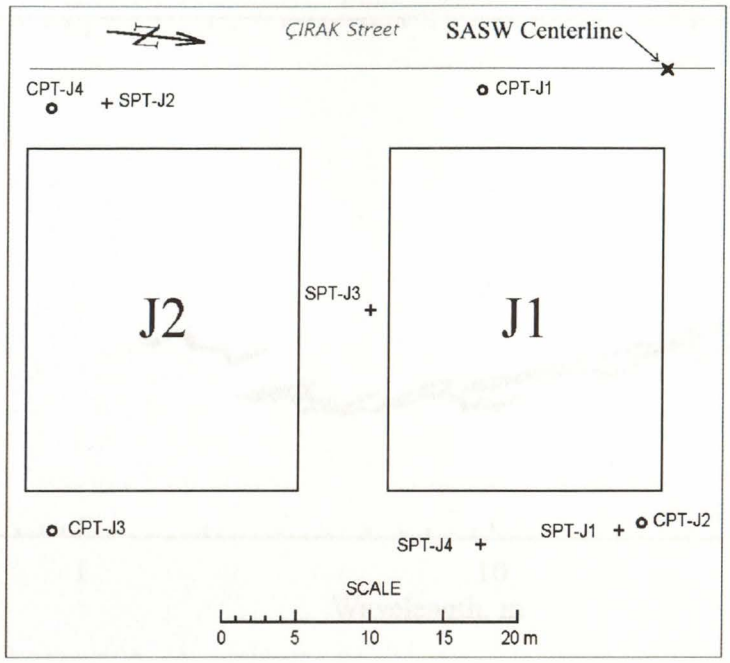

Figure 3.35 Plan view of Site J showing the location of one SASW centerline (modified from www.eerc.berkeley.edu/turkey/adapazari).

Figure 3.36 Photograph showing the liquefaction-induced settlement at Site J. Notice the liquefaction ejecta (from www.eerc.berkeley.edu/turkey/adapazari).

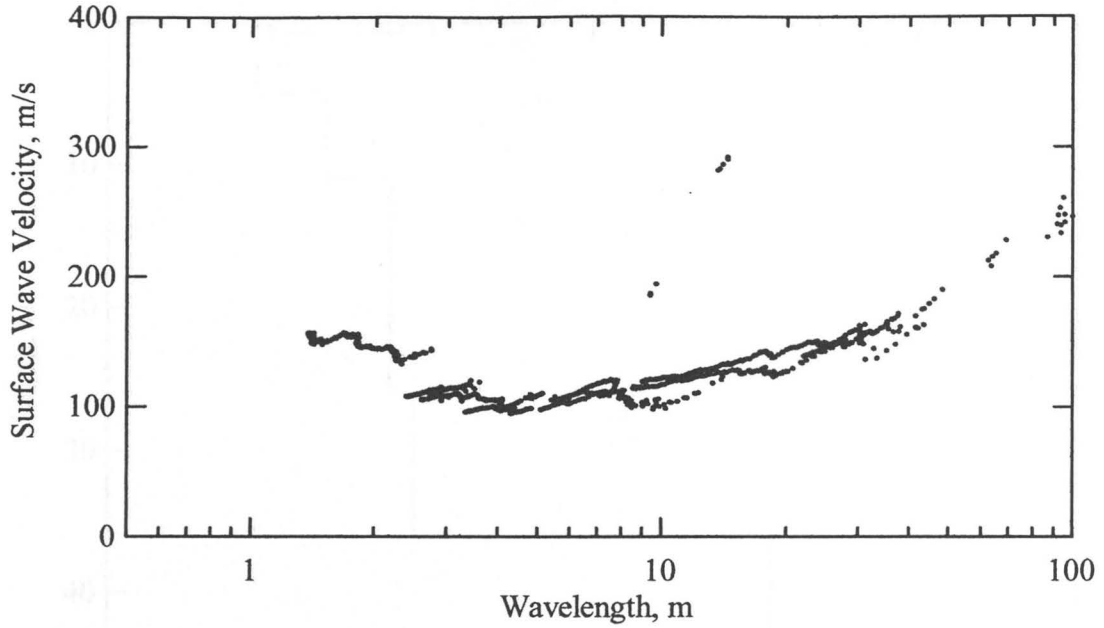

Figure 3.37 Experimental dispersion curve measured at Site J, Aug. 21, 2000, Adapazari, Turkey.

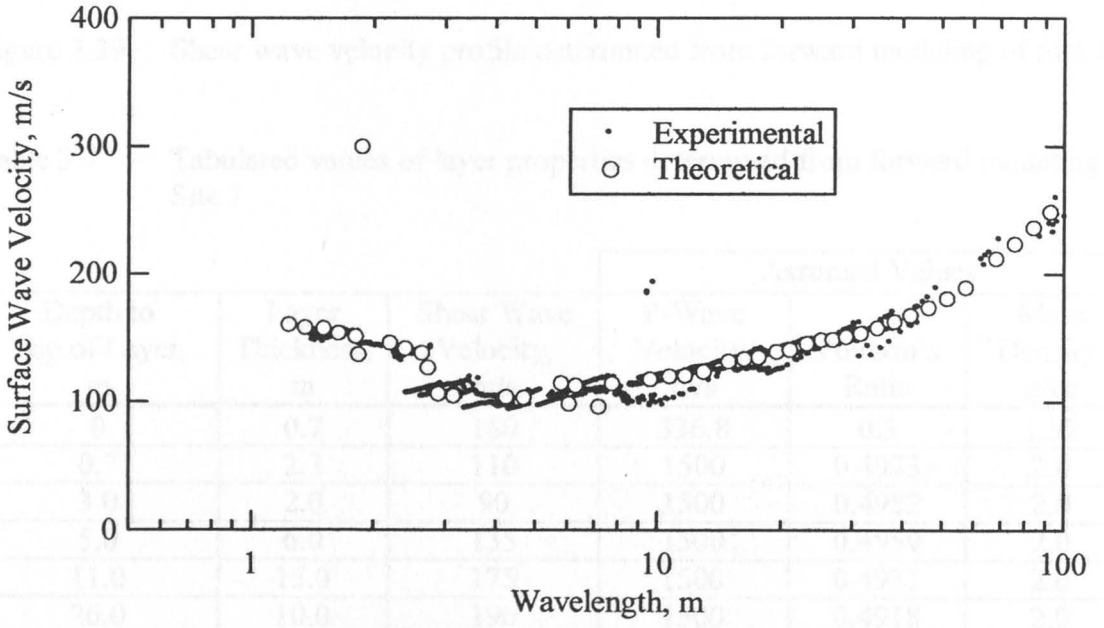

Figure 3.38 Comparison of experimental and theoretical dispersion curves from Site J.

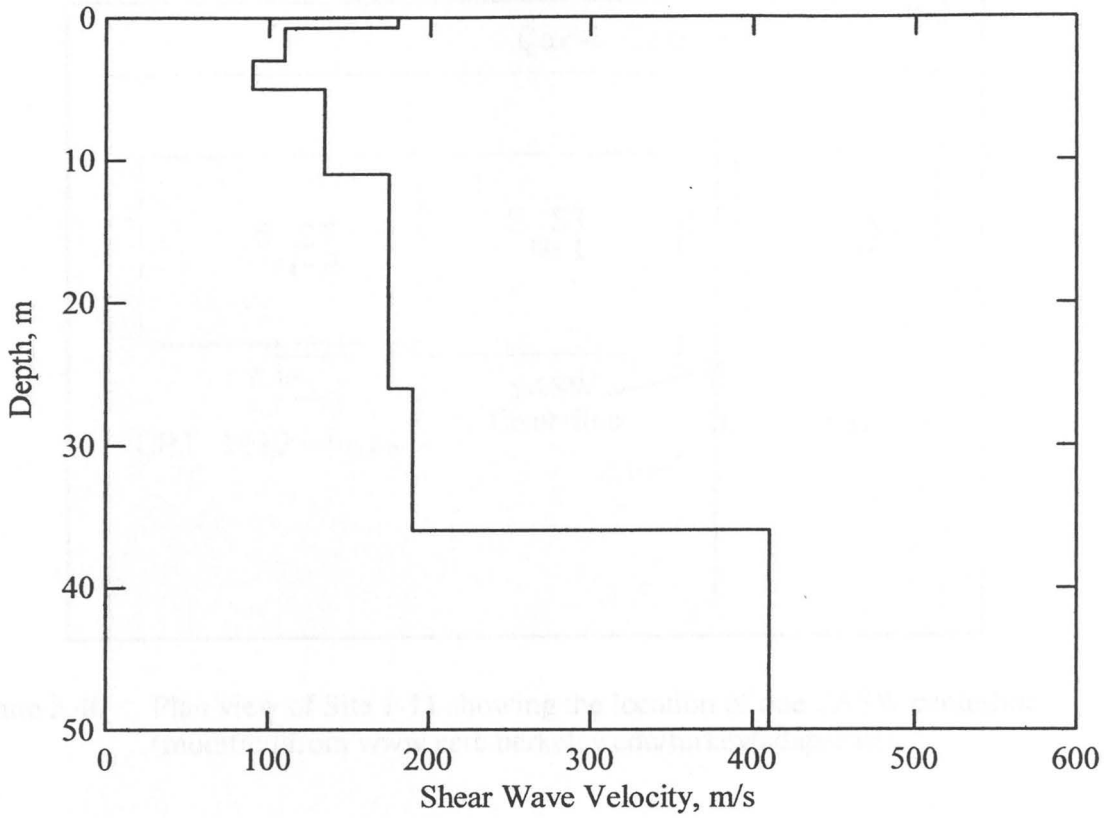

Figure 3.39 Shear wave velocity profile determined from forward modeling of Site J.

Table 3.7 Tabulated values of layer properties determined from forward modeling of Site J

			Assumed Values		
Depth to Top of Layer, m	Layer Thickness, m	Shear Wave Velocity, m/s	P-Wave Velocity, m/s	Poisson's Ratio	Mass Density, g/cc
0	0.7	180	336.8	0.3	1.92
0.7	2.3	110	1500	0.4973	2.0
3.0	2.0	90	1500	0.4982	2.0
5.0	6.0	135	1500	0.4959	2.0
11.0	15.0	175	1500	0.4931	2.0
26.0	10.0	190	1500	0.4918	2.0
36.0	14.0	410	1500	0.4596	2.0

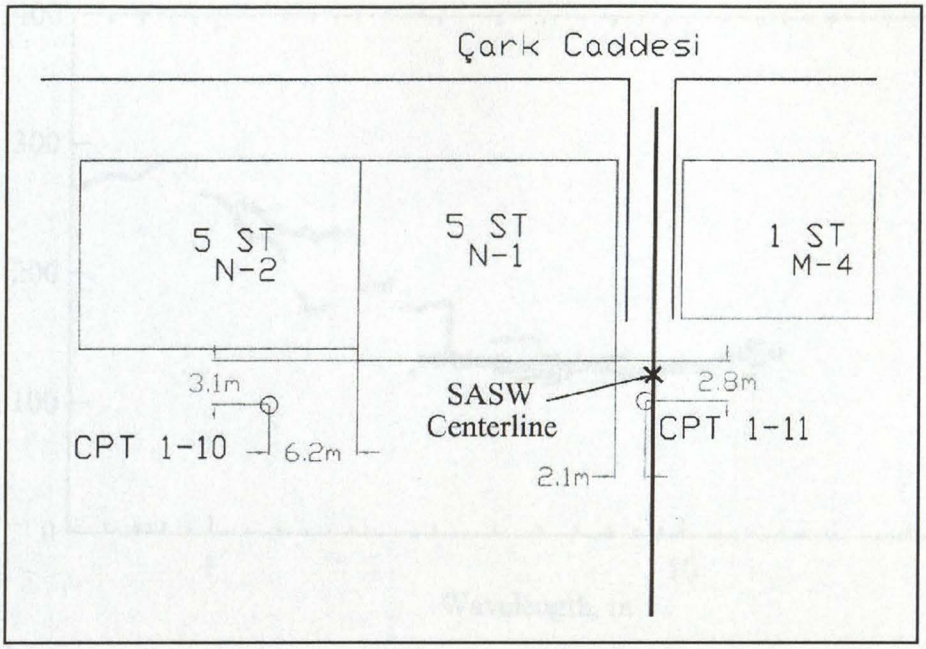

Figure 3.40 Plan view of Site 1-11 showing the location of one SASW centerline (modified from www.eerc.berkeley.edu/turkey/adapazari).

Figure 3.41 Photograph showing approximately 30 cm of settlement between the stairs and the doorway of building N-1 at Site 1-11.

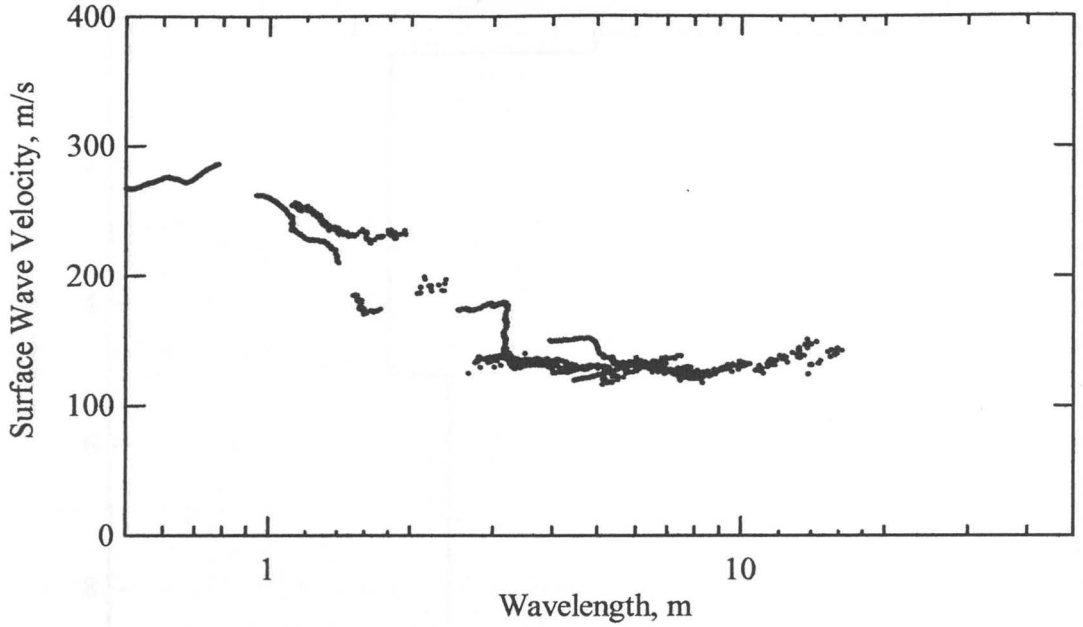

Figure 3.42 Experimental dispersion curve measured at Site 1-11, Aug. 15, 2000, Adapazari, Turkey.

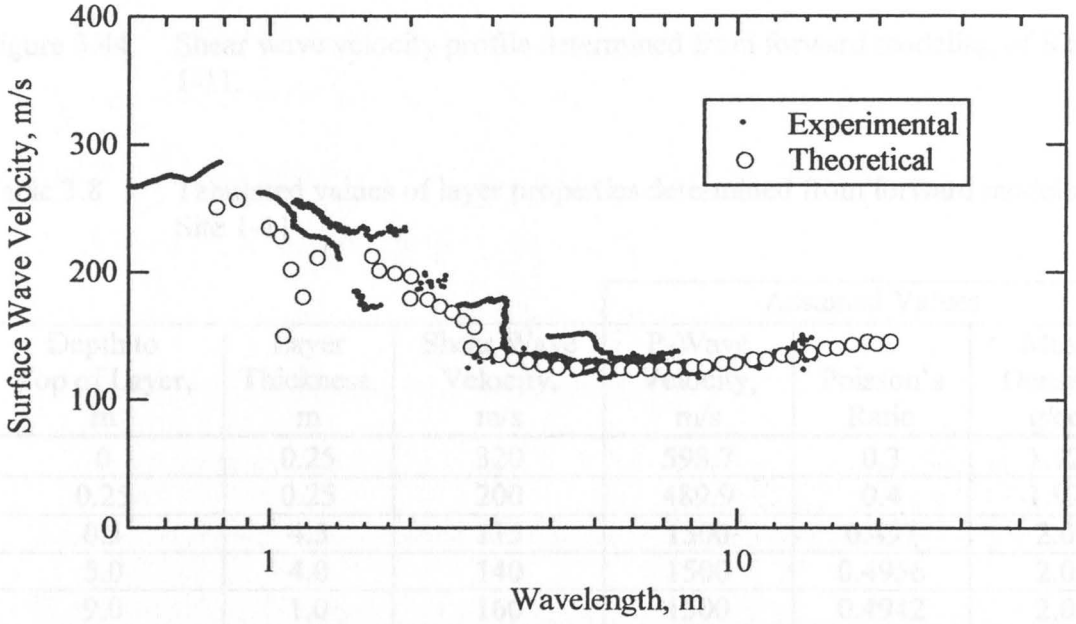

Figure 3.43 Comparison of experimental and theoretical dispersion curves from Site 1-11.

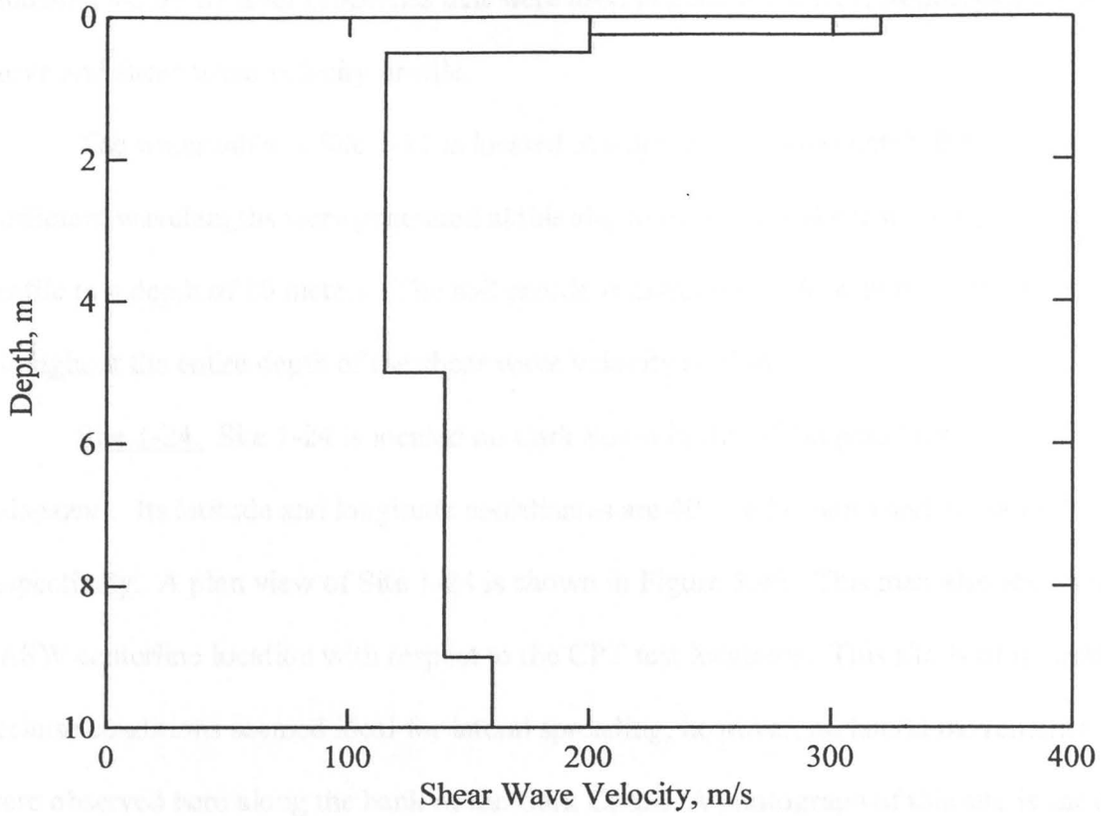

Figure 3.44 Shear wave velocity profile determined from forward modeling of Site 1-11.

Table 3.8 Tabulated values of layer properties determined from forward modeling of Site 1-11

			Assumed Values		
Depth to Top of Layer, m	Layer Thickness, m	Shear Wave Velocity, m/s	P-Wave Velocity, m/s	Poisson's Ratio	Mass Density, g/cc
0	0.25	320	598.7	0.3	1.92
0.25	0.25	200	489.9	0.4	1.92
0.5	4.5	115	1500	0.497	2.0
5.0	4.0	140	1500	0.4956	2.0
9.0	1.0	160	1500	0.4942	2.0

tabulated values of layer properties that were used to generate the theoretical dispersion curve and shear wave velocity profile.

The water table at Site 1-11 is located at a depth of approximately 0.5 meters. Sufficient wavelengths were generated at this site to extend the shear wave velocity profile to a depth of 10 meters. The soil profile is extremely soft from the water table throughout the entire depth of the shear wave velocity profile.

Site 1-24. Site 1-24 is located on Cark Street in the Mithatpasa District of Adapazari. Its latitude and longitude coordinates are 40.77629° north and 30.38307° east, respectively. A plan view of Site 1-24 is shown in Figure 3.45. This map also shows the SASW centerline location with respect to the CPT test locations. This site is of interest because conditions seemed ideal for lateral spreading, however, no lateral movements were observed here along the bank of the Cark Canal. A photograph of this site is shown in Figure 3.46. Figure 3.47 shows the experimental dispersion curve measured at Site 1-24. Figure 3.48 shows the comparison between the experimental dispersion curve and the final theoretical dispersion curve determined from forward modeling. Figure 3.49 shows the shear wave velocity profile at the site determined from forward modeling, and Table 3.9 presents the tabulated values of layer properties that were used to generate the theoretical dispersion curve and shear wave velocity profile.

The water table at Site 1-24 is located at a depth of approximately 2.5 meters. Sufficient wavelengths were generated at this site to extend the shear wave velocity profile to a depth of 15 meters. The soil profile is extremely soft from a depth of 1 meter throughout the entire depth of the shear wave velocity profile.

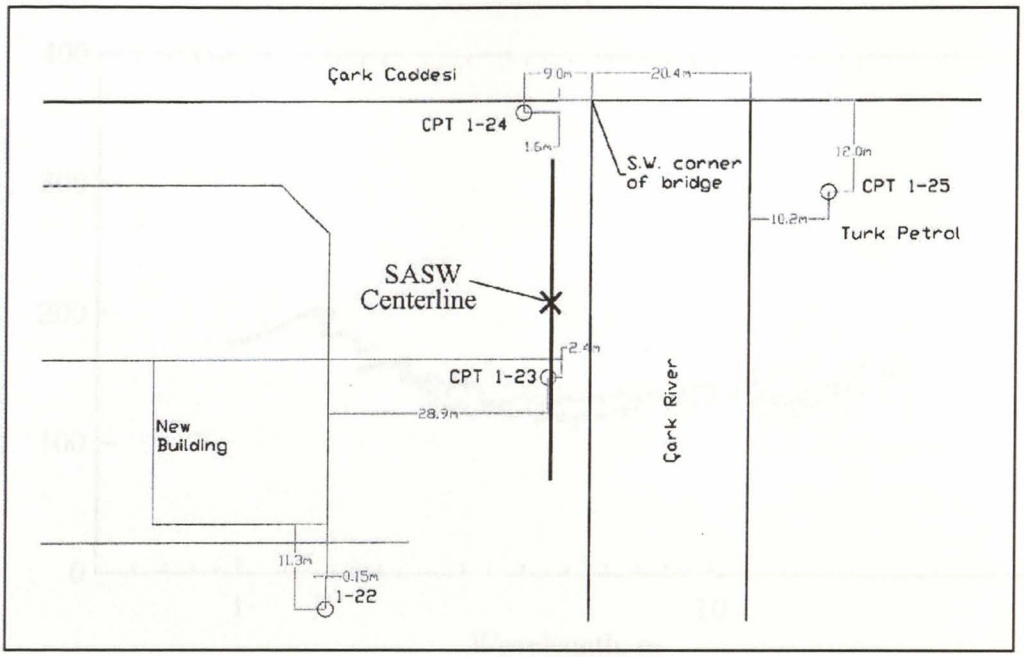

Figure 3.45 Plan view of Site 1-24 showing the location of one SASW centerline (modified from www.eerc.berkeley.edu/turkey/adapazari).

Figure 3.46 Photograph of Site 1-24. No lateral movements were noticed here along the banks of the Cark Canal.

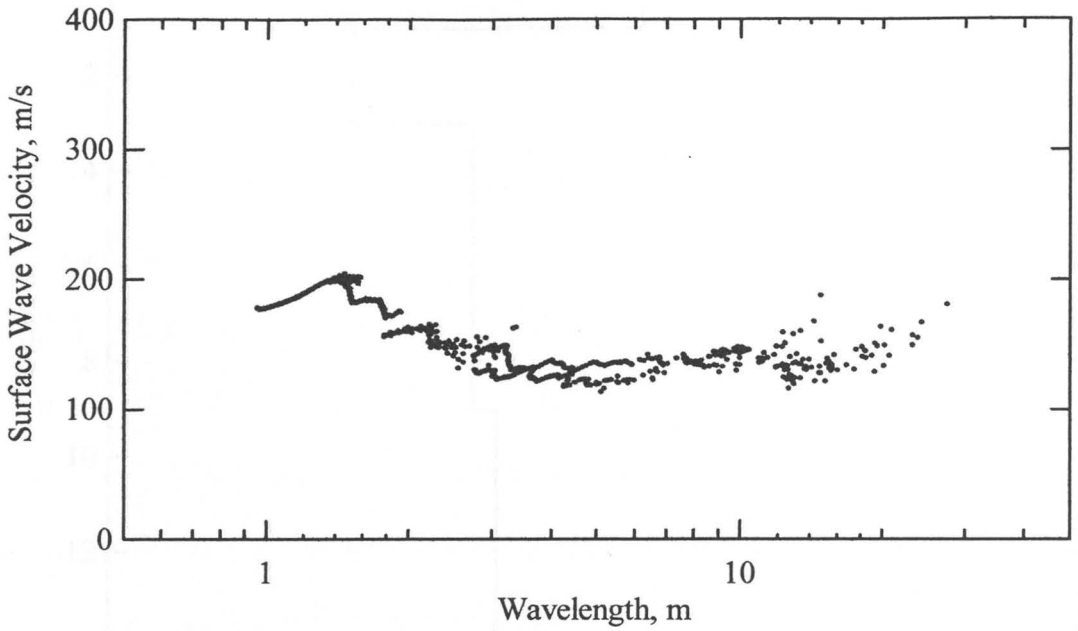

Figure 3.47 Experimental dispersion curve measured at Site 1-24, Aug. 15, 2000, Adapazari, Turkey.

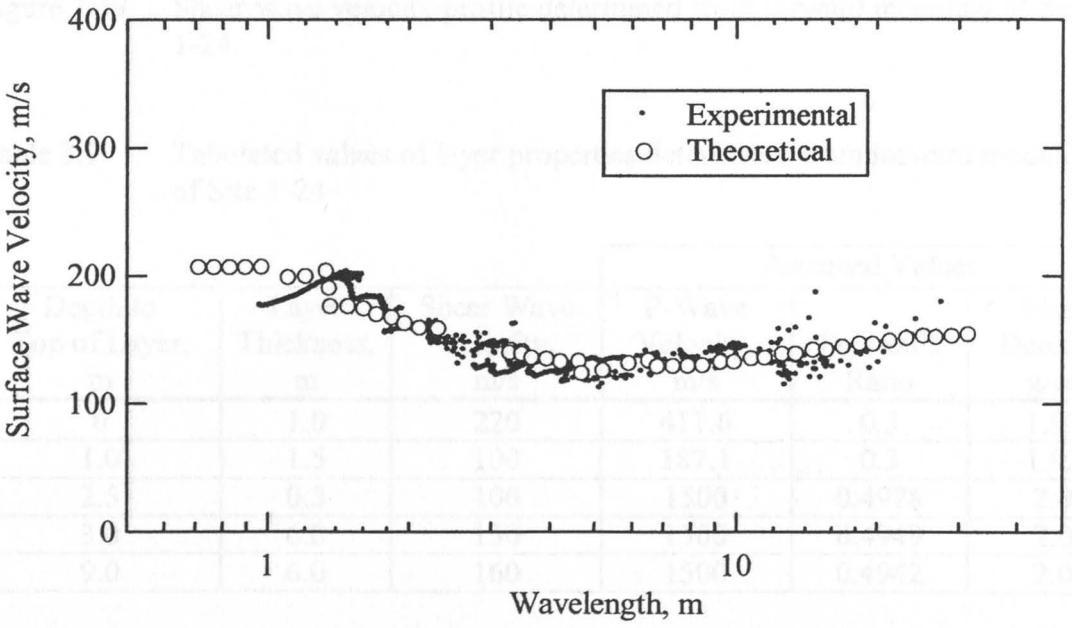

Figure 3.48 Comparison of experimental and theoretical dispersion curves from Site 1-24.

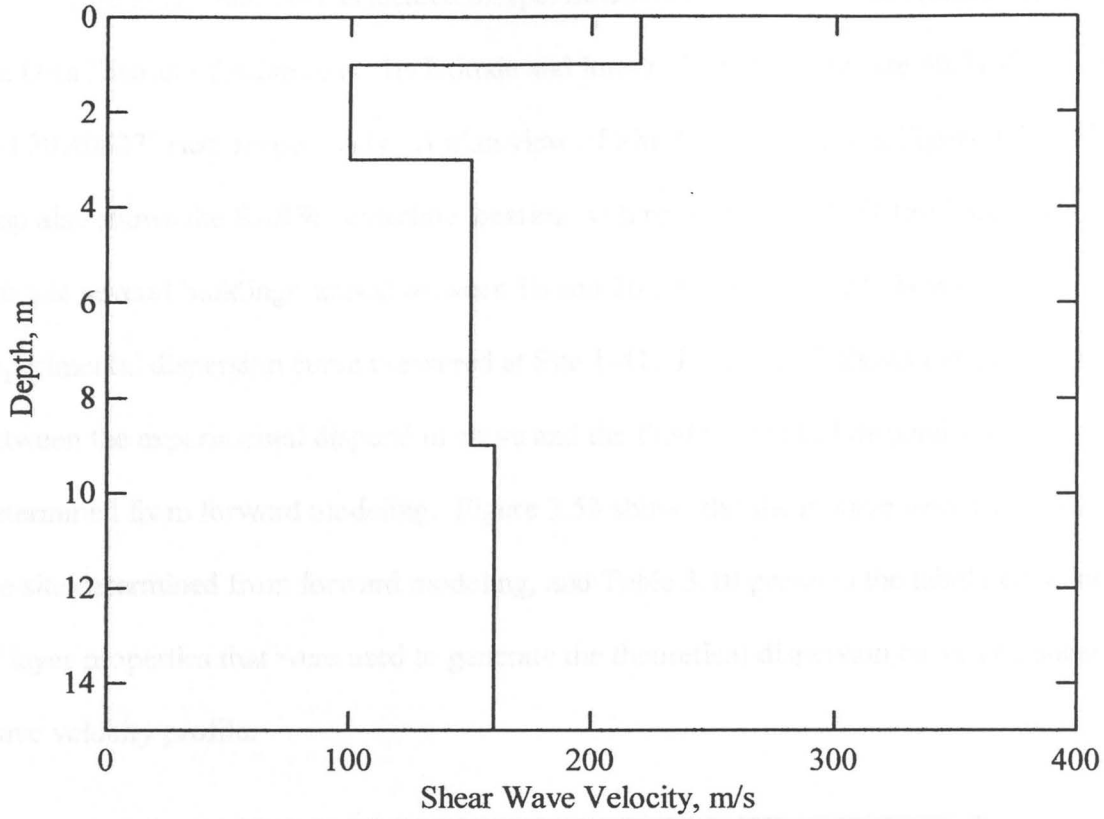

Figure 3.49 Shear wave velocity profile determined from forward modeling of Site 1-24.

Table 3.9 Tabulated values of layer properties determined from forward modeling of Site 1-24

			Assumed Values		
Depth to Top of Layer, m	Layer Thickness, m	Shear Wave Velocity, m/s	P-Wave Velocity, m/s	Poisson's Ratio	Mass Density, g/cc
0	1.0	220	411.6	0.3	1.92
1.0	1.5	100	187.1	0.3	1.92
2.5	0.5	100	1500	0.4978	2.0
3.0	6.0	150	1500	0.4949	2.0
9.0	6.0	160	1500	0.4942	2.0

Site 1-41. Site 1-41 is located on Ipci Sokak one block south of Ankara Street in the Orta District of Adapazari. Its latitude and longitude coordinates are 40.77906° north and 30.40523° east, respectively. A plan view of Site 1-41 is shown in Figure 3.50. This map also shows the SASW centerline location with respect to the CPT test locations. At this site several buildings settled between 10 and 20 cm. Figure 3.51 shows the experimental dispersion curve measured at Site 1-41. Figure 3.52 shows the comparison between the experimental dispersion curve and the final theoretical dispersion curve determined from forward modeling. Figure 3.53 shows the shear wave velocity profile at the site determined from forward modeling, and Table 3.10 presents the tabulated values of layer properties that were used to generate the theoretical dispersion curve and shear wave velocity profile.

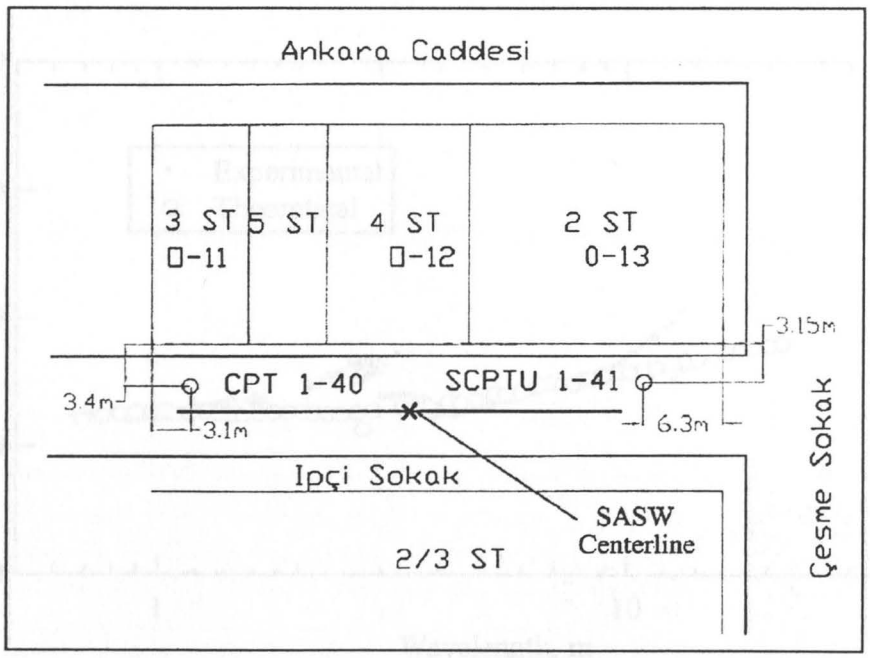

Figure 3.50 Plan view of Site 1-41 showing the location of one SASW centerline (modified from www.eerc.berkeley.edu/turkey/adapazari).

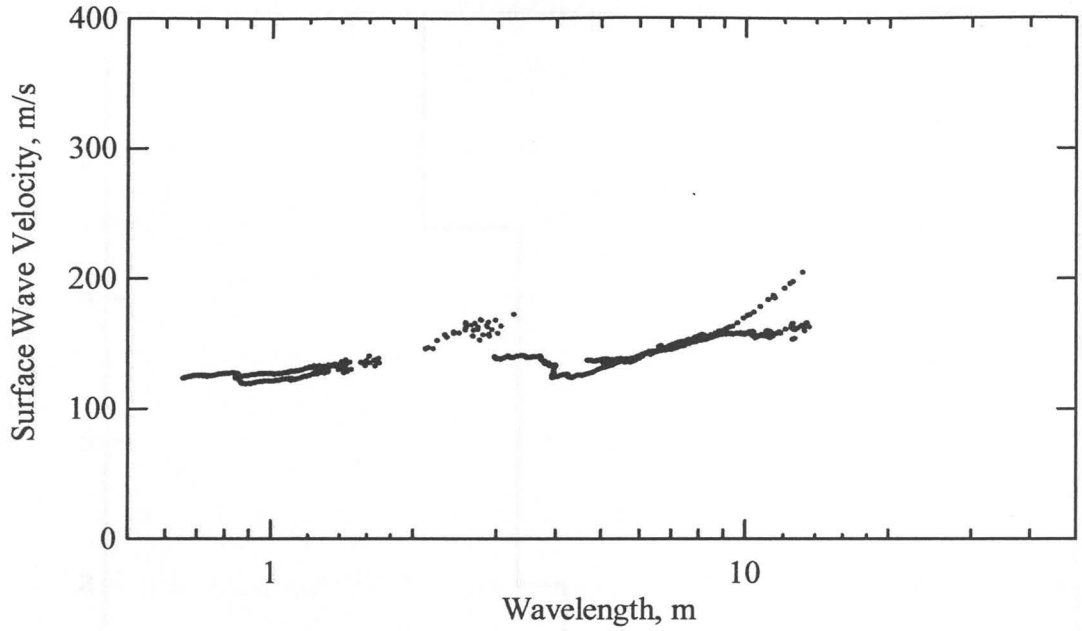

Figure 3.51 Experimental dispersion curve measured at Site 1-41, Aug. 17, 2000, Adapazari, Turkey.

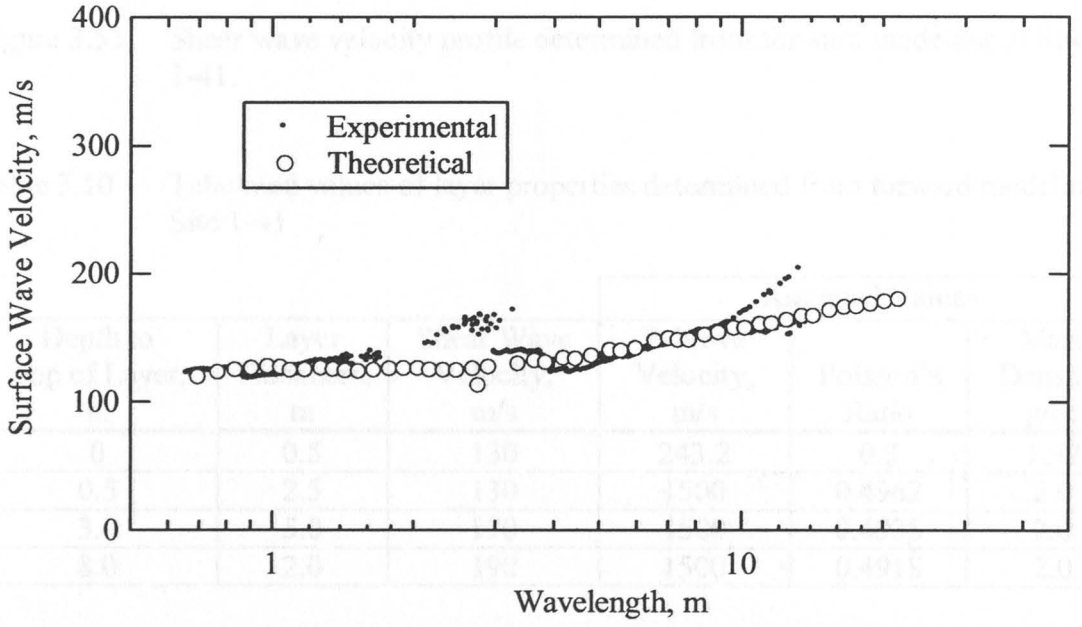

Figure 3.52 Comparison of experimental and theoretical dispersion curves from Site 1-41.

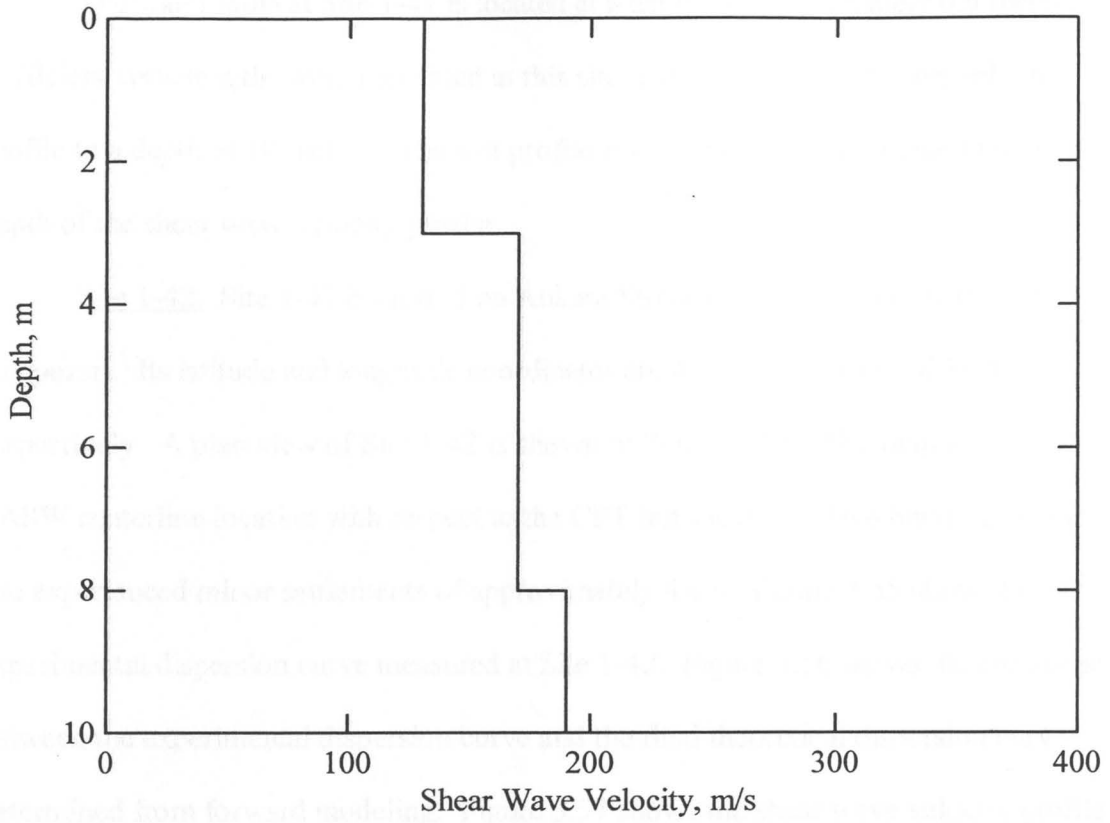

Figure 3.53 Shear wave velocity profile determined from forward modeling of Site 1-41.

Table 3.10 Tabulated values of layer properties determined from forward modeling of Site 1-41

			Assumed Values		
Depth to Top of Layer, m	Layer Thickness, m	Shear Wave Velocity, m/s	P-Wave Velocity, m/s	Poisson's Ratio	Mass Density, g/cc
0	0.5	130	243.2	0.3	1.92
0.5	2.5	130	1500	0.4962	2.0
3.0	5.0	170	1500	0.4935	2.0
8.0	2.0	190	1500	0.4918	2.0

The water table at Site 1-41 is located at a depth of approximately 0.5 meters. Sufficient wavelengths were generated at this site to extend the shear wave velocity profile to a depth of 10 meters. The soil profile is extremely soft throughout the entire depth of the shear wave velocity profile.

Site 1-42. Site 1-42 is located on Ankara Street in the Yahyalar District of Adapazari. Its latitude and longitude coordinates are 40.77948° north and 30.40696° east, respectively. A plan view of Site 1-42 is shown in Figure 3.54. This map also shows the SASW centerline location with respect to the CPT test location. Two buildings at this site experienced minor settlements of approximately 4 cm. Figure 3.55 shows the experimental dispersion curve measured at Site 1-42. Figure 3.56 shows the comparison between the experimental dispersion curve and the final theoretical dispersion curve determined from forward modeling. Figure 3.57 shows the shear wave velocity profile at

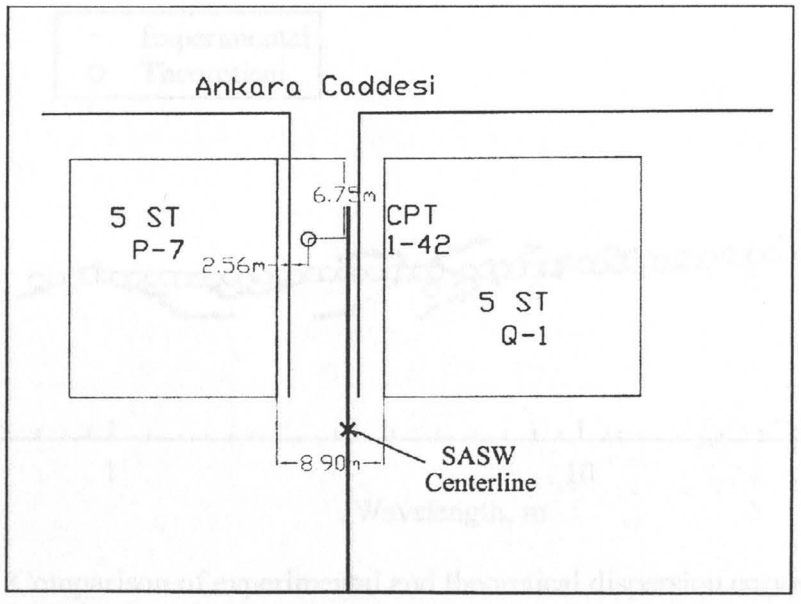

Figure 3.54 Plan view of Site 1-42 showing the location of one SASW centerline (modified from www.eerc.berkeley.edu/turkey/adapazari).

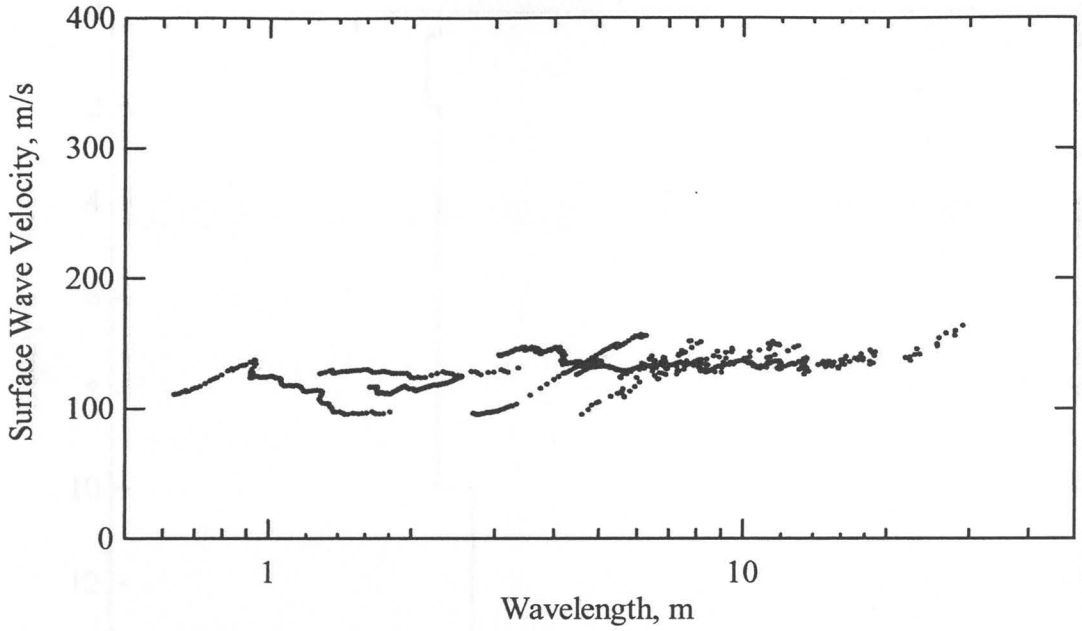

Figure 3.55 Experimental dispersion curve measured at Site 1-42, Aug. 17, 2000, Adapazari, Turkey.

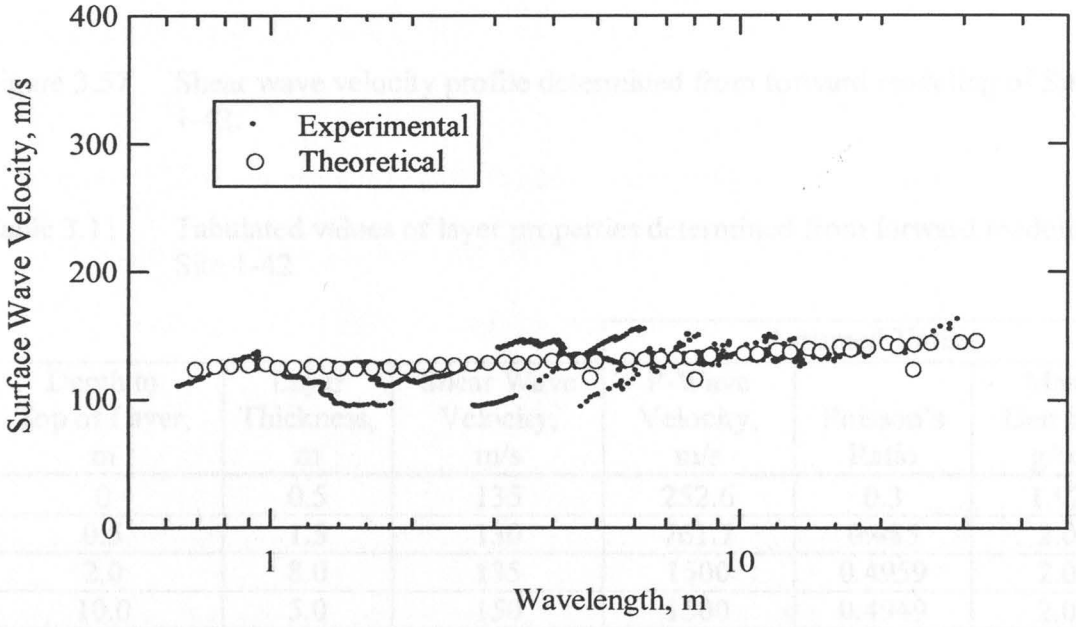

Figure 3.56 Comparison of experimental and theoretical dispersion curves from Site 1-42.

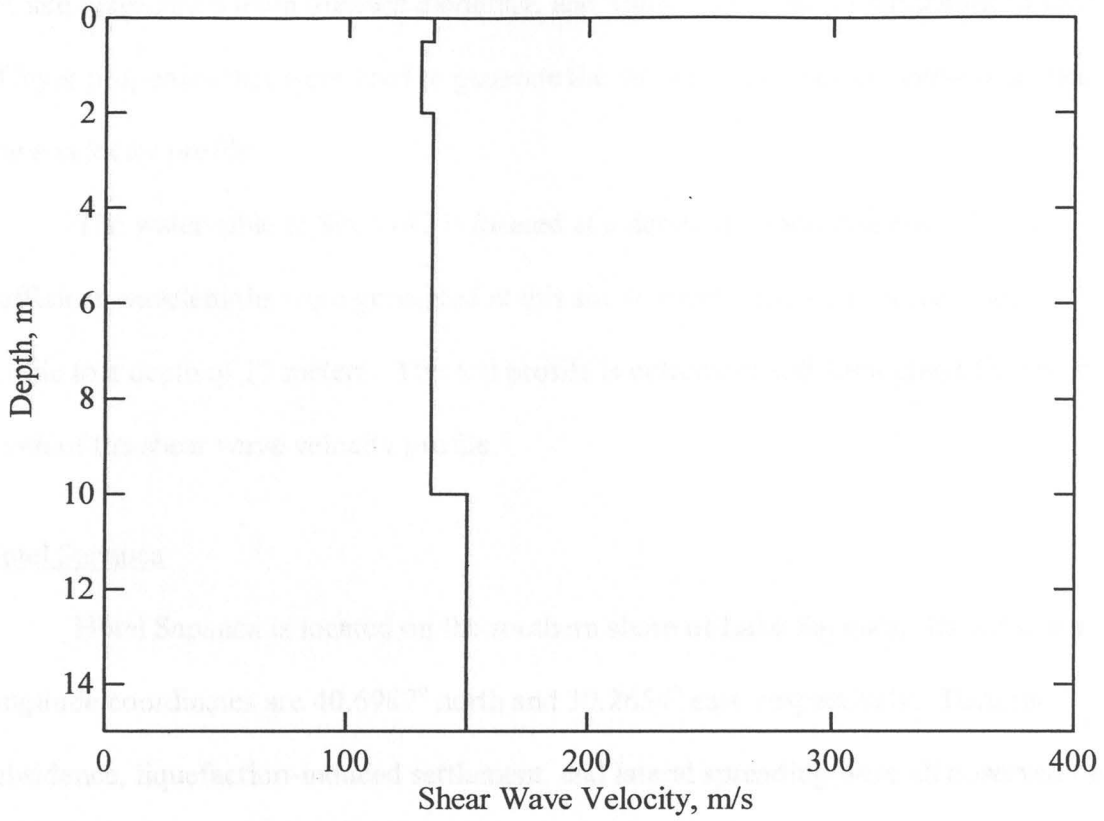

Figure 3.57 Shear wave velocity profile determined from forward modeling of Site 1-42.

Table 3.11 Tabulated values of layer properties determined from forward modeling of Site 1-42

			Assumed Values		
Depth to Top of Layer, m	Layer Thickness, m	Shear Wave Velocity, m/s	P-Wave Velocity, m/s	Poisson's Ratio	Mass Density, g/cc
0	0.5	135	252.6	0.3	1.92
0.5	1.5	130	761.7	0.485	2.0
2.0	8.0	135	1500	0.4959	2.0
10.0	5.0	150	1500	0.4949	2.0

the site determined from forward modeling, and Table 3.11 presents the tabulated values of layer properties that were used to generate the theoretical dispersion curve and shear wave velocity profile.

The water table at Site 1-42 is located at a depth of approximately 0.5 meters. Sufficient wavelengths were generated at this site to extend the shear wave velocity profile to a depth of 15 meters. The soil profile is extremely soft throughout the entire depth of the shear wave velocity profile.

Hotel Sapanca

Hotel Sapanca is located on the southern shore of Lake Sapanca. Its latitude and longitude coordinates are 40.6987° north and 30.2654° east, respectively. Tectonic subsidence, liquefaction-induced settlement, and lateral spreading were all observed on hotel grounds during the Kocaeli earthquake. As a result of these events, the four-story hotel was carried partially into the lake (see Figure 3.58). Lateral movements toward the lake were on the order of 2 meters and the hotel settled between 20-50 cm. These two phenomena, coupled with tectonic subsidence, resulted in movement of the shoreline inward by 30-50 meters. People fleeing the hotel after the earthquake reported water and soil "boiling out of the ground" (EERI, 2000).

Four SASW centerlines were used at this location in order to investigate the full extent of the on-shore portion of the lateral spread. The centerlines were spaced at 22.5 meters along a line oriented approximately 15 degrees west-of-north that ran from the northeast corner of the hotel to the entrance. A site map showing the locations of the SASW test arrays is shown in Figure 3.59. Figure 3.60 shows the experimental

Figure 3.58 Hotel Sapanca carried partially into the lake as a result of several earthquake phenomena (from www.eerc.berkeley.edu/turkey/adapazari).

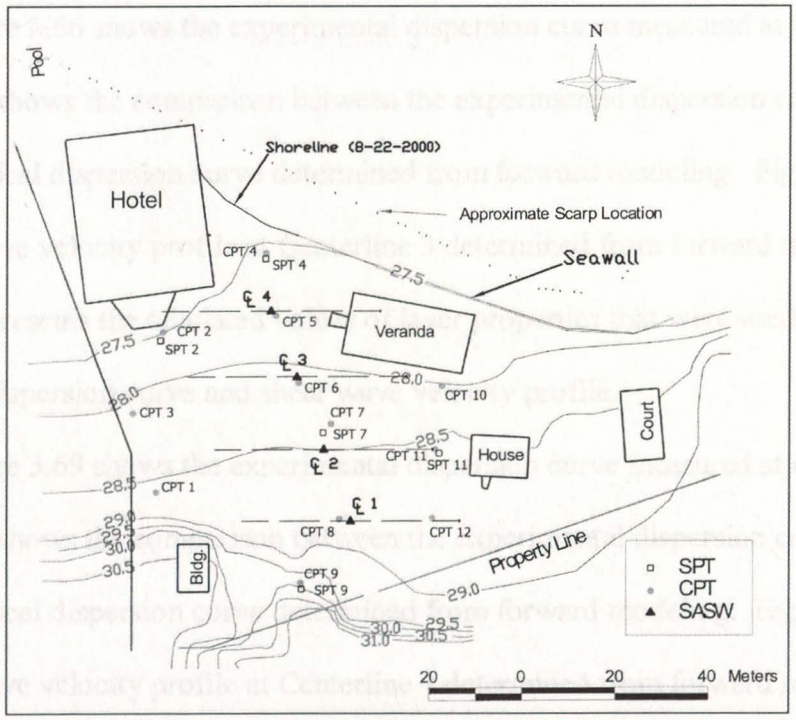

Figure 3.59 Plan view of Hotel Sapanca showing the location of four SASW centerlines (modified from www.eerc.berkeley.edu/turkey/adapazari).

dispersion curve measured at Centerline 1. Figure 3.61 shows the comparison between the experimental dispersion curve and the final theoretical dispersion curve determined from forward modeling. Figure 3.62 shows the shear wave velocity profile at Centerline 1 determined from forward modeling, and Table 3.12 presents the tabulated values of layer properties that were used to generate the theoretical dispersion curve and shear wave velocity profile.

Figure 3.63 shows the experimental dispersion curve measured at Centerline 2. Figure 3.64 shows the comparison between the experimental dispersion curve and the final theoretical dispersion curve determined from forward modeling. Figure 3.65 shows the shear wave velocity profile at Centerline 2 determined from forward modeling, and Table 3.13 presents the tabulated values of layer properties that were used to generate the theoretical dispersion curve and shear wave velocity profile.

Figure 3.66 shows the experimental dispersion curve measured at Centerline 3. Figure 3.67 shows the comparison between the experimental dispersion curve and the final theoretical dispersion curve determined from forward modeling. Figure 3.68 shows the shear wave velocity profile at Centerline 3 determined from forward modeling, and Table 3.14 presents the tabulated values of layer properties that were used to generate the theoretical dispersion curve and shear wave velocity profile.

Figure 3.69 shows the experimental dispersion curve measured at Centerline 4. Figure 3.70 shows the comparison between the experimental dispersion curve and the final theoretical dispersion curve determined from forward modeling. Figure 3.71 shows the shear wave velocity profile at Centerline 4 determined from forward modeling, and Table 3.15 presents the tabulated values of layer properties that were used to generate the

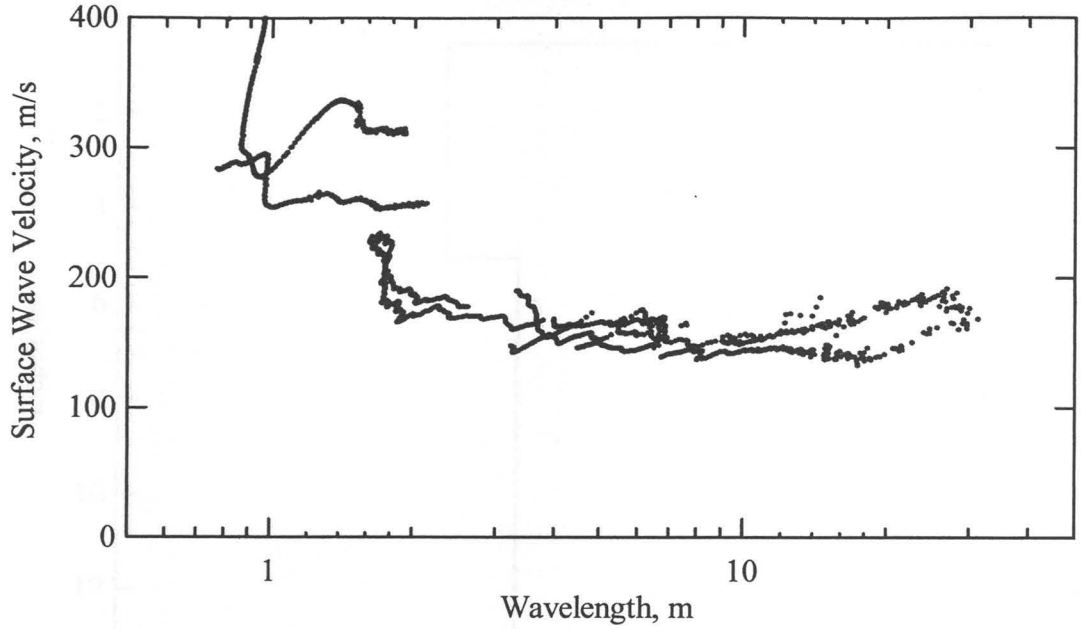

Figure 3.60 Experimental dispersion curve measured at Hotel Sapanca Centerline 1, Aug. 18, 2000, Sapanca, Turkey.

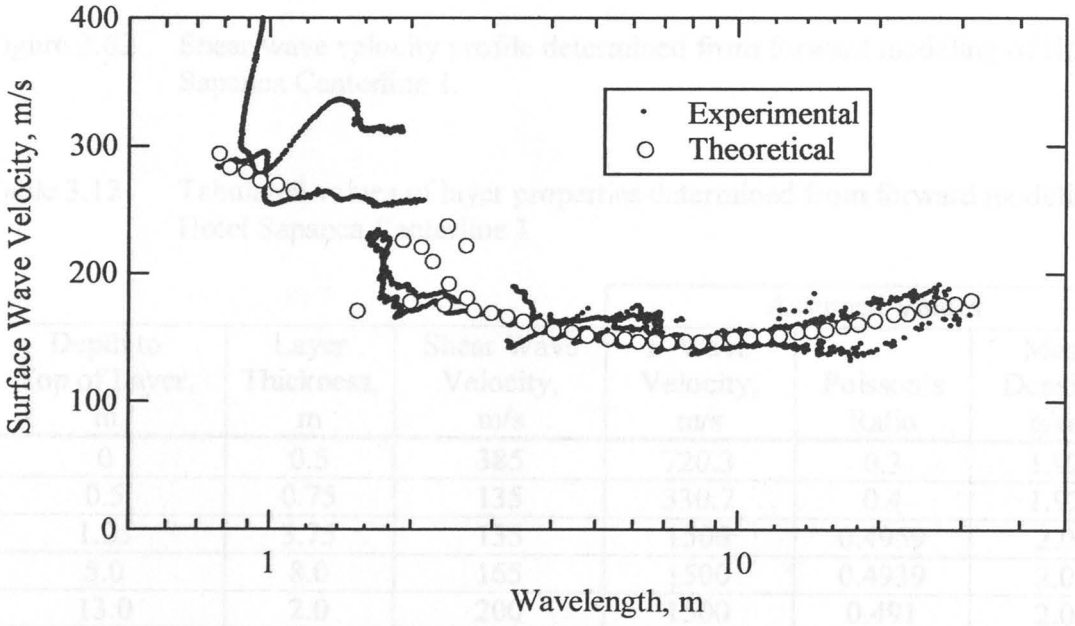

Figure 3.61 Comparison of experimental and theoretical dispersion curves from Hotel Sapanca Centerline 1.

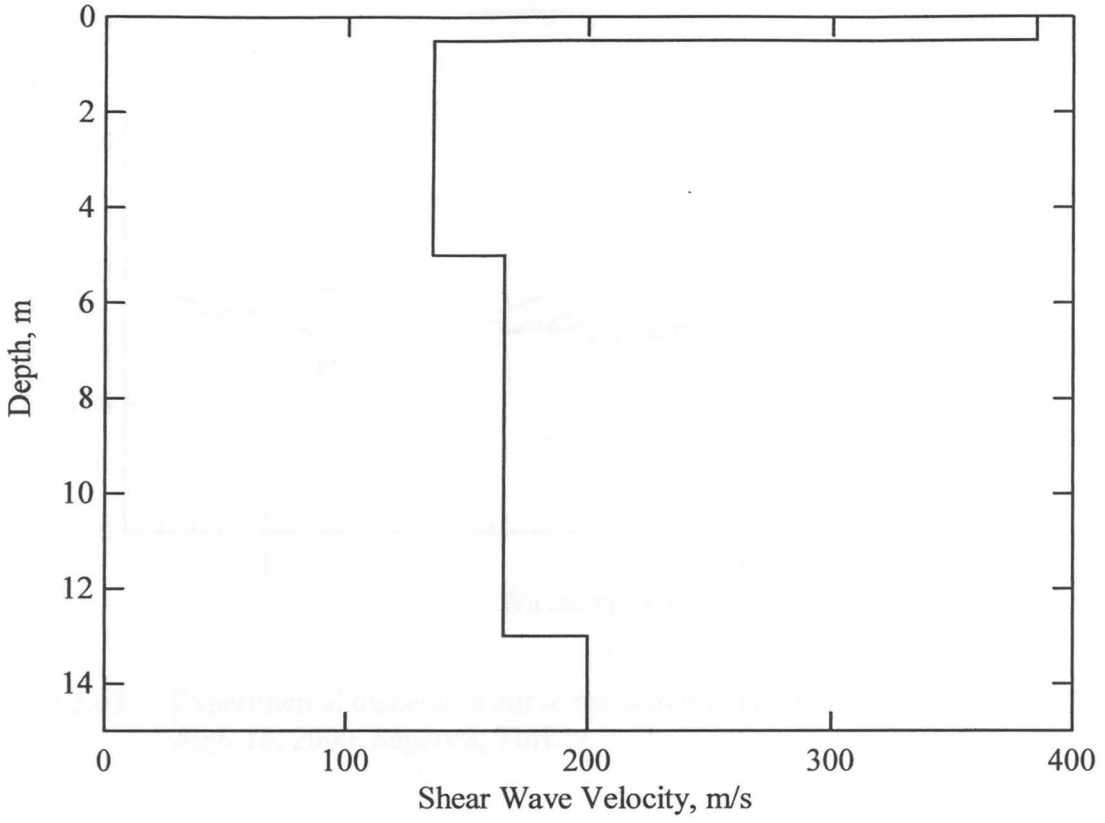

Figure 3.62 Shear wave velocity profile determined from forward modeling of Hotel Sapanca Centerline 1.

Table 3.12 Tabulated values of layer properties determined from forward modeling of Hotel Sapanca Centerline 1

			Assumed Values		
Depth to Top of Layer, m	Layer Thickness, m	Shear Wave Velocity, m/s	P-Wave Velocity, m/s	Poisson's Ratio	Mass Density, g/cc
0	0.5	385	720.3	0.3	1.92
0.5	0.75	135	330.7	0.4	1.92
1.25	3.75	135	1500	0.4959	2.0
5.0	8.0	165	1500	0.4939	2.0
13.0	2.0	200	1500	0.491	2.0

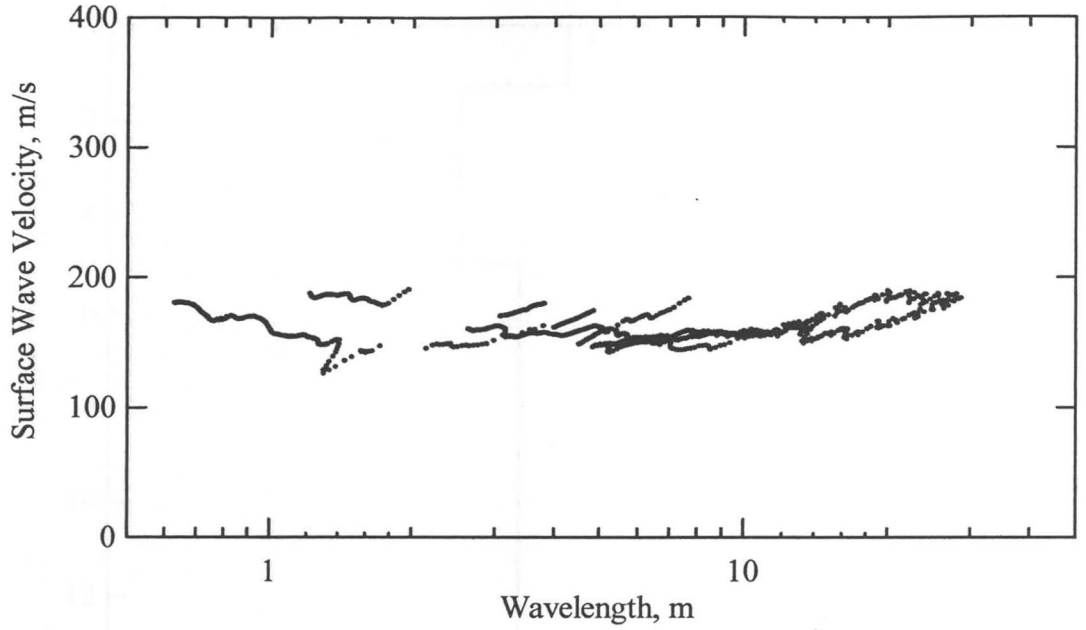

Figure 3.63 Experimental dispersion curve measured at Hotel Sapanca Centerline 2, Aug. 18, 2000, Sapanca, Turkey.

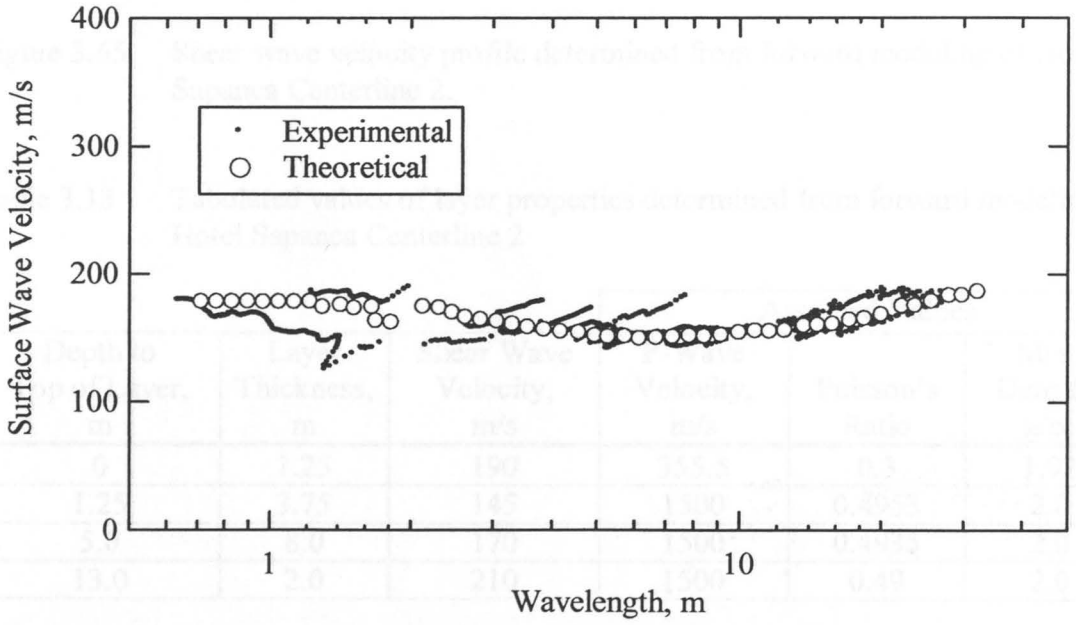

Figure 3.64 Comparison of experimental and theoretical dispersion curves from Hotel Sapanca Centerline 2.

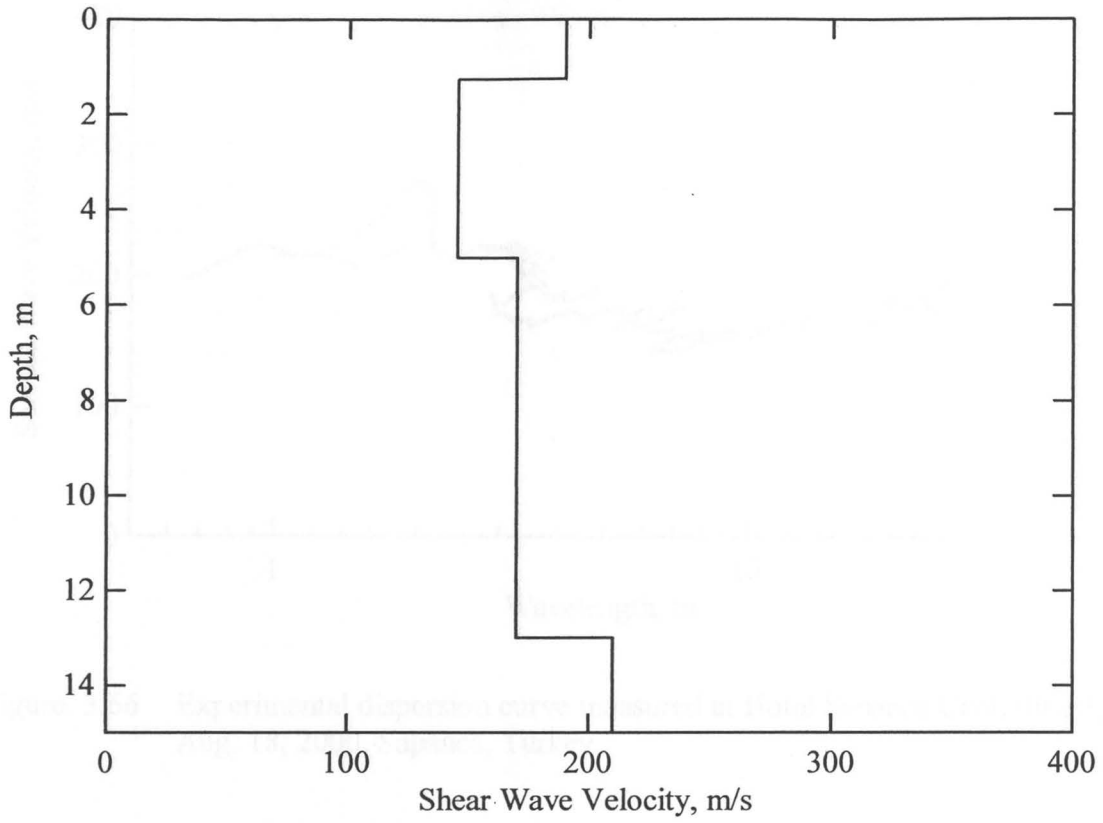

Figure 3.65 Shear wave velocity profile determined from forward modeling of Hotel Sapanca Centerline 2.

Table 3.13 Tabulated values of layer properties determined from forward modeling of Hotel Sapanca Centerline 2

			Assumed Values		
Depth to Top of Layer, m	Layer Thickness, m	Shear Wave Velocity, m/s	P-Wave Velocity, m/s	Poisson's Ratio	Mass Density, g/cc
0	1.25	190	355.5	0.3	1.92
1.25	3.75	145	1500	0.4953	2.0
5.0	8.0	170	1500	0.4935	2.0
13.0	2.0	210	1500	0.49	2.0

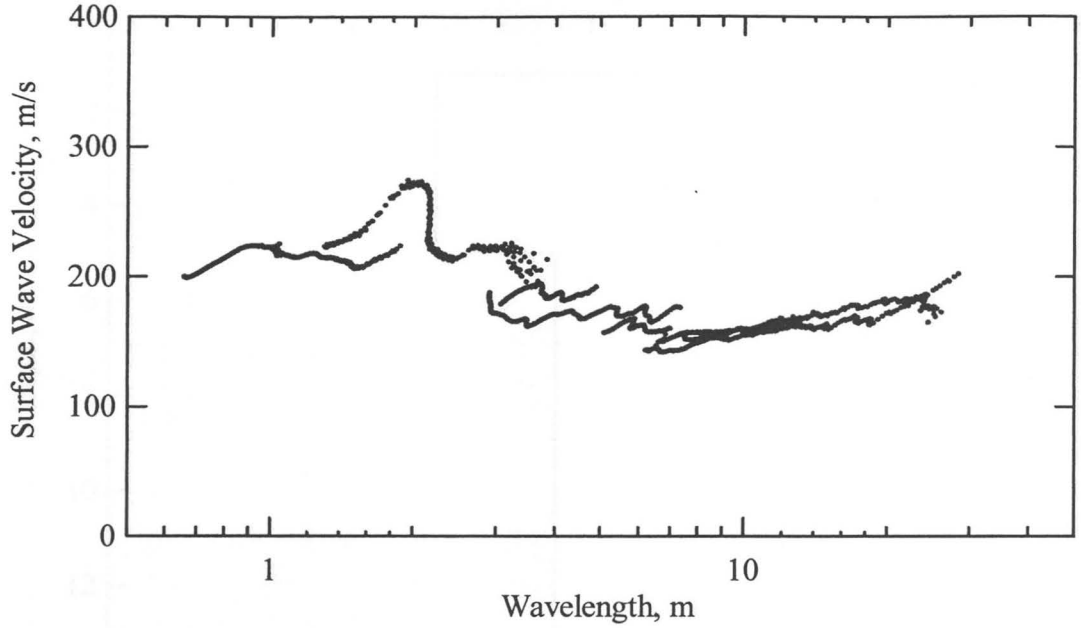

Figure. 3.66 Experimental dispersion curve measured at Hotel Sapanca Centerline 3, Aug. 18, 2000, Sapanca, Turkey.

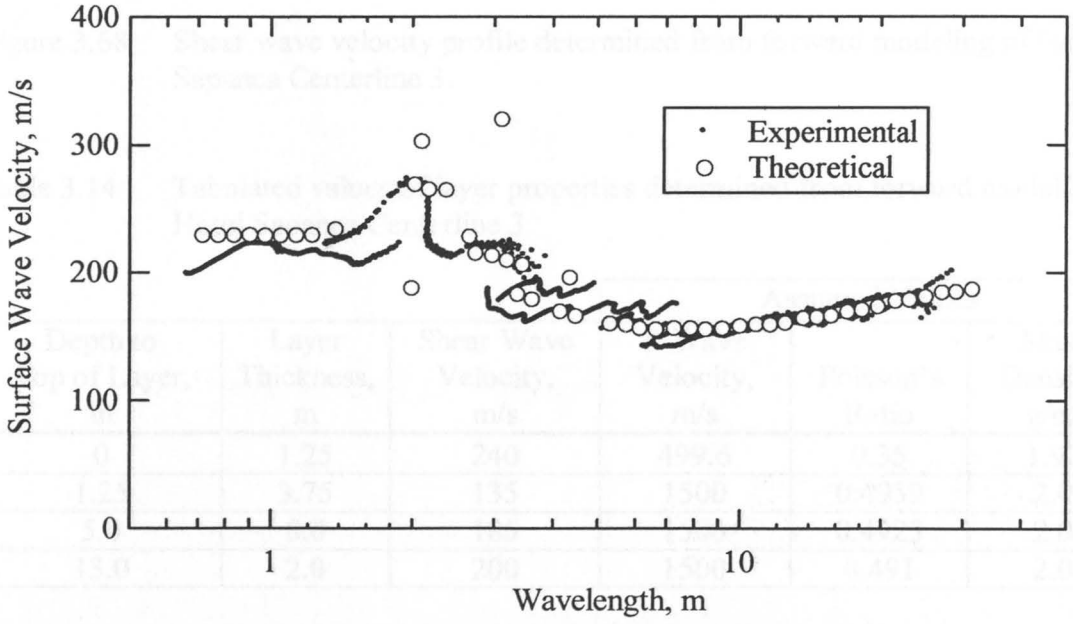

Figure 3.67 Comparison of experimental and theoretical dispersion curves from Hotel Sapanca Centerline 3.

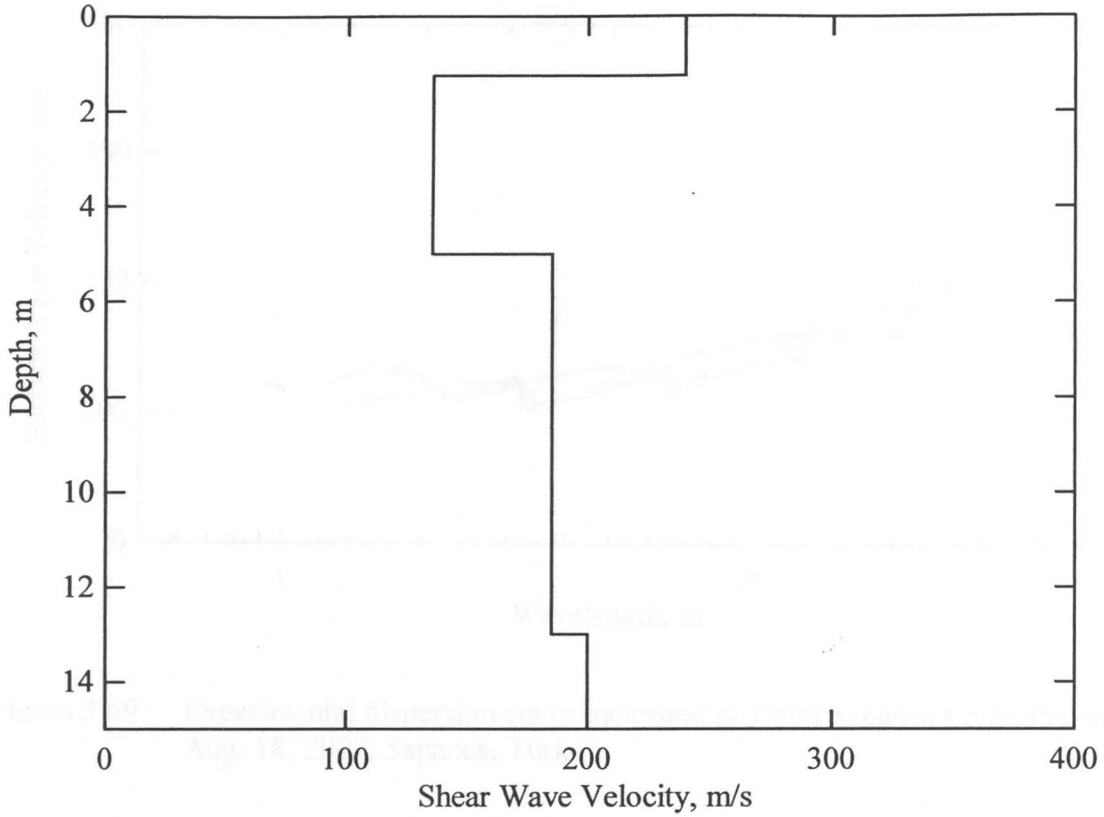

Figure 3.68 Shear wave velocity profile determined from forward modeling of Hotel Sapanca Centerline 3.

Table 3.14 Tabulated values of layer properties determined from forward modeling of Hotel Sapanca Centerline 3

			Assumed Values		
Depth to Top of Layer, m	Layer Thickness, m	Shear Wave Velocity, m/s	P-Wave Velocity, m/s	Poisson's Ratio	Mass Density, g/cc
0	1.25	240	499.6	0.35	1.92
1.25	3.75	135	1500	0.4959	2.0
5.0	8.0	185	1500	0.4923	2.0
13.0	2.0	200	1500	0.491	2.0

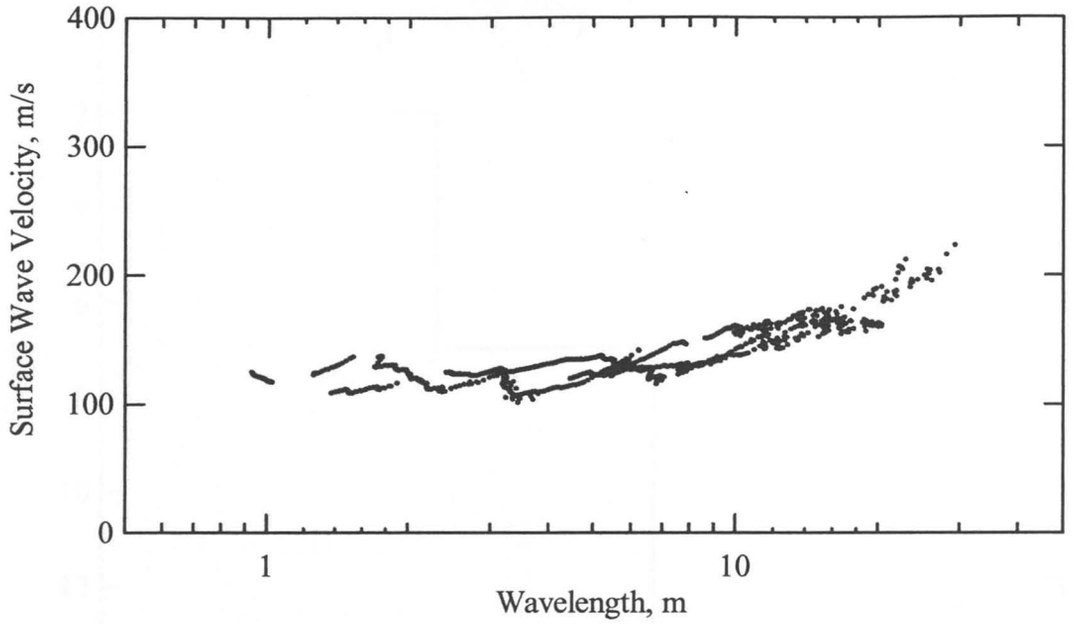

Figure 3.69 Experimental dispersion curve measured at Hotel Sapanca Centerline 4, Aug. 18, 2000, Sapanca, Turkey.

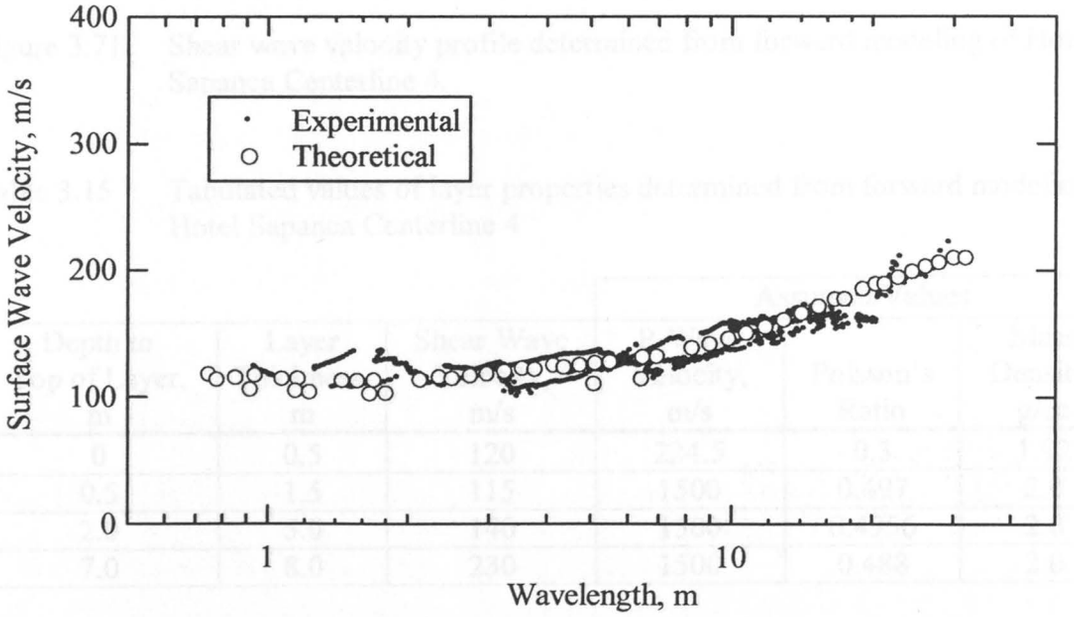

Figure 3.70 Comparison of experimental and theoretical dispersion curves from Hotel Sapanca Centerline 4.

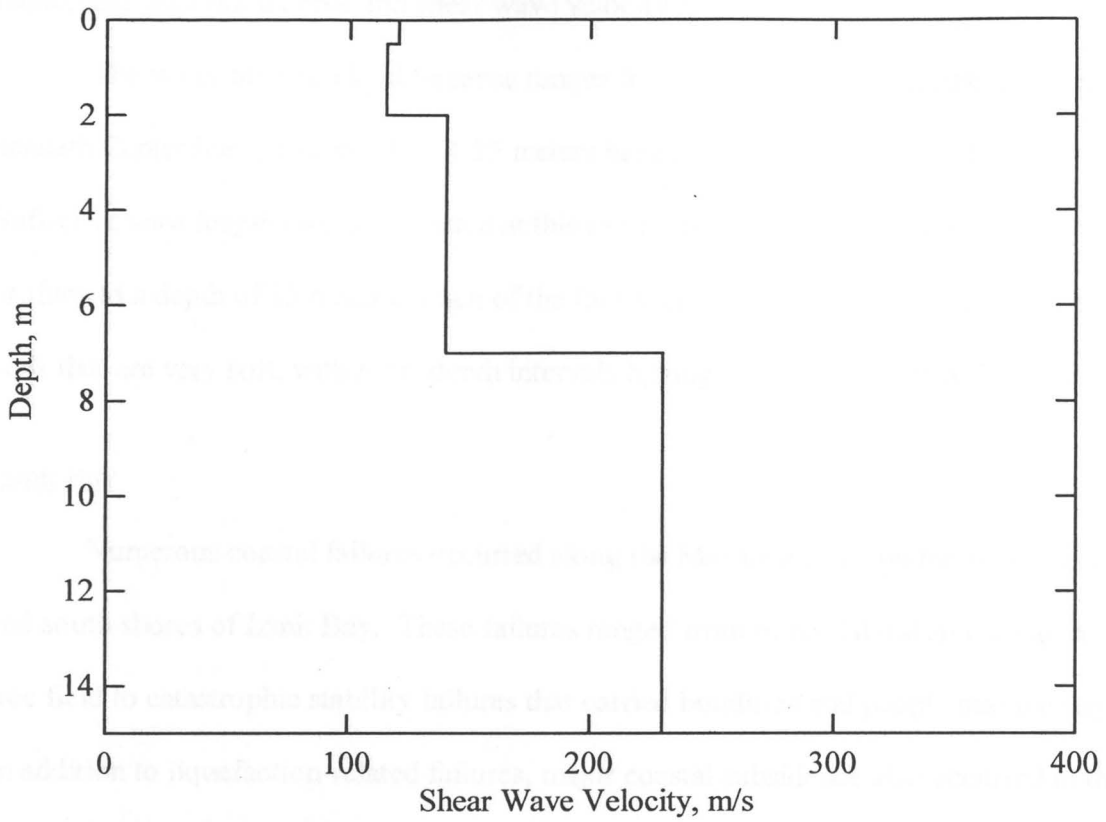

Figure 3.71 Shear wave velocity profile determined from forward modeling of Hotel Sapanca Centerline 4.

Table 3.15 Tabulated values of layer properties determined from forward modeling of Hotel Sapanca Centerline 4

			Assumed Values		
Depth to Top of Layer, m	Layer Thickness, m	Shear Wave Velocity, m/s	P-Wave Velocity, m/s	Poisson's Ratio	Mass Density, g/cc
0	0.5	120	224.5	0.3	1.92
0.5	1.5	115	1500	0.497	2.0
2.0	5.0	140	1500	0.4956	2.0
7.0	8.0	230	1500	0.488	2.0

theoretical dispersion curve and shear wave velocity profile.

The water table at Hotel Sapanca ranges from a depth of approximately 0.5 meters beneath Centerline 4, to a depth of 1.25 meters beneath Centerlines 3, 2, and 1. Sufficient wavelengths were generated at this site to extend the shear wave velocity profiles to a depth of 15 meters. Each of the four shear wave velocity profiles shows soils that are very soft, with most depth intervals having velocities less than 200 m/s.

Izmit Bay

Numerous coastal failures occurred along the Marmara coast on the north, east, and south shores of Izmit Bay. These failures ranged from minor lateral spreading in the free field to catastrophic stability failures that carried buildings and people into the bay. In addition to liquefaction-related failures, major coastal subsidence also occurred in the Golcuk area (EERI, 2000). Four liquefaction-induced lateral spread sites located in this region will be discussed below. Refer back to Figure 3.4 for site locations.

Degirmendere Nose. Degirmendere Nose is located on the south shore of Izmit Bay in Degirmendere. Its latitude and longitude coordinates are 40.7219° north and 29.7820° east, respectively. A plan view of Degirmendere Nose is shown in Figure 3.72. This map also shows the SASW centerline location with respect to the SPT and CPT test locations. The largest and most devastating coastal stability failure occurred here. A large section of fill, along with a hotel and two restaurants, was carried into the bay. Notice the former shoreline and new shoreline designations in Figure 3.72. Figure 3.73 is an aerial view of the site that shows a barge-mounted crane searching for the remains of those who died in the hotel. The cause of this enormous failure is not fully understood.

those who died in the hotel. The cause of this enormous failure is not fully understood. Small lateral spread cracks were observed along the on-shore part of the failure behind a large head scarp. Figure 3.74 shows the experimental dispersion curve measured at the site. Figure 3.75 shows the comparison between the experimental dispersion curve and the final theoretical dispersion curve determined from forward modeling. Figure 3.76 shows the shear wave velocity profile at the site determined from forward modeling, and Table 3.16 presents the tabulated values of layer properties that were used to generate the theoretical dispersion curve and shear wave velocity profile.

The water table at Degirmendere Nose is located at a depth of approximately 1.5 meters. Sufficient wavelengths were generated at this site to extend the shear wave velocity profile to a depth of 15 meters. The majority of the soil profile here consists of soils that have a shear wave velocity of 200 m/s.

Police Station. Police Station is a lateral spread site at the eastern end of Izmit Bay. The reason this site is designated as Police Station is obscure, as there are no nearby police stations. Its latitude and longitude coordinates are 40.7215° north and 29.9373° east, respectively. A plan view of Police Station is shown in Figure 3.77. This map also shows the SASW centerline location with respect to the SPT and CPT test locations. This site is directly adjacent to where the fault surface rupture exits the eastern end of Izmit Bay. No structures are located nearby. Figure 3.78 shows a picture of the large ground cracking that occurred here. Some evidence of liquefaction ejecta was also observed. Figure 3.79 shows the experimental dispersion curve measured at the site.

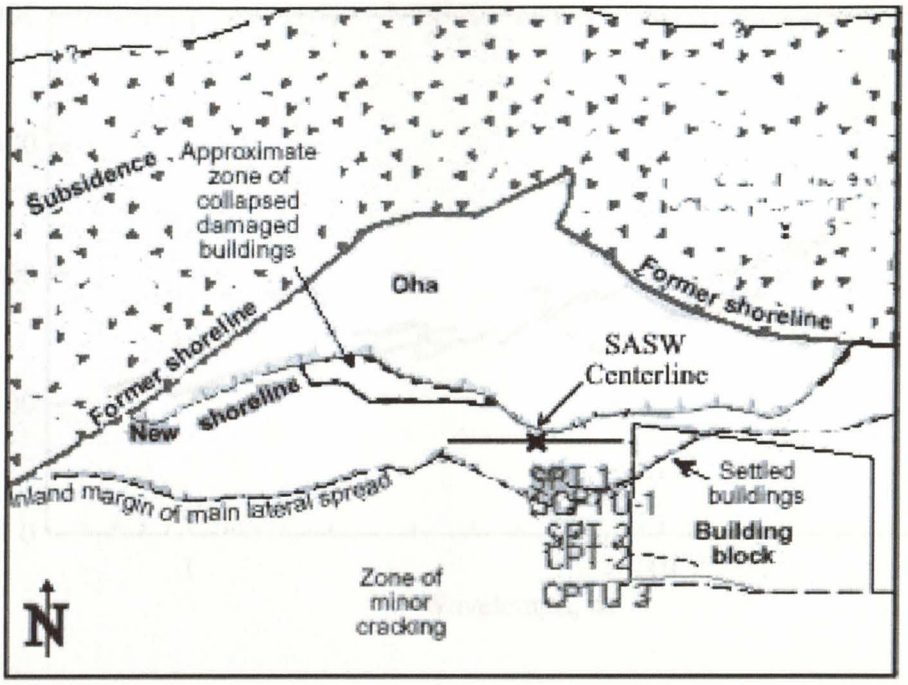

Figure 3.72 Plan view of Degirmendere Nose showing the location of one SASW centerline (modified from www.eerc.berkeley.edu/turkey/adapazari).

Figure 3.73 Photograph showing the barge-mounted crane that was used to search for the remains of people carried into the bay at Degirmendere Nose (from www.eerc.berkeley.edu/turkey/adapazari).

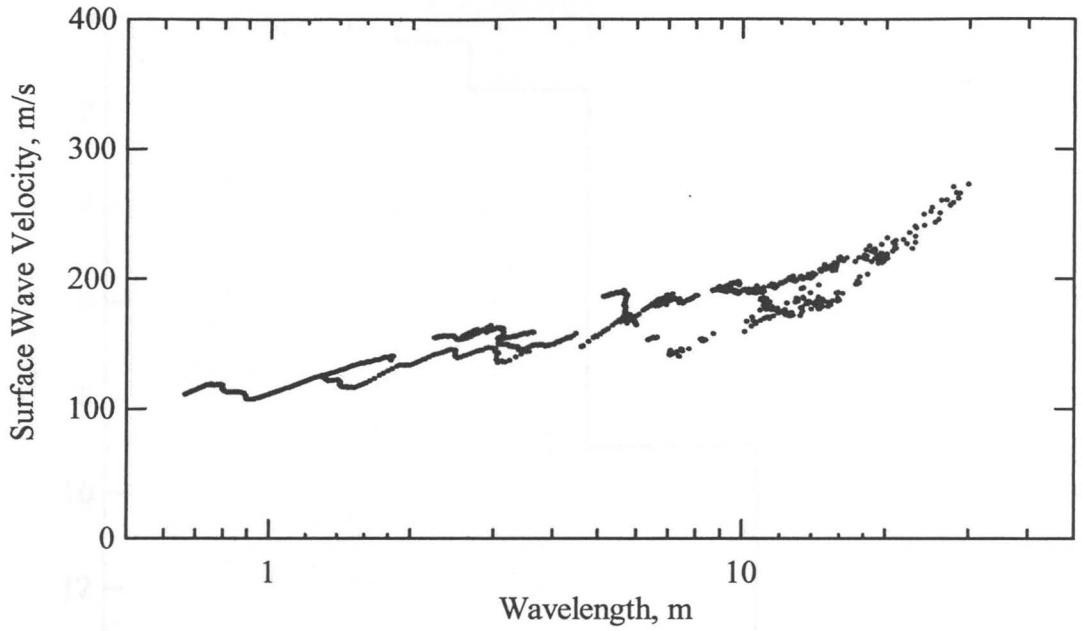

Figure 3.74 Experimental dispersion curve measured at Degirmendere Nose, Aug. 23, 2000, Adapazari, Turkey.

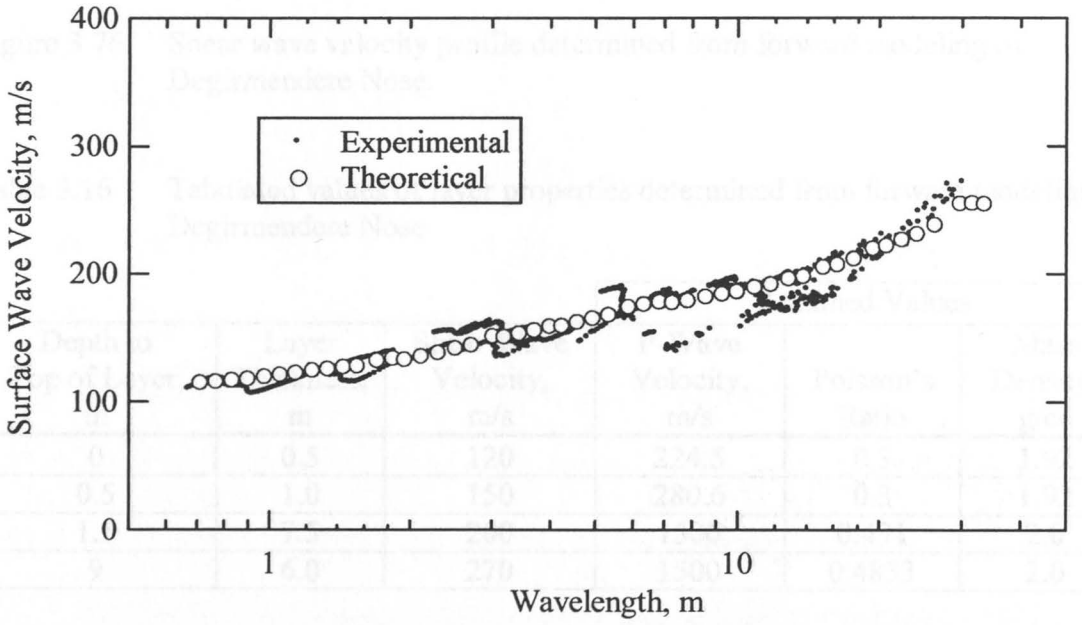

Figure 3.75 Comparison of experimental and theoretical dispersion curves from Degirmendere Nose.

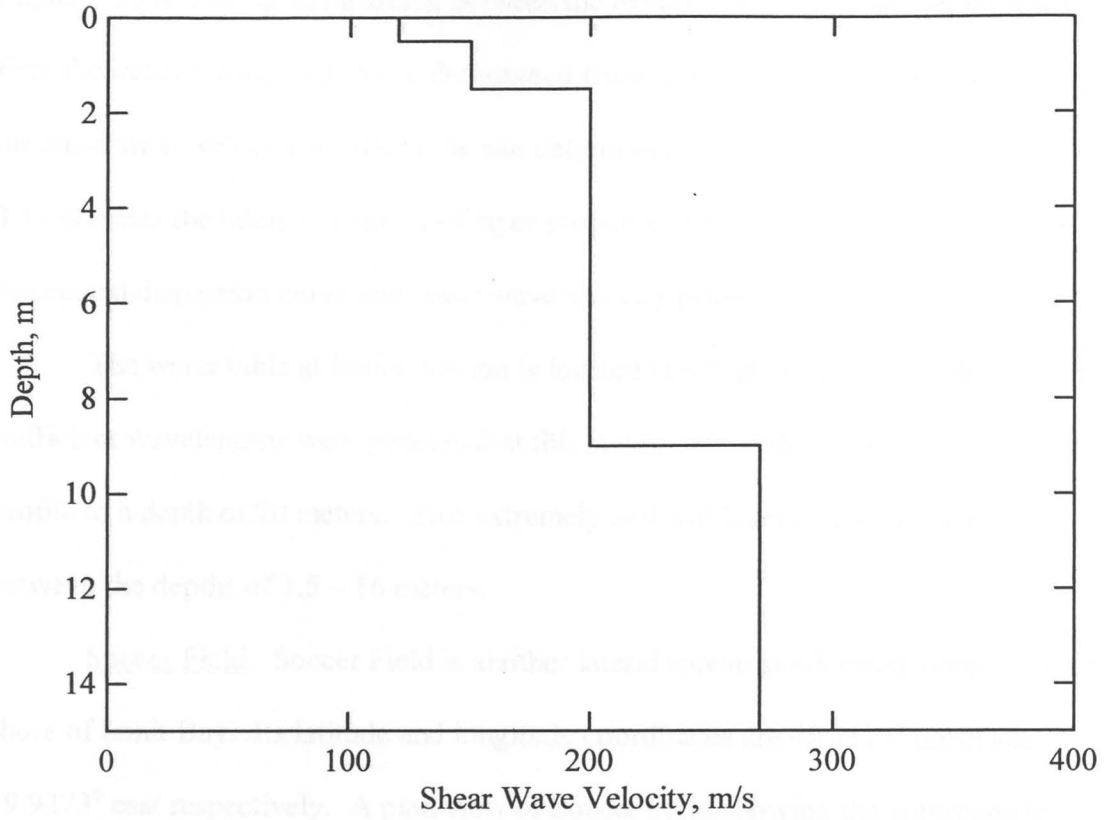

Figure 3.76 Shear wave velocity profile determined from forward modeling of Degirmendere Nose.

Table 3.16 Tabulated values of layer properties determined from forward modeling of Degirmendere Nose

			Assumed Values		
Depth to Top of Layer, m	Layer Thickness, m	Shear Wave Velocity, m/s	P-Wave Velocity, m/s	Poisson's Ratio	Mass Density, g/cc
0	0.5	120	224.5	0.3	1.92
0.5	1.0	150	280.6	0.3	1.92
1.5	7.5	200	1500	0.491	2.0
9	6.0	270	1500	0.4833	2.0

Figure 3.80 shows the comparison between the experimental dispersion curve and the final theoretical dispersion curve determined from forward modeling. Figure 3.81 shows the shear wave velocity profile at the site determined from forward modeling, and Table 3.17 presents the tabulated values of layer properties that were used to generate the theoretical dispersion curve and shear wave velocity profile.

The water table at Police Station is located at a depth of approximately 1.0 meter. Sufficient wavelengths were generated at this site to extend the shear wave velocity profile to a depth of 20 meters. Two extremely soft soil layers were identified here between the depths of 1.5 – 16 meters.

Soccer Field. Soccer Field is another lateral spread site located along the south shore of Izmit Bay. Its latitude and longitude coordinates are 40.7177° north and 29.9273° east respectively. A plan view of Soccer Field showing the approximate location of the SASW centerline is shown in Figure 3.82. The site is a small soccer field where large ground cracks occurred due to lateral spreading into the Bay. A photograph of the site is shown in Figure 3.83. Figure 3.84 shows the experimental dispersion curve measured at the site. Figure 3.85 shows the comparison between the experimental dispersion curve and the final theoretical dispersion curve determined from forward modeling. Figure 3.86 shows the shear wave velocity profile at the site determined from forward modeling, and Table 3.18 presents the tabulated values of layer properties that were used to generate the theoretical dispersion curve and shear wave velocity profile.

The water table at Soccer Field is located at a depth of approximately 1.0 meter. Sufficient wavelengths were generated at this site to extend the shear wave velocity

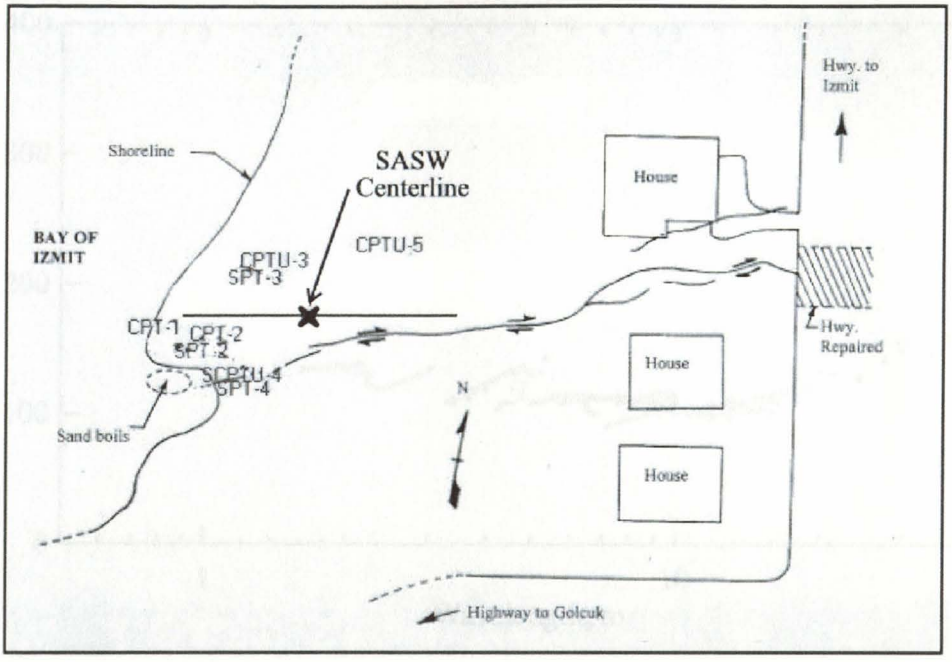

Figure 3.77 Plan view of Police Station showing the location of one SASW centerline (modified from www.eerc.berkeley.edu/turkey/adapazari).

Figure 3.78 Photograph showing the large ground cracking that occurred at Police Station during the earthquake. The surface fault rupture exits the bay near here.

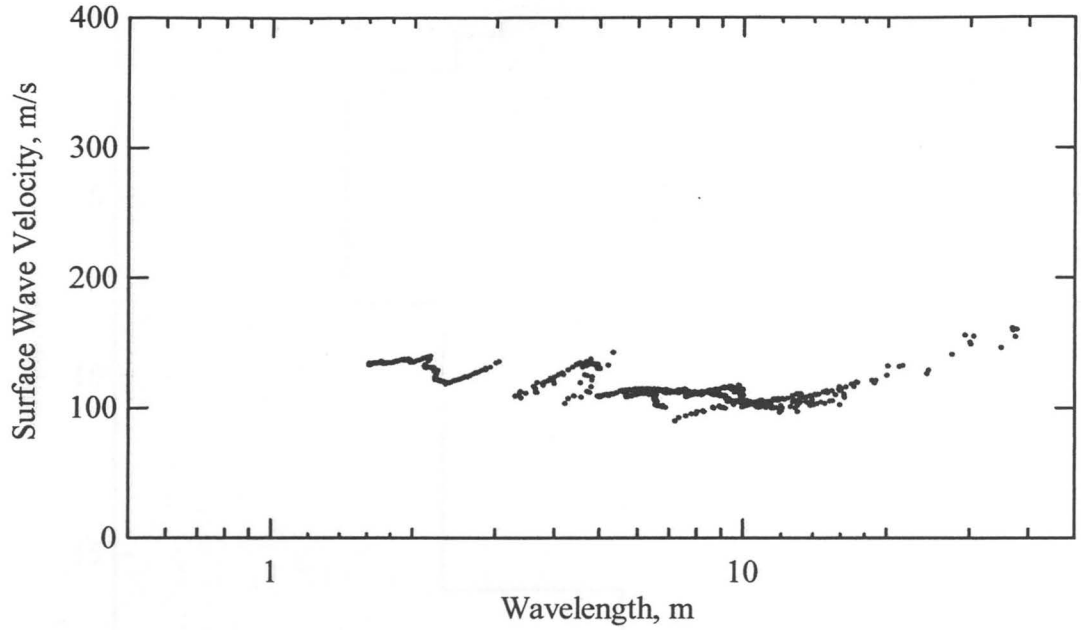

Figure 3.79 Experimental dispersion curve measured at Police Station, Aug. 23, 2000, Golcuk, Turkey.

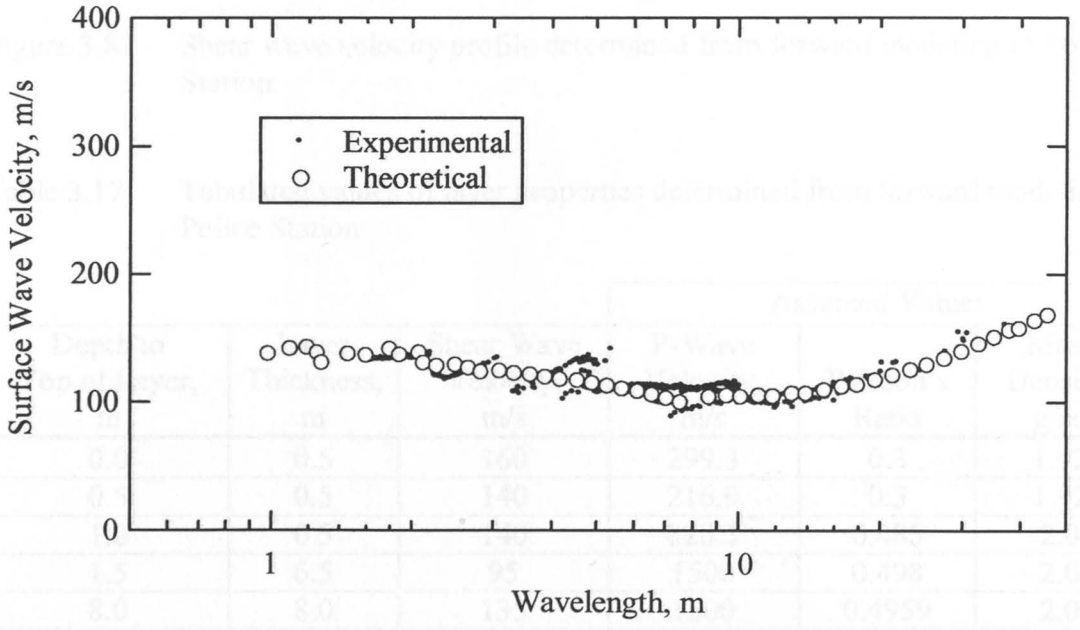

Figure 3.80 Comparison of experimental and theoretical dispersion curves from Police Station.

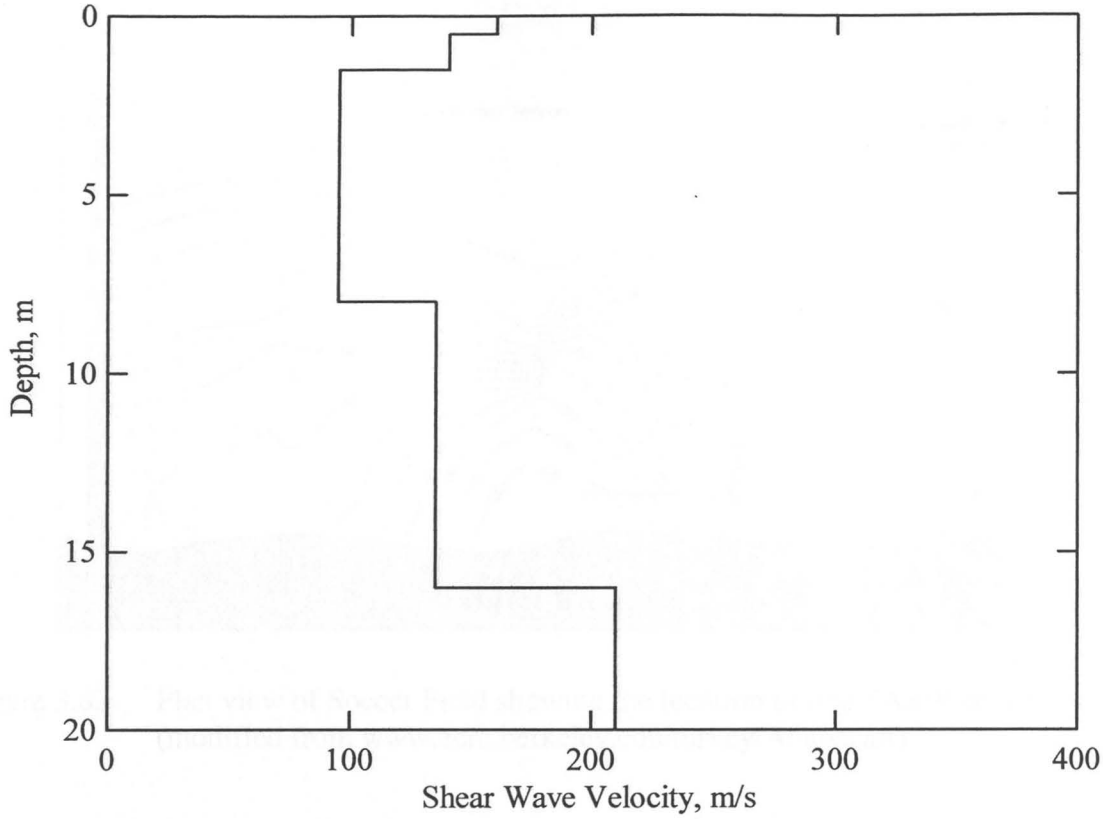

Figure 3.81 Shear wave velocity profile determined from forward modeling of Police Station.

Table 3.17 Tabulated values of layer properties determined from forward modeling of Police Station

			Assumed Values		
Depth to Top of Layer, m	Layer Thickness, m	Shear Wave Velocity, m/s	P-Wave Velocity, m/s	Poisson's Ratio	Mass Density, g/cc
0.0	0.5	160	299.3	0.3	1.92
0.5	0.5	140	216.9	0.3	1.92
1.0	0.5	140	820.3	0.485	2.0
1.5	6.5	95	1500	0.498	2.0
8.0	8.0	135	1500	0.4959	2.0
16.0	4.0	210	1500	0.49	2.0

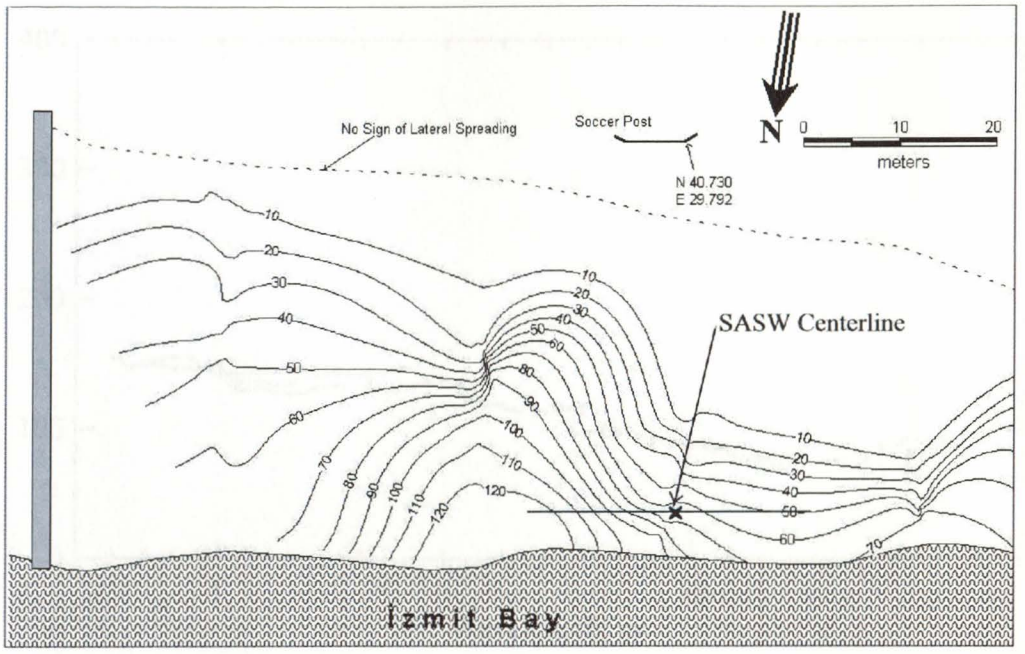

Figure 3.82 Plan view of Soccer Field showing the location of one SASW centerline (modified from www.eerc.berkeley.edu/turkey/Adapazari).

Figure 3.83 Photograph showing the ground cracks caused by lateral spreading into Izmit Bay at Soccer Field (from www.eerc.berkeley.edu/turkey/adapazari).

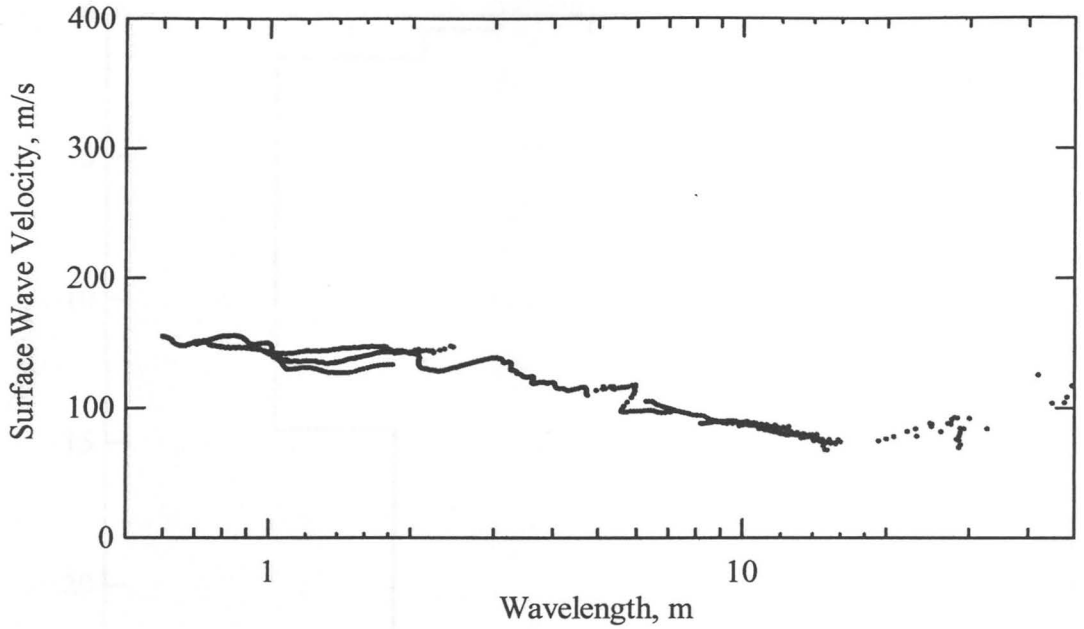

Figure 3.84 Experimental dispersion curve measured at Soccer Field, Aug. 23, 2000, Golcuk, Turkey.

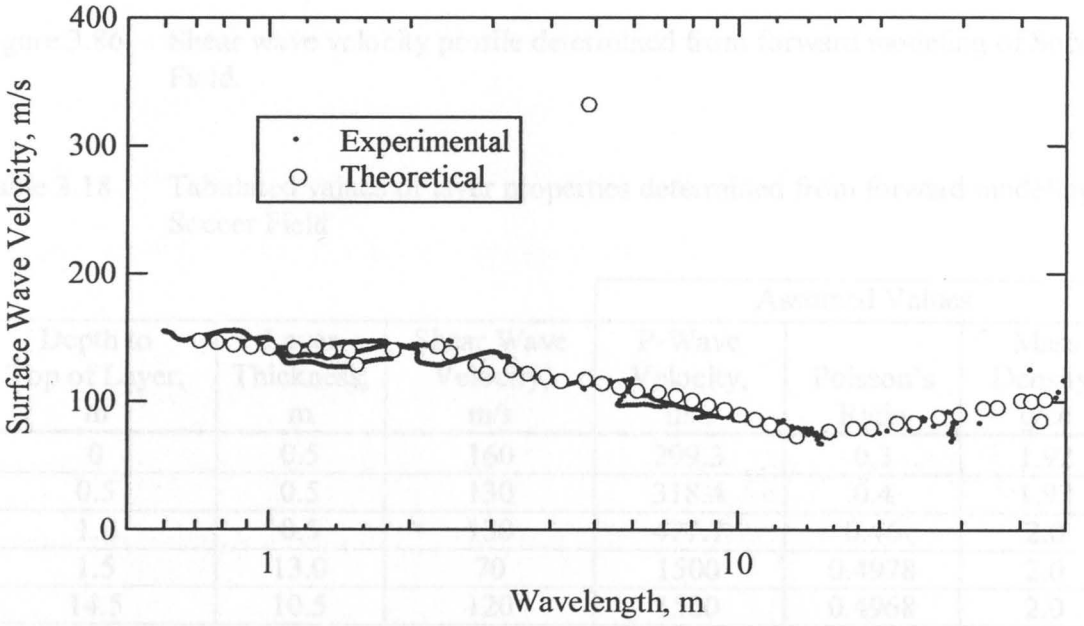

Figure 3.85 Comparison of experimental and theoretical dispersion curves from Soccer Field.

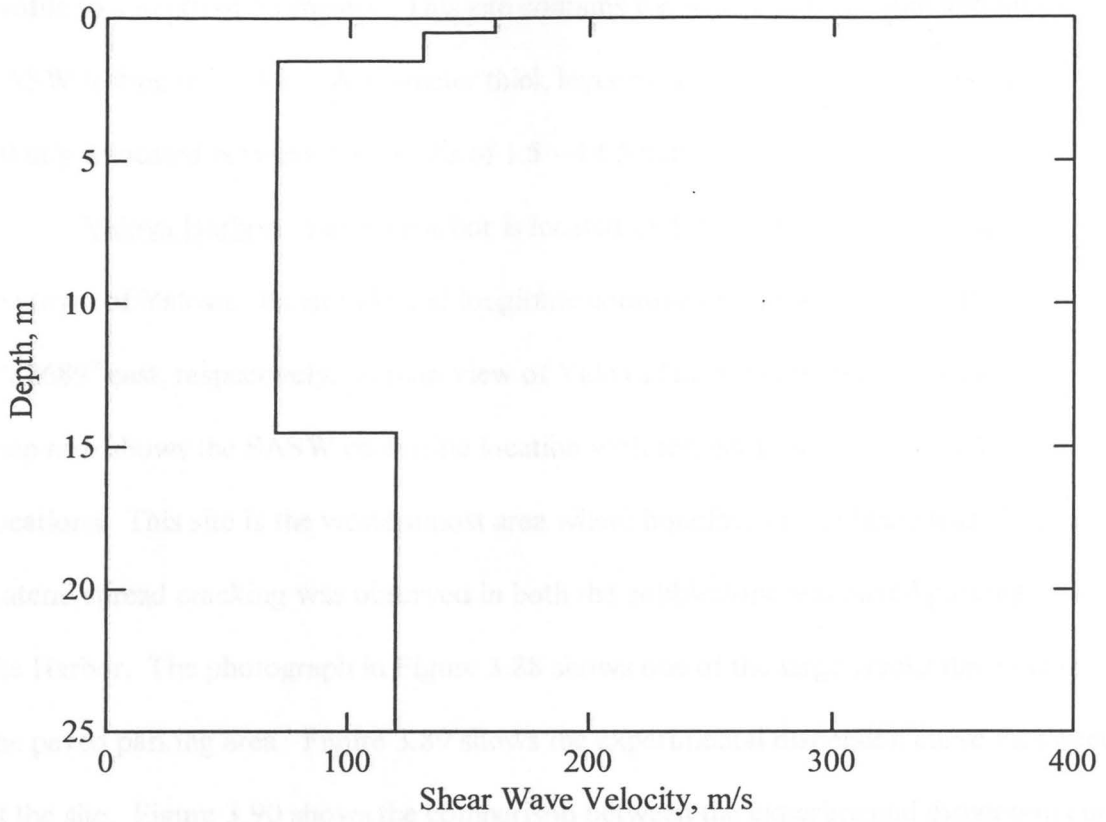

Figure 3.86 Shear wave velocity profile determined from forward modeling of Soccer Field.

Table 3.18 Tabulated values of layer properties determined from forward modeling of Soccer Field

			Assumed Values		
Depth to Top of Layer, m	Layer Thickness, m	Shear Wave Velocity, m/s	P-Wave Velocity, m/s	Poisson's Ratio	Mass Density, g/cc
0	0.5	160	299.3	0.3	1.92
0.5	0.5	130	318.4	0.4	1.92
1.0	0.5	130	477.7	0.46	2.0
1.5	13.0	70	1500	0.4978	2.0
14.5	10.5	120	1500	0.4968	2.0

profile to a depth of 25 meters. This site contains the softest soil encountered during SASW testing in Turkey. A 13-meter thick layer of soil having a shear wave velocity of 70 m/s is located between the depths of 1.5 – 14.5 meters

Yalova Harbor. Yalova Harbor is located on the southern shore of Izmit Bay in the town of Yalova. Its latitude and longitude coordinates are 40.6597° north and 29.2689° east, respectively. A plan view of Yalova Harbor is shown in Figure 3.87. This map also shows the SASW centerline location with respect to the SPT and CPT test locations. This site is the westernmost area where liquefaction evidence was observed. Lateral spread cracking was observed in both the cobblestone and paved parking areas at the Harbor. The photograph in Figure 3.88 shows one of the large cracks that occurred in the paved parking area. Figure 3.89 shows the experimental dispersion curve measured at the site. Figure 3.90 shows the comparison between the experimental dispersion curve and the final theoretical dispersion curve determined from forward modeling. Figure 3.91 shows the shear wave velocity profile at the site determined from forward modeling, and Table 3.19 presents the tabulated values of layer properties that were used to generate the theoretical dispersion curve and shear wave velocity profile.

The water table at Yalova Harbor is located at a depth of approximately 0.75 meters. Sufficient wavelengths were generated at this site to extend the shear wave velocity profile to a depth of 10 meters. The top layer shows the stiff cobblestone crust. The remainder of the soil profile is extremely soft.

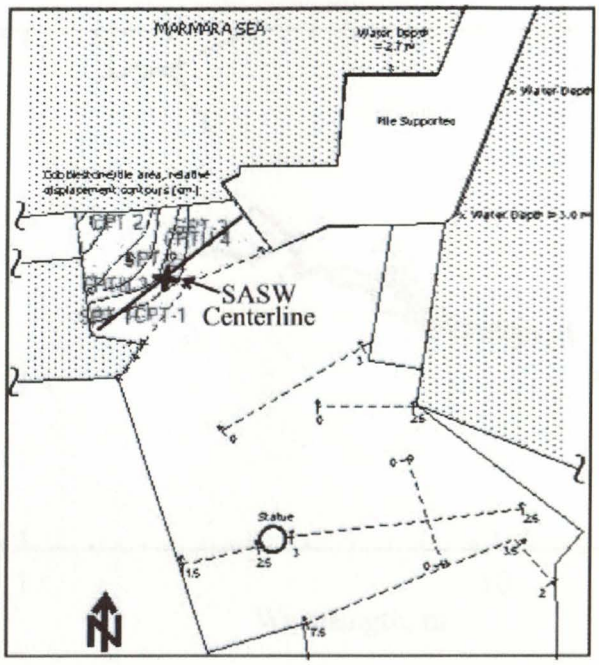

Figure 3.87 Plan view of Yalova Harbor showing the location of one SASW centerline (modified from www.eerc.berkeley.edu/turkey/adapazari).

Figure 3.88 Photograph showing a lateral spread crack that developed in the paved parking area at Yalova Harbor. The cobblestone parking area was also damaged (from www.eerc.berkeley.edu/turkey/adapazari).

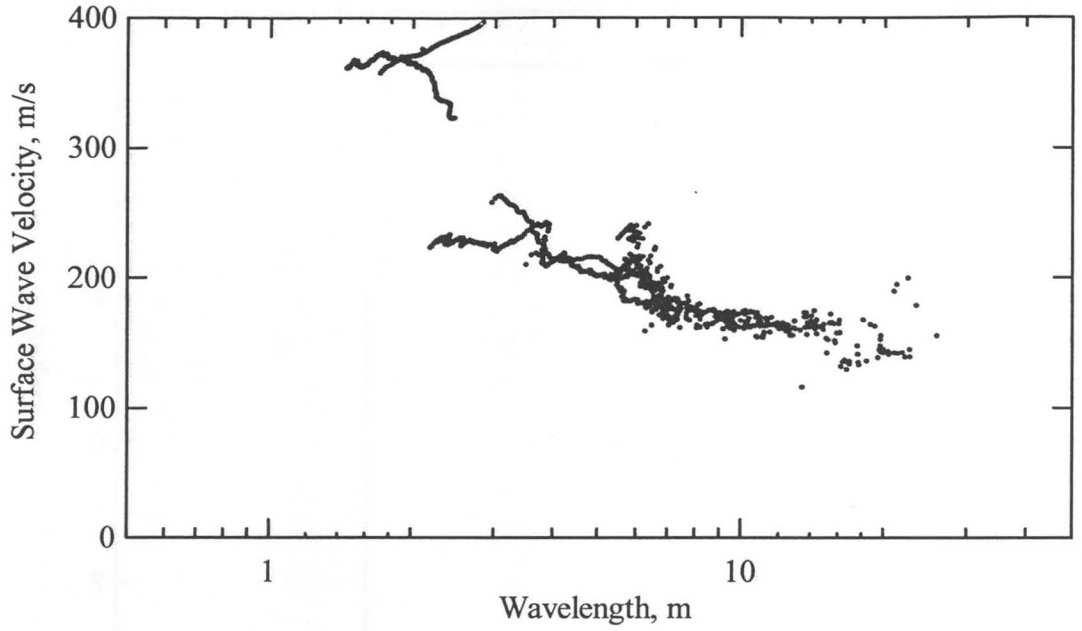

Figure 3.89 Experimental dispersion curve measured at Yalova Harbor, Aug. 23, 2000, Yalova, Turkey.

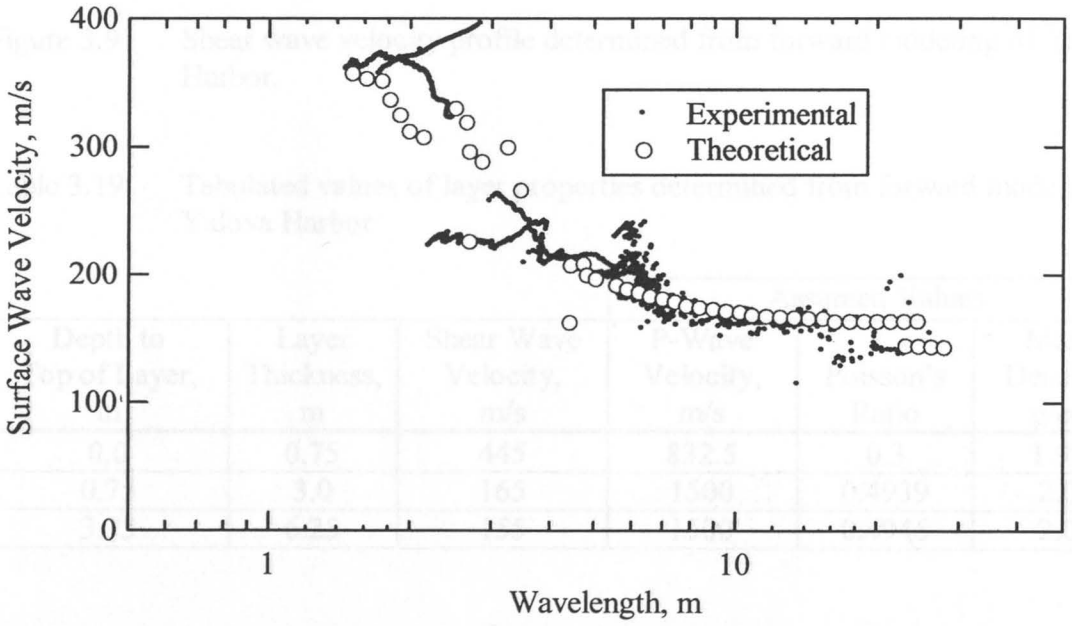

Figure 3.90 Comparison of experimental and theoretical dispersion curves from Yalova Harbor.

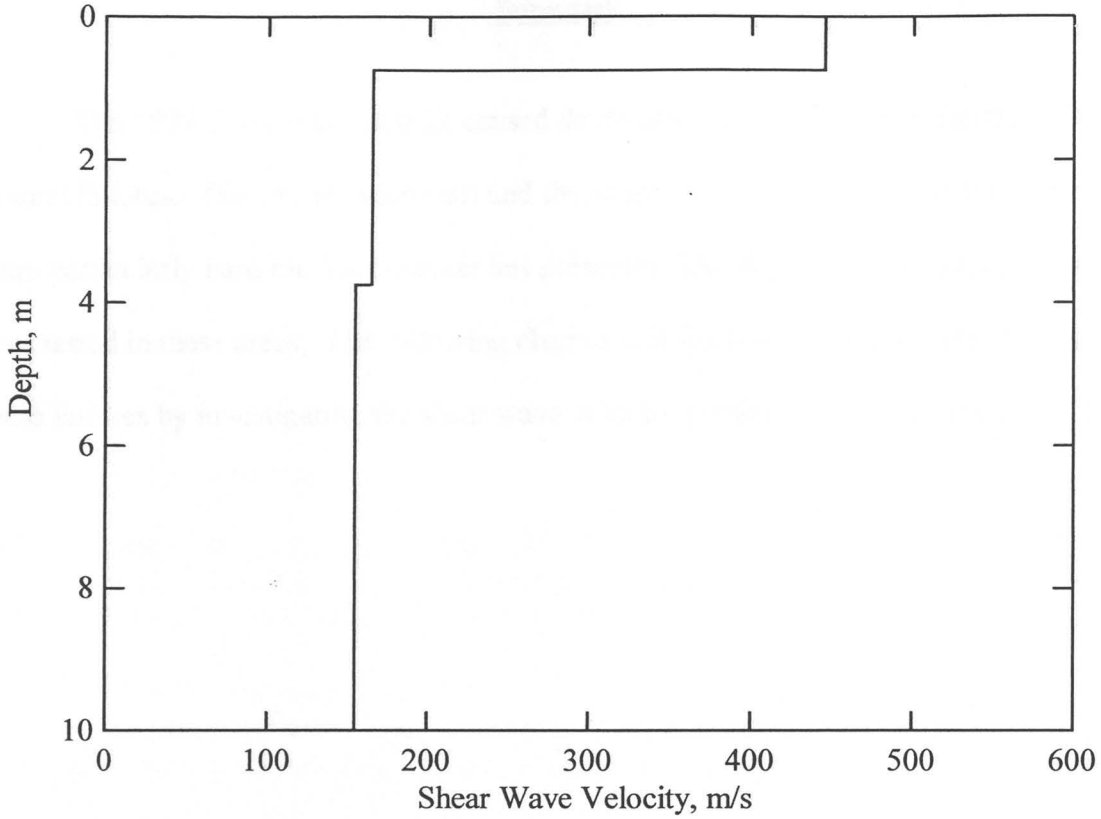

Figure 3.91 Shear wave velocity profile determined from forward modeling of Yalova Harbor.

Table 3.19 Tabulated values of layer properties determined from forward modeling of Yalova Harbor

			Assumed Values		
Depth to Top of Layer, m	Layer Thickness, m	Shear Wave Velocity, m/s	P-Wave Velocity, m/s	Poisson's Ratio	Mass Density, g/cc
0.0	0.75	445	832.5	0.3	1.92
0.75	3.0	165	1500	0.4939	2.0
3.75	6.25	155	1500	0.4946	2.0

Summary

The 1999 Kocaeli earthquake caused devastating amounts of liquefaction-induced ground failures. The city of Adapazari and the shores of Lake Sapanca and Izmit Bay were particularly hard hit. This chapter has presented SASW results from 15 liquefaction sites tested in these areas. The following chapter will focus on evaluating the cause of these failures by investigating the shear wave velocity profiles and soil data at each site.

CHAPTER 4

LIQUEFACTION ANALYSIS

Chapter 3 presented site descriptions and shear wave velocity profiles for the liquefaction sites that were tested after the 1999 Kocaeli, Turkey earthquake. This chapter focuses on the procedures used to determine which soil layers most likely participated in liquefaction at each site. The first step in this process was to delineate a potentially liquefiable region at each site. This was accomplished through use of the simplified shear wave velocity method. All depths within the soil profile that had higher CSR's than CRR's were considered potentially liquefiable, meaning that the soil was soft enough to liquefy. However, soil stiffness alone does not control liquefaction. Therefore, the second step in determining which soil layers most likely liquefied was to separate liquefiable soils from nonliquefiable soils. At sites where actual soil samples were available, this was accomplished by using the Chinese Criteria and the Andrews and Martin Criteria. At sites where only CPT data were available, this was accomplished by developing profiles of the soil behavior type index (I_C). At some sites, all soil layers within the potentially liquefiable region were found to be nonliquefiable. This suggests that current liquefaction analysis techniques may not provide correct predictions for every type of soil.

Full descriptions of the simplified shear wave velocity procedure, the Chinese Criteria, the Andrews and Martin Criteria, and obtaining I_C values from CPT data can be found in Chapter 2. All soil sample data, CPT data, and depths to ground water at each site were obtained from SPT and CPT studies performed by the cooperative of

researchers mentioned in Chapter 3. The information they have provided is greatly appreciated and a full account of their research can be found at www.eerc.berkeley.edu /turkey/adapazari. The remainder of this chapter will discuss the liquefaction analysis procedure that was used, and the results that were obtained at each liquefaction site.

Delineating the Potentially Liquefiable Region

This section outlines the shear wave velocity simplified procedure that was used at each site to delineate the potentially liquefiable region. This procedure basically entails computing an earthquake induced cyclic stress ratio (CSR), and a soil layers natural cyclic resistance ratio (CRR) as obtained from shear wave velocity measurements. Layers in the soil profile having a CSR that is higher than the CRR are considered soft enough to liquefy.

Calculation of CRRs

The calculation of CRR's requires both an overburden corrected shear wave velocity and a maximum liquefiable velocity. All corrected shear wave velocities were calculated (refer to Equation 2.3) from the measured shear wave velocity profiles that were presented in Chapter 3. Figure 4.1 shows an example of a measured shear wave velocity profile (V_S) and its corresponding overburden corrected shear wave velocity profile (V_{S1}).

Determination of the maximum liquefiable shear wave velocity (V^*_{S1}) requires some knowledge about the fines content of the soil profile (refer to Equation 2.7). At

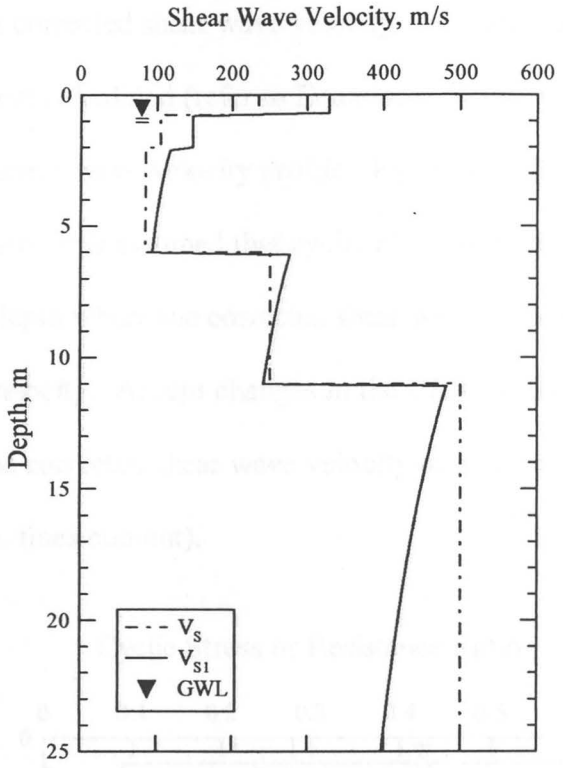

Figure 4.1 Example of the shear wave velocity (V_S) and corrected shear wave velocity (V_{S1}) profiles that were developed at each liquefaction site.

sites where soil sample data were available, fines content information was provided. This allowed for very accurate determinations of fines content within each soil profile. At sites where only CPT data were available, fines contents were inferred from I_C values (refer to Equation 2.14). Because the accuracy of this method is limited, most CPT sites were only distinguished as having fines values of less than 5% or greater than 35%. In depth intervals where fines content was not readily apparent, a conservative estimate of less than 5% was used. A more detailed discussion about how fines contents were determined at each site is discussed further below. Suffice it here to say that fines contents were evaluated and that maximum liquefiable velocities were obtained from these values.

Once values for corrected shear wave velocity and maximum liquefiable velocity were known, CRR's were calculated (refer to Equation 2.5) every one-tenth of a meter over the depth of each shear wave velocity profile. Figure 4.2 shows an example of CRR's plotted with depth. It is assumed that cyclic resistance ratios are infinite above the water table and at any depth where the corrected shear wave velocity exceeds the maximum liquefiable velocity. Abrupt changes in the CRR profile are always explained by either a change in the corrected shear wave velocity or a change in the maximum liquefiable velocity (i.e. fines content).

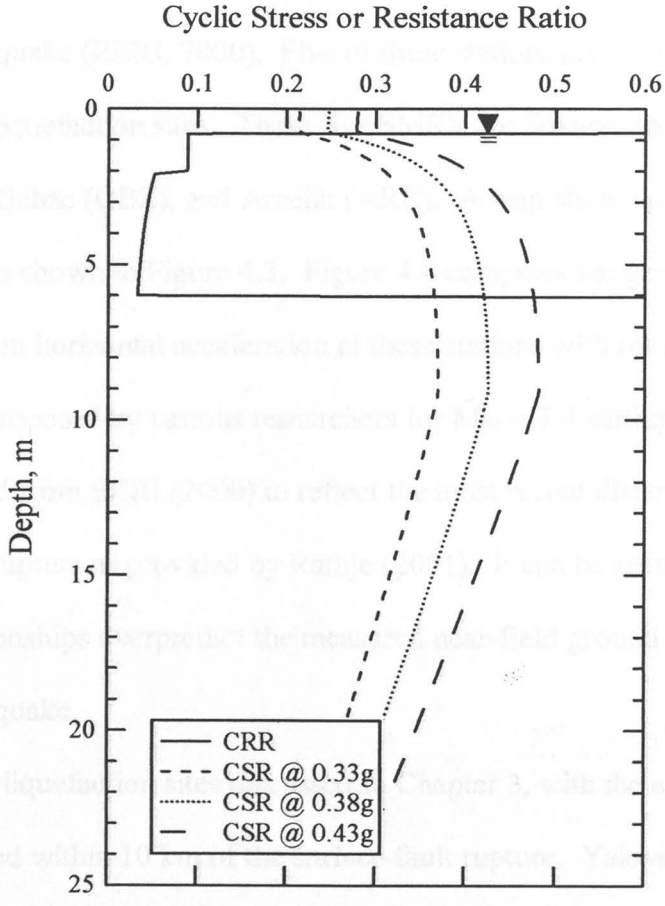

Figure 4.2 Example of the cyclic resistance ratio (CRR) and cyclic stress ratio (CSR) profiles that were developed for each liquefaction site.

Calculation of CSRs

In order to calculate CSR's an estimate of maximum ground surface acceleration must first be made. Traditionally ground accelerations at liquefaction sites have been predicted using attenuation relationships that were developed from large databases of recorded earthquake ground-motions. However, prior to the 1999 Kocaeli earthquake, there were fewer than 10 ground-motion records for moment magnitude (M_W) 7.0 or greater earthquakes recorded within 20 kilometers of the fault rupture. Distances less than approximately 20 kilometers from the fault rupture have been termed the "near-field." Six near-field Strong Motion Stations (SMS's) recorded ground-motions during the Kocaeli earthquake (EERI, 2000). Five of these stations are located in close proximity to the liquefaction sites. These five SMS's are Sakarya (SKR), Izmit (IZT), Yarimca (YPT), Gebze (GBZ), and Arcelik (ARC). A map showing the locations of test sites and SMS's is shown in Figure 4.3. Figure 4.4 compares the geometric mean of the recorded maximum horizontal acceleration at these stations with rock attenuation relationships as proposed by various researchers for $M_W = 7.4$ earthquakes. This figure has been modified from EERI (2000) to reflect the most recent distances from SMS's to the surface fault rupture as provided by Rathje (2001). It can be seen that current attenuation relationships overpredict the measured near-field ground accelerations from the Kocaeli earthquake.

All of the liquefaction sites discussed in Chapter 3, with the exception of Yalova Harbor, are located within 10 km of the surface fault rupture. Yalova Harbor is located within 25 km. Thus for all intents and purposes, all of the liquefaction case histories discussed in this paper are located within the near-field region. Therefore, ground

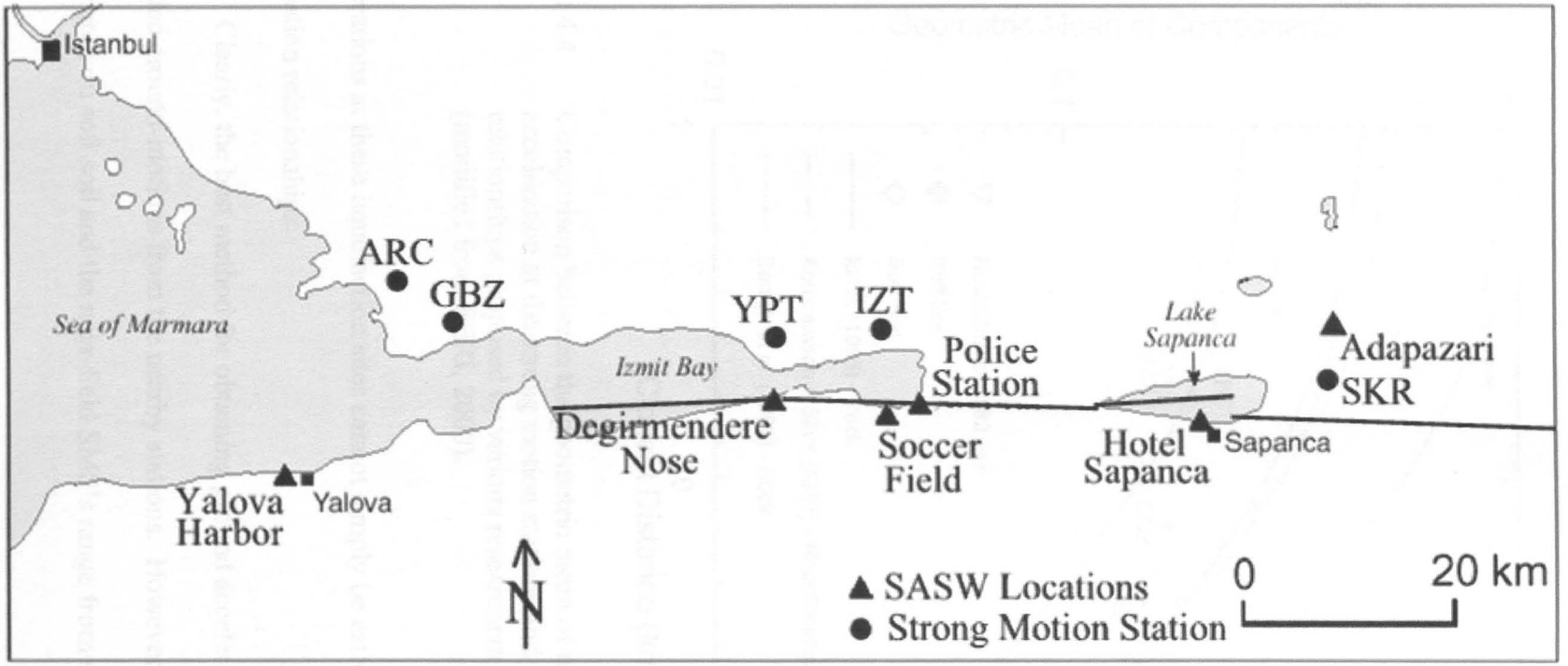

Figure 4.3 Locations of five near-field strong motion stations in relation to the SASW liquefaction test sites. Also shown is the approximate location of the surface fault rupture (modified from www.eerc.berkeley.edu/turkey/adapazari).

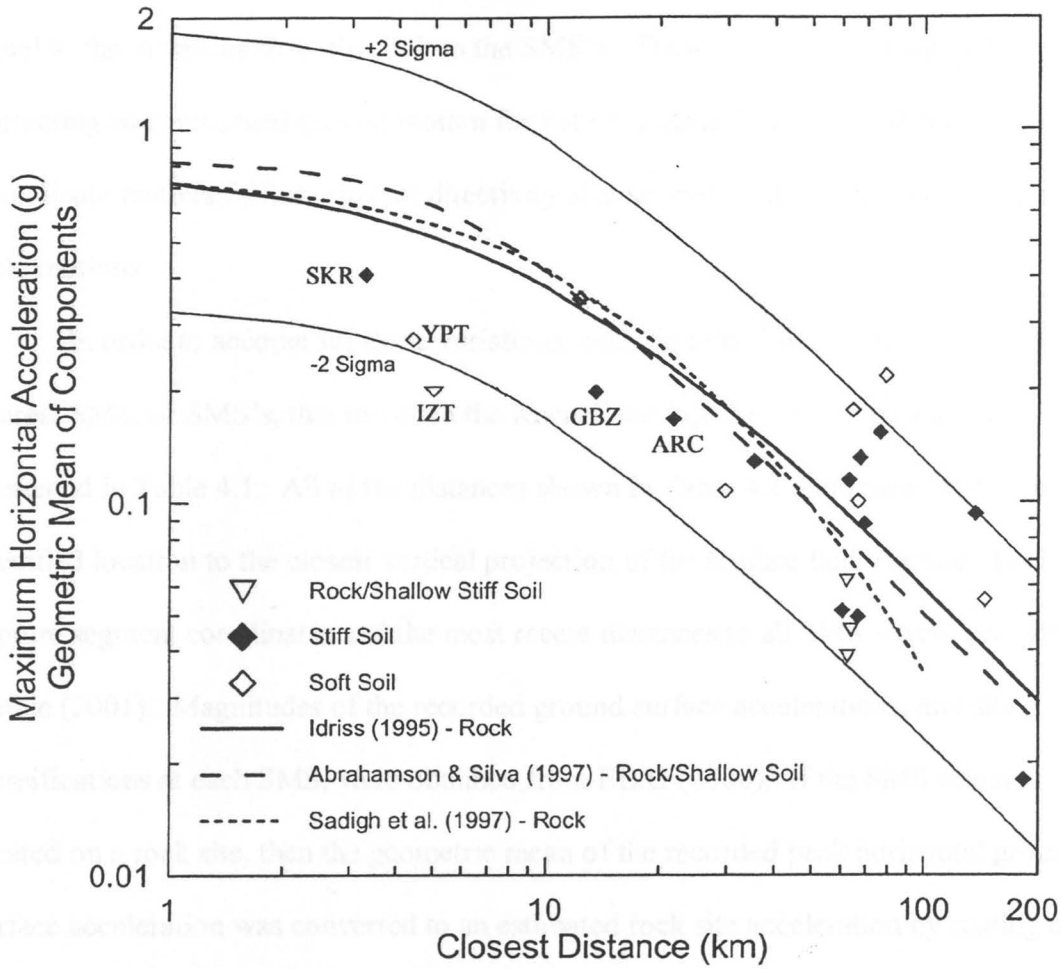

Figure 4.4 Comparison between the geometric mean of the recorded horizontal acceleration at the strong motion stations and rock attenuation relationships proposed by various researchers for $M_W = 7.4$ earthquakes (modified from EERI, 2000).

accelerations at these liquefaction sites cannot simply be estimated from current attenuation relationships.

Clearly, the best method for obtaining ground accelerations at these sites is to use recorded ground-motions from the nearby stations. However, all of the liquefaction sites are located on soft soil and the near-field SMS's range from soft soil to rock site

classifications. Additionally, distances from the fault to the liquefaction sites are not equal to the distances from the fault to the SMS's. These concerns necessitated correcting each recorded ground motion for both site classification and distance. To complicate matters further, rupture directivity also strongly influenced recorded near-field motions.

In order to account for these variations, each liquefaction site was paired with the nearest SMS, or SMS's, that recorded the Kocaeli earthquake. These parings are presented in Table 4.1. All of the distances shown in Table 4.1 were measured from the specified location to the closest vertical projection of the surface fault rupture. Fault rupture segment coordinates and the most recent distances to all SMS's were provided by Rathje (2001). Magnitudes of the recorded ground surface accelerations, and site classifications at each SMS, were obtained from EERI (2000). If the SMS was not located on a rock site, then the geometric mean of the recorded peak horizontal ground surface acceleration was converted to an estimated rock site acceleration by scaling off values from the graph proposed by Idriss as shown in Figure 4.5 (Kramer, 1996). This curve provides a rough relationship between rock accelerations and soft soil accelerations. Accelerations from SMS's located on stiff soil were converted to estimated rock accelerations by using values halfway between the 1-to-1 curve and the soft soil curve. In this way, all SMS acceleration recordings were converted to estimated rock accelerations.

In order to use the estimated rock accelerations at the SMS's to estimate rock accelerations at the liquefaction sites, the difference in distance between the site and the paired SMS needed to be accounted for. It was decided to use the attenuation

Table 4.1 Methodology used to obtain estimated soft soil accelerations at each liquefaction site

Liquefaction Sites	Distance [1] from Fault to Site (km)	Nearest [2] Strong Motion Stations (SMS)	Distance [1] from Fault to SMS (km)	Recorded [3] Geometric Mean of PGA at SMS (g)	SMS [3] Site Class	Estimated [4] Rock Acceleration at SMS (g)	Predicted [5] Rock Acceleration at SMS (g)	Predicted [5] Rock Acceleration at Site (g)	Ratio of [6] Site-to-SMS Predicted Rock Accelerations	Estimated [7] Rock Acceleration at Site (g)	Estimated [8] Soft Soil Acceleratoin at Site (g)
Adapazari Sites	8.0	SKR	3.4	0.41	Stiff Soil	0.42	0.61	0.47	0.77	0.32	**0.38**
Hotel Sapanca	3.0	SKR	3.4	0.41	Stiff Soil	0.42	0.61	0.63	1.03	0.43	**0.40**
Degirmendere Nose, Soccer Field, and Police Station	< 1	IZT	5.0	0.19	Rock	0.19	0.55	0.72	1.31	0.25	**0.34**
		YPT	4.4	0.28	Soft Soil	0.15	0.57	0.72	1.26	0.19	**0.30**
Yalova Harbor	24.0	GBZ	13.5	0.20	Stiff Soil	0.13	0.34	0.22	0.65	0.08	**0.22**
		ARC	21.6	0.17	Stiff Soil	0.11	0.25	0.22	0.88	0.10	**0.24**

1. All distances are from the specified location to the closest vertical projection of the surface fault rupture. Fault rupture segment coordinates and most recent distances to all SMS were provided by Rathje (2001). Distances from the fault to each site were obtained from the latitude and longitude coordinates given in Chapter 3.
2. Figure 4.3 shows the location of the SMS with respect to the liquefaction sites and the surface fault rupture.
3. All SMS accelerations and preliminary site classifications were obtained from EERI (2000).
4. Accelerations from stiff and soft soil sites were converted to rock accelerations by scaling values from the graph developed by Idriss (Kramer, 1996) as shown in Figure 4.5.
5. Predicted rock accelerations were obtained by scaling values at the given distances from the attenuation curve by Sadigh et al. (EERI, 2000) as shown in Figure 4.4.
6. This ratio reflects the rate of attenuation (not magnitude) over the distance between the liquefaction site and the given SMS. If the liquefaction site is closer to the fault than the SMS then this value is greater than 1.
7. Estimated rock accelerations at liquefaction sites were obtained by multiplying the estimated rock accelerations for the SMS by the ratio of site-to-SMS predicted rock accelerations.
8. Estimated rock accelerations at liquefaction sites were converted to estimated soft soil accelerations by scaling values from the graph developed by Idriss (Kramer, 1996) as shown in Figure 4.5.

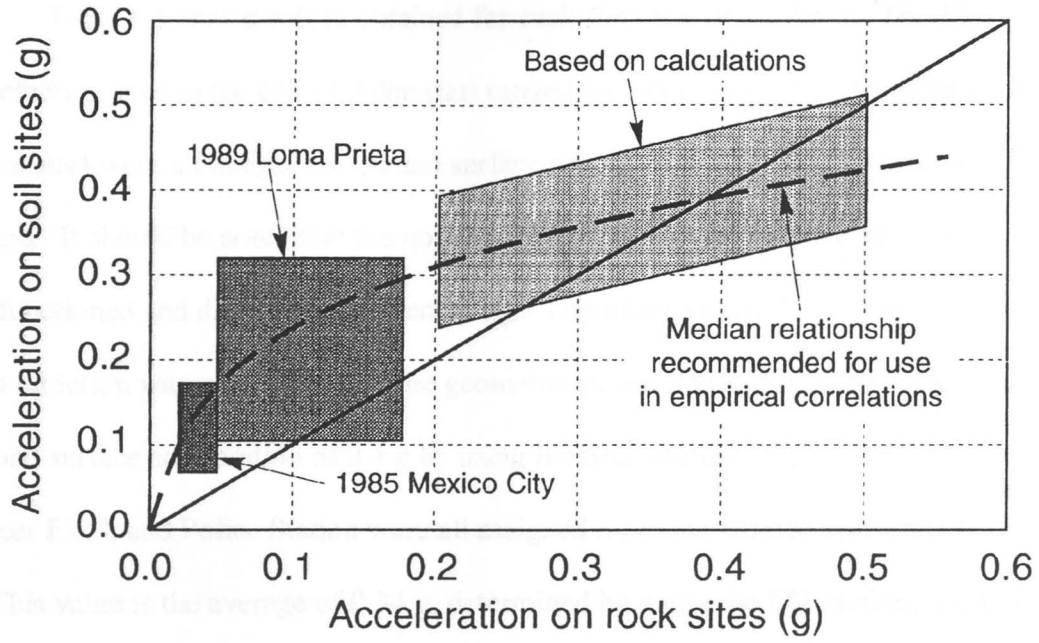

Figure 4.5 Curve developed by Idriss to approximate the relationship between peak accelerations on rock and soft soil sites (from Kramer, 1996).

relationships from Figure 4.4 to account for the rate of acceleration attenuation (not the magnitude) over the distance separating the liquefaction site and the paired SMS. The curve by Sadigh et al. (EERI, 2000) was used to obtain predicted rock accelerations at the SMS distance and the liquefaction site distance. These values were then converted into a ratio by dividing the predicted liquefaction site rock acceleration by the predicted SMS rock acceleration. If the liquefaction site was closer to the fault than the SMS, then this ratio was greater than 1. If not, it was less than 1. An estimation of the rock acceleration at the liquefaction site was then obtained by multiplying the estimated rock acceleration at the SMS by the ratio of site-to-SMS predicted rock acceleration. Estimated rock accelerations at the liquefaction sites were then converted to estimated soft soil accelerations by using Figure 4.5.

Table 4.1 shows values obtained for each step described above. The 10 liquefaction sites in the city of Adapazari ranged between 7 and 9 km from the fault. These sites were all assigned a ground surface acceleration of 0.38 g by using the SKR station. It should be noted that the north-south component of the SKR station malfunctioned and did not make a recording. Therefore, the peak acceleration in the east-west direction was used instead of the geometric mean. Hotel Sapanca was assigned a ground surface acceleration of 0.4 g by using the SKR station. Degirmendere Nose, Soccer Field, and Police Station were all assigned a ground surface acceleration of 0.32 g. This value is the average of 0.34 g, determined by using the IZT station, and 0.30 g, determined by using the YPT station. Yalova Harbor was assigned a ground surface acceleration of 0.23 g. This value is the average of 0.22 g, determined by using the GBZ station, and 0.24 g, determined by using the ARC station.

These ground surface accelerations were used to calculate CSR's (see Equation 2.1) at each liquefaction site. CSR's were calculated every one-tenth of a meter over the depth of the shear wave velocity profile. An example of these calculated CSR's is shown in Figure 4.2. In order to account for the uncertainty in the procedure that was used to estimate maximum ground surface accelerations at each site, CSR's were also calculated for values of acceleration deviating by +/- 0.05 g from the estimated value.

Summary

Comparing the calculated CSR's and CRR's allowed for the determination of the potentially liquefiable region at each site. Any depth interval that had a higher stress ratio than resistance ratio was considered to be potentially liquefiable. Many depth

intervals at the liquefaction sites had ratios of CRR/CSR equal to 0.1 - 0.25. In other words, this means that the earthquake-induced stress was in many instances more than four times as much as the soil would be predicted to withstand. However, soil stiffness alone does not control liquefaction. The type of soil and its properties also determine to a large extent the degree of excess pore water pressure buildup.

Determination of Liquefiable and Nonliquefiable Soils

As mentioned previously, in-depth SPT and CPT investigations were performed by a cooperative of researchers at liquefaction sites throughout the region affected by the Kocaeli earthquake (www.eerc.berkeley.edu/turkey/adapazari). Through coordination with these researchers, shear wave velocity measurements were made at many of these same locations. This allowed for sharing and comparison of test results in order to best understand the soil failures that occurred at each site. The soil sample data examined in this chapter were obtained through split-spoon sampling. These data were used to determine liquefiable and nonliquefiable soils according to the Chinese Criteria and the Andrews and Martin Criteria. At sites where soil sample data were not yet available, CPT data were used as a substitute method for determining liquefiable and nonliquefiable soils. The general procedures used to make these determinations are discussed below.

Sites with soil sample data

Soil data were provided for this research in the standard form as shown in Table 4.2. This particular set of data is from borehole #4 at Site A. As can be seen, the samples at each depth were assigned a natural water content (W_n), liquid limit (LL), plasticity

Table 4.2 Soil data from each borehole was provided in this format (from www.eerc.berkeley.edu/turkey/adapazari)

Sample	Depth (m)	W_n	LL	PI	FC	% 2μm	% 5μm	USCS
A4-1A	1.50	33	42	17	94	34	45	CL/ML
A4-1B	1.50	24	34	11	80	24	35	CL/ML
A4-2	2.30	35	48	24	99	25	32	CL
A4-4	4.10	32	36	10	97	18	24	ML
A4-5	5.00	39	49	22	98	42	56	CL/MH
A4-6	6.50	37	38	14	92	37	43	CL
A4-7	8.00	25	25	NP	66	32	35	ML
A4-8	9.50	18	NP	NP	8	NM	NM	SP-SM
A4-9	11.00	17	NP	NP	10	NM	NM	SW-SM
A4-10	12.50	16	NP	NP	7	NM	NM	SP-SM
A4-11	15.00	37	69	45	100	73	86	CH

index (PI), fines content (FC), clay content (both 2 and 5 μm particle sizes), and then classified by the Unified Soil Classification System (USCS). It is important to note here that NP stands for non-plastic, and that some "non-plastic" ML samples may have been slightly plastic but were not assigned a plastic limit (PL) due to the difficult nature of performing this test at very high silt contents (Sancio, 2001).

Obtaining soil property profiles. At nearly all of the liquefaction sites, soil samples were obtained from more than one borehole. In order to examine each site as a whole, it was necessary to combine the data from individual boreholes and divide the subsurface into an idealized layered system. This was accomplished by grouping all of the data from each available borehole and plotting the given information with respect to depth. In this way, similar soils were divided into layers by visually observing changes in either soil classification or soil properties with depth. Once dividing depths had been assumed, a USCS classification was given to each layer as shown in Figure 4.6a. This classification was the classification that the majority of the samples within the layer had

previously been assigned. The total number of samples within each assumed layer was reported along with the number of these samples that were considered as non-plastic. Values for fines content, water content, plastic limit, and liquid limit were averaged within the assumed soil layers. These average values were then plotted at the center of their respective layers as shown in Figure 4.6b. In order to reflect the horizontal and vertical variability at each site, standard deviations for these values were also calculated and plotted as an error bar in each layer. It should be understood that when a layer contained both plastic and non-plastic samples, only the plastic samples were included in the average values obtained for liquid limit and plastic limit. The 2 μm and 5 μm clay contents were also averaged. However, since these measurements were made on a smaller percentage of samples, it was decided to plot every individual value that was provided. An example of these plotted values is shown in Figure 4.6c.

Dividing each site into layers, and providing averaged values for key soil properties within these layers, allowed for a layer-by-layer evaluation of liquefaction susceptibility for all soils within the potentially liquefiable region. This layer-by-layer evaluation was performed according to the Chinese Criteria and the Andrews and Martin Criteria.

The Chinese Criteria and the Andrews and Martin Criteria. Each potentially liquefiable region was broken into depth intervals as shown in Table 4.3. These depth intervals basically represented the individual soil layers as determined from the soil sample evaluation. However, if the entire soil layer was not within the potentially

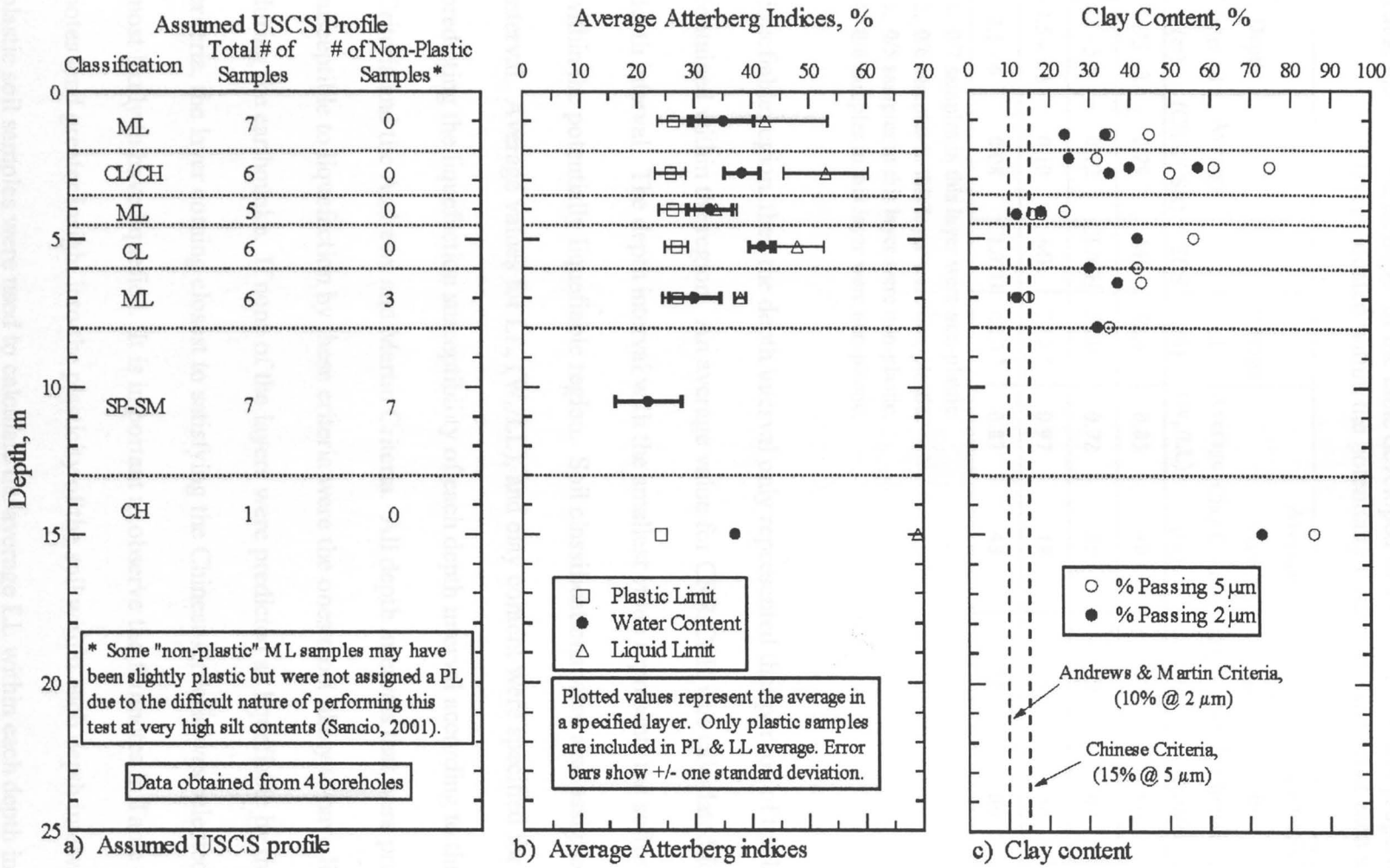

Figure 4.6 An example of the graphs developed at each site to delineate soils susceptible to liquefaction using the Chinese Criteria and the Andrews and Martin Criteria (soil data from www.eerc.berkeley.edu/turkey/adapazari).

Table 4.3 An example of the table developed to show the average properties for soil layers located within the potentially liquefiable region at each site

Depth Interval (m)	Average (CRR/CSR)	USCS	Average LL (%)	Average (W_n/LL)	Average 5 μm Clay Content (%)	Average 2 μm Clay Content (%)	Liquefiable by Chinese Criteria	Liquefiable by Andrews & Martin Criteria
0.75 - 2	0.29	ML	42.4 [1]	0.83	40	29	no	no
2 - 3.5	0.12	CL/CH	53.0 [2]	0.72	55	39	no	no
3.5 - 4.5	0.10	ML	33.8 [3]	0.97	18	14	no	no
4.5 - 6	0.08	CL/CH	48.0 [4]	0.87	43	36	no	no

1. 0/7 samples in this layer were non-plastic.
2. 0/6 samples in this layer were non-plastic.
3. 0/5 samples in this layer were non-plastic.
4. 0/6 samples in this layer were non-plastic.

liquefiable region, then the depth interval only represented that portion of the layer contained within the region. An average value for CRR/CSR was calculated for each depth interval. The depth interval with the smallest value represents the softest layer within the potentially liquefiable region. Soil classifications were also assigned for each interval. Average values for LL, (W_n/LL), and clay content were specified for use in predicting the liquefaction susceptibility of each depth interval according to the Chinese Criteria and the Andrews and Martin Criteria. All depth intervals that were predicted as susceptible to liquefaction by these criteria were the ones most likely to have liquefied during the earthquake. If none of the layers were predicted as liquefiable by these criteria, the layer coming closest to satisfying the Chinese Criteria was selected as the one most likely to have liquefied. It is important to observe the footnotes in Table 4.3. These notes lend greater insight into the plasticity of the soil within each depth interval. Only plastic soil samples were used to calculate the average LL within each depth interval.

Sites with CPT data

Split-spoon sampling was performed at all of the sites where shear wave velocity measurements were made. However, at the time of this paper, not all of the soil sample testing had been made available. Therefore, it was decided to use the available CPT results from these sites to make rough determinations of soils that may have been predicted as nonliquefiable due to high clay contents. As discussed in Chapter 2, values for soil behavior type index (I_C) can be used to make this evaluation.

Obtaining soil behavior type profiles. Between three and five CPT soundings were analyzed at each site where soil samples were not available. For each sounding, raw tip resistance and sleeve friction were used to develop plots of normalized cone resistance (refer to Equation 2.12), normalized friction ratio (refer to Equation 2.13), soil behavior type index (refer to Equation 2.11), and apparent fines content (refer to Equation 2.14). Figure 4.7 shows an example of these four plots for one of the CPT soundings at Police Station. Figure 4.7c includes the soil behavior type boundaries as determined from I_C values (refer to Table 2.1). Figure 4.8 shows an idealized soil profile as determined by combining all of the available CPT soundings at one site. The layer divisions, approximate I_C values, and fines contents were determined by visually inspecting each of the soundings for a given site.

Liquefaction susceptibility. Each potentially liquefiable region was broken into depth intervals (refer to Table 4.4). These depth intervals basically represented the individual soil layers as determined from the CPT evaluation. However, if the entire soil layer was not within the potentially liquefiable region, then the depth interval only

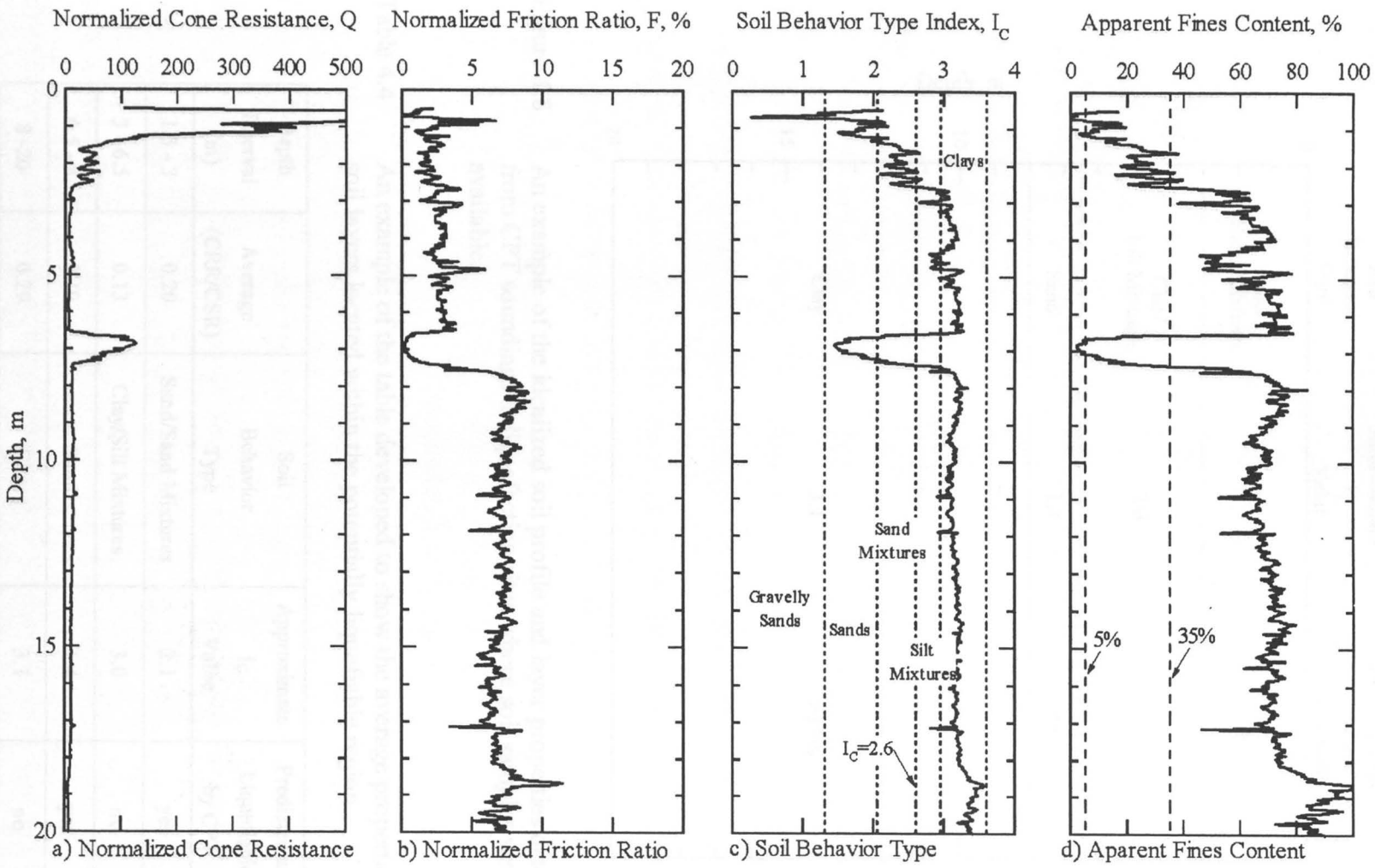

Figure 4.7 An example of the graphs developed from CPT data to characterize the subsurface at liquefaction sites where soil samples were not available (raw cone data from www.eerc.berkeley.edu/turkey/adapazari).

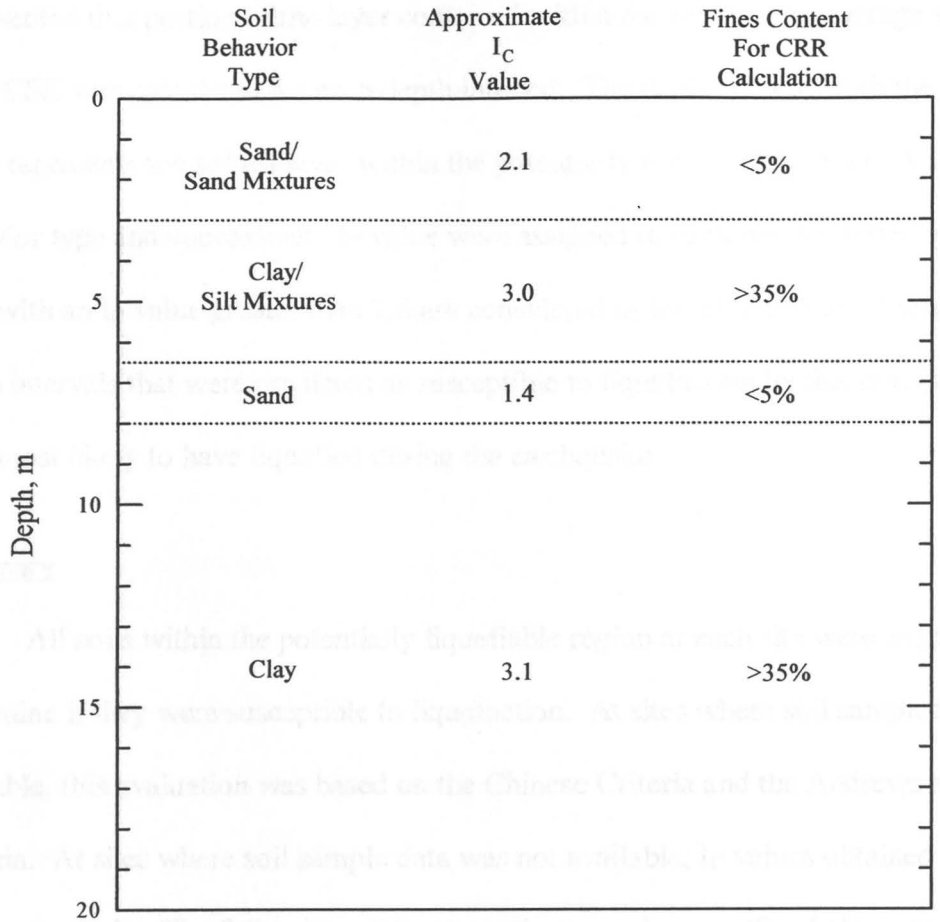

Figure 4.8 An example of the idealized soil profile and layer properties determined from CPT soundings at liquefaction sites where soil samples were not available.

Table 4.4 An example of the table developed to show the average properties for soil layers located within the potentially liquefiable region

Depth Interval (m)	Average (CRR/CSR)	Soil Behavior Type	Approximate I_C Value	Predicted as Liquefiable by CPT
1.5 - 3	0.20	Sand/Sand Mixtures	2.1	yes
3 - 6.5	0.13	Clay/Silt Mixtures	3.0	no
6.5 - 8	0.10	Sand	1.4	yes
8 -20	0.29	Clay	3.1	no

represented that portion of the layer contained within the region. An average value for CRR/CSR was calculated for each depth interval. The depth interval with the smallest value represents the softest layer within the potentially liquefiable region. A soil behavior type and approximate I_C value were assigned to each depth interval. In general, soils with an I_C value greater than 2.6 are considered as too clay-rich to liquefy. The depth intervals that were predicted as susceptible to liquefaction by this criteria were the ones most likely to have liquefied during the earthquake.

Summary

All soils within the potentially liquefiable region at each site were examined to determine if they were susceptible to liquefaction. At sites where soil samples were available, this evaluation was based on the Chinese Criteria and the Andrews and Martin Criteria. At sites where soil sample data was not available, I_C values obtained from CPT data were used. The following section uses the procedures outlined above to determine which soil layers induced liquefaction at each site.

Liquefaction Site Evaluations

The following section uses the procedures outlined above in order to evaluate the cause of liquefaction at each site. The layer, or layers, most susceptible to liquefaction have been determined through combining shear wave velocity data, soil sample data, and CPT data. Descriptions for each liquefaction site are found in Chapter 3. Soil sample data, obtained from split-spoon sampling, were available at all liquefaction sites in the city of Adapazari. Therefore, the potentially liquefiable region at each of these sites was

evaluated for liquefaction susceptibility by using the Chinese Criteria and the Andrews and Martin Criteria. Soil sample data were not yet available for any of the other liquefaction sites. Therefore, the potentially liquefiable region at each of these sites was evaluated for liquefaction susceptibility by using I_C values calculated from CPT data.

Adapazari

Site A. The graphs developed for Site A, to delineate potentially liquefiable soil using the shear wave velocity simplified procedure, are shown in Figure 4.9. Figure 4.9a shows the shear wave velocity profile (V_S) and the corrected shear wave velocity profile (V_{S1}) for the site. Figure 4.9b shows the average fines content from all samples within each layer. Figure 4.9c shows the CRR of the soil along with three CSR profiles. The central profile represents the CSR generated using the most probable ground acceleration predicted for this site. The other two profiles result from bracketing this acceleration by +/- 0.05 g. From this graph, it can be seen that the potentially liquefiable region is between the depths of 0.75 - 6 meters. The graphs developed for Site A, to delineate soils susceptible to liquefaction using the Chinese Criteria and the Andrews and Martin Criteria, are shown in Figure 4.10. The soil data for this site was obtained from four separate boreholes. Figure 4.10a shows the assumed USCS profile along with the total number of samples, and the number of non-plastic samples, included in each layer. Figure 4.10b shows average values for plastic limit, water content, and liquid limit in each layer. The 2 and 5 μm clay contents are plotted in Figure 4.10c.

Table 4.5 summarizes the data for all soil layers located within the potentially liquefiable region at Site A. None of these layers appear to be susceptible to liquefaction

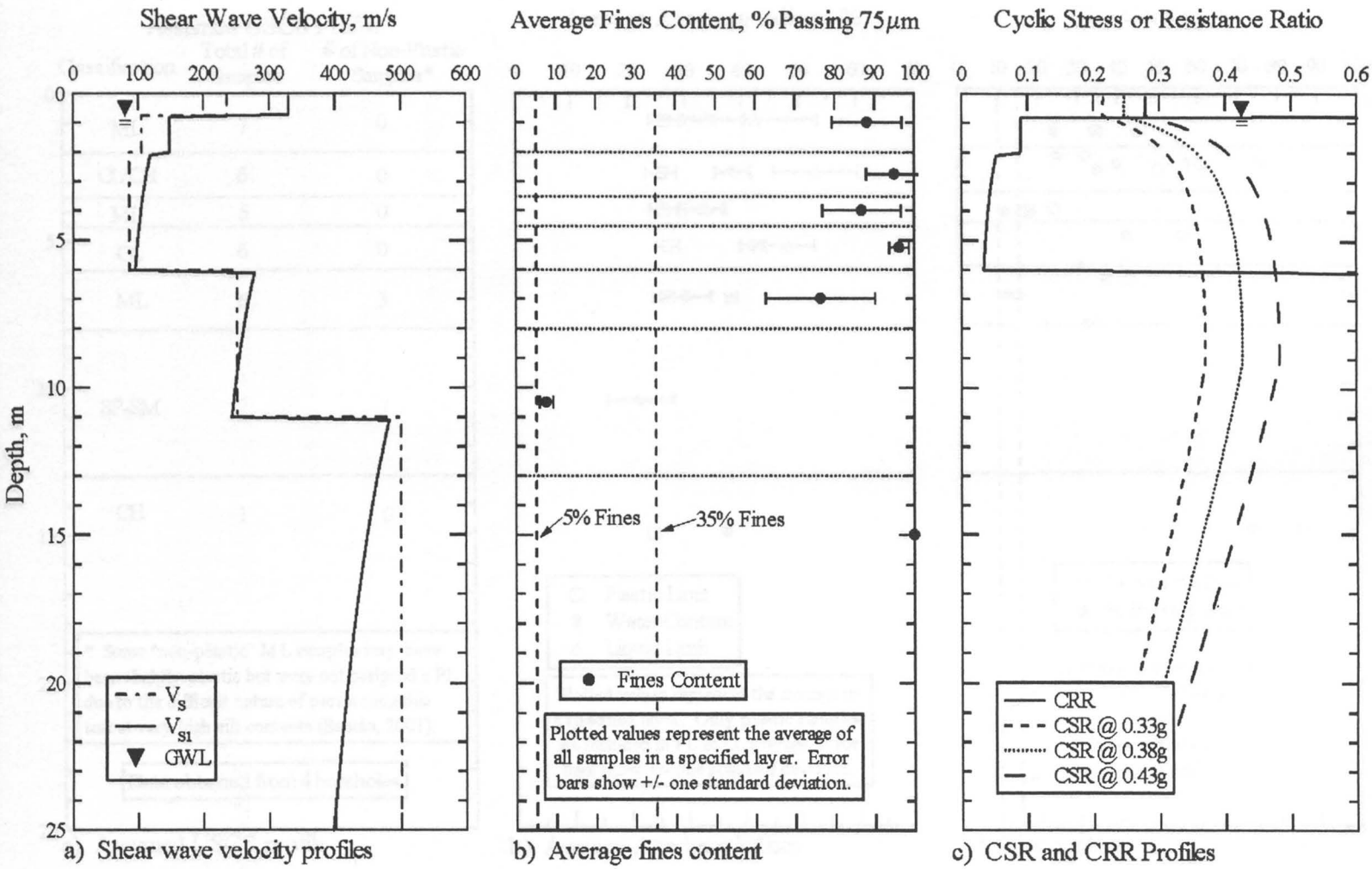

Figure 4.9 Graphs developed to delineate liquefiable soil using the simplified shear wave velocity procedure at Site A, Adapazari, Turkey (fines content obtained from www.eerc.berkeley.edu/turkey/adapazari).

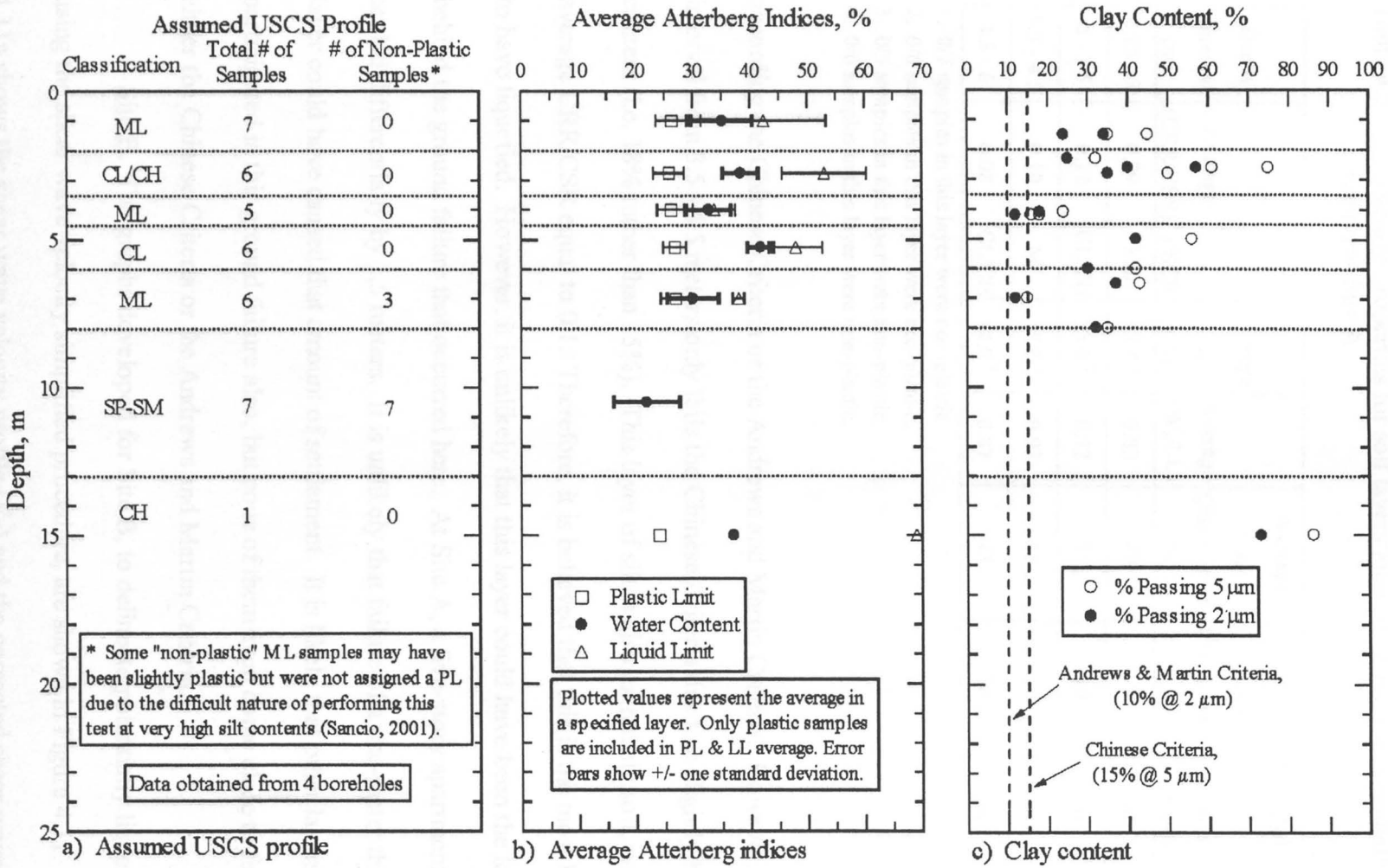

Figure 4.10 Graphs developed to delineate soils susceptible to liquefaction using the Chinese Criteria and the Andrews and Martin Criteria at Site A, Adapazari, Turkey (raw soil data from www.eerc.berkeley.edu/turkey/adapazari).

Table 4.5 Average properties for soil layers located within the potentially liquefiable region at Site A

Depth Interval (m)	Average (CRR/CSR)	USCS	Average LL (%)	Average (W_n/LL)	Average 5 μm Clay Content (%)	Average 2 μm Clay Content (%)	Liquefiable by Chinese Criteria	Liquefiable by Andrews & Martin Criteria
0.75 - 2	0.29	ML	42.4 [1]	0.83	40	29	no	no
2 - 3.5	0.12	CL/CH	53.0 [2]	0.72	55	39	no	no
3.5 - 4.5	0.10	ML	33.8 [3]	0.97	18	14	no	no
4.5 - 6	0.08	CL/CH	48.0 [4]	0.87	43	36	no	no

1. 0/7 samples in this layer were non-plastic.
2. 0/6 samples in this layer were non-plastic.
3. 0/5 samples in this layer were non-plastic.
4. 0/6 samples in this layer were non-plastic.

according the Chinese Criteria or the Andrews and Martin Criteria. However, the depth interval from 3.5 - 4.5 meters only fails the Chinese Criteria due to a slightly high clay content (i.e. 18% rather than 15%). This layer of silt is also extremely soft, with an average CRR/CSR equal to 0.1. Therefore, it is believed that this is the most likely layer to have liquefied. However, it is unlikely that this layer could have been the lone culprit behind the ground failure that occurred here. At Site A, a five-story apartment building settled differentially by 1.5 meters. It is unlikely that failure of a one-meter thick silt layer could have caused that amount of settlement. It is likely that other layers participated in this ground failure also, but none of them even come close to fulfilling either the Chinese Criteria or the Andrews and Martin Criteria.

Site B. The graphs developed for Site B, to delineate potentially liquefiable soil using the shear wave velocity simplified procedure, are shown in Figure 4.11. Figure 4.11a shows the shear wave velocity profile (V_S) and the corrected shear wave velocity

profile (V_{S1}) for the site. Figure 4.11b shows the average fines content from all samples within each layer. Figure 4.11c shows the CRR of the soil along with three CSR profiles. The central profile represents the CSR generated using the most probable ground acceleration predicted for this site. The other two profiles result from bracketing this acceleration by +/- 0.05 g. From this graph, it can be seen that the potentially liquefiable region is broken into two portions. This is due to the corrected shear wave velocity having a value just over 215 m/s from approximately 3 - 4.5 meters. The liquefiable region is between the depths of 2 - 3 meters, and 5 - 7 meters. The graphs developed for Site B, to delineate soils susceptible to liquefaction using the Chinese Criteria and the Andrews and Martin Criteria, are shown in Figure 4.12. The soil data for this site were obtained from two separate boreholes. Figure 4.12a shows the assumed USCS profile along with the total number of samples, and the number of non-plastic samples, included in each layer. Figure 4.12b shows average values for plastic limit, water content, and liquid limit in each layer. The 2 and 5 μm clay contents are plotted in Figure 4.12c.

Table 4.6 summarizes the data for all soil layers located within the potentially liquefiable region at Site B. The softest layer is between the depths of 2 - 3 meters. However, this layer is predicted nonliquefiable by both the Chinese Criteria and the Andrews and Martin Criteria. The material most likely to have liquefied is the 2-meter layer of sand between the depths of 5 - 7 meters. This weakened soil induced a bearing capacity failure that toppled a five-story building.

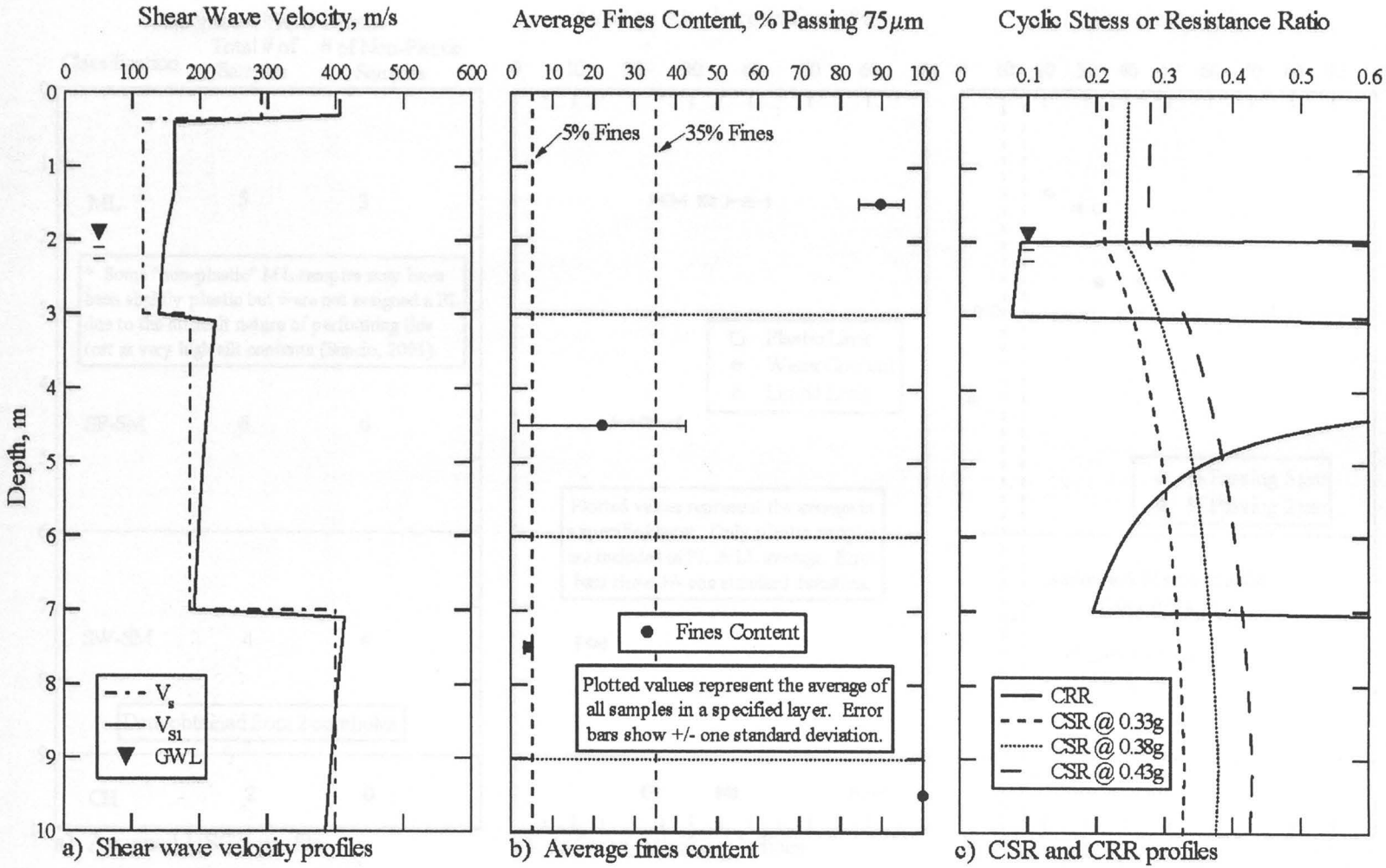

Figure 4.11 Graphs developed to delineate liquefiable soil using the simplified shear wave velocity procedure at Site B, Adapazari, Turkey (fines content obtained from www.eerc.berkeley.edu/turkey/adapazari).

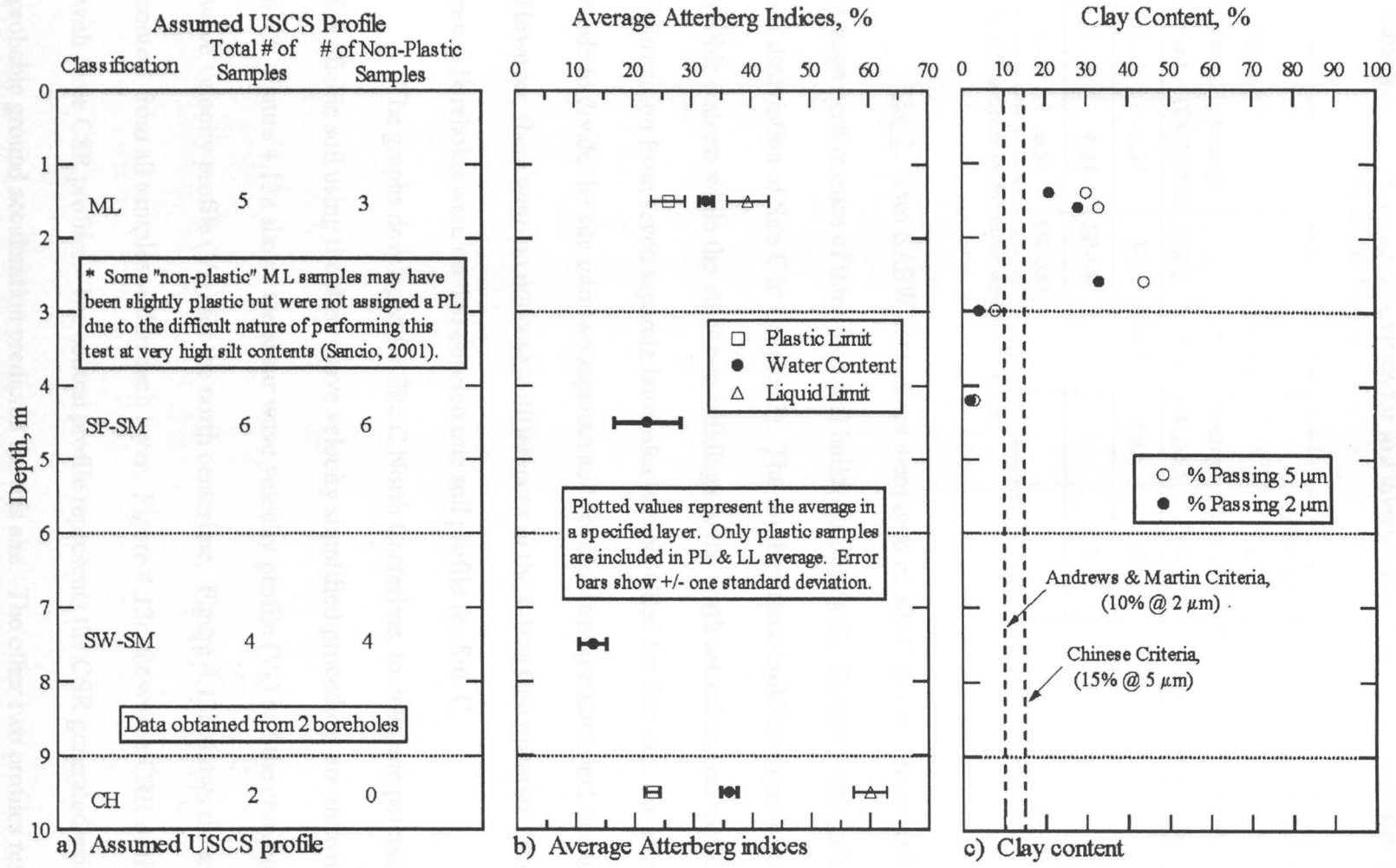

Figure 4.12 Graphs developed to delineate soils susceptible to liquefaction using the Chinese Criteria and the Andrews and Martin Criteria at Site B, Adapazari, Turkey (raw soil data from www.eerc.berkeley.edu/turkey/adapazari).

Table 4.6 Average properties for soil layers located within the potentially liquefiable region at Site B

Depth Interval (m)	Average (CRR/CSR)	USCS	Average LL (%)	Average (W_n/LL)	Average 5 μm Clay Content (%)	Average 2 μm Clay Content (%)	Liquefiable by Chinese Criteria	Liquefiable by Andrews & Martin Criteria
2 - 3	0.31	ML	39.5 [1]	0.82	29	22	no	no
5 - 6	0.81	SP-SM	-	-	3	2	yes	yes
6 - 7	0.59	SW-SM	-	-	-	-	yes	yes

1. 3/7 samples in this layer were non-plastic.

Site C. Two SASW centerlines were used at Site C in order to investigate the strange performance of three identical buildings during the Kocaeli earthquake (refer to the description of Site C in Chapter 3). The southernmost building experienced no visible distress while the other two buildings to the north settled considerably. Soil information from seven separate boreholes was provided for this site. An attempt was made to divide the site into two separate soil profiles (one the north and one to the south). However, there were no noticeable differences in the subsurface material. Therefore, all seven boreholes were used to develop one soil profile for Site C.

The graphs developed for Site C North Centerline, to delineate potentially liquefiable soil using the shear wave velocity simplified procedure, are shown in Figure 4.13. Figure 4.13a shows the shear wave velocity profile (V_S) and the corrected shear wave velocity profile (V_{S1}) for the north centerline. Figure 4.13b shows the average fines content from all samples within each layer. Figure 4.13c shows the CRR of the soil along with three CSR profiles. The central profile represents the CSR generated using the most probable ground acceleration predicted for this site. The other two profiles result from

bracketing this acceleration by +/- 0.05 g. From this graph it can be seen that the potentially liquefiable region is broken into two portions. This is due to the corrected shear wave velocity having a value just over 200 m/s from approximately 5 – 5.75 meters. With the exception of this small area, the entire depth of the shear wave velocity profile below the water table appears to be potentially liquefiable.

The graphs developed for Site C South Centerline, to delineate potentially liquefiable soil using the shear wave velocity simplified procedure, are shown in Figure 4.14. Figure 4.14a shows the shear wave velocity profile (V_S) and the corrected shear wave velocity profile (V_{S1}) for the south centerline. Figure 4.14b shows the average fines content from all samples within each layer. Figure 4.14c shows the CRR of the soil along with three CSR profiles. The central profile represents the CSR generated using the most probable ground acceleration predicted for this site. The other two profiles result from bracketing this acceleration by +/- 0.05 g. At this centerline, it can be seen that the potentially liquefiable region extends from the water table throughout the entire depth of the shear wave velocity profile.

The graphs developed for Site C, to delineate soils susceptible to liquefaction using the Chinese Criteria and the Andrews and Martin Criteria, are shown in Figure 4.15. As explained above, these soil data were used for both centerlines. Figure 4.15a shows the assumed USCS profile along with the total number of samples, and the number of non-plastic samples, included in each layer. Figure 4.15b shows average values for plastic limit, water content, and liquid limit in each layer. The 2 and 5 μm clay contents are plotted in Figure 4.15c.

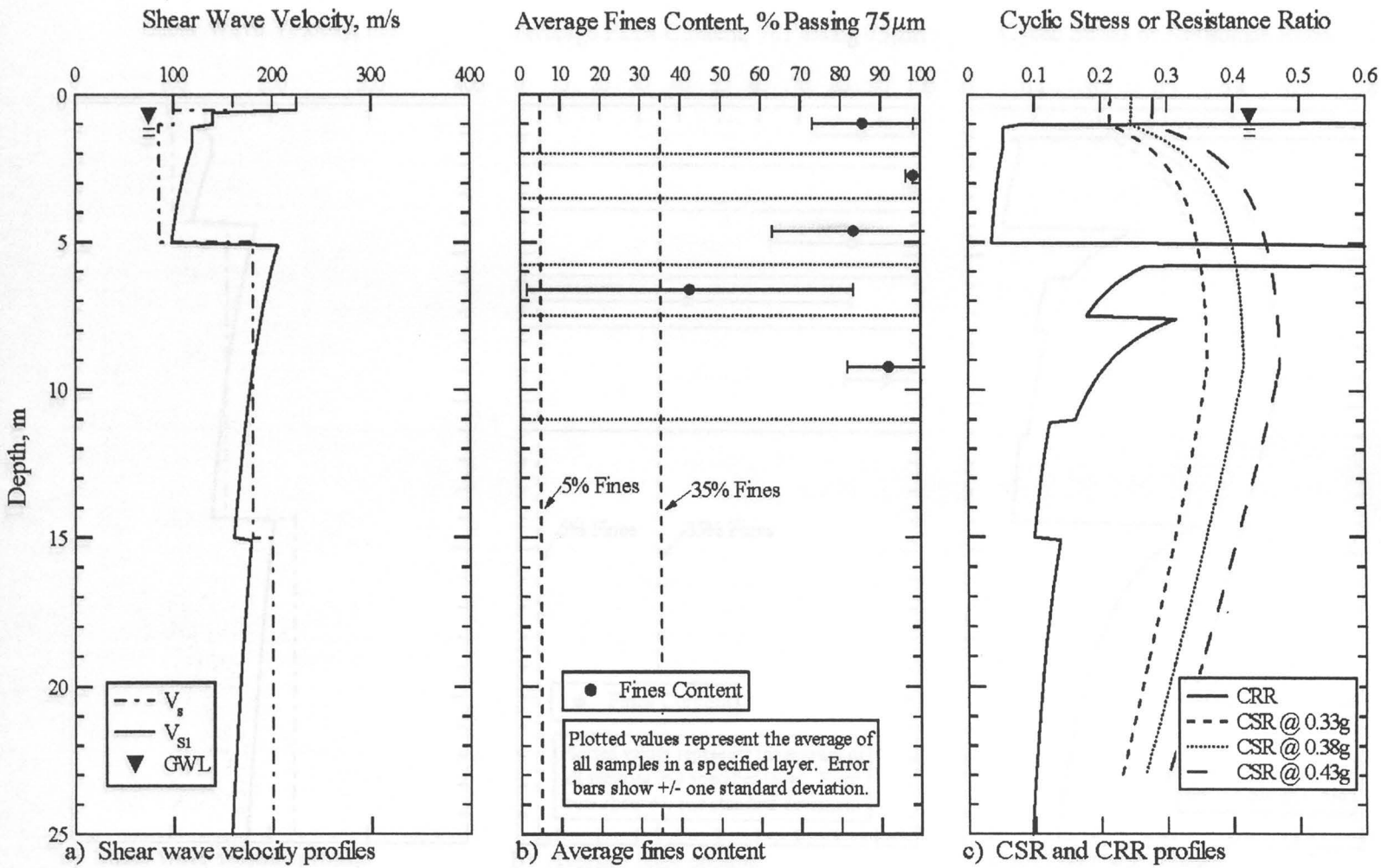

Figure 4.13 Graphs developed to delineate liquefiable soil using the simplified shear wave velocity procedure at Site C North Centerline, Adapazari, Turkey (fines content obtained from www.eerc.berkeley.edu/turkey/adapazari).

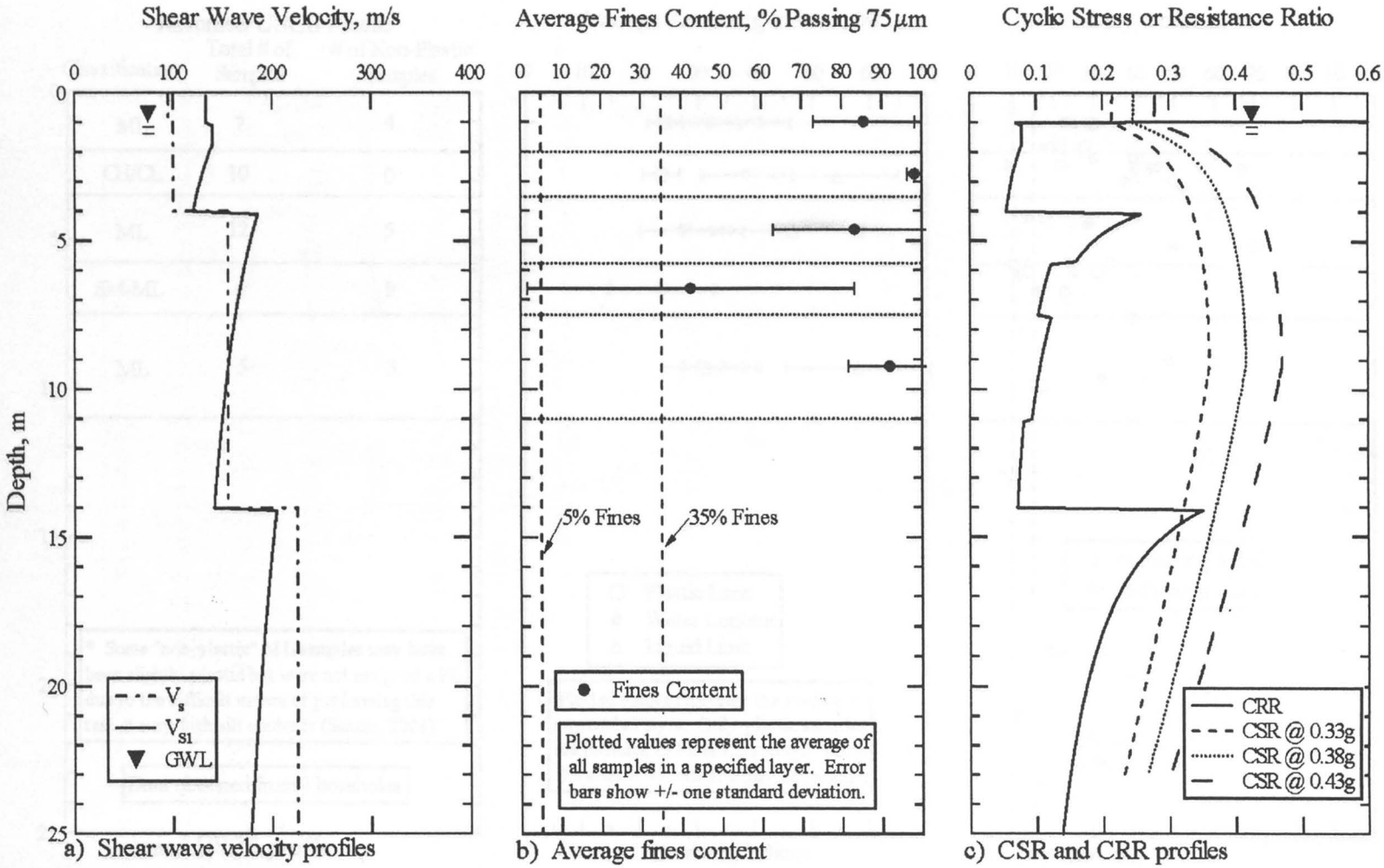

Figure 4.14 Graphs developed to delineate liquefiable soil using the simplified shear wave velocity procedure at Site C South Centerline, Adapazari, Turkey (fines content obtained from www.eerc.berkeley.edu/turkey/adapazari).

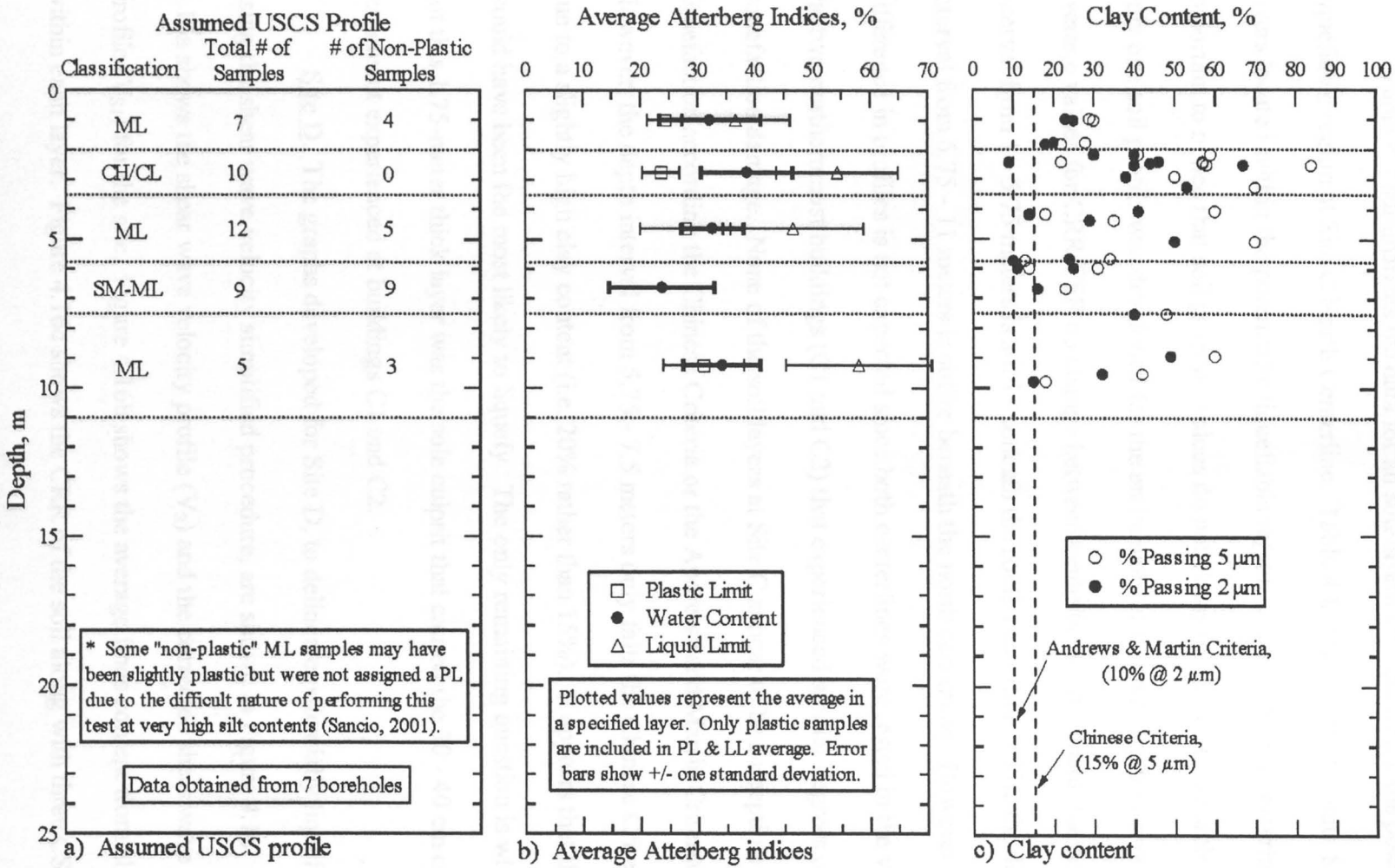

Figure 4.15 Graphs developed to delineate soils susceptible to liquefaction using the Chinese Criteria and the Andrews and Martin Criteria at Site C South Centerline, Adapazari, Turkey (raw soil data from www.eerc.berkelev.edu/turkev/adapazari).

Table 4.7 summarizes the data for all soil layers located within the potentially liquefiable region at Site C North Centerline. Table 4.8 summarizes the data for all soil layers located within the potentially liquefiable region at Site C South Centerline. It is important to notice that soil property values do not change between these tables because only one soil profile was developed for the entire site. However, depth intervals and average values for CRR/CSR do change between centerlines. In general the depth interval from 1 - 5.75 meters is stiffer beneath the south centerline, while the depth interval from 5.75 - 11 meters is stiffer beneath the north centerline. However, a great difference in profiles is not expected since both centerlines were tested in the vicinity of the two northernmost buildings (C1 and C2) that experienced similar degrees of liquefaction damage. None of the soil layers at Site C appear to be susceptible to liquefaction according the Chinese Criteria or the Andrews and Martin Criteria. However, the depth interval from 5.75 - 7.5 meters only fails the Chinese Criteria only due to a slightly high clay content (i.e. 20% rather than 15%). It appears that this layer would have been the most likely to liquefy. The only remaining question is whether or not this 1.75-meter thick layer was the sole culprit that caused the 30 - 40 cm of settlement experienced at buildings C1 and C2.

Site D. The graphs developed for Site D, to delineate potentially liquefiable soil using the shear wave velocity simplified procedure, are shown in Figure 4.16. Figure 4.16a shows the shear wave velocity profile (V_S) and the corrected shear wave velocity profile (V_{S1}) for the site. Figure 4.16b shows the average fines content from all samples within each layer. Figure 4.16c shows the CRR of the soil along with three CSR profiles.

Table 4.7 Average properties for soil layers located within the potentially liquefiable region at Site C North Centerline

Depth Interval (m)	Average (CRR/CSR)	USCS	Average LL (%)	Average (W_n/LL)	Average 5 μm Clay Content (%)	Average 2 μm Clay Content (%)	Liquefiable by Chinese Criteria	Liquefiable by Andrews & Martin Criteria
1 - 2	0.19	ML	36.7 [1]	0.88	27	22	no	no
2 - 3.5	0.13	CH/CL	54.3 [2]	0.71	55	45	no	no
3.5 - 5	0.10	ML	46.6 [3]	0.70	43	32	no	no
5.75 - 7.5	0.52	SM-ML	-	-	20	16	no	no
7.5 - 11	0.52	ML	58.0 [4]	0.59	42	34	no	no

1. 4/7 samples in this layer were non-plastic.
2. 0/10 samples in this layer were non-plastic.
3. 5/12 samples in this layer were non-plastic.
4. 3/5 samples in this layer were non-plastic.

Table 4.8 Average properties for soil layers located within the potentially liquefiable region at Site C South Centerline

Depth Interval (m)	Average (CRR/CSR)	USCS	Average LL (%)	Average (W_n/LL)	Average 5 μm Clay Content (%)	Average 2 μm Clay Content (%)	Liquefiable by Chinese Criteria	Liquefiable by Andrews & Martin Criteria
1 - 2	0.27	ML	36.7 [1]	0.88	27	22	no	no
2 - 3.5	0.18	CH/CL	54.3 [2]	0.71	55	45	no	no
3.5 - 5.75	0.42	ML	46.6 [3]	0.70	43	32	no	no
5.75 - 7.5	0.27	SM-ML	-	-	20	16	no	no
7.5 - 11	0.26	ML	58.0 [4]	0.59	42	34	no	no

1. 4/7 samples in this layer were non-plastic.
2. 0/10 samples in this layer were non-plastic.
3. 5/12 samples in this layer were non-plastic.
4. 3/5 samples in this layer were non-plastic.

The central profile represents the CSR generated using the most probable ground acceleration predicted for this site. The other two profiles result from bracketing this acceleration by +/- 0.05 g. From this graph it can be seen that the potentially liquefiable region extends from a depth of approximately 2.3 meters throughout the entire depth of the shear wave velocity profile. The graphs developed for Site D, to delineate soils susceptible to liquefaction using the Chinese Criteria and the Andrews and Martin Criteria, are shown in Figure 4.17. The soil data for this site were obtained from three separate boreholes. Figure 4.17a shows the assumed USCS profile along with the total number of samples, and the number of non-plastic samples, included in each layer. Figure 4.17b shows average values for plastic limit, water content, and liquid limit in each layer. The 2 and 5 μm clay contents are plotted in Figure 4.17c.

Table 4.9 summarizes the data for all soil layers located within the potentially liquefiable region at Site D. The softest layer is between the depths of 4.3 - 8 meters. This layer is also granular and would be expected to liquefy. The other layers in the liquefiable region are predicted as nonliquefiable by both the Chinese Criteria and the Andrews and Martin Criteria. Hence, the nearly 4-meter thick layer of sand most likely caused this five-story building to settle 44 cm.

Site G. The graphs developed for Site G, to delineate potentially liquefiable soil using the shear wave velocity simplified procedure, are shown in Figure 4.18. Figure 4.18a shows the shear wave velocity profile (V_S) and the corrected shear wave velocity profile (V_{S1}) for the site. Figure 4.18b shows the average fines content from all samples within each layer. Figure 4.18c shows the CRR of the soil along with three CSR profiles.

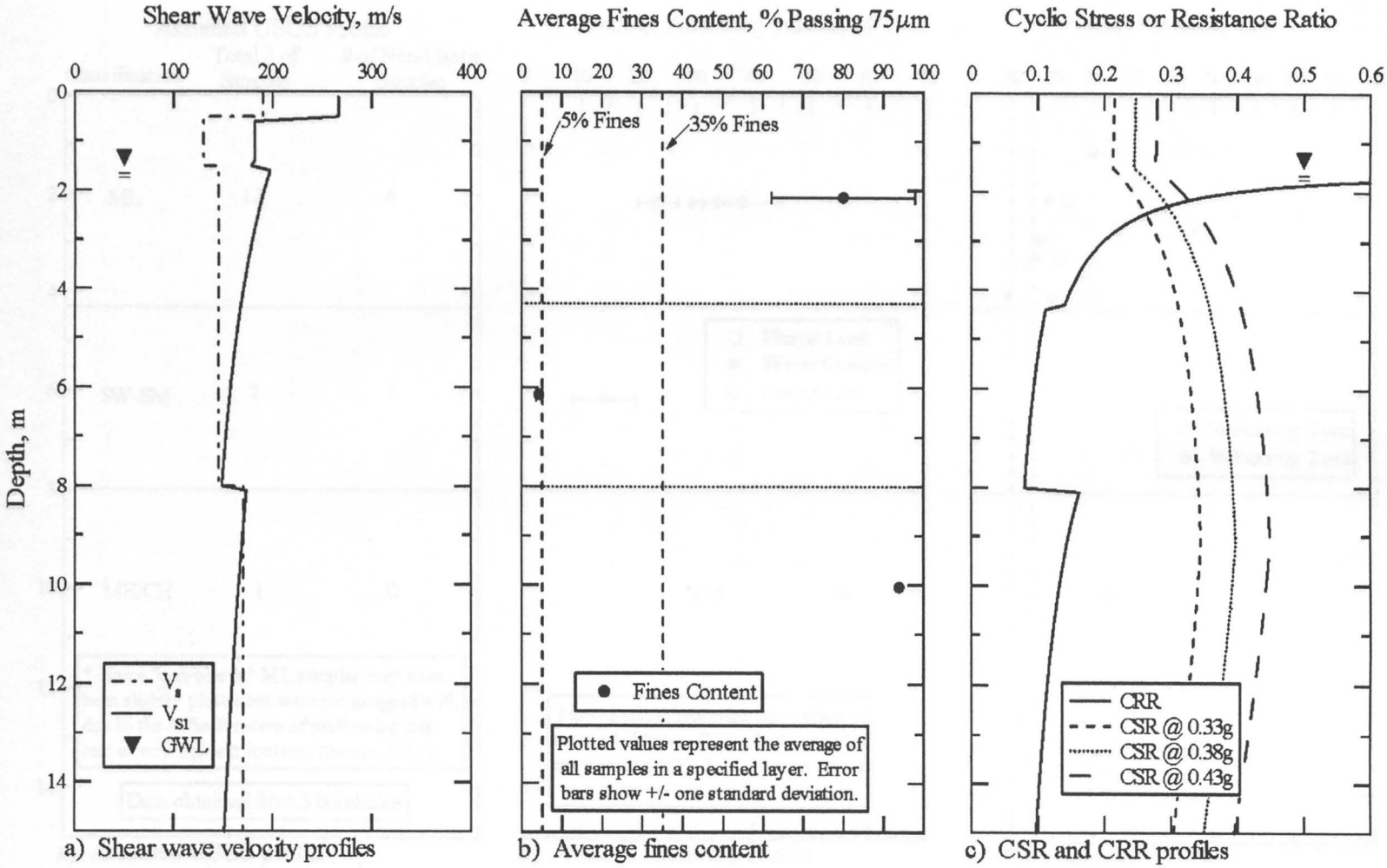

Figure 4.16 Graphs developed to delineate liquefiable soil using the simplified shear wave velocity procedure at Site D, Adapazari, Turkey (fines content obtained from www.eerc.berkeley.edu/turkey/adapazari).

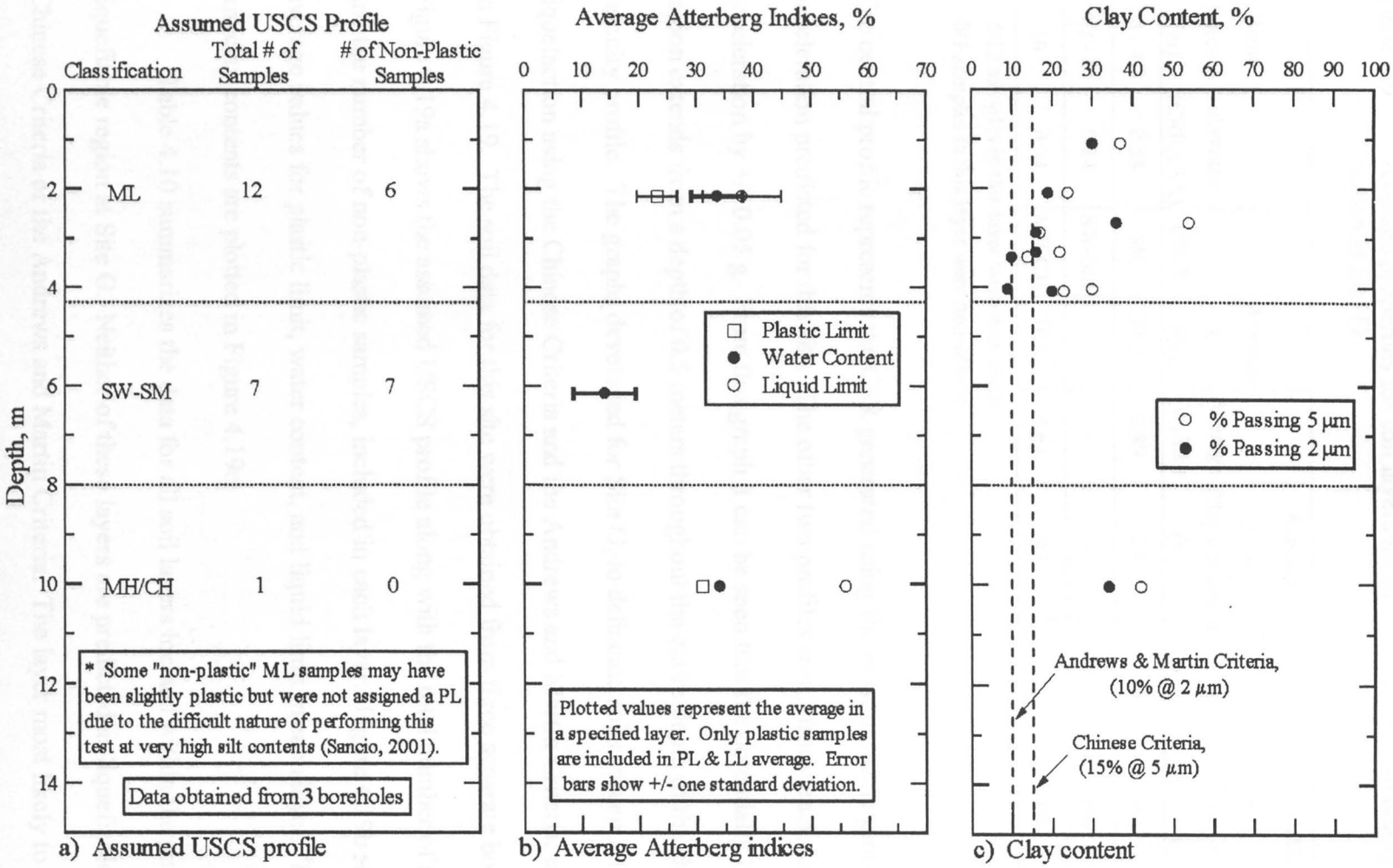

Figure 4.17 Graphs developed to delineate soils susceptible to liquefaction using the Chinese Criteria and the Andrews and Martin Criteria at Site D, Adapazari, Turkey (raw soil data from www.eerc.berkeley.edu/turkey/adapazari).

Table 4.9 Average properties for soil layers located within the potentially liquefiable region at Site D

Depth Interval (m)	Average (CRR/CSR)	USCS	Average LL (%)	Average (W_n/LL)	Average 5 μm Clay Content (%)	Average 2 μm Clay Content (%)	Liquefiable by Chinese Criteria	Liquefiable by Andrews & Martin Criteria
2.3 - 4.3	0.58	ML	38.0 [1]	0.89	28	20	no	no
4.3 - 8	0.24	SW-SM	-	-	-	-	yes	yes
10	0.34	MH/CH	56.0 [2]	0.61	43	32	no	no

1. 6/12 samples in this layer were non-plastic.
2. 0/1 samples in this layer were non-plastic.

The central profile represents the CSR generated using the most probable ground acceleration predicted for this site. The other two profiles result from bracketing this acceleration by +/- 0.05 g. From this graph it can be seen that the potentially liquefiable region extends from a depth of 0.5 meters throughout the entire depth of the shear wave velocity profile. The graphs developed for Site G, to delineate soils susceptible to liquefaction using the Chinese Criteria and the Andrews and Martin Criteria, are shown in Figure 4.19. The soil data for this site were obtained from three separate boreholes. Figure 4.19a shows the assumed USCS profile along with the total number of samples, and the number of non-plastic samples, included in each layer. Figure 4.19b shows average values for plastic limit, water content, and liquid limit in each layer. The 2 and 5 μm clay contents are plotted in Figure 4.19c.

Table 4.10 summarizes the data for all soil layers located within the potentially liquefiable region at Site G. Neither of these layers are predicted as liquefiable by the Chinese Criteria or the Andrews and Martin Criteria. The layer most likely to have liquefied is located between 0.5 - 7 meters. It is important to notice that this layer is

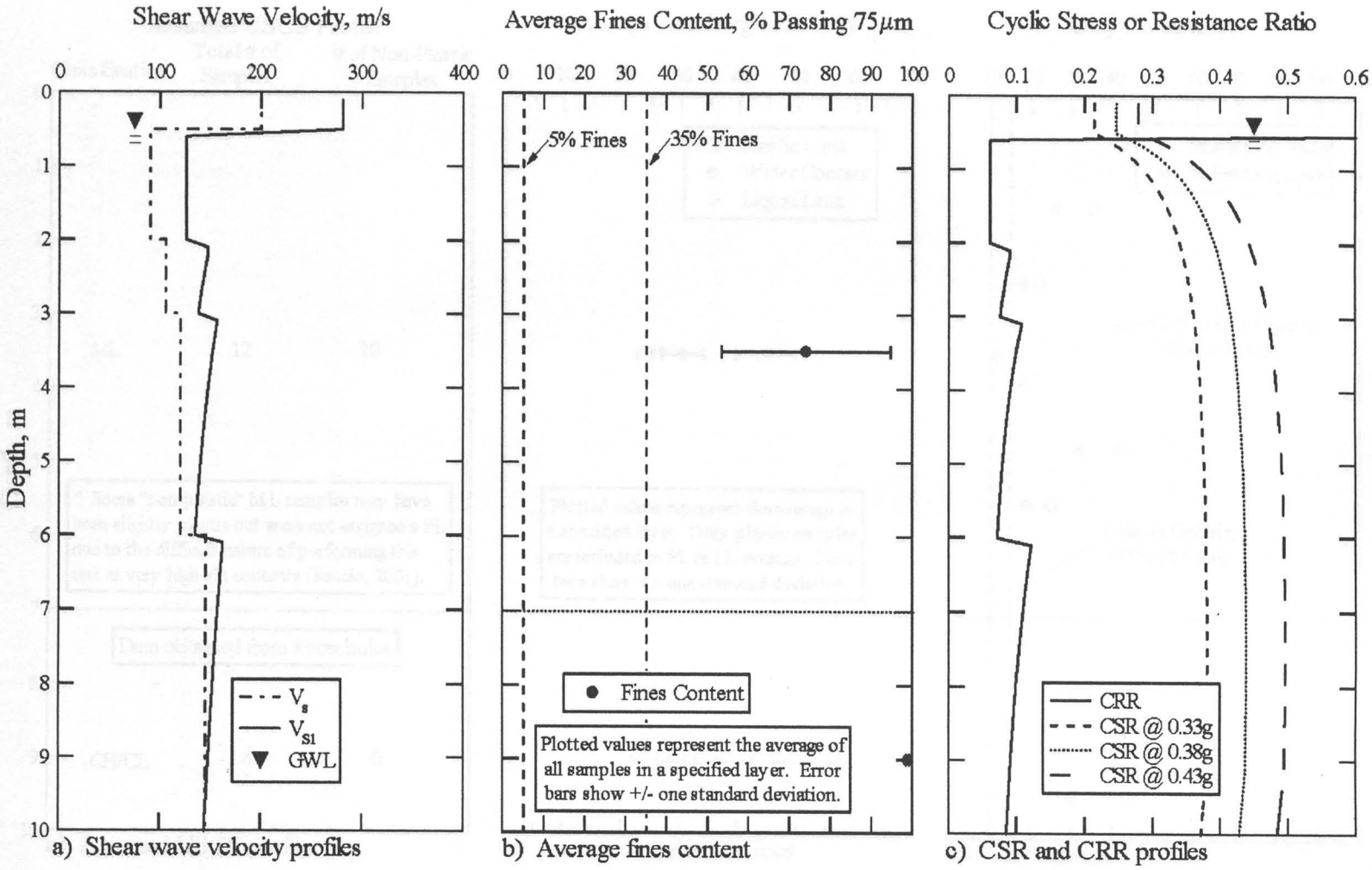

Figure 4.18 Graphs developed to delineate liquefiable soil using the simplified shear wave velocity procedure at Site G, Adapazari, Turkey (fines content obtained from www.eerc.berkeley.edu/turkey/adapazari).

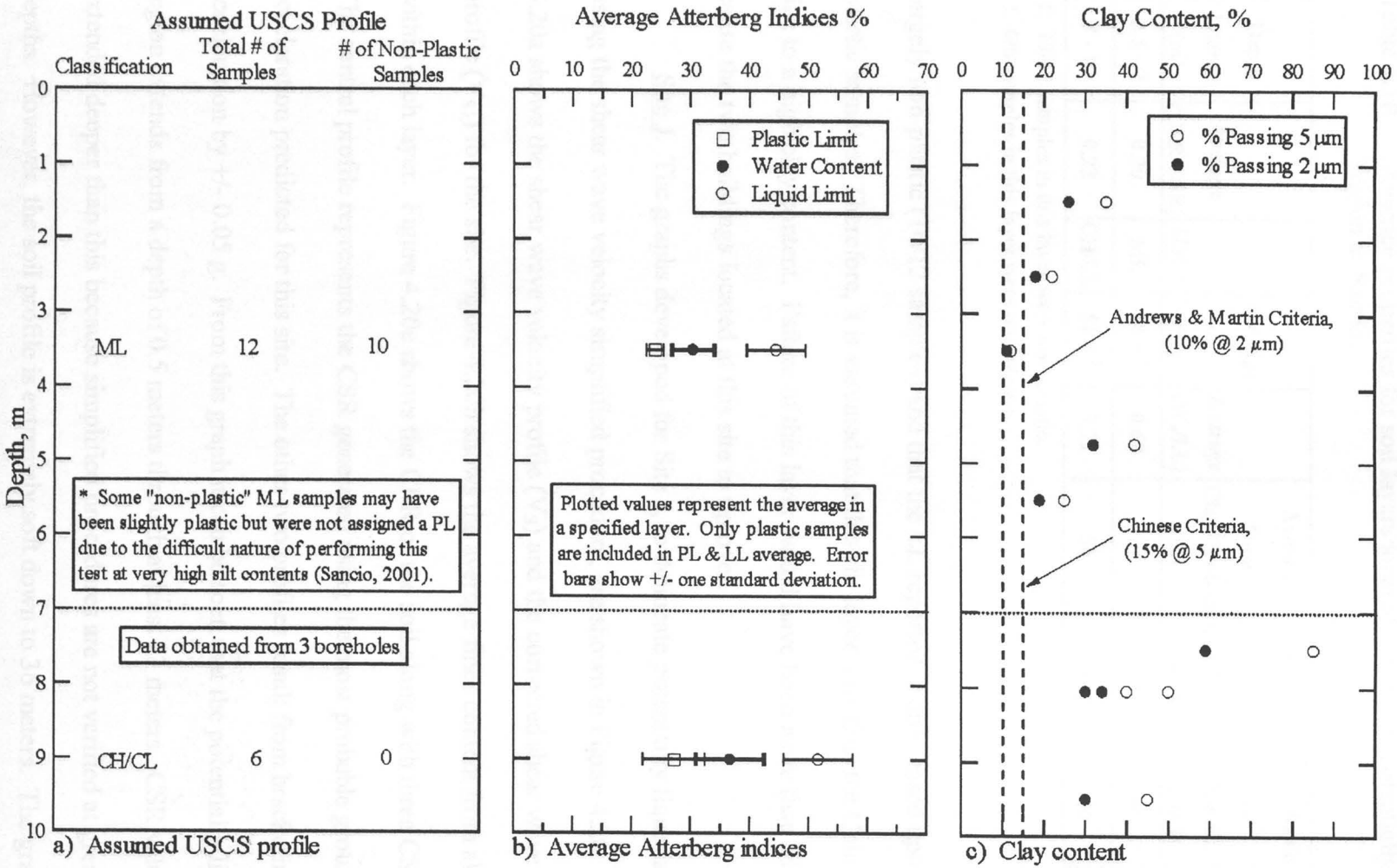

Figure 4.19 Graphs developed to delineate soils susceptible to liquefaction using the Chinese Criteria and the Andrews and Martin Criteria at Site G, Adapazari, Turkey (raw soil data from www.eerc.berkeley.edu/turkey/adapazari).

Table 4.10 Average properties for soil layers located within the potentially liquefiable region at Site G.

Depth Interval (m)	Average (CRR/CSR)	USCS	Average LL (%)	Average (W_n/LL)	Average 5 μm Clay Content (%)	Average 2 μm Clay Content (%)	Liquefiable by Chinese Criteria	Liquefiable by Andrews & Martin Criteria
0.5 - 7	0.20	ML	44.5 [1]	0.68	27	24	no	no
7 - 10	0.22	CH/CL	51.7 [2]	0.71	56	41	no	no

1. 10/12 samples in this layer were non-plastic.
2. 0/6 samples in this layer were non-plastic.

largely non-plastic (10/12 samples) and that the LL reported is only based upon two plastic samples. Therefore, it is assumed that this silt layer only fails the Chinese Criteria due to a high clay content. Failure of this layer would have been more than adequate to cause the two buildings located at this site to tip over.

Site J. The graphs developed for Site J, to delineate potentially liquefiable soil using the shear wave velocity simplified procedure, are shown in Figure 4.20. Figure 4.20a shows the shear wave velocity profile (V_S) and the corrected shear wave velocity profile (V_{S1}) for the site. Figure 4.20b shows the average fines content from all samples within each layer. Figure 4.20c shows the CRR of the soil along with three CSR profiles. The central profile represents the CSR generated using the most probable ground acceleration predicted for this site. The other two profiles result from bracketing this acceleration by +/- 0.05 g. From this graph it can be seen that the potentially liquefiable region extends from a depth of 0.5 meters through at least 23 meters. CSR values are not extended deeper than this because simplified procedures are not verified at greater depths. However, the soil profile is extremely soft down to 36 meters. The graphs

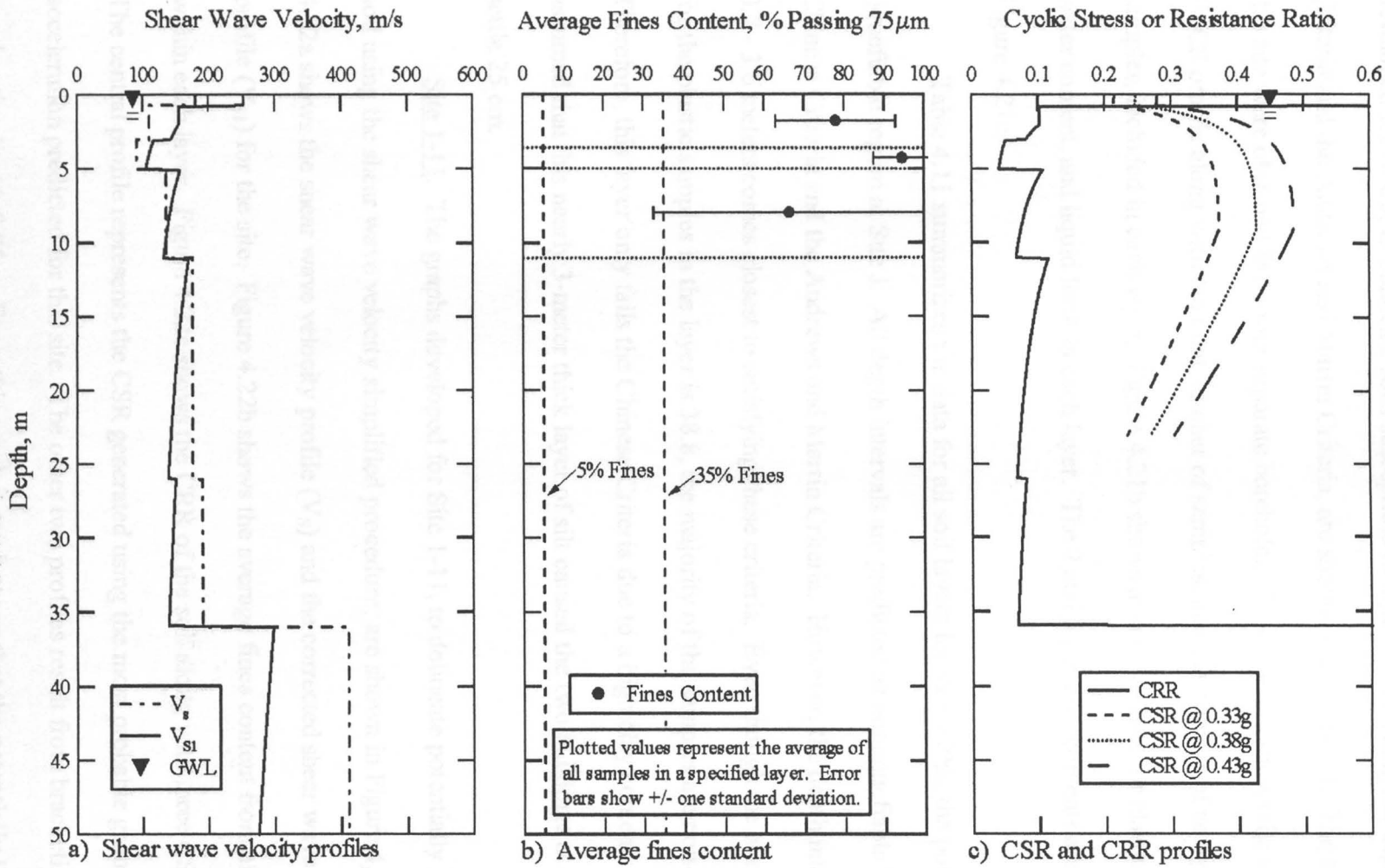

Figure 4.20 Graphs developed to delineate liquefiable soil using the simplified shear wave velocity procedure at Site J, Adapazari, Turkey (fines content obtained from www.eerc.berkeley.edu/turkey/adapazari).

developed for Site J, to delineate soils susceptible to liquefaction using the Chinese Criteria and the Andrews and Martin Criteria, are shown in Figure 4.21. The soil data for this site were obtained from four separate boreholes. Figure 4.21a shows the assumed USCS profile along with the total number of samples, and the number of non-plastic samples, included in each layer. Figure 4.21b shows average values for plastic limit, water content, and liquid limit in each layer. The 2 and 5 μm clay contents are plotted in Figure 4.21c.

Table 4.11 summarizes the data for all soil layers located within the potentially liquefiable region at Site J. All depth intervals are predicted as nonliquefiable by the Chinese Criteria and the Andrews and Martin Criteria. However, the depth interval from 0.7 - 3.6 meters comes closest to satisfying these criteria. Even though the average LL for the plastic samples in the layer is 38.8, the majority of the samples are non-plastic. Therefore, this layer only fails the Chinese Criteria due to a high clay content. It is assumed that this nearly 3-meter thick layer of silt caused the two buildings at Site J to settle 25 cm.

Site 1-11. The graphs developed for Site 1-11, to delineate potentially liquefiable soil using the shear wave velocity simplified procedure, are shown in Figure 4.22. Figure 4.22a shows the shear wave velocity profile (V_S) and the corrected shear wave velocity profile (V_{S1}) for the site. Figure 4.22b shows the average fines content from all samples within each layer. Figure 4.22c shows the CRR of the soil along with three CSR profiles. The central profile represents the CSR generated using the most probable ground acceleration predicted for this site. The other two profiles result from bracketing this acceleration by +/- 0.05 g. From this graph it can be seen that the potentially liquefiable

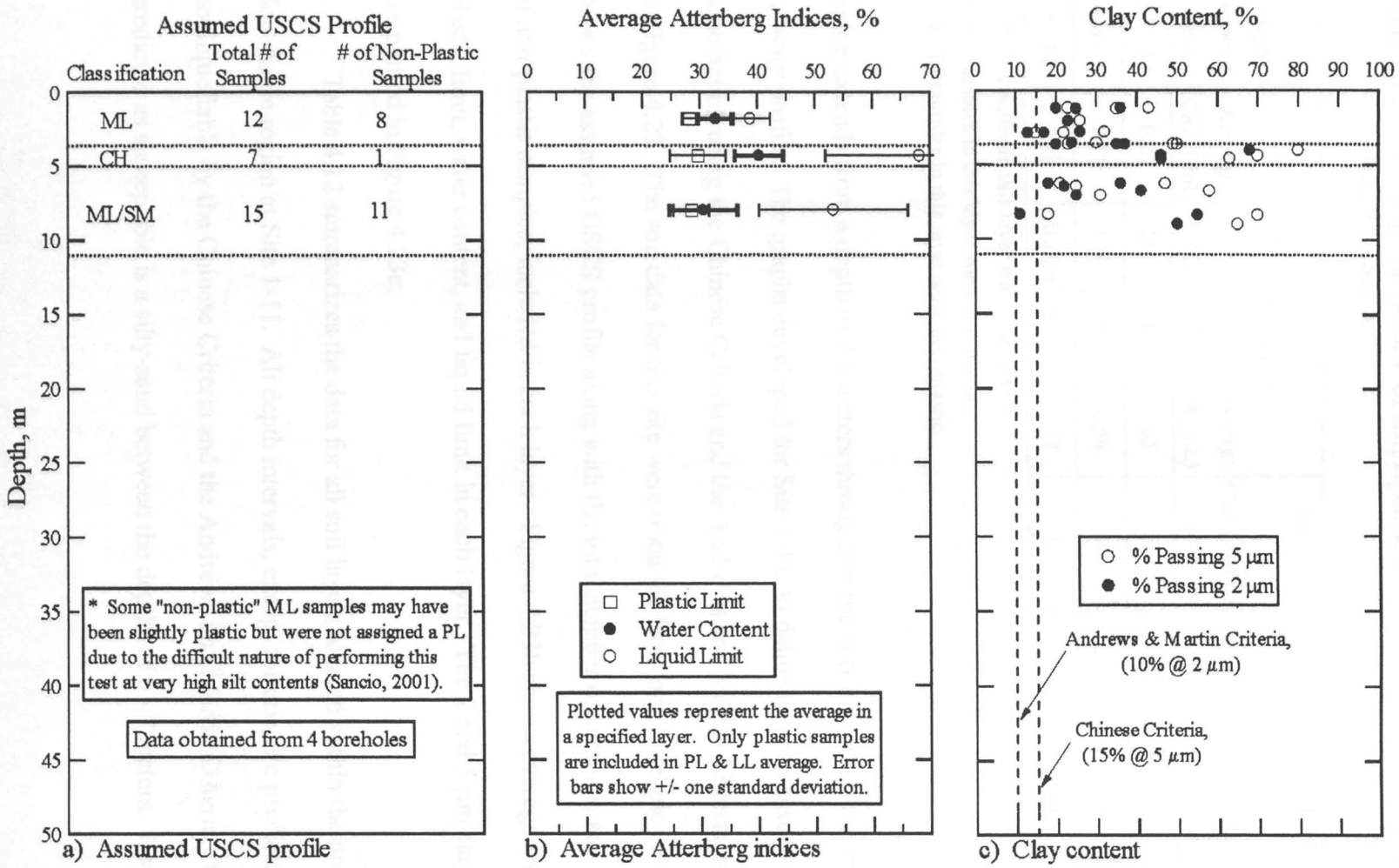

Figure 4.21 Graphs developed to delineate soils susceptible to liquefaction using the Chinese Criteria and the Andrews and Martin Criteria at Site J, Adapazari, Turkey (raw soil data from www.eerc.berkeley.edu/turkey/adapazari).

Table 4.11 Average properties for soil layers located within the potentially liquefiable region at Site J

Depth Interval (m)	Average (CRR/CSR)	USCS	Average LL (%)	Average (W_n/LL)	Average 5 μm Clay Content (%)	Average 2 μm Clay Content (%)	Liquefiable by Chinese Criteria	Liquefiable by Andrews & Martin Criteria
0.7 - 3.6	0.25	ML	38.8 [1]	0.85	28	23	no	no
3.6 - 5	0.11	CH	68.2 [2]	0.59	56	42	no	no
5 - 11	0.19	ML/SM	53.3 [3]	0.57	42	32	no	no

1. 8/12 samples in this layer were non-plastic.
2. 1/7 samples in this layer were non-plastic.
3. 11/15 samples in this layer were non-plastic.

region extends from a depth of 0.5 meters throughout the entire depth of the shear wave velocity profile. The graphs developed for Site 1-11, to delineate soils susceptible to liquefaction using the Chinese Criteria and the Andrews and Martin Criteria, are shown in Figure 4.23. The soil data for this site were obtained from one borehole. Figure 4.23a shows the assumed USCS profile along with the total number of samples, and the number of non-plastic samples, included in each layer. Figure 4.23b shows average values for plastic limit, water content, and liquid limit in each layer. The 2 and 5 μm clay contents are plotted in Figure 4.23c.

Table 4.12 summarizes the data for all soil layers located within the potentially liquefiable region at Site 1-11. All depth intervals, except for one, are predicted as nonliquefiable by the Chinese Criteria and the Andrews and Martin Criteria. The layer predicted as susceptible is a silty-sand between the depths of 6 - 7 meters. However, it is

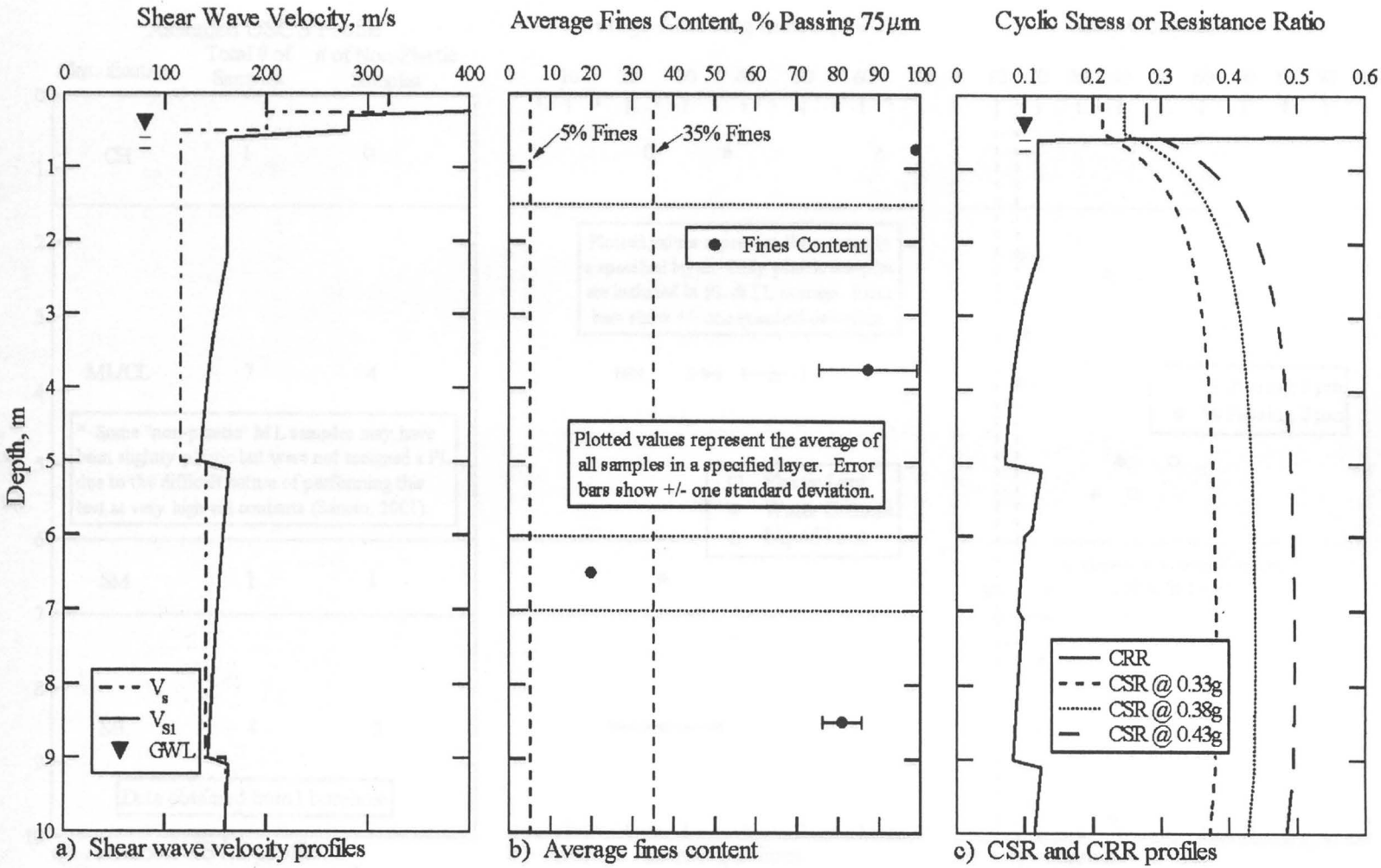

Figure 4.22 Graphs developed to delineate liquefiable soil using the simplified shear wave velocity procedure at Site 1-11, Adapazari, Turkey (fines content obtained from www.eerc.berkeley.edu/turkey/adapazari).

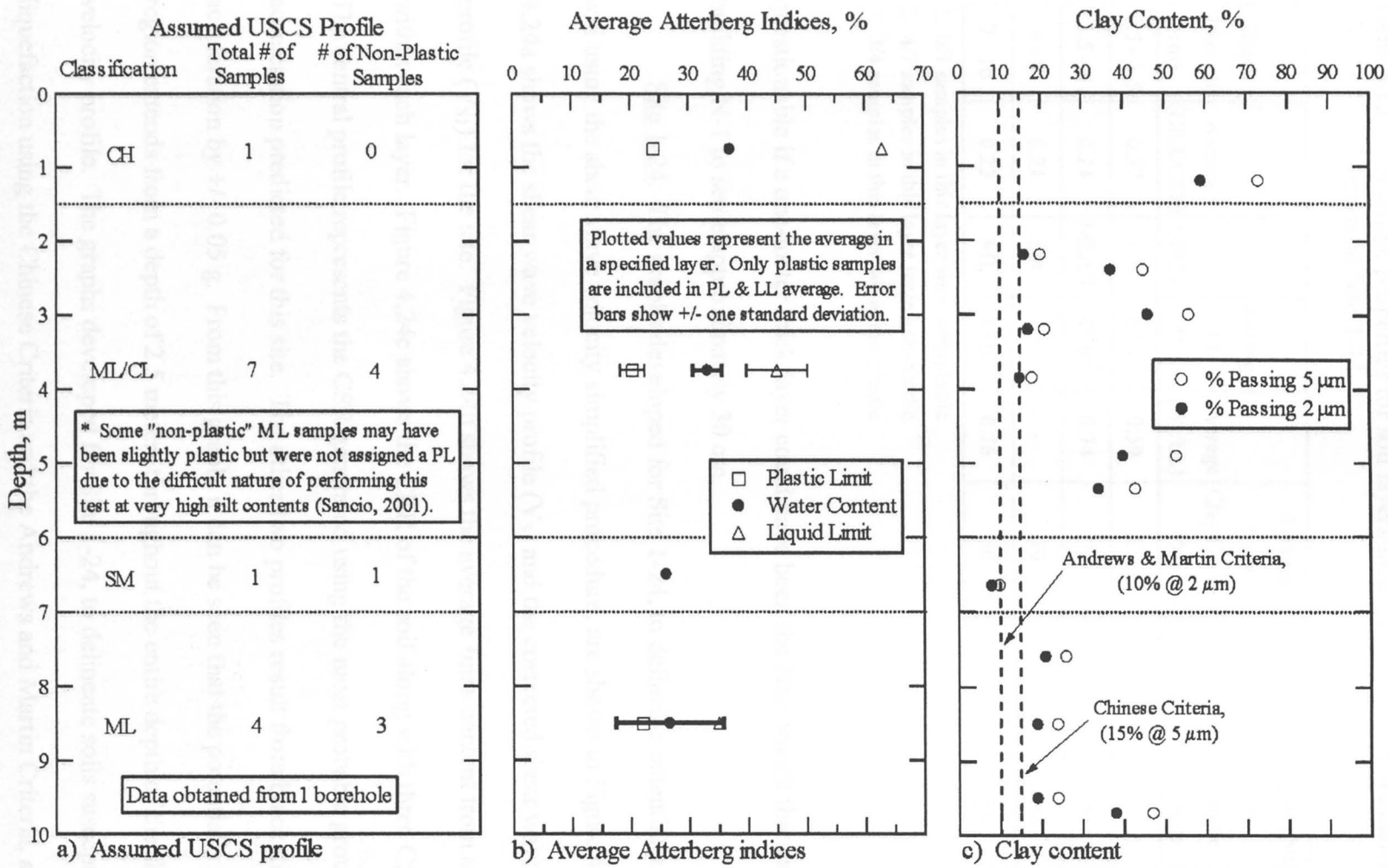

Figure 4.23 Graphs developed to delineate soils susceptible to liquefaction using the Chinese Criteria and the Andrews and Martin Criteria at Site 1-11, Adapazari, Turkey (raw soil data from www.eerc.berkeley.edu/turkey/adapazari).

Table 4.12 Average properties for soil layers located within the potentially liquefiable region at Site 1-11

Depth Interval (m)	Average (CRR/CSR)	USCS	Average LL (%)	Average (W_n/LL)	Average 5 μm Clay Content (%)	Average 2 μm Clay Content (%)	Liquefiable by Chinese Criteria	Liquefiable by Andrews & Martin Criteria
0.5 - 1.5	0.37	CH	63.0 [1]	0.59	73	59	no	no
1.5 - 6	0.24	ML/CL	45.0 [2]	0.74	37	29	no	no
6 - 7	0.21	SM	-	-	10	8	yes	yes
7 - 10	0.23	ML	35.0 [3]	0.76	30	24	no	no

1. 0/1 samples in this layer were non-plastic.
2. 4/7 samples in this layer were non-plastic.
3. 3/4 samples in this layer were non-plastic.

questionable if a one-meter thick layer could have been the lone culprit that caused building N-1 to settle approximately 30 cm.

Site 1-24. The graphs developed for Site 1-24, to delineate potentially liquefiable soil using the shear wave velocity simplified procedure, are shown in Figure 4.24. Figure 4.24a shows the shear wave velocity profile (V_S) and the corrected shear wave velocity profile (V_{S1}) for the site. Figure 4.24b shows the average fines content from all samples within each layer. Figure 4.24c shows the CRR of the soil along with three CSR profiles. The central profile represents the CSR generated using the most probable ground acceleration predicted for this site. The other two profiles result from bracketing this acceleration by +/- 0.05 g. From this graph, it can be seen that the potentially liquefiable region extends from a depth of 2.5 meters throughout the entire depth of the shear wave velocity profile. The graphs developed for Site 1-24, to delineate soils susceptible to liquefaction using the Chinese Criteria and the Andrews and Martin Criteria, are shown

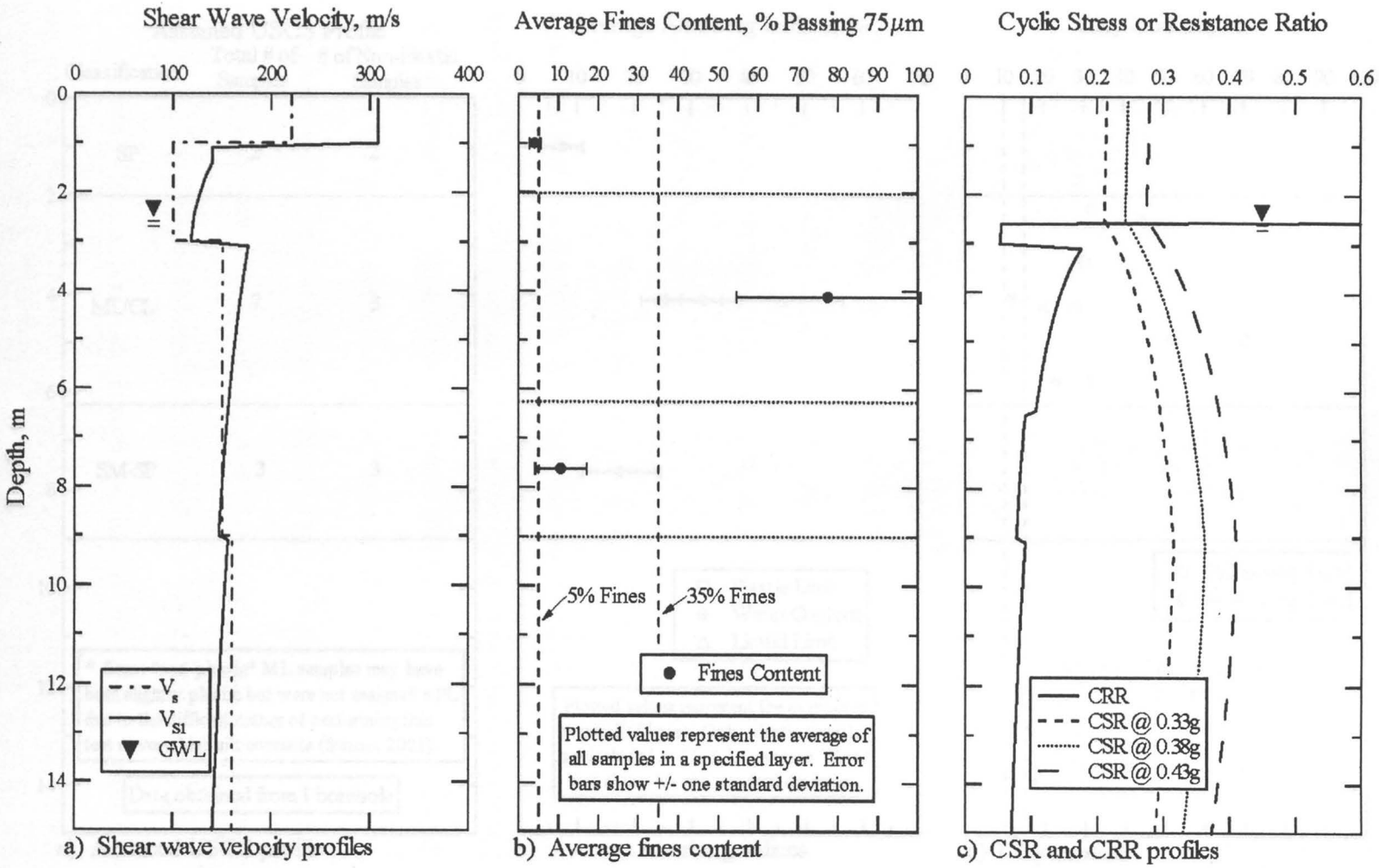

Figure 4.24 Graphs developed to delineate liquefiable soil using the simplified shear wave velocity procedure at Site 1-24, Adapazari, Turkey (fines content obtained from www.eerc.berkeley.edu/turkey/adapazari).

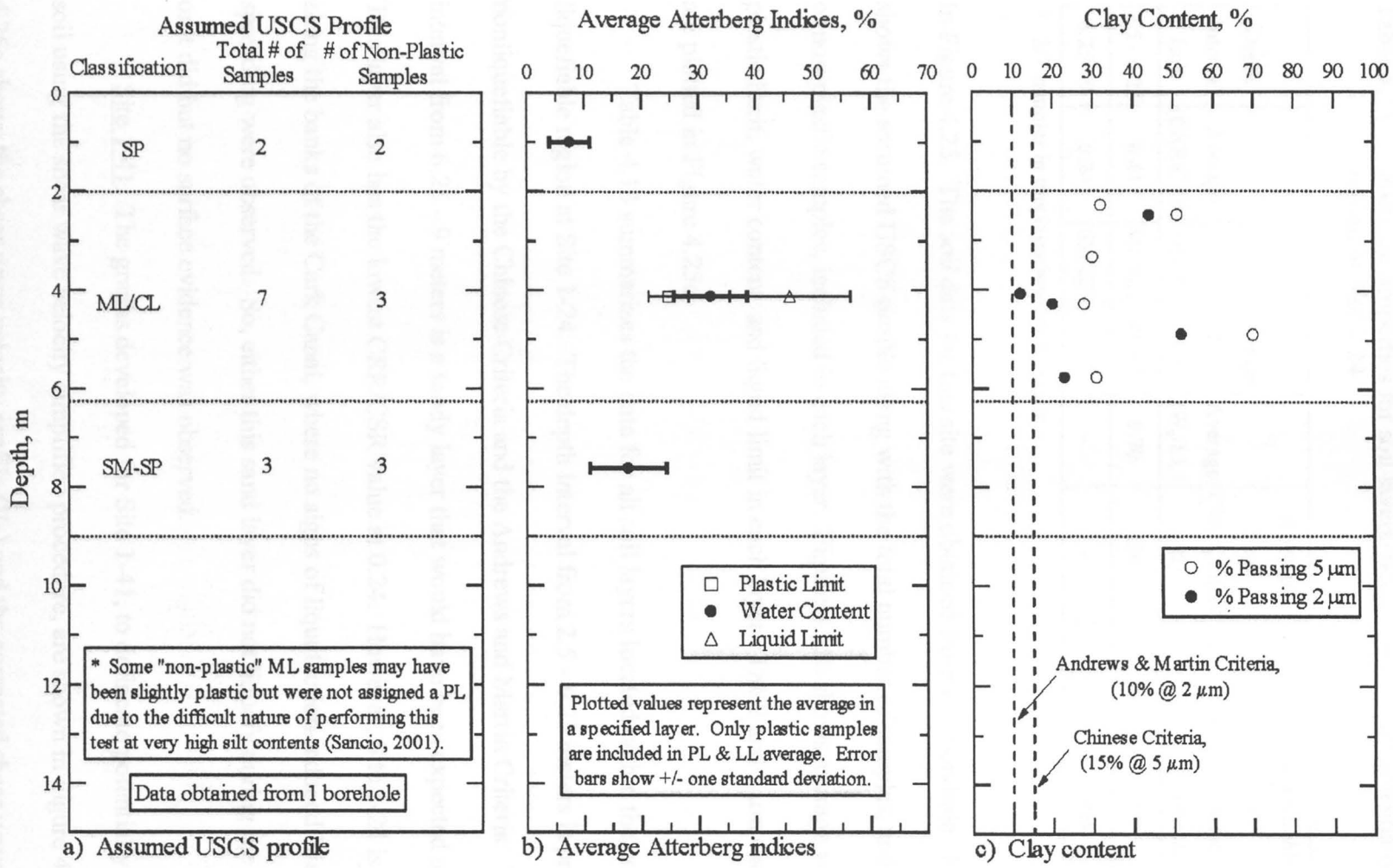

Figure 4.25 Graphs developed to delineate soils susceptible to liquefaction using the Chinese Criteria and the Andrews and Martin Criteria at Site 1-24, Adapazari, Turkey (raw soil data from www.eerc.berkeley.edu/turkey/adapazari).

Table 4.13 Average properties for soil layers located within the potentially liquefiable region at Site 1.24

Depth Interval (m)	Average (CRR/CSR)	USCS	Average LL (%)	Average (W_n/LL)	Average 5 μm Clay Content (%)	Average 2 μm Clay Content (%)	Liquefiable by Chinese Criteria	Liquefiable by Andrews & Martin Criteria
2.5 - 6.25	0.41	ML/CL	46.0 [1]	0.70	36	30	no	no
6.25 - 9	0.24	SM-SP	-	-	-	-	yes	yes

1. 3/7 samples in this layer were non-plastic.

In Figure 4.25. The soil data for this site were obtained from one borehole. Figure 4.25a shows the assumed USCS profile along with the total number of samples, and the number of non-plastic samples, included in each layer. Figure 4.25b shows average values for plastic limit, water content, and liquid limit in each layer. The 2 and 5 μm clay contents are plotted in Figure 4.25c.

Table 4.13 summarizes the data for all soil layers located within the potentially liquefiable region at Site 1-24. The depth interval from 2.5 - 6.25 meters is predicted as nonliquefiable by the Chinese Criteria and the Andrews and Martin Criteria. The depth interval from 6.25 - 9 meters is a sandy layer that would have been expected to liquefy. This layer also has the lowest CRR/CSR value at 0.24. However, Site 1-24 is located along the banks of the Cark Canal, where no signs of liquefaction-induced lateral spreading were observed. So, either this sand layer did not liquefy during the earthquake, or it did but no surface evidence was observed.

Site 1-41. The graphs developed for Site 1-41, to delineate potentially liquefiable soil using the shear wave velocity simplified procedure, are shown in Figure 4.26. Figure 4.26a shows the shear wave velocity profile (V_S) and the corrected shear wave velocity

profile (V_{S1}) for the site. Figure 4.26b shows the average fines content from all samples within each layer. Figure 4.26c shows the CRR of the soil along with three CSR profiles. The central profile represents the CSR generated using the most probable ground acceleration predicted for this site. The other two profiles result from bracketing this acceleration by +/- 0.05 g. From this graph, it can be seen that the potentially liquefiable region is broken into several portions. This is due to the corrected shear wave velocity being very close to the maximum liquefiable velocity of 200 m/s. The liquefiable region is between the depths of 0.5 - 3 meters, and 5.25 - 8 meters. It appears that there might be another portion of the liquefiable region below 9.5 meters but no soil data are available at this site below 10 meters. The graphs developed for Site 1-41, to delineate soils susceptible to liquefaction using the Chinese Criteria and the Andrews and Martin Criteria, are shown in Figure 4.27. The soil data for this site were obtained from one borehole. Figure 4.27a shows the assumed USCS profile along with the total number of samples, and the number of non-plastic samples, included in each layer. Figure 4.27b shows average values for plastic limit, water content, and liquid limit in each layer. The 2 and 5 μm clay contents are plotted in Figure 4.27c.

Table 4.14 summarizes the data for all soil layers located within the potentially liquefiable region at Site 1-41. The depth interval from 0.5 - 3 meters is predicted as nonliquefiable by the Chinese Criteria and the Andrews and Martin Criteria. The depth interval from 5.25 - 8 meters is a sandy layer that would be expected to liquefy. This layer also has the lowest CRR/CSR value at 0.39. This layer most likely caused the 10 - 20 cm of building settlement that occurred here.

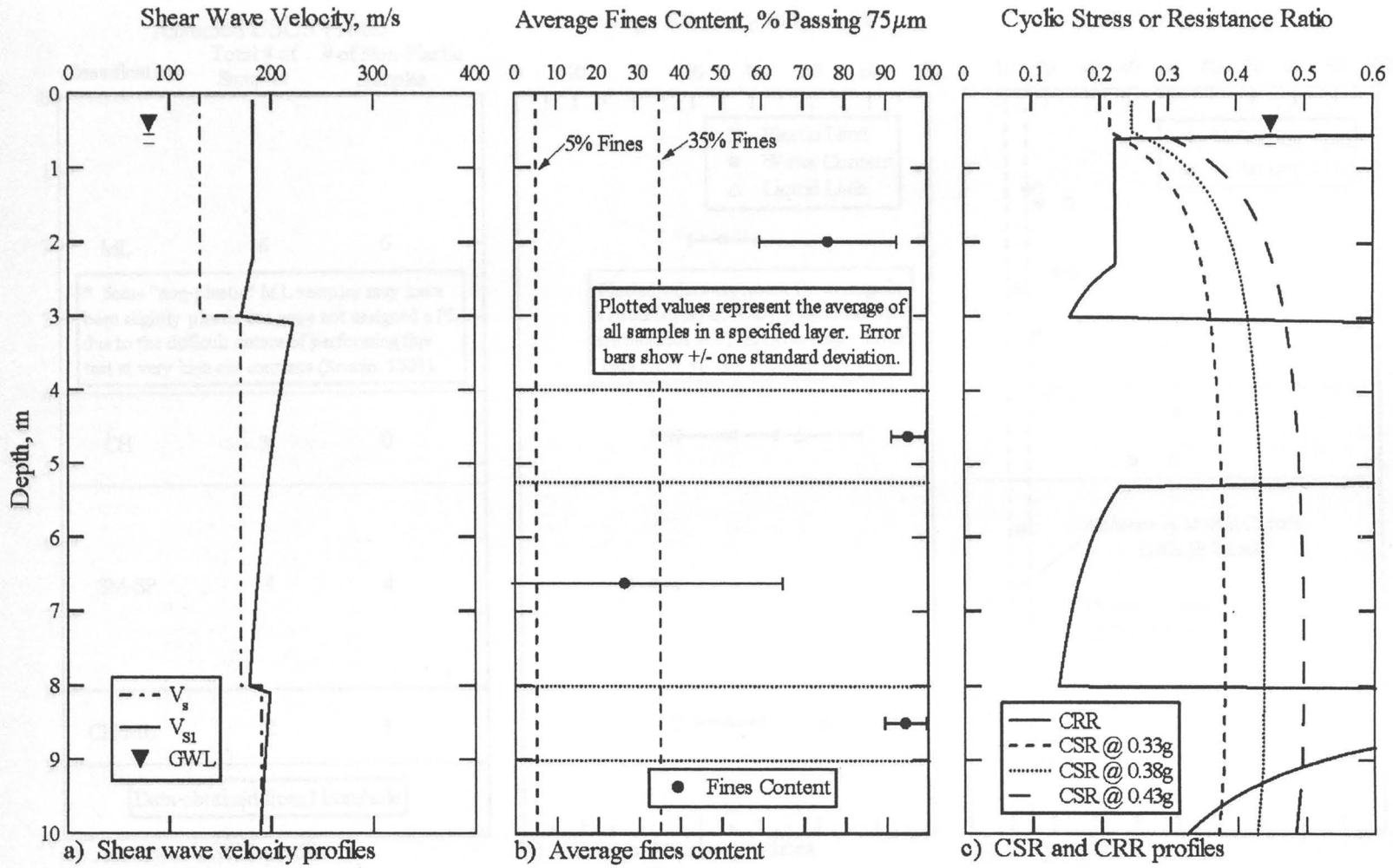

Figure 4.26 Graphs developed to delineate liquefiable soil using the simplified shear wave velocity procedure at Site 1-41, Adapazari, Turkey (fines content obtained from www.eerc.berkeley.edu/turkey/adapazari).

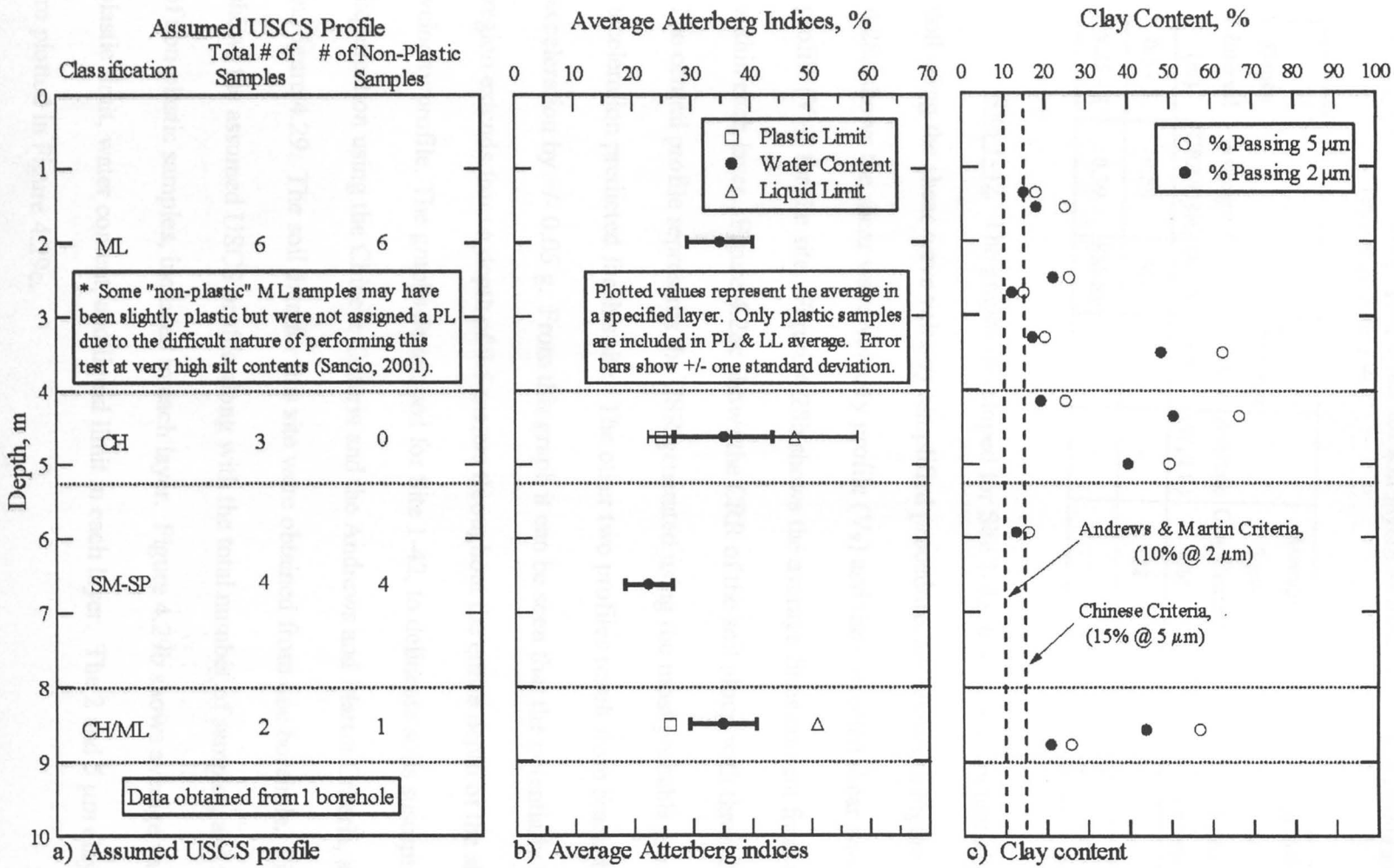

Figure 4.27 Graphs developed to delineate soils susceptible to liquefaction using the Chinese Criteria and the Andrews and Martin Criteria at Site 1-41, Adapazari, Turkey (raw soil data from www.eerc.berkeley.edu/turkey/adapazari).

Table 4.14 Average properties for soil layers located within the potentially liquefiable region at Site 1-41

Depth Interval (m)	Average (CRR/CSR)	USCS	Average LL (%)	Average (W_n/LL)	Average 5 μm Clay Content (%)	Average 2 μm Clay Content (%)	Liquefiable by Chinese Criteria	Liquefiable by Andrews & Martin Criteria
0.5 - 3	0.58	ML	-	-	28	22	no	no
5.25 - 8	0.39	SM-SP	-	-	-	-	yes	yes

Site 1-42. The graphs developed for Site 1-42, to delineate potentially liquefiable soil using the shear wave velocity simplified procedure, are shown in Figure 4.28. Figure 4.28a shows the shear wave velocity profile (V_S) and the corrected shear wave velocity profile (V_{S1}) for the site. Figure 4.28b shows the average fines content from all samples within each layer. Figure 4.28c shows the CRR of the soil along with three CSR profiles. The central profile represents the CSR generated using the most probable ground acceleration predicted for this site. The other two profiles result from bracketing this acceleration by +/- 0.05 g. From this graph it can be seen that the potentially liquefiable region extends from a depth of 0.5 meters throughout the entire depth of the shear wave velocity profile. The graphs developed for Site 1-42, to delineate soils susceptible to liquefaction using the Chinese Criteria and the Andrews and Martin Criteria, are shown in Figure 4.29. The soil data for this site were obtained from one borehole. Figure 4.29a shows the assumed USCS profile along with the total number of samples, and the number of non-plastic samples, included in each layer. Figure 4.29b shows average values for plastic limit, water content, and liquid limit in each layer. The 2 and 5 μm clay contents are plotted in Figure 4.29c.

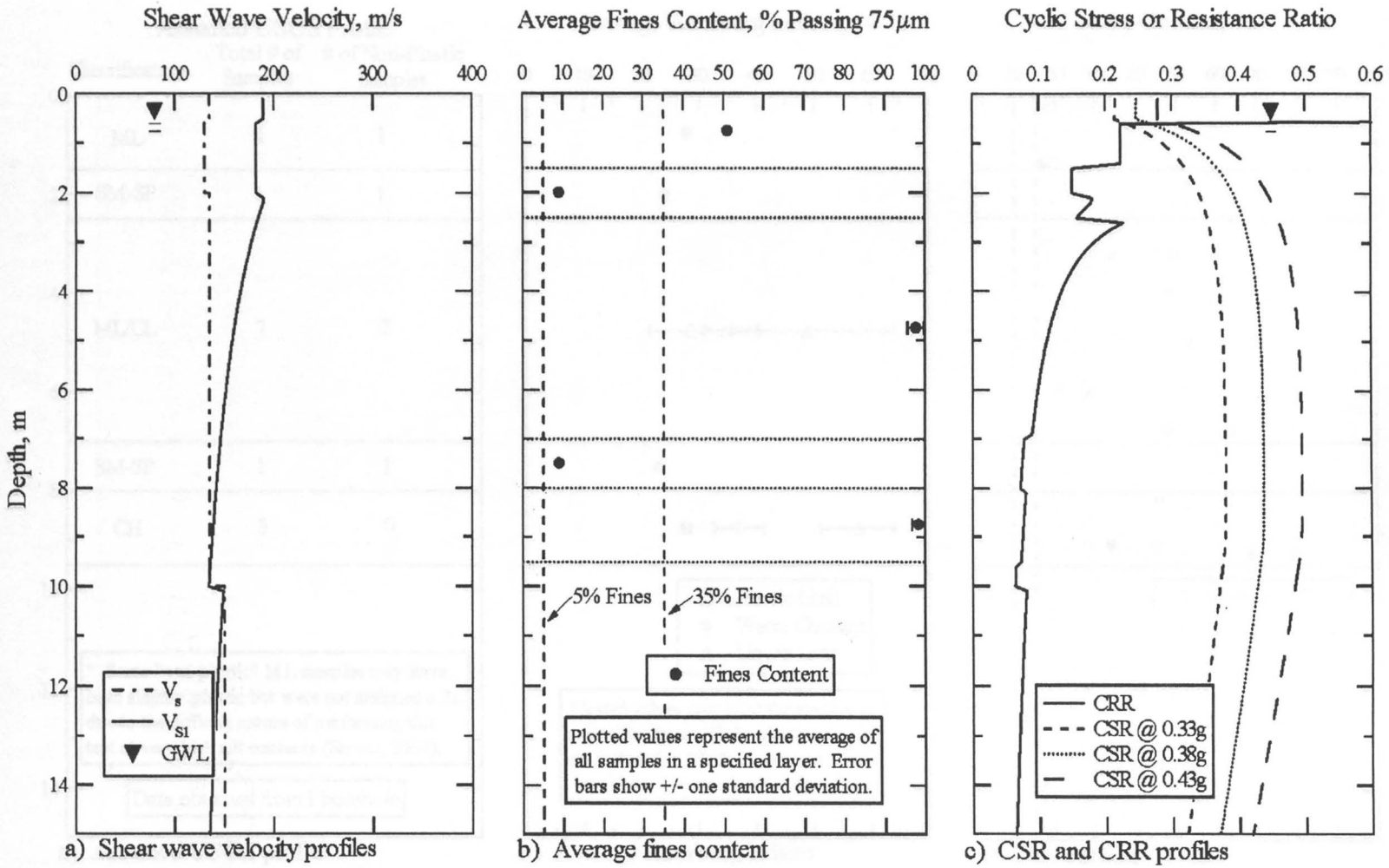

Figure 4.28 Graphs developed to delineate liquefiable soil using the simplified shear wave velocity procedure at Site 1-42, Adapazari, Turkey (fines content obtained from www.eerc.berkeley.edu/turkey/adapazari).

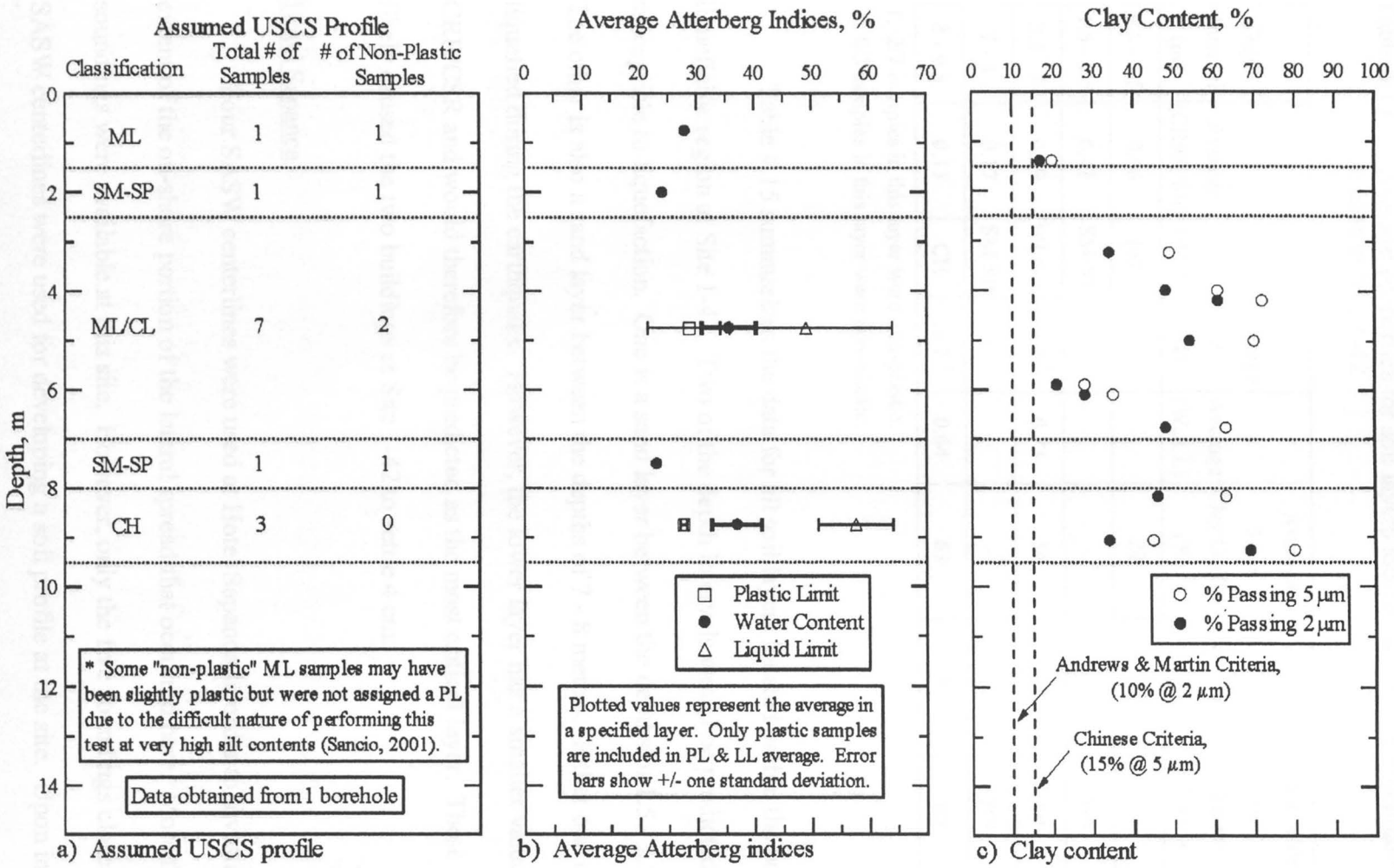

Figure 4.29 Graphs developed to delineate soils susceptible to liquefaction using the Chinese Criteria and the Andrews and Martin Criteria at Site 1-42, Adapazari, Turkey (raw soil data from www.eerc.berkeley.edu/turkey/adapazari).

Table 4.15 Average properties for soil layers located within the potentially liquefiable region at Site 1-42

Depth Interval (m)	Average (CRR/CSR)	USCS	Average LL (%)	Average (W_n/LL)	Average 5 μm Clay Content (%)	Average 2 μm Clay Content (%)	Liquefiable by Chinese Criteria	Liquefiable by Andrews & Martin Criteria
0.5 - 1.5	0.66	ML	-	-	20	17	no	no
1.5 - 2.5	0.41	SM-SP	-	-	-	-	yes	yes
2.5 - 7	0.29	ML/CL	49.0 [1]	0.73	54	42	no	no
7 - 8	0.17	SM-SP	-	-	-	-	yes	yes
8 - 9.5	0.17	CH	57.7 [2]	0.64	63	50	no	no

1. 2/7 samples in this layer were non-plastic.
2. 0/3 samples in this layer were non-plastic.

Table 4.15 summarizes the data for all soil layers located within the potentially liquefiable region at Site 1-42. Two of the depth intervals would be predicted as susceptible to liquefaction. One is a sand layer between the depths of 1.5 - 2.5 meters. The other is also a sand layer between the depths of 7 - 8 meters. Either one could have liquefied during the earthquake. However, the lower layer has a smaller value of CRR/CSR and would therefore be predicted as the most critical layer. These layers most likely caused the two buildings at Site 1-42 to settle 4 cm.

Hotel Sapanca

Four SASW centerlines were used at Hotel Sapanca in order to investigate the full extent of the on-shore portion of the lateral spread that occurred here. More than 10 CPT soundings were available at this site. However, only the five soundings closest to the SASW centerlines were used for developing a soil profile at the site. Upon investigation of these soundings, it was clear that the soil over the entire area was very uniform,

consisting of sand/sand mixtures throughout. Therefore, only one soil profile was developed for the site. Refer to Figure 3.59 in Chapter 3 for the CPT and centerline locations.

The graphs developed for Centerline 1 at Hotel Sapanca, to delineate potentially liquefiable soil using the shear wave velocity simplified procedure, are shown in Figure 4.30. Figure 4.30a shows the shear wave velocity profile (V_S) and the corrected shear wave velocity profile (V_{S1}) for the site. Figure 4.30b shows the fines content used for the calculation of CRR's. Figure 4.30c shows the CRR of the soil along with three CSR profiles. The central profile represents the CSR generated using the most probable ground acceleration predicted for this site. The other two profiles result from bracketing this acceleration by +/- 0.05 g. From this graph it can be seen that the potentially liquefiable region extends from a depth of 1.25 meters throughout the entire depth of the shear wave velocity profile.

The graphs developed for Centerline 2 at Hotel Sapanca, to delineate potentially liquefiable soil using the shear wave velocity simplified procedure, are shown in Figure 4.31. Figure 4.31a shows the shear wave velocity profile (V_S) and the corrected shear wave velocity profile (V_{S1}) for the site. Figure 4.31b shows the fines content used for the calculation of CRR's. Figure 4.31c shows the CRR of the soil along with three CSR profiles. The central profile represents the CSR generated using the most probable ground acceleration predicted for this site. The other two profiles result from bracketing this acceleration by +/- 0.05 g. From this graph it can be seen that the potentially liquefiable region extends from a depth of 1.6 meters throughout the entire depth of the shear wave velocity profile.

The graphs developed for Centerline 3 at Hotel Sapanca, to delineate potentially liquefiable soil using the shear wave velocity simplified procedure, are shown in Figure 4.32. Figure 4.32a shows the shear wave velocity profile (V_S) and the corrected shear wave velocity profile (V_{S1}) for the site. Figure 4.32b shows the fines content used for the calculation of CRR's. Figure 4.32c shows the CRR of the soil along with three CSR profiles. The central profile represents the CSR generated using the most probable ground acceleration predicted for this site. The other two profiles result from bracketing this acceleration by +/- 0.05 g. From this graph, it can be seen that the potentially liquefiable region is broken into two portions. This is due to the corrected shear wave velocity having a value just over 215 m/s from approximately 5 - 5.5 meters. The liquefiable region is between the depths of 1.25 - 5 meters, and 5.5 - 15 meters.

The graphs developed for Centerline 4 at Hotel Sapanca, to delineate potentially liquefiable soil using the shear wave velocity simplified procedure, are shown in Figure 4.33. Figure 4.33a shows the shear wave velocity profile (V_S) and the corrected shear wave velocity profile (V_{S1}) for the site. Figure 4.33b shows the fines content used for the calculation of CRR's. Figure 4.33c shows the CRR of the soil along with three CSR profiles. The central profile represents the CSR generated using the most probable ground acceleration predicted for this site. The other two profiles result from bracketing this acceleration by +/- 0.05 g. From this graph it can be seen that the potentially liquefiable region extends from a depth of 0.5 - 7 meters.

As mentioned above, five CPT soundings were analyzed at Hotel Sapanca. The graphs developed from CPT-SH4, to characterize the subsurface, are shown in Figure 4.34. The graphs developed from CPT-SH5, to characterize the subsurface, are shown in

Figure 4.35. The graphs developed from CPT-SH6, to characterize the subsurface, are shown in Figure 4.36. The graphs developed from CPT-SH7, to characterize the subsurface, are shown in Figure 4.37. The graphs developed from CPT-SH8, to characterize the subsurface, are shown in Figure 4.38. Figure 4.39 shows the idealized soil profile and layer properties at Hotel Sapanca as determined from combining the data from these five cone soundings.

Table 4.16 summarizes the data for the depth intervals located within the potentially liquefiable region at Centerline 1. Table 4.17 summarizes the data for the depth intervals located within the potentially liquefiable region at Centerline 2. Table 4.18 summarizes the data for the depth intervals located within the potentially liquefiable region at Centerline 3. Table 4.19 summarizes the data for the depth intervals located within the potentially liquefiable region at Centerline 4. The soil properties in each of these tables are the same and show a sand/sand mixture soil profile with an approximate I_C value of 1.7. Each centerline varies slightly in values for CRR/CSR. However, there is plenty of sandy soil predicted as liquefiable underneath all four centerlines. These types of conditions would explain the dramatic subsidence and lateral spreading that caused the Hotel to be carried partially into the lake.

Izmit Bay

Degirmendere Nose. The graphs developed for Degirmendere Nose, to delineate potentially liquefiable soil using the shear wave velocity simplified procedure, are shown in Figure 4.40. Figure 4.40a shows the shear wave velocity profile (V_S) and the corrected shear wave velocity profile (V_{S1}) for the site. Figure 4.40b shows the fines content used

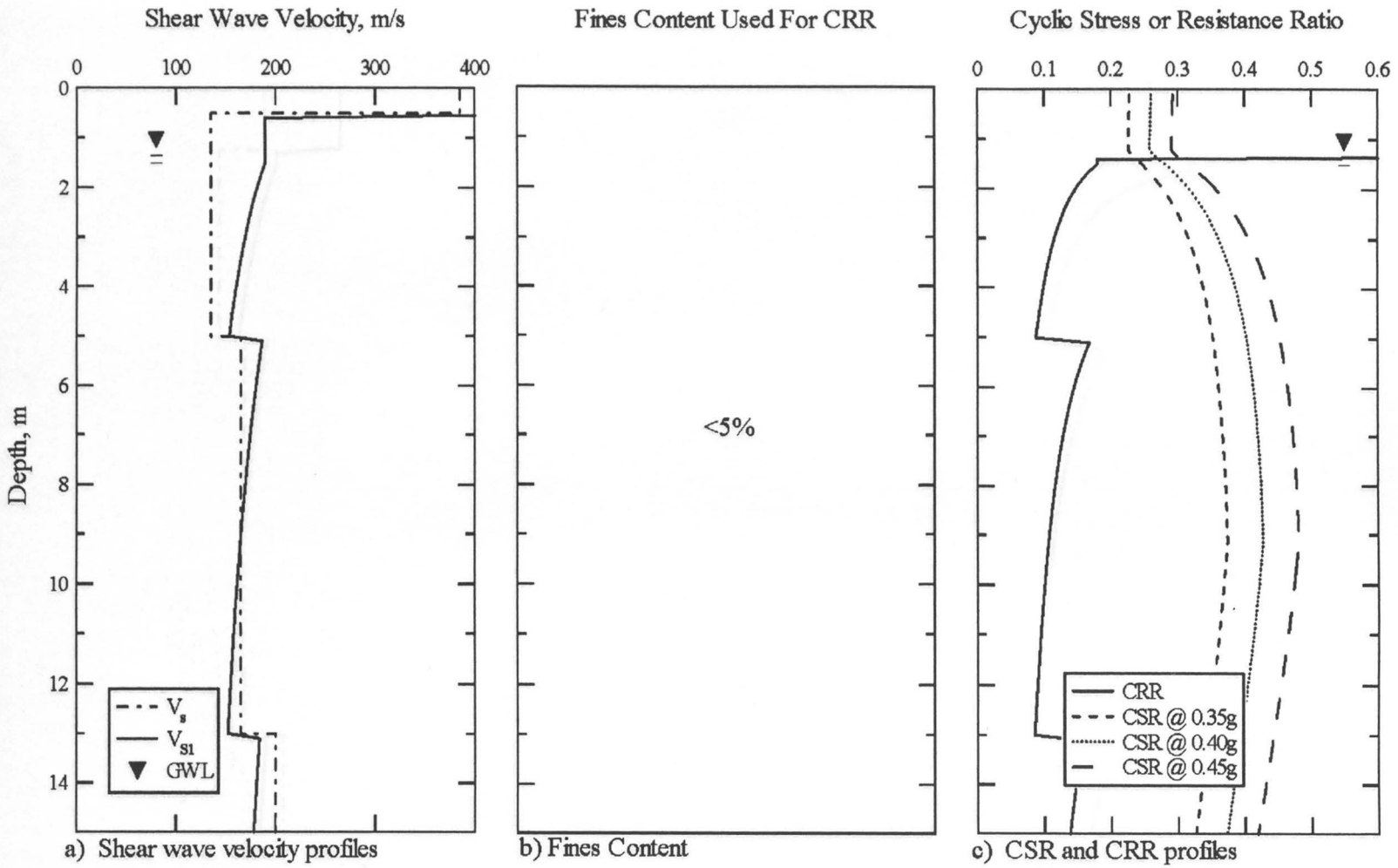

Figure 4.30 Graphs developed to delineate liquefiable soil using the simplified shear wave velocity procedure at Centerline 1, Hotel Sapanca, Sapanca, Turkey.

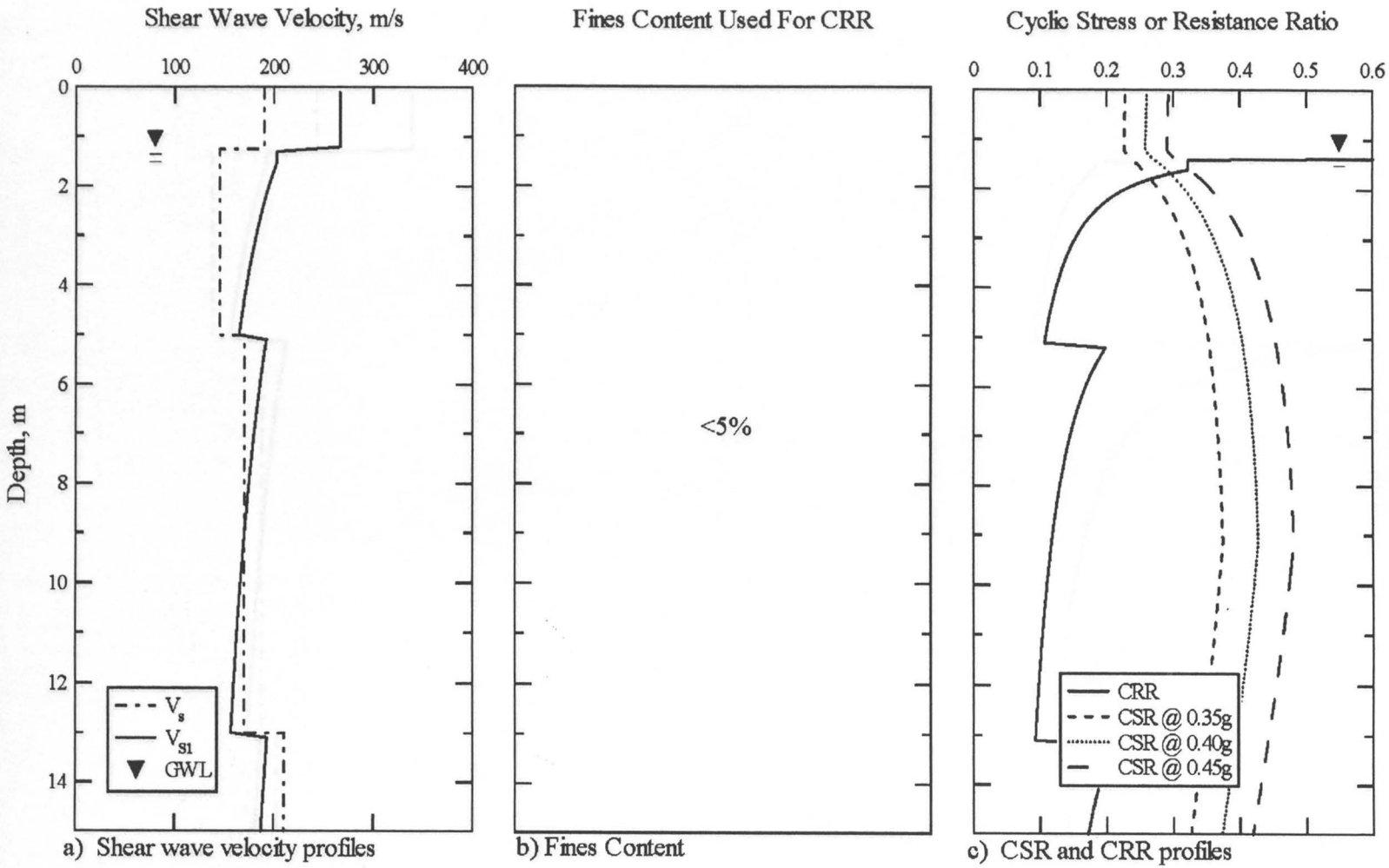

Figure 4.31 Graphs developed to delineate liquefiable soil using the simplified shear wave velocity procedure at Centerline 2, Hotel Sapanca, Sapanca, Turkey.

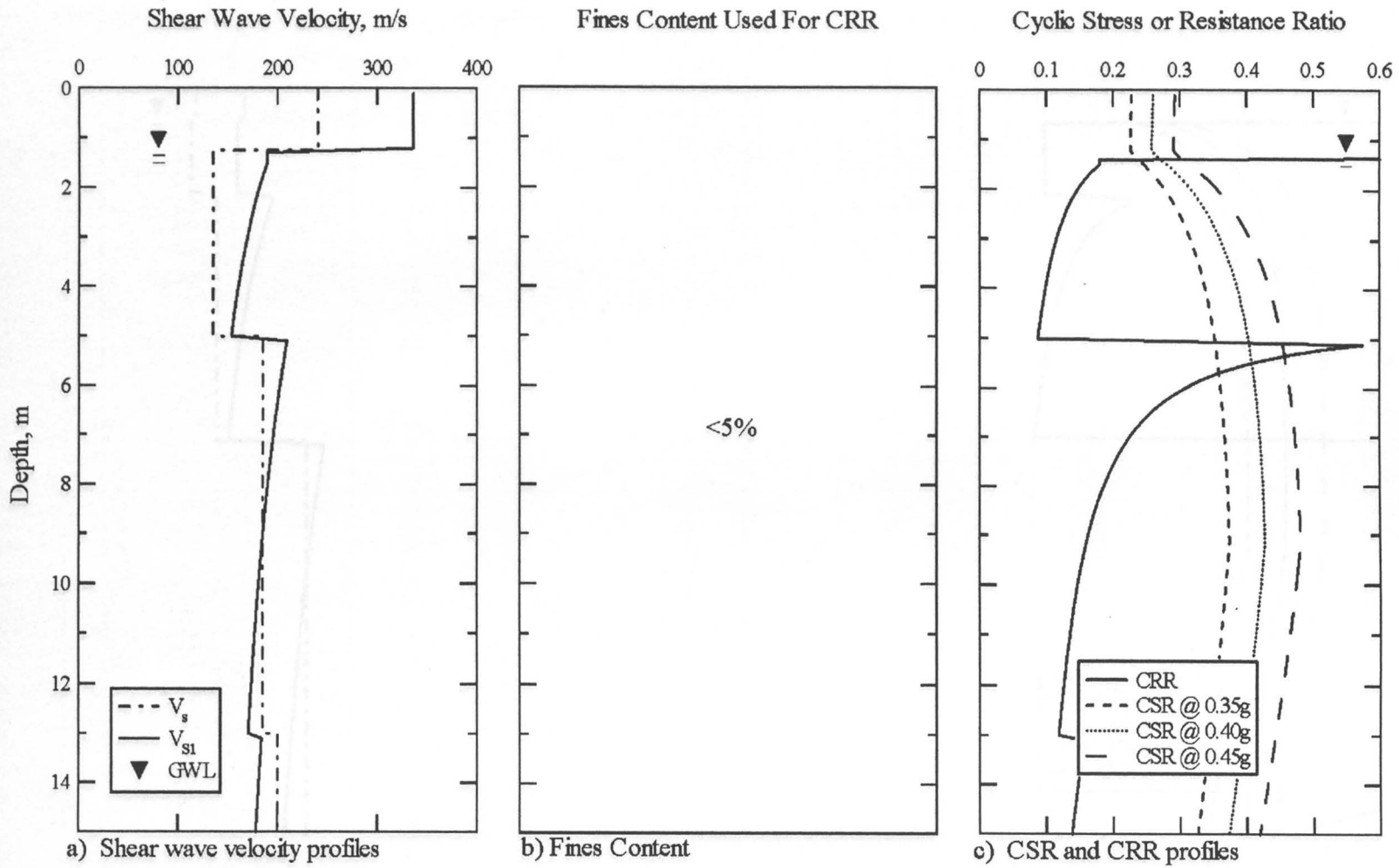

Figure 4.32 Graphs developed to delineate liquefiable soil using the simplified shear wave velocity procedure at Centerline 3, Hotel Sapanca, Sapanca, Turkey.

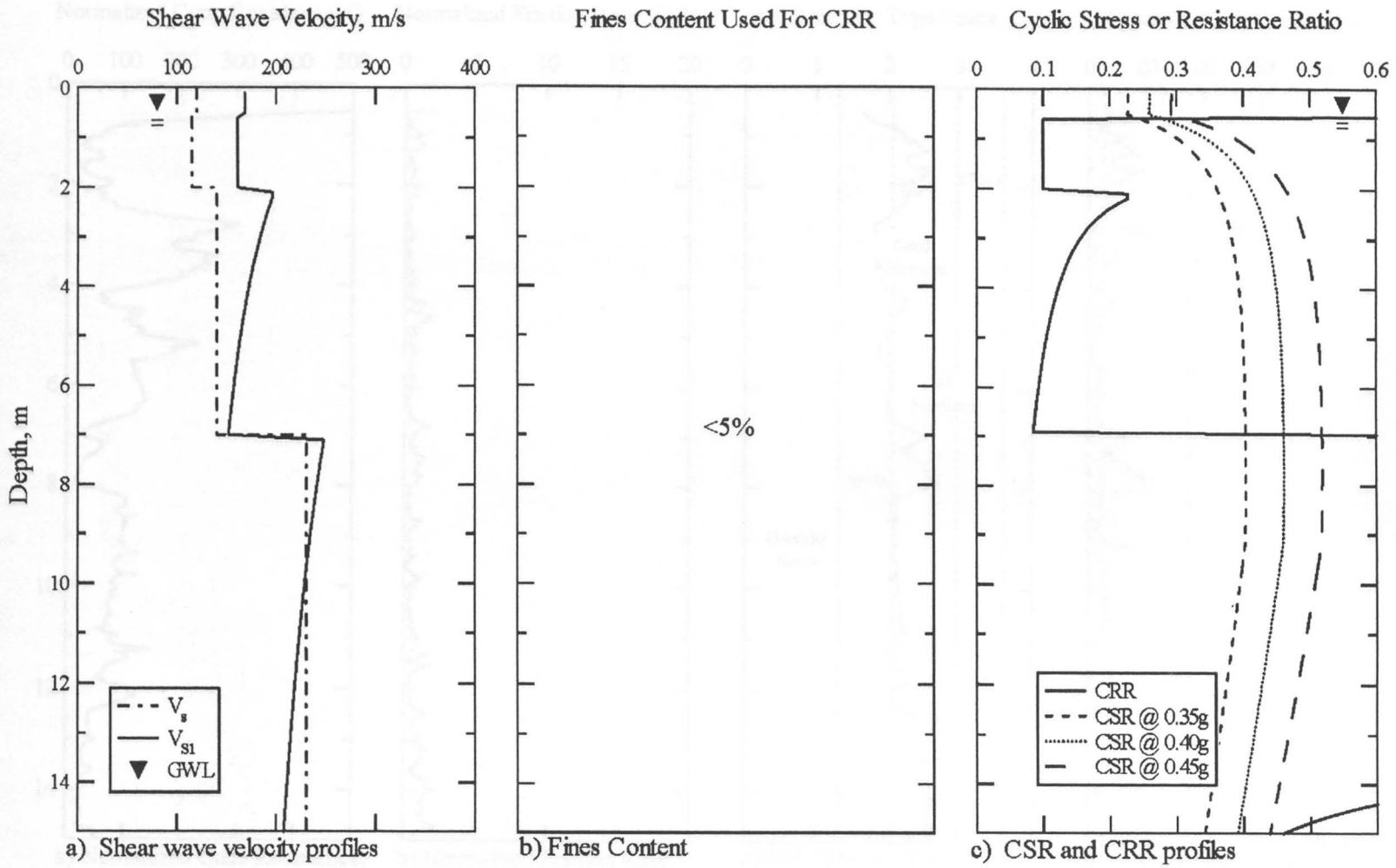

Figure 4.33 Graphs developed to delineate liquefiable soil using the simplified shear wave velocity procedure at Centerline 4, Hotel Sapanca, Sapanca, Turkey.

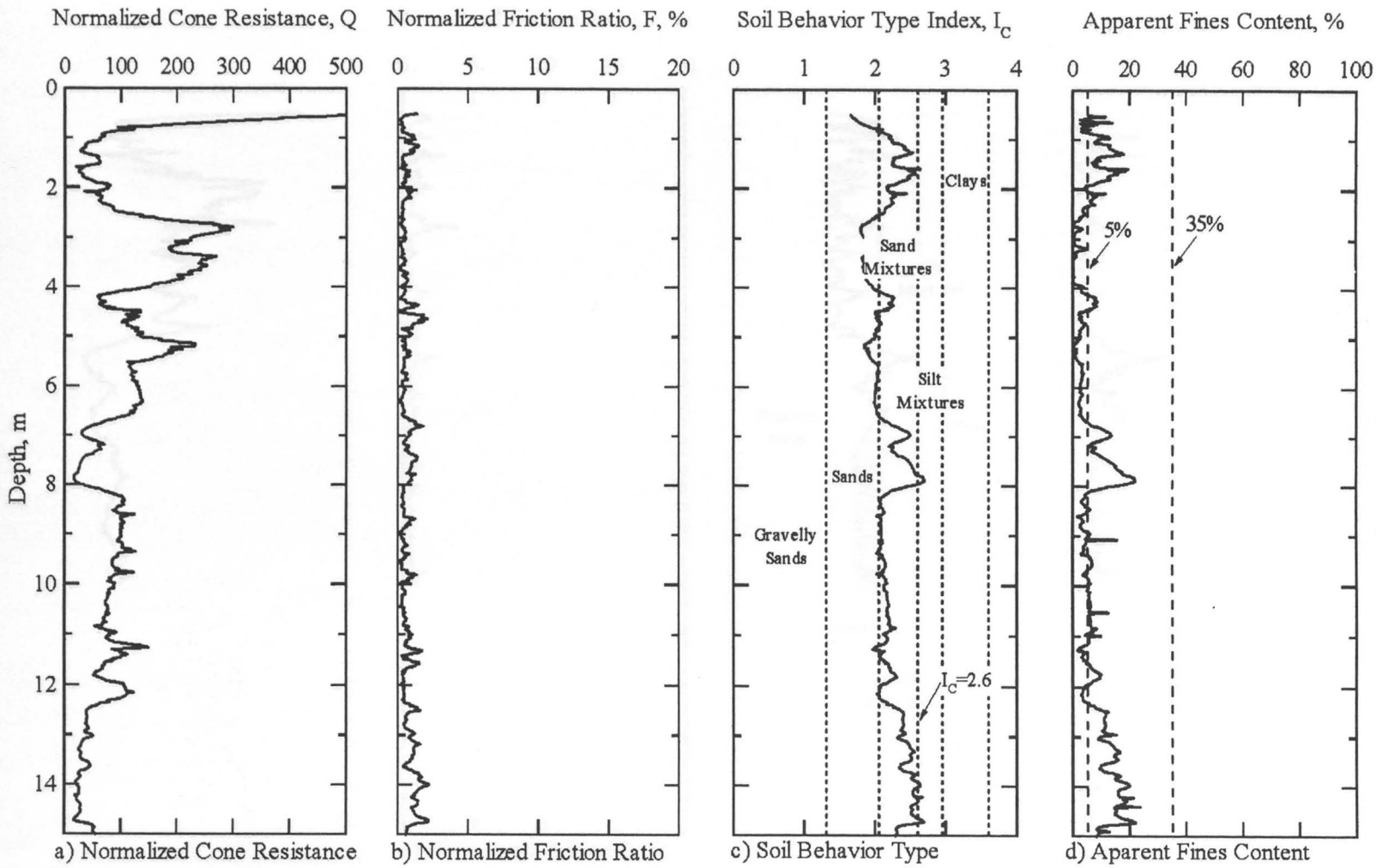

Figure 4.34 Graphs developed from CPT-SH4 to characterize the subsurface at Hotel Sapanca, Sapanca, Turkey (raw cone data from www.eerc.berkeley.edu/turkey/adapazari).

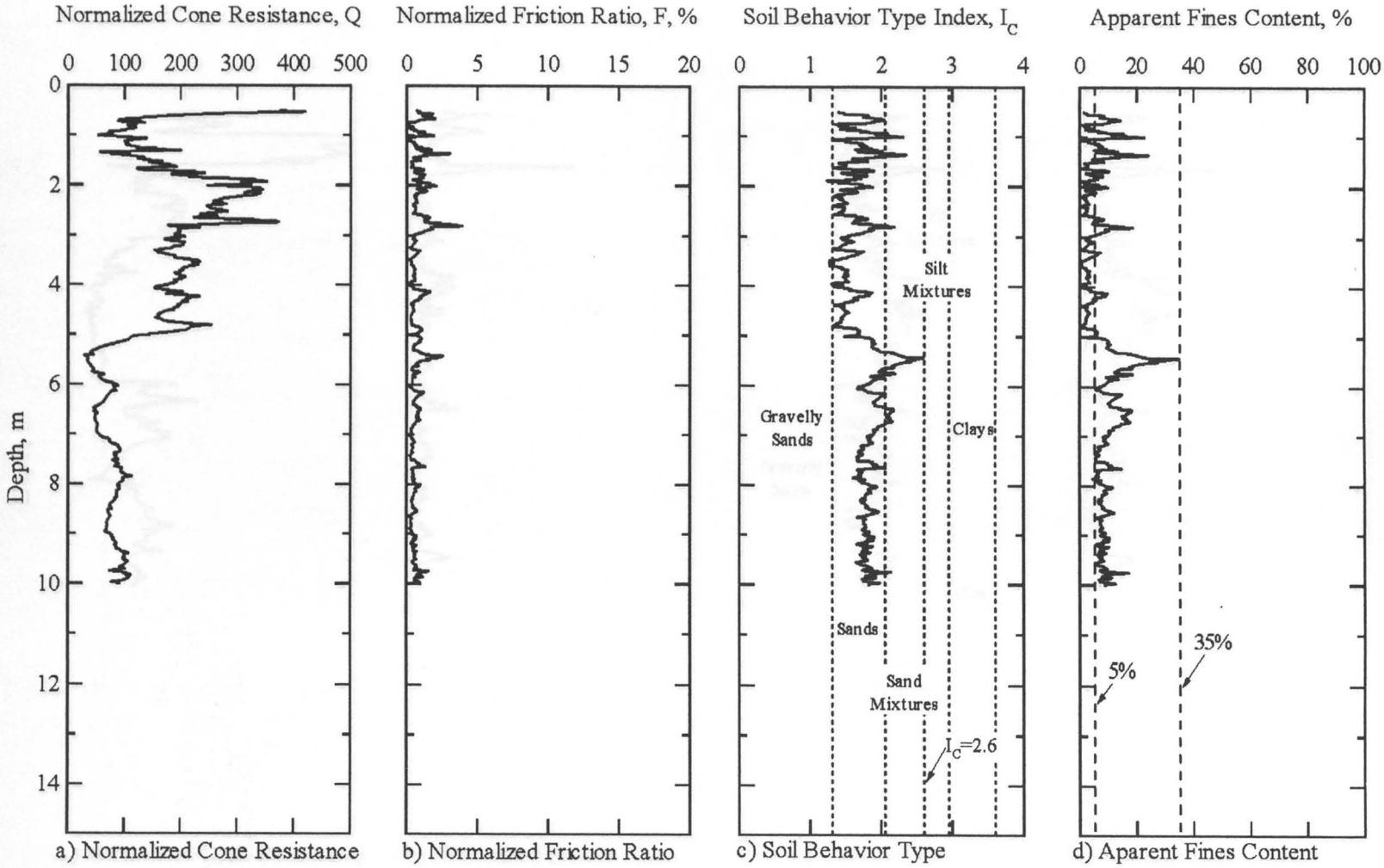

Figure 4.35 Graphs developed from CPT-SH5 to characterize the subsurface at Hotel Sapanca, Sapanca, Turkey (raw cone data from www.eerc.berkeley.edu/turkey/adapazari).

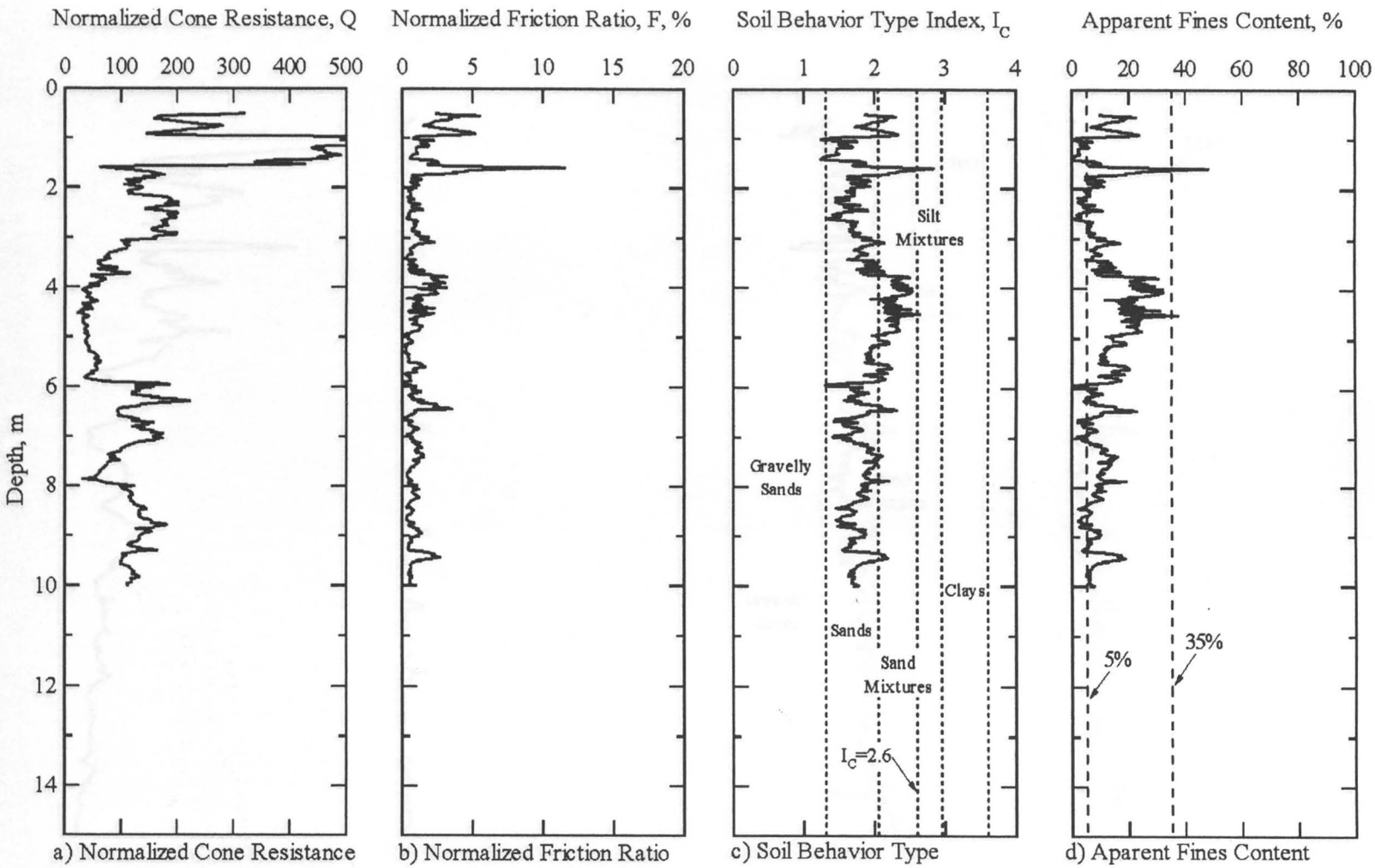

Figure 4.36 Graphs developed from CPT-SH6 to characterize the subsurface at Hotel Sapanca, Sapanca, Turkey (raw cone data from www.eerc.berkeley.edu/turkey/adapazari).

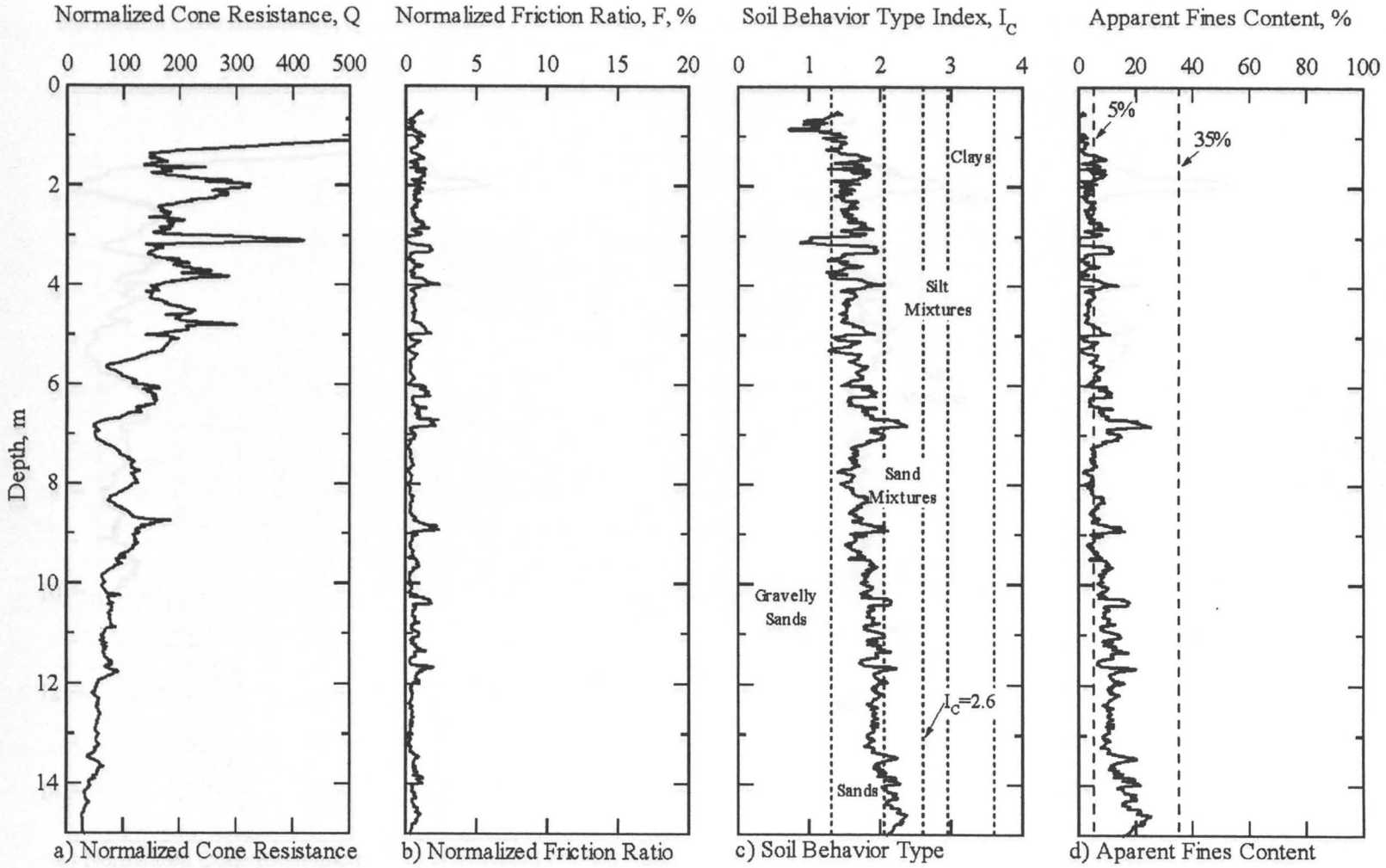

Figure 4.37 Graphs developed from CPT-SH7 to characterize the subsurface at Hotel Sapanca, Sapanca, Turkey (raw cone data from www.eerc.berkeley.edu/turkey/adapazari).

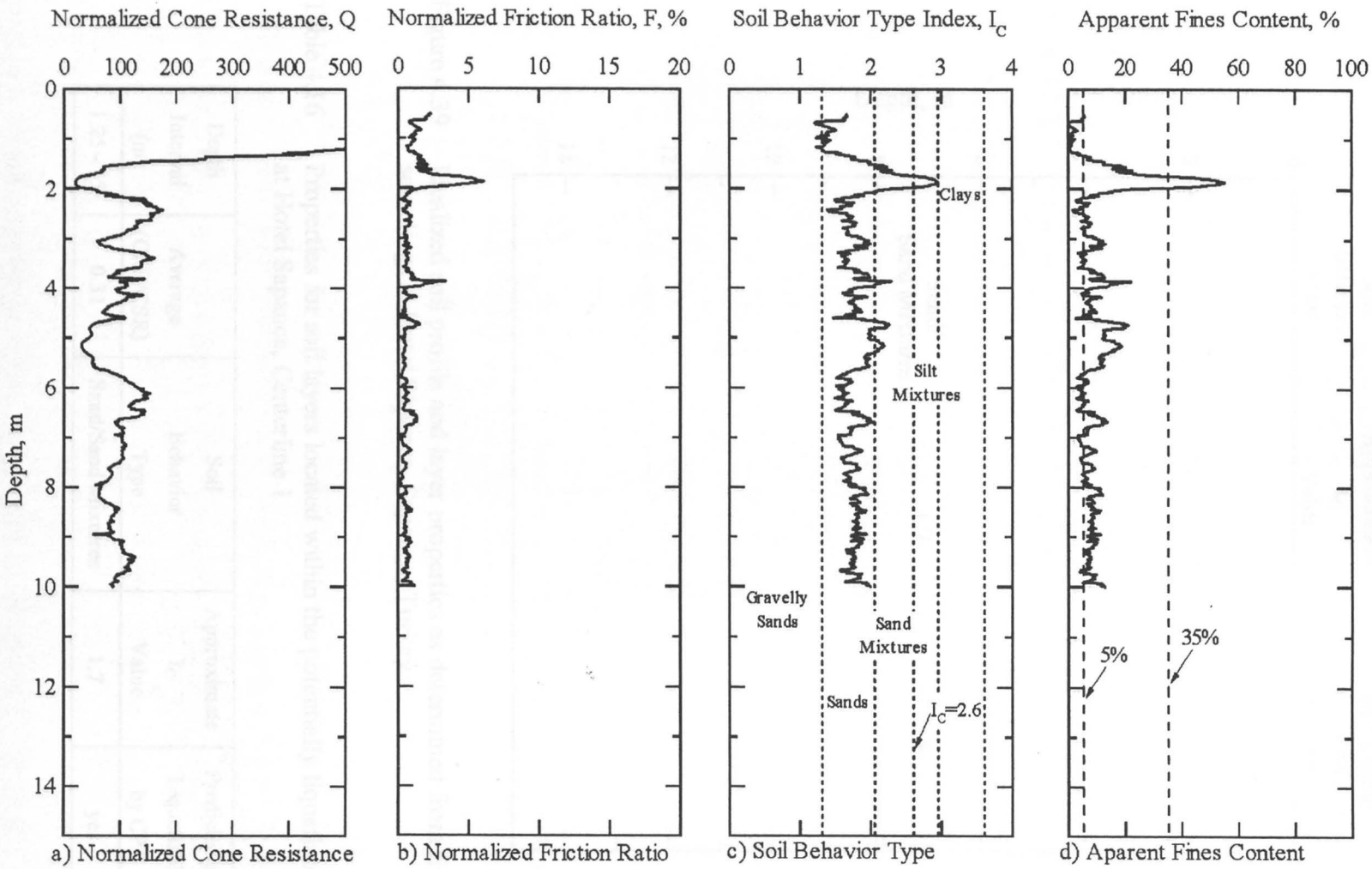

Figure 4.38 Graphs developed from CPT-SH8 to characterize the subsurface at Hotel Sapanca, Sapanca, Turkey (raw cone data from www.eerc.berkeley.edu/turkey/adapazari).

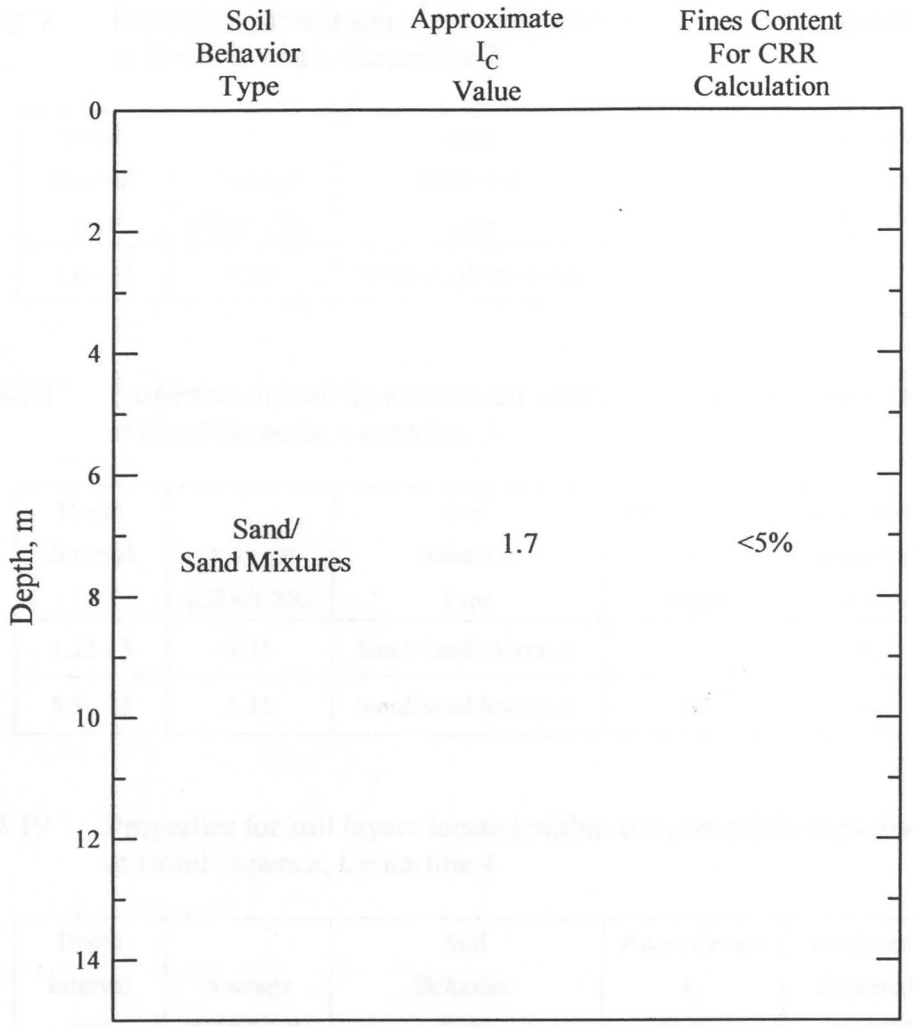

Figure 4.39 Idealized soil profile and layer properties as determined from five CPT soundings at Hotel Sapanca, Sapanca, Turkey.

Table 4.16 Properties for soil layers located within the potentially liquefiable region at Hotel Sapanca, Centerline 1

Depth Interval (m)	Average (CRR/CSR)	Soil Behavior Type	Approximate I_C Value	Predicted as Liquefiable by CPT
1.25 - 15	0.31	Sand/Sand Mixtures	1.7	yes

Table 4.17 Properties for soil layers located within the potentially liquefiable region at Hotel Sapanca, Centerline 2

Depth Interval (m)	Average (CRR/CSR)	Soil Behavior Type	Approximate I_C Value	Predicted as Liquefiable by CPT
1.6 - 15	0.36	Sand/Sand Mixtures	1.7	yes

Table 4.18 Properties for soil layers located within the potentially liquefiable region at Hotel Sapanca, Centerline 3

Depth Interval (m)	Average (CRR/CSR)	Soil Behavior Type	Approximate I_C Value	Predicted as Liquefiable by CPT
1.25 - 5	0.35	Sand/Sand Mixtures	1.7	yes
5.5 - 15	0.42	Sand/Sand Mixtures	1.7	yes

Table 4.19 Properties for soil layers located within the potentially liquefiable region at Hotel Sapanca, Centerline 4

Depth Interval (m)	Average (CRR/CSR)	Soil Behavior Type	Approximate I_C Value	Predicted as Liquefiable by CPT
.5 - 7	0.28	Sand/Sand Mixtures	1.7	yes

for the calculation of CRR's. Figure 4.40c shows the CRR of the soil along with three CSR profiles. The central profile represents the CSR generated using the most probable ground acceleration predicted for this site. The other two profiles result from bracketing this acceleration by +/- 0.05 g. From this graph it can be seen that the potentially liquefiable region only extends between the depths of 8 - 9 meters. Three CPT soundings were available at Degirmendere Nose. The graphs developed from CPT-DN1, to

characterize the subsurface, are shown in Figure 4.41. The graphs developed from CPT-DN2, to characterize the subsurface, are shown in Figure 4.42. The graphs developed from CPT-DN3, to characterize the subsurface, are shown in Figure 4.43. Figure 4.44 shows the idealized soil profile and layer properties at Degirmendere Nose as determined from combining the data from these three cone soundings.

Table 4.20 summarizes the data for the depth interval located within the potentially liquefiable region at Degirmendere Nose. The soil at the site is composed of sand/sand mixtures and would have been predicted to liquefy. All of the soil at this site, except for the 8 - 9 meter interval, is considered as too stiff to liquefy according to the simplified shear wave velocity evaluation. The largest and most devastating coastal stability failure from the Kocaeli earthquake occurred at this location (refer to Chapter 3). Certainly tectonic deformation and settlement also occurred here.

Police Station. The graphs developed for Police Station, to delineate potentially liquefiable soil using the shear wave velocity simplified procedure, are shown in Figure 4.45. Figure 4.45a shows the shear wave velocity profile (V_S) and the corrected shear wave velocity profile (V_{S1}) for the site. Figure 4.45b shows the fines content used for the calculation of CRR's in each layer. Figure 4.45c shows the CRR of the soil along with three CSR profiles. The central profile represents the CSR generated using the most probable ground acceleration predicted for this site. The other two profiles result from bracketing this acceleration by +/- 0.05 g. From this graph it can be seen that the potentially liquefiable region extends from a depth of 1.5 meters throughout the entire

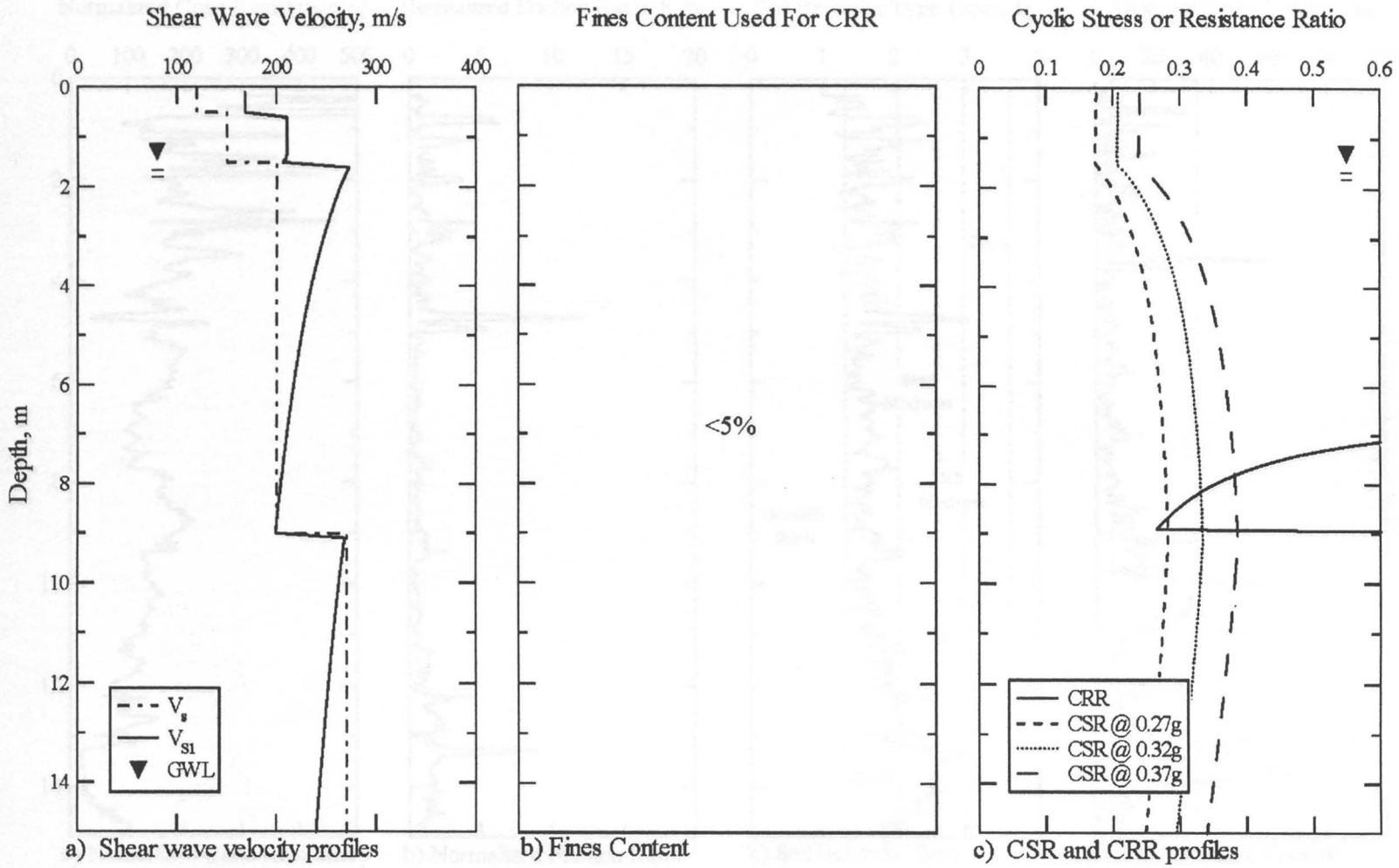

Figure 4.40 Graphs developed to delineate liquefiable soil using the simplified shear wave velocity procedure at Degirmendere Nose, Degirmendere, Turkey.

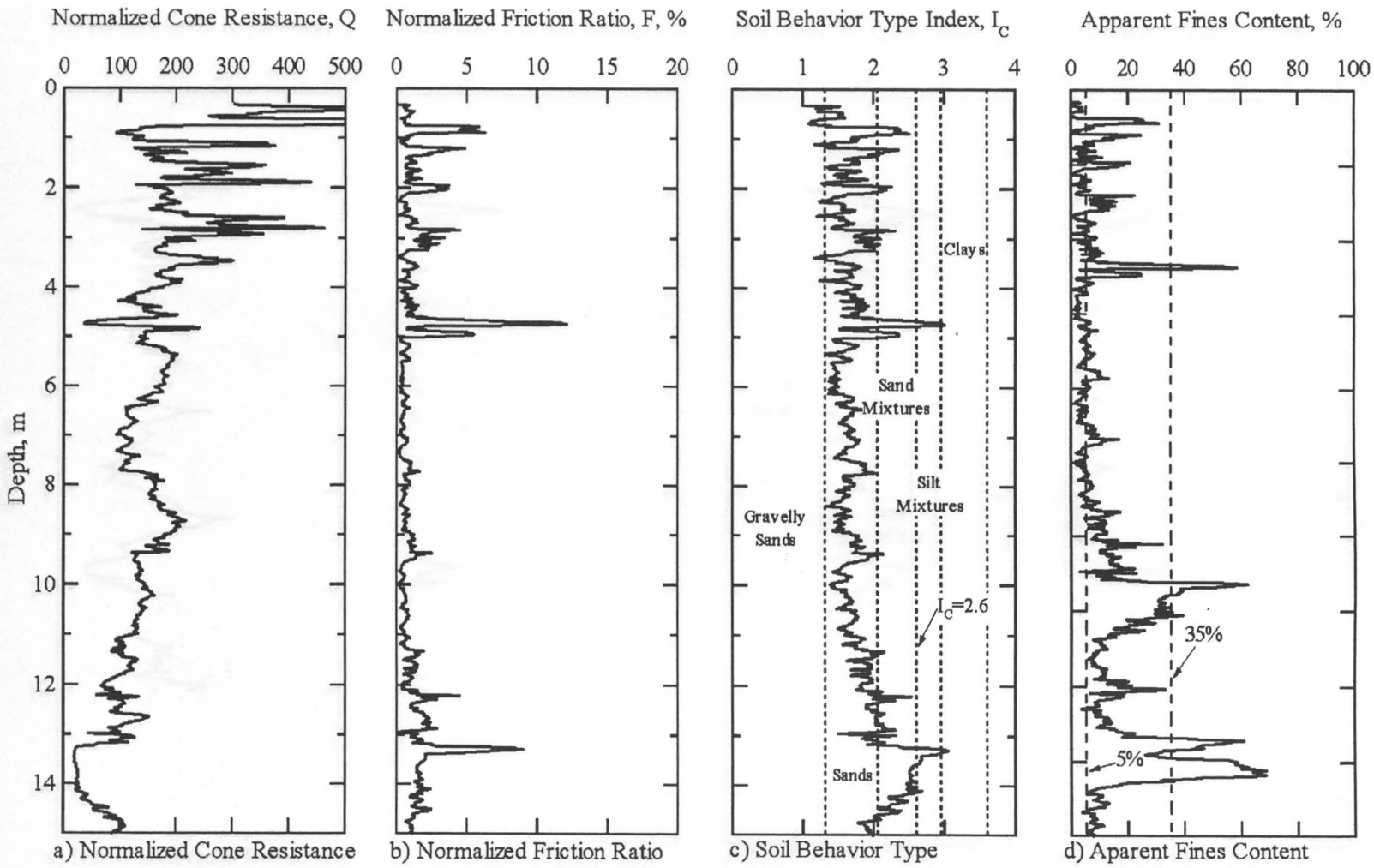

Figure 4.41 Graphs developed from CPT-DN1 to characterize the subsurface at Degirmendere Nose, Degirmendere, Turkey (raw cone data from www.eerc.berkeley.edu/turkey/adapazari).

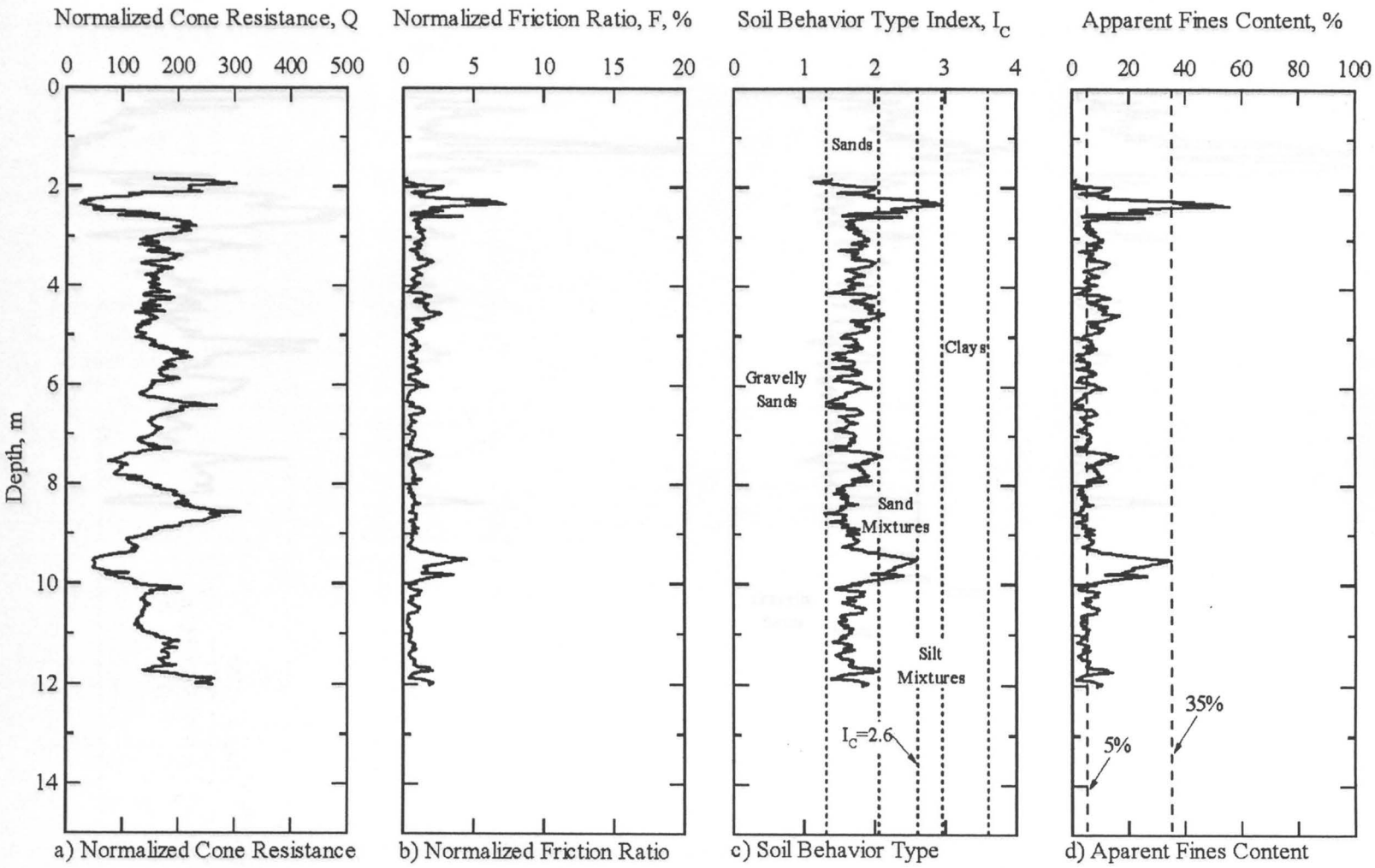

Figure 4.42 Graphs developed from CPT-DN2 to characterize the subsurface at Degirmendere Nose, Degirmendere, Turkey (raw cone data from www.eerc.berkeley.edu/turkey/adapazari).

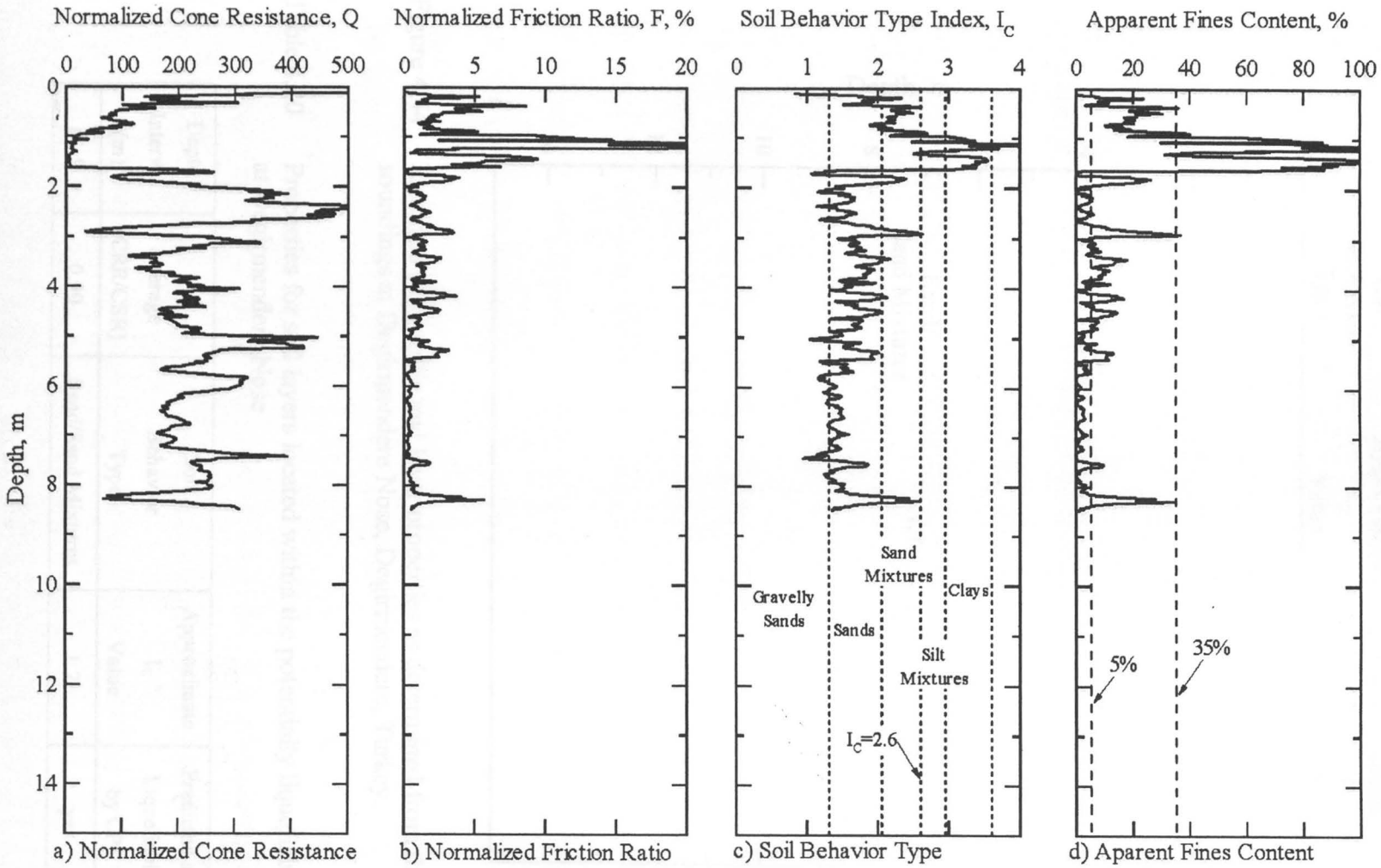

Figure 4.43 Graphs developed from CPT-DN3 to characterize the subsurface at Degirmendere Nose, Degirmendere, Turkey (raw cone data from www.eerc.berkeley.edu/turkey/adapazari).

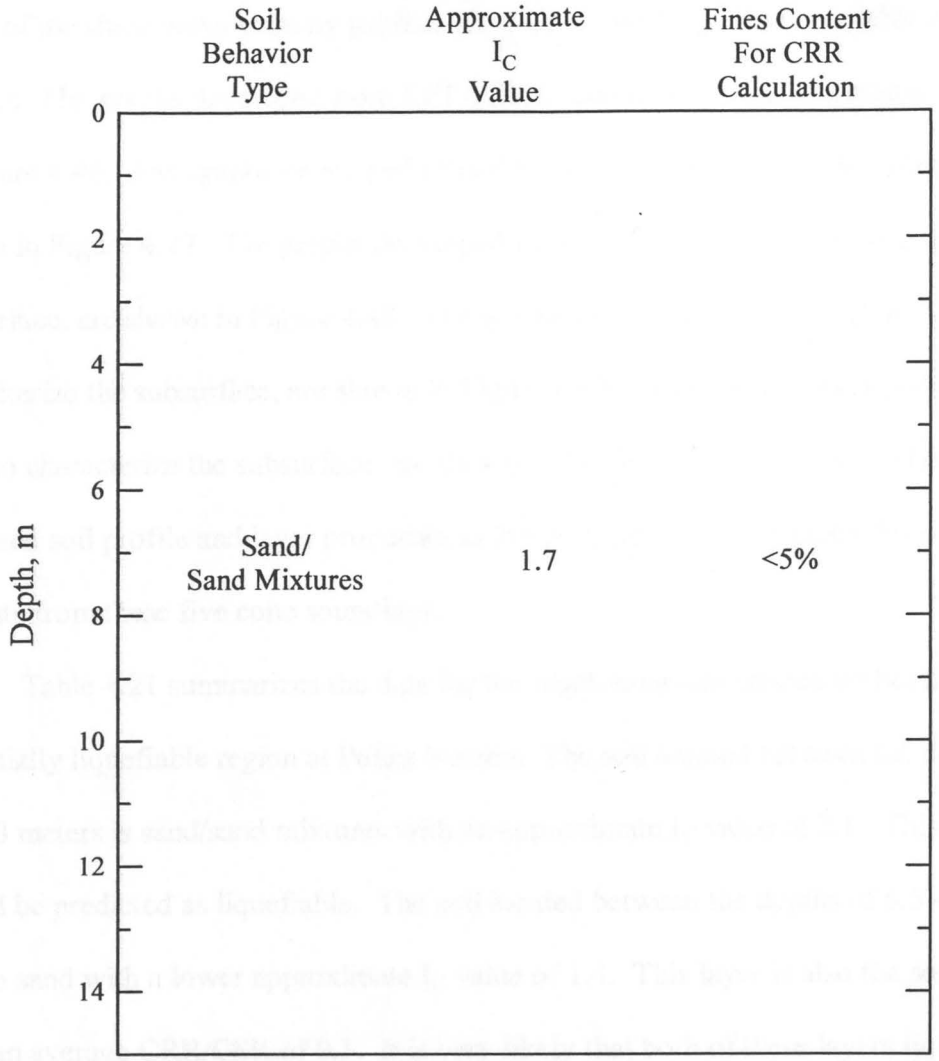

Figure 4.44 Idealized soil profile and layer properties as determined from three CPT soundings at Degirmendere Nose, Degirmendere, Turkey.

Table 4.20 Properties for soil layers located within the potentially liquefiable region at Degirmendere Nose

Depth Interval (m)	Average (CRR/CSR)	Soil Behavior Type	Approximate I_C Value	Predicted as Liquefiable by CPT
8 - 9	0.90	Sand/Sand Mixtures	1.7	yes

depth of the shear wave velocity profile. Five CPT soundings were available at Police Station. The graphs developed from CPT-PS1, to characterize the subsurface, are shown in Figure 4.46. The graphs developed from CPT-PS2, to characterize the subsurface, are shown in Figure 4.47. The graphs developed from CPT-PS3, to characterize the subsurface, are shown in Figure 4.48. The graphs developed from CPT-PS4, to characterize the subsurface, are shown in Figure 4.49. The graphs developed from CPT-PS5, to characterize the subsurface, are shown in Figure 4.50. Figure 4.51 shows the idealized soil profile and layer properties at Police Station as determined from combining the data from these five cone soundings.

Table 4.21 summarizes the data for the depth intervals located within the potentially liquefiable region at Police Station. The soil located between the depths of 1.5 - 3 meters is sand/sand mixtures with an approximate I_C value of 2.1. This layer would be predicted as liquefiable. The soil located between the depths of 6.5 - 8 meters is also sand with a lower approximate I_C value of 1.4. This layer is also the softest layer with an average CRR/CSR of 0.1. It is very likely that both of these layers liquefied during the earthquake, inducing the lateral spreading that occurred here. All of the other depth intervals at this site have I_C values greater than 2.6 and are considered as nonliquefiable.

Soccer Field. The graphs developed for Soccer Field, to delineate potentially liquefiable soil using the shear wave velocity simplified procedure, are shown in Figure 4.52. Figure 4.52a shows the shear wave velocity profile (V_S) and the corrected shear wave velocity profile (V_{S1}) for the site. Figure 4.52b shows the fines content used for the

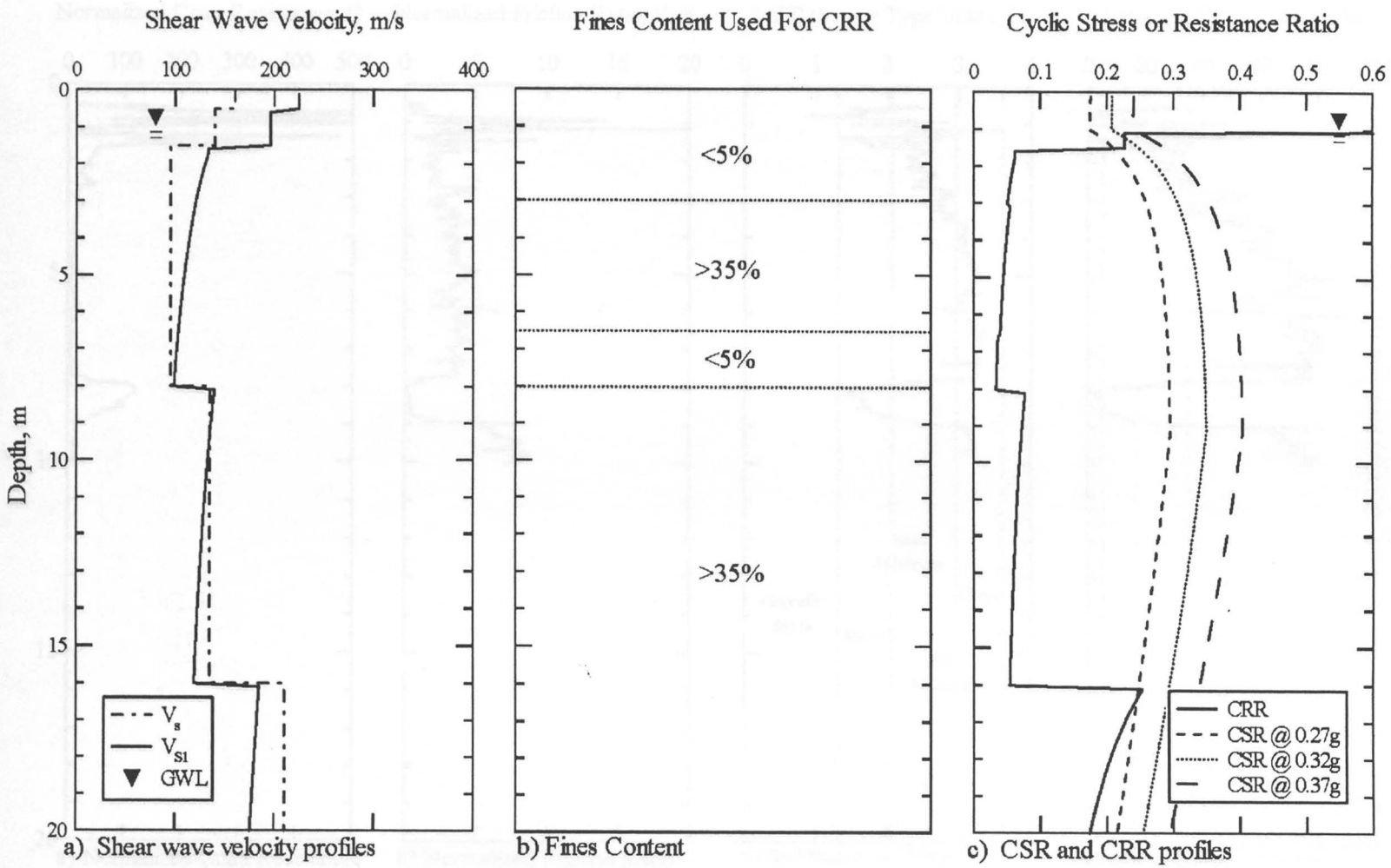

Figure 4.45 Graphs developed to delineate liquefiable soil using the simplified shear wave velocity procedure at Police Station, Golcuk, Turkey.

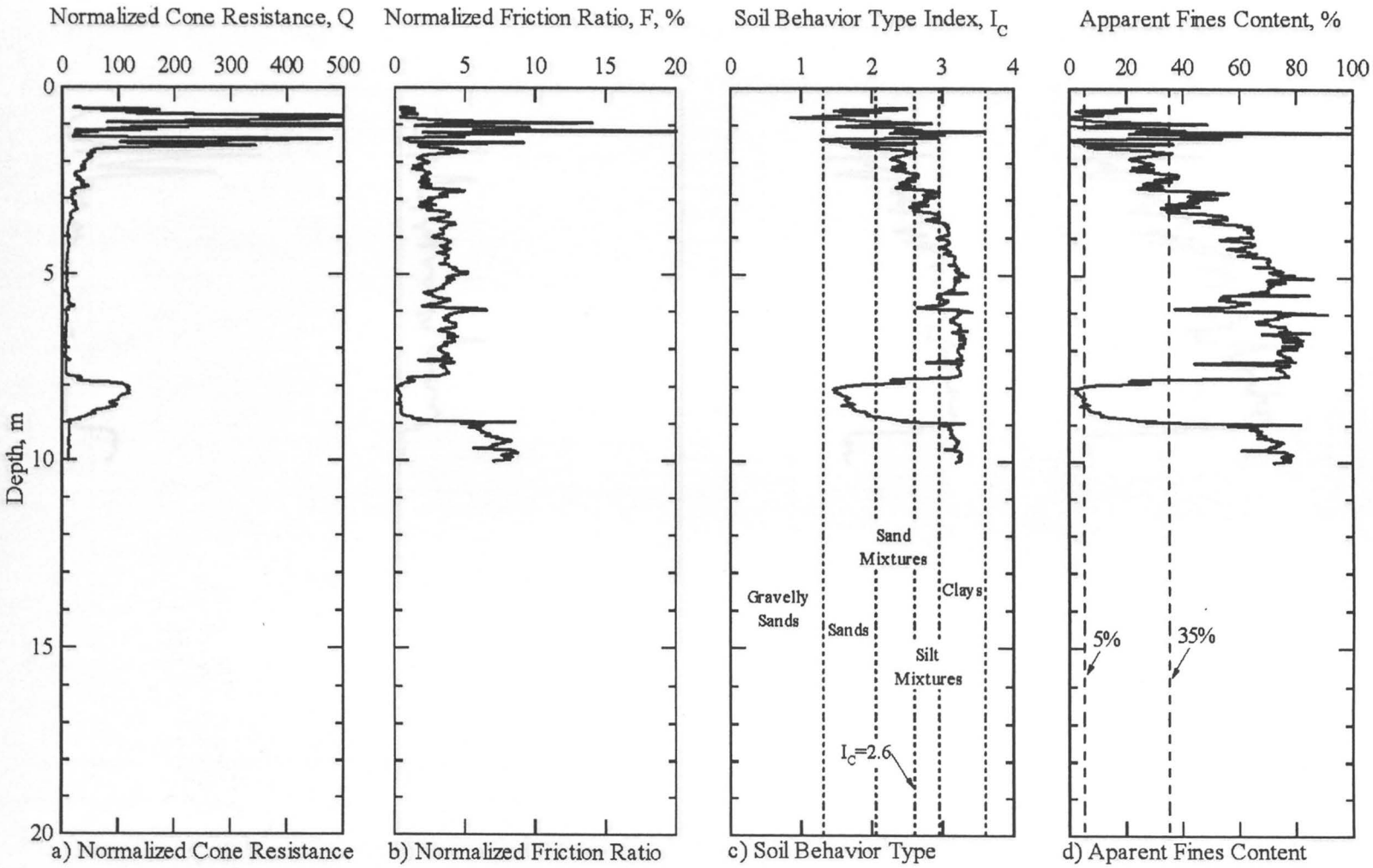

Figure 4.46 Graphs developed from CPT-PS1 to characterize the subsurface at Police Station, Golcuk, Turkey (raw cone data from www.eerc.berkeley.edu/turkey/adapazari).

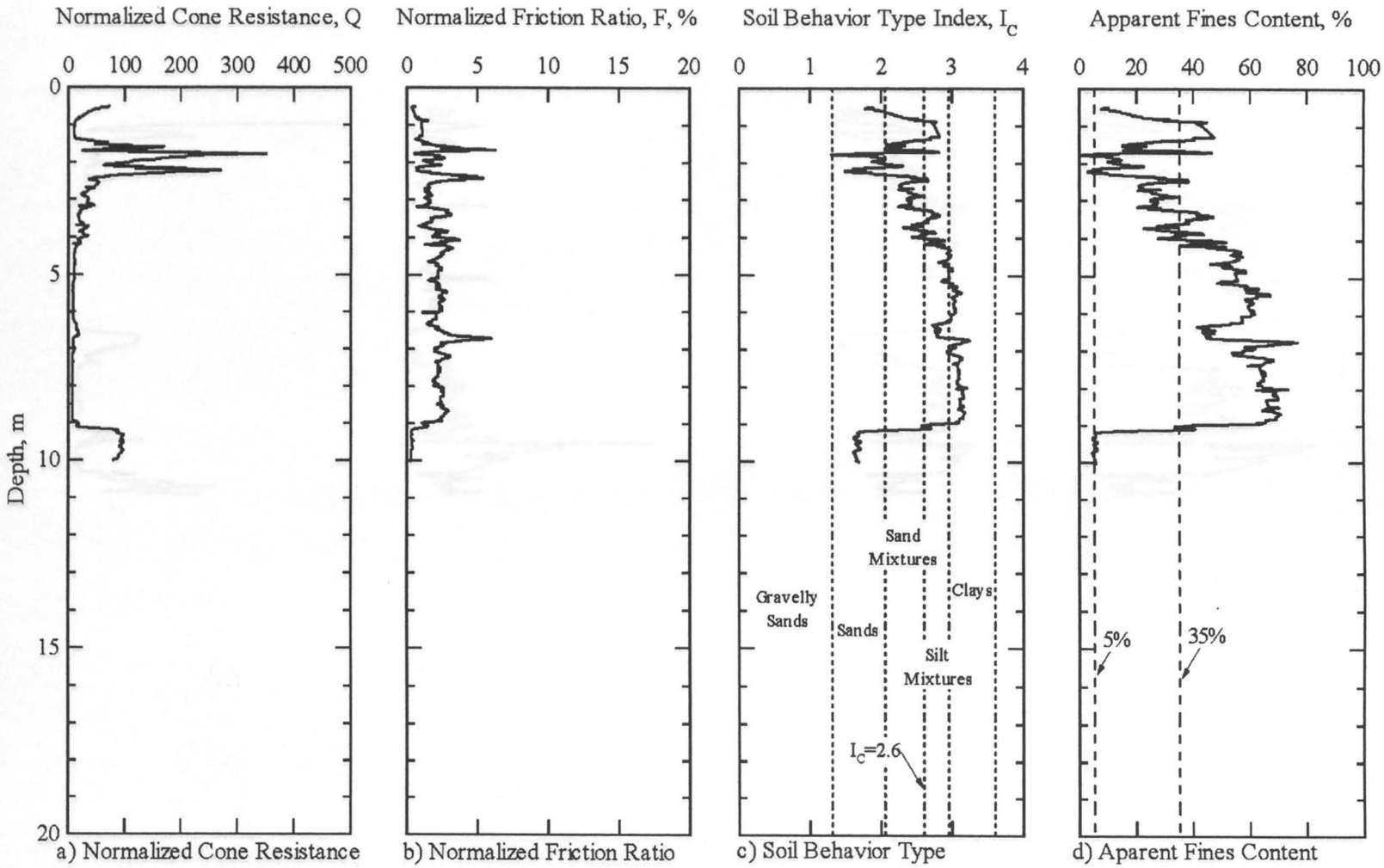

Figure 4.47 Graphs developed from CPT-PS2 to characterize the subsurface at Police Station, Golcuk, Turkey (raw cone data from www.eerc.berkeley.edu/turkey/adapazari).

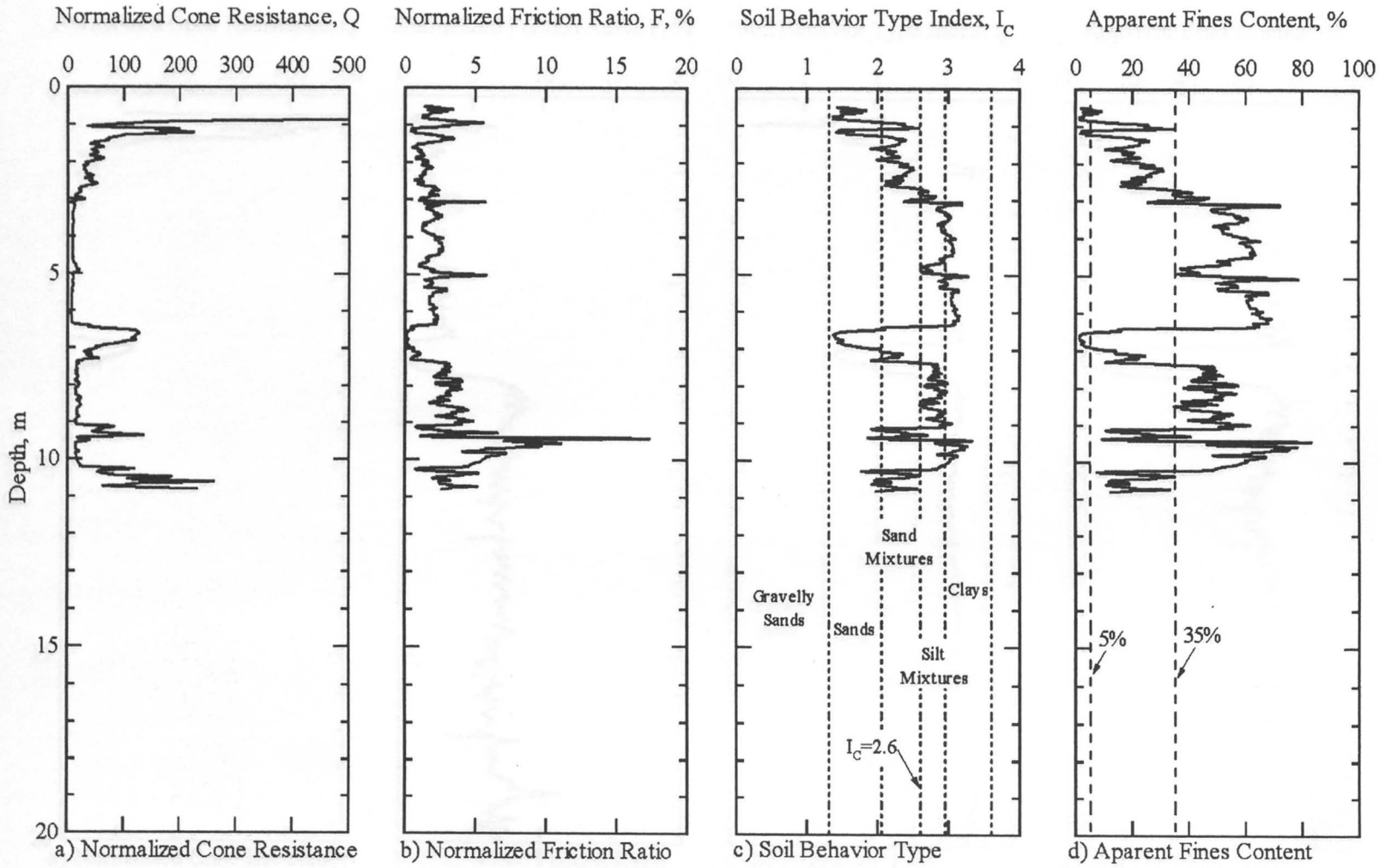

Figure 4.48 Graphs developed from CPT-PS3 to characterize the subsurface at Police Station, Golcuk, Turkey (raw cone data from www.eerc.berkeley.edu/turkey/adapazari).

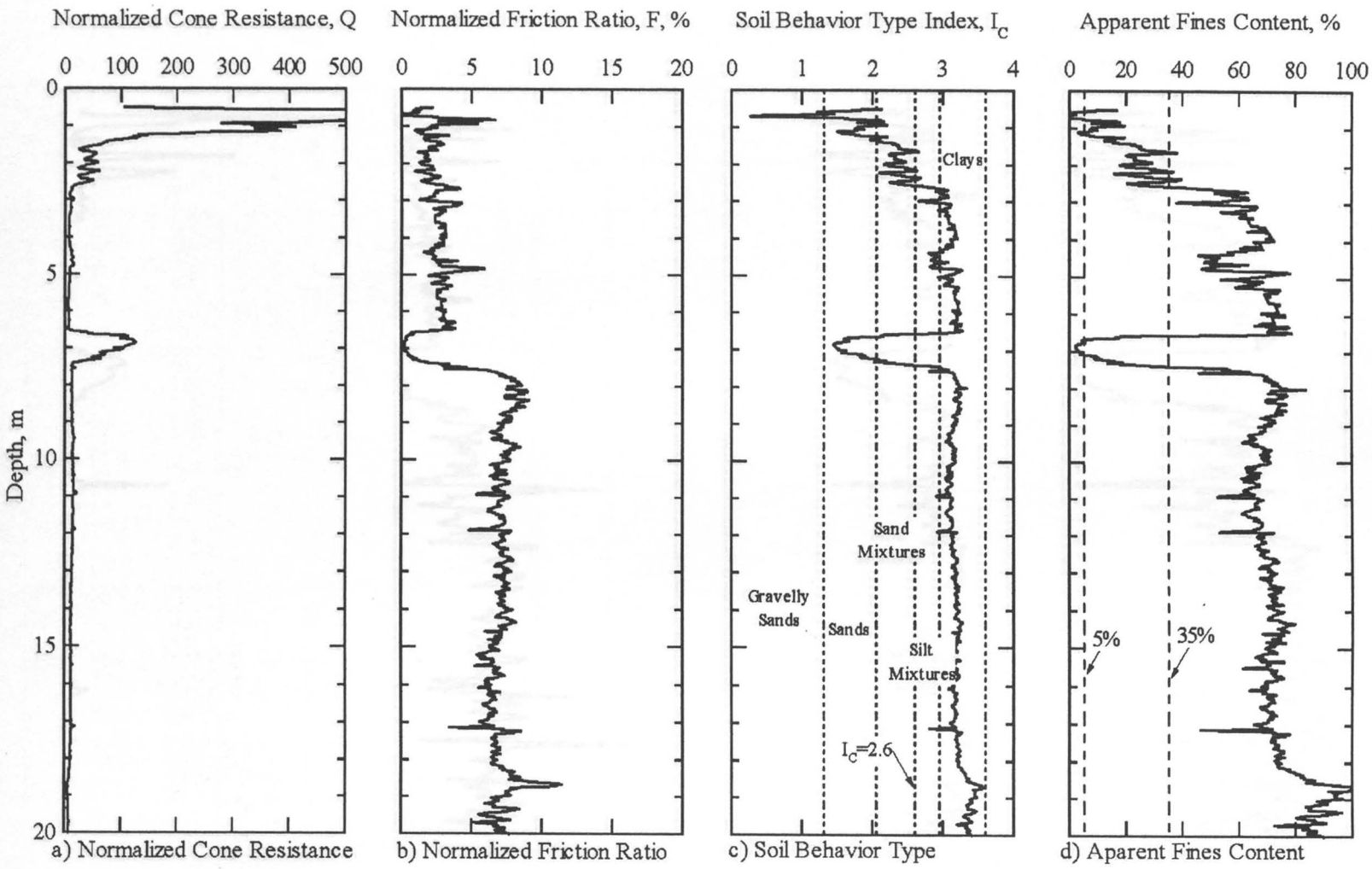

Figure 4.49 Graphs developed from CPT-PS4 to characterize the subsurface at Police Station, Golcuk, Turkey (raw cone data from www.eerc.berkeley.edu/turkey/adapazari).

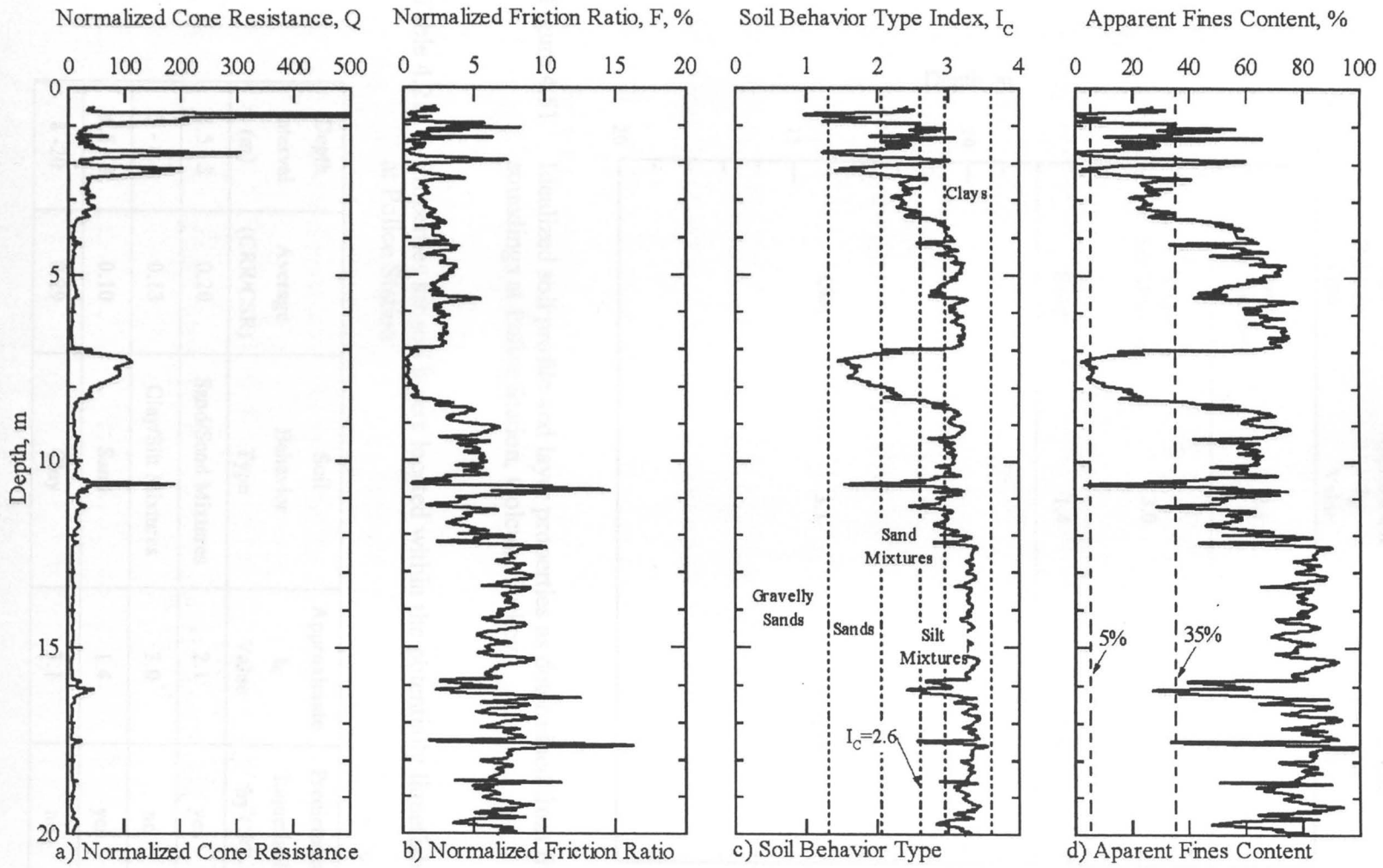

Figure 4.50 Graphs developed from CPT-PS5 to characterize the subsurface at Police Station, Golcuk, Turkey (raw cone data from www.eerc.berkeley.edu/turkey/adapazari).

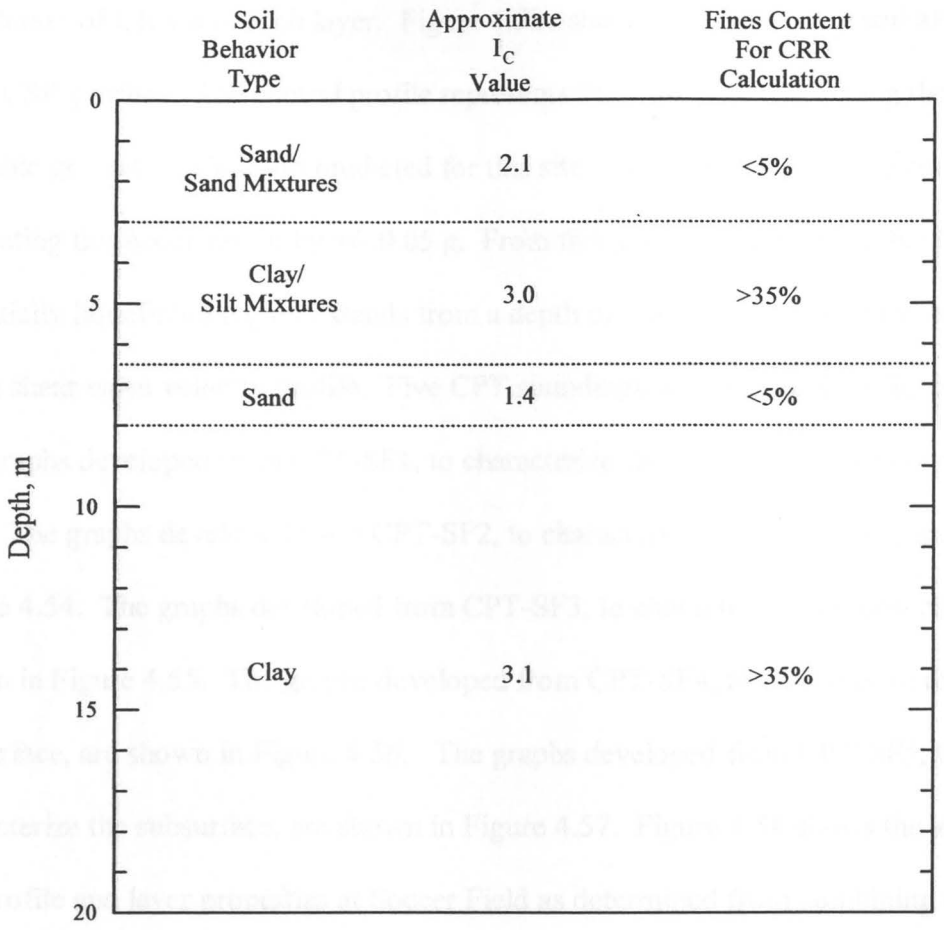

Figure 4.51 Idealized soil profile and layer properties as determined from five CPT soundings at Police Station, Golcuk, Turkey.

Table 4.21 Properties for soil layers located within the potentially liquefiable region at Police Station

Depth Interval (m)	Average (CRR/CSR)	Soil Behavior Type	Approximate I_C Value	Predicted as Liquefiable by CPT
1.5 - 3	0.20	Sand/Sand Mixtures	2.1	yes
3 - 6.5	0.13	Clay/Silt Mixtures	3.0	no
6.5 - 8	0.10	Sand	1.4	yes
8 -20	0.29	Clay	3.1	no

calculation of CRR's in each layer. Figure 4.52c shows the CRR of the soil along with three CSR profiles. The central profile represents the CSR generated using the most probable ground acceleration predicted for this site. The other two profiles result from bracketing this acceleration by +/- 0.05 g. From this graph it can be seen that the potentially liquefiable region extends from a depth of 1 meter throughout the entire depth of the shear wave velocity profile. Five CPT soundings were available at Soccer Field. The graphs developed from CPT-SF1, to characterize the subsurface, are shown in Figure 4.53. The graphs developed from CPT-SF2, to characterize the subsurface, are shown in Figure 4.54. The graphs developed from CPT-SF3, to characterize the subsurface, are shown in Figure 4.55. The graphs developed from CPT-SF4, to characterize the subsurface, are shown in Figure 4.56. The graphs developed from CPT-SF5, to characterize the subsurface, are shown in Figure 4.57. Figure 4.58 shows the idealized soil profile and layer properties at Soccer Field as determined from combining the data from these five cone soundings.

Table 4.22 summarizes the data for the depth intervals located within the potentially liquefiable region at Soccer Field. The soil located between the depths of 1 - 3 meters is sand/sand mixtures with an approximate I_C value of 2.3. This layer would be predicted as liquefiable and is the one most likely to have liquefied and induced the lateral spreading at this site. The remainder of the profile is extremely soft with an average CRR/CSR of 0.09. However, it is unlikely that this clayey material would have liquefied.

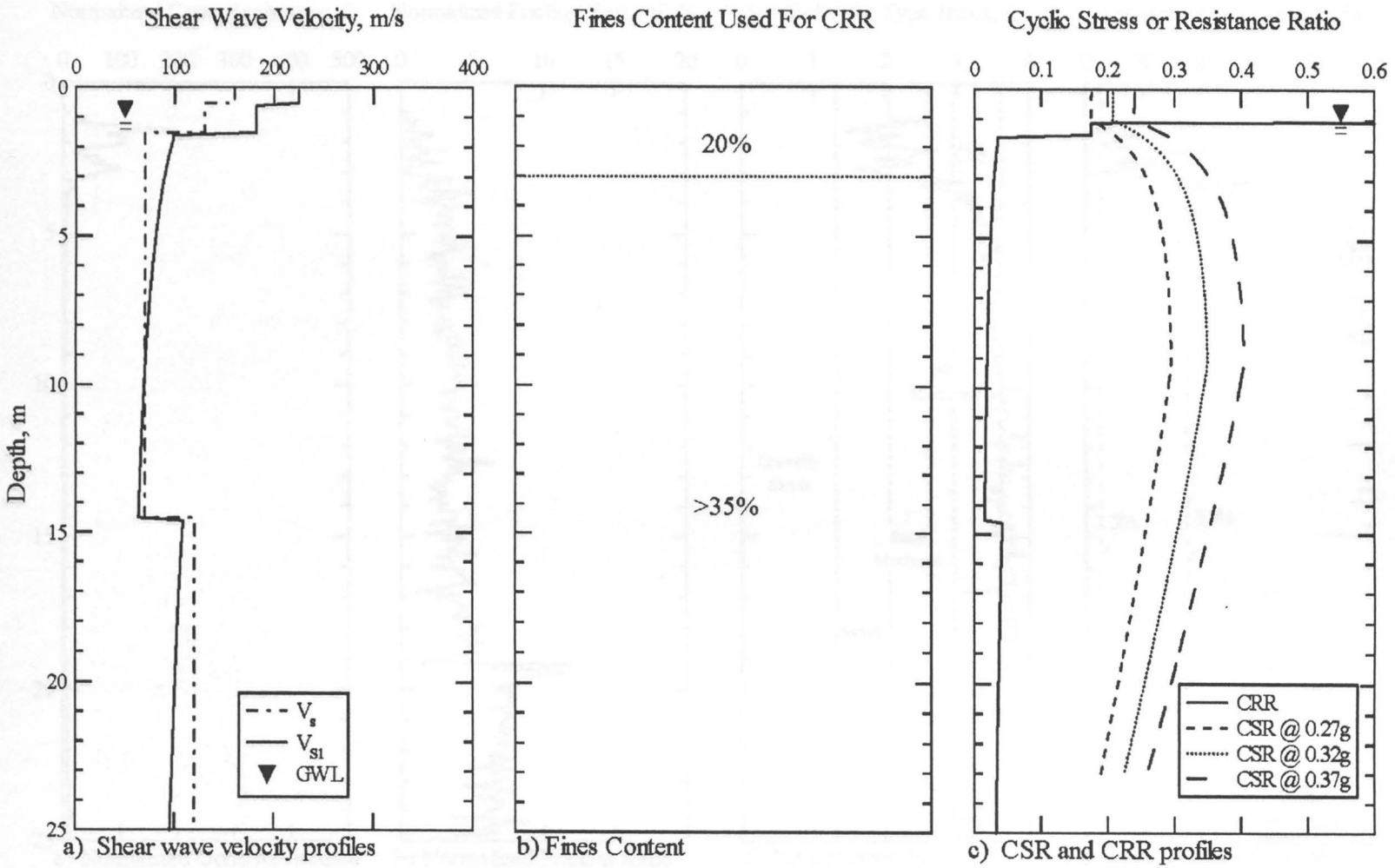

Figure 4.52 Graphs developed to delineate liquefiable soil using the simplified shear wave velocity procedure at Soccer Field, Golcuk, Turkey.

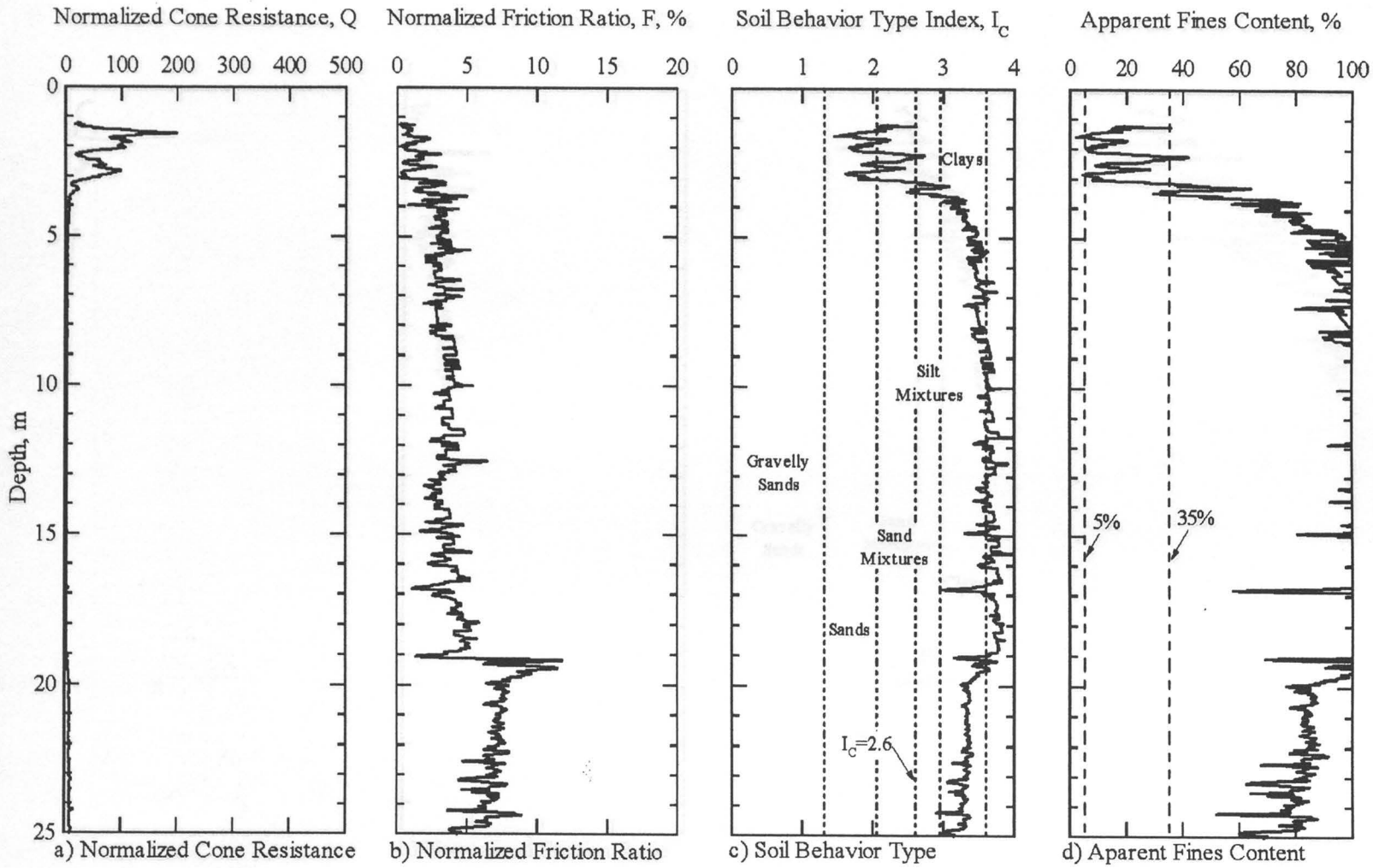

Figure 4.53 Graphs developed from CPT-SF1 to characterize the subsurface at Soccer Field, Golcuk, Turkey (raw cone data from www.eerc.berkeley.edu/turkey/adapazari).

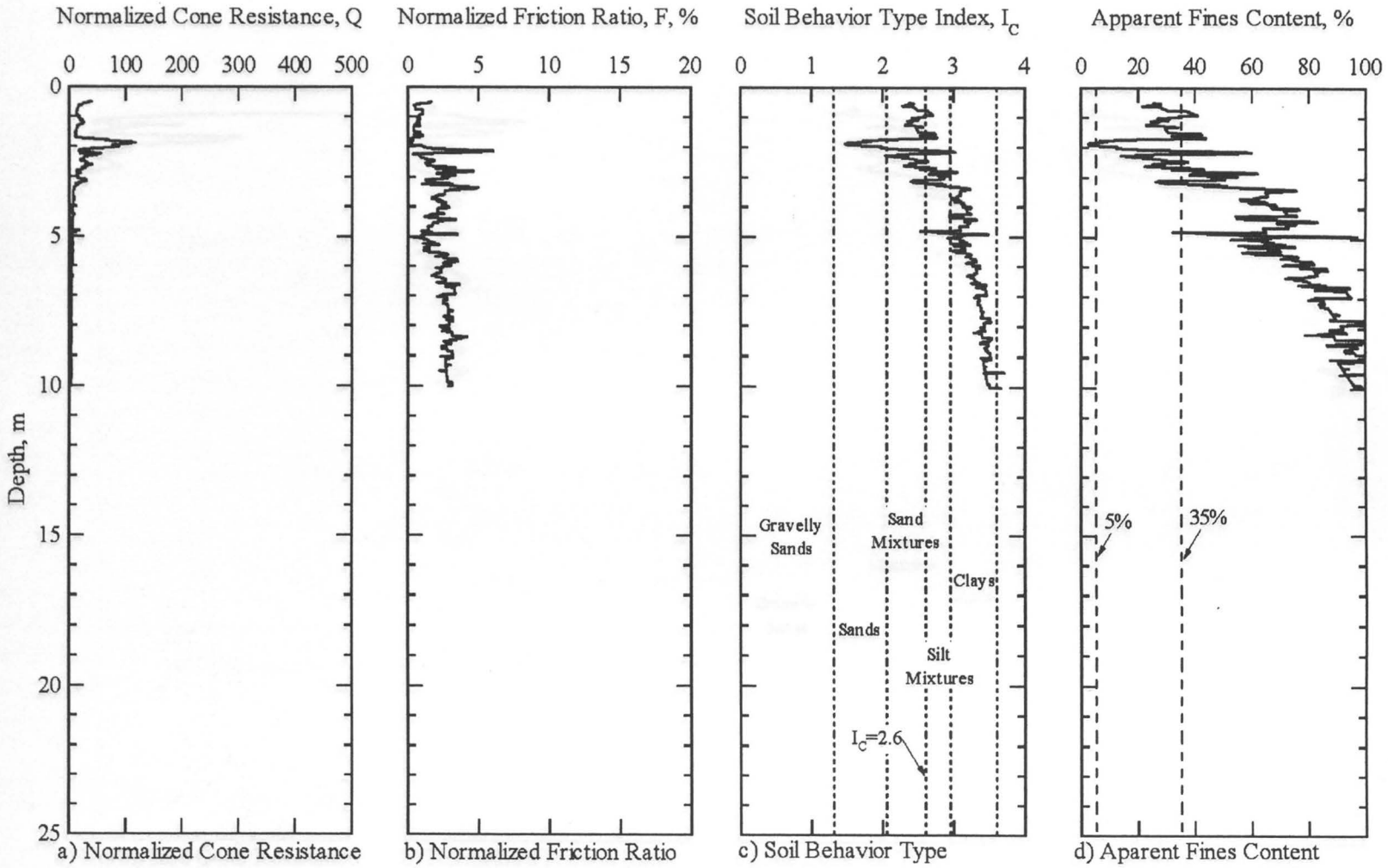

Figure 4.54 Graphs developed from CPT-SF2 to characterize the subsurface at Soccer Field, Golcuk, Turkey (raw cone data from www.eerc.berkeley.edu/turkey/adapazari).

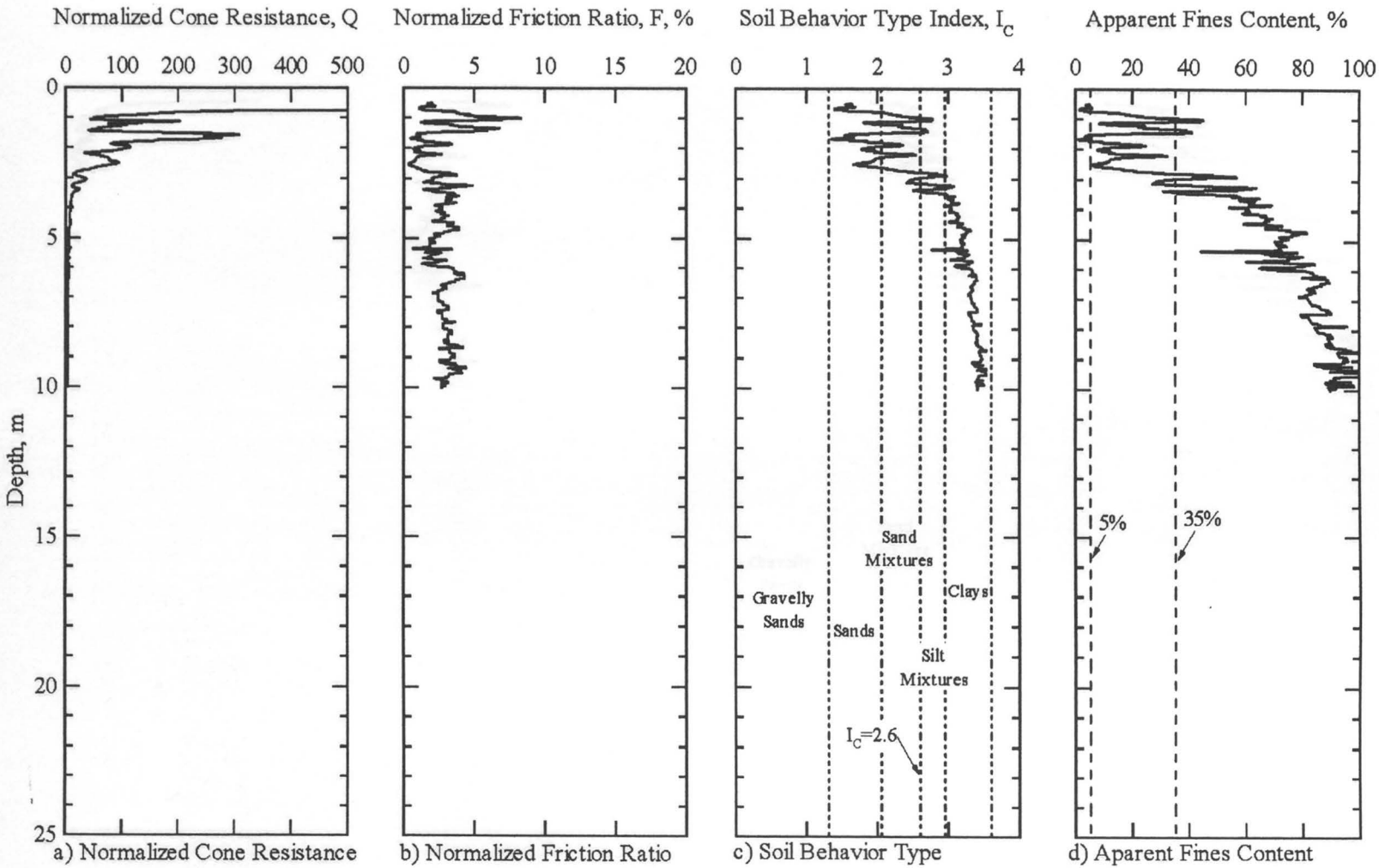

Figure 4.55 Graphs developed from CPT-SF3 to characterize the subsurface at Soccer Field, Golcuk, Turkey (raw cone data from www.eerc.berkeley.edu/turkey/adapazari).

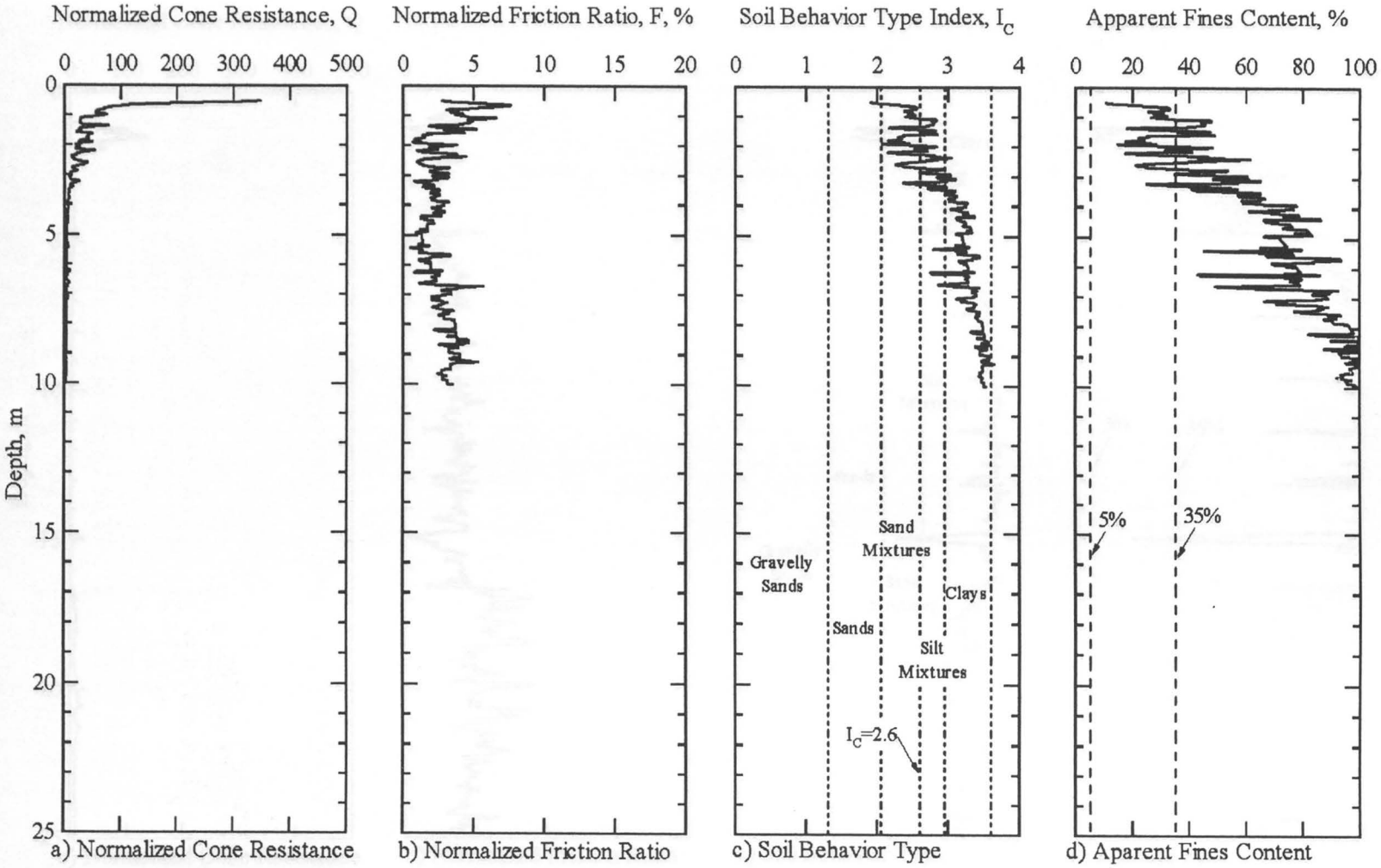

Figure 4.56 Graphs developed from CPT-SF4 to characterize the subsurface at Soccer Field, Golcuk, Turkey (raw cone data from www.eerc.berkeley.edu/turkey/adapazari).

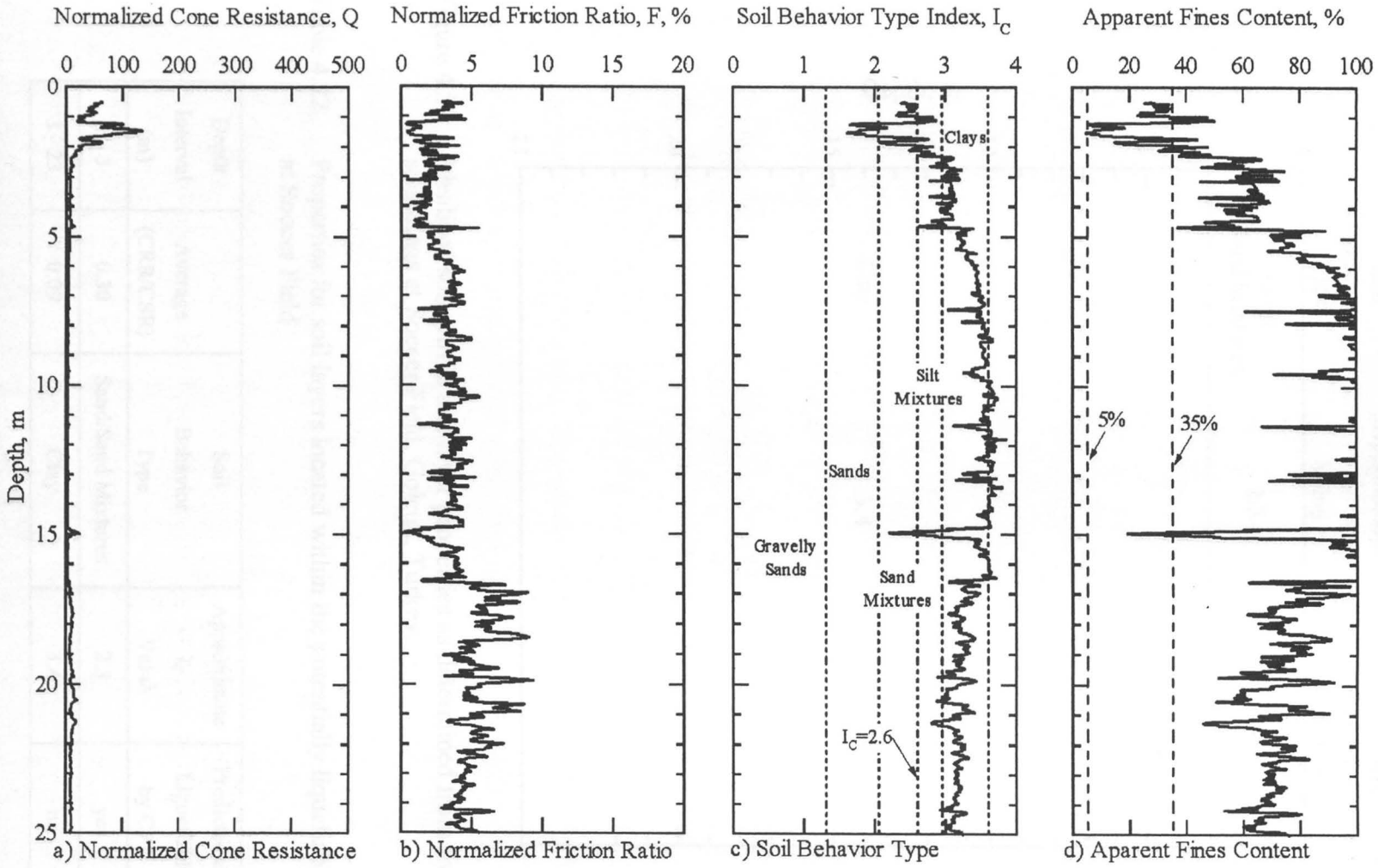

Figure 4.57 Graphs developed from CPT-SF5 to characterize the subsurface at Soccer Field, Golcuk, Turkey (raw cone data from www.eerc.berkeley.edu/turkey/adapazari).

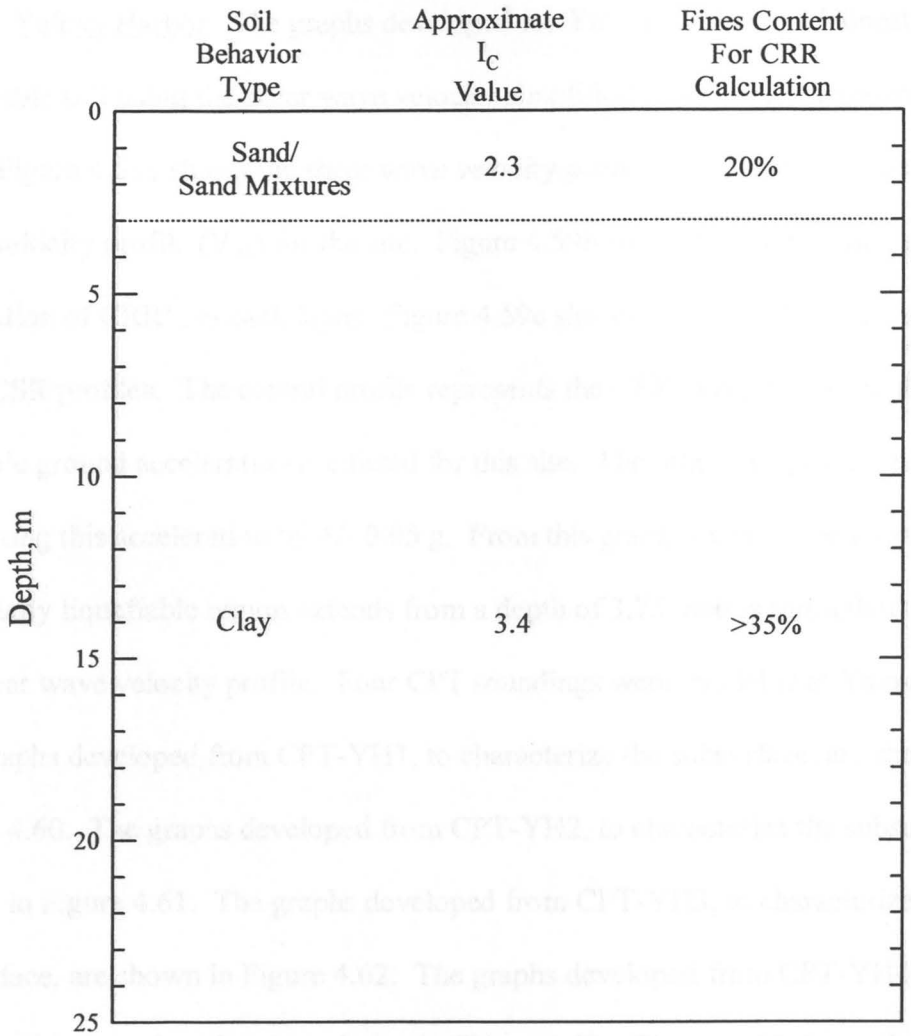

Figure 4.58 Idealized soil profile and layer properties as determined from five CPT soundings at Soccer Field, Golcuk, Turkey.

Table 4.22 Properties for soil layers located within the potentially liquefiable region at Soccer Field

Depth Interval (m)	Average (CRR/CSR)	Soil Behavior Type	Approximate I_C Value	Predicted as Liquefiable by CPT
1 - 3	0.30	Sand/Sand Mixtures	2.3	yes
3 - 23	0.09	Clay	3.4	no

Yalova Harbor. The graphs developed for Yalova Harbor, to delineate potentially liquefiable soil using the shear wave velocity simplified procedure, are shown in Figure 4.59. Figure 4.59a shows the shear wave velocity profile (V_S) and the corrected shear wave velocity profile (V_{S1}) for the site. Figure 4.59b shows the fines content used for the calculation of CRR's in each layer. Figure 4.59c shows the CRR of the soil along with three CSR profiles. The central profile represents the CSR generated using the most probable ground acceleration predicted for this site. The other two profiles result from bracketing this acceleration by +/- 0.05 g. From this graph it can be seen that the potentially liquefiable region extends from a depth of 3.75 meters throughout the rest of the shear wave velocity profile. Four CPT soundings were available at Yalova Harbor. The graphs developed from CPT-YH1, to characterize the subsurface, are shown in Figure 4.60. The graphs developed from CPT-YH2, to characterize the subsurface, are shown in Figure 4.61. The graphs developed from CPT-YH3, to characterize the subsurface, are shown in Figure 4.62. The graphs developed from CPT-YH4, to characterize the subsurface, are shown in Figure 4.63. Figure 4.64 shows the idealized soil profile and layer properties at Yalova Harbor as determined from combining the data from these four cone soundings.

Table 4.23 summarizes the data for the depth intervals located within the potentially liquefiable region at Yalova Harbor. The soil located between the depths of 3 - 8 meters is sand/sand mixtures with an approximate I_C value of 1.8. This layer would be predicted as liquefiable and is the one most likely to have liquefied and induced the lateral spreading at this site. The remainder of the profile is clay/silt mixtures that would be predicted as unlikely to have liquefied.

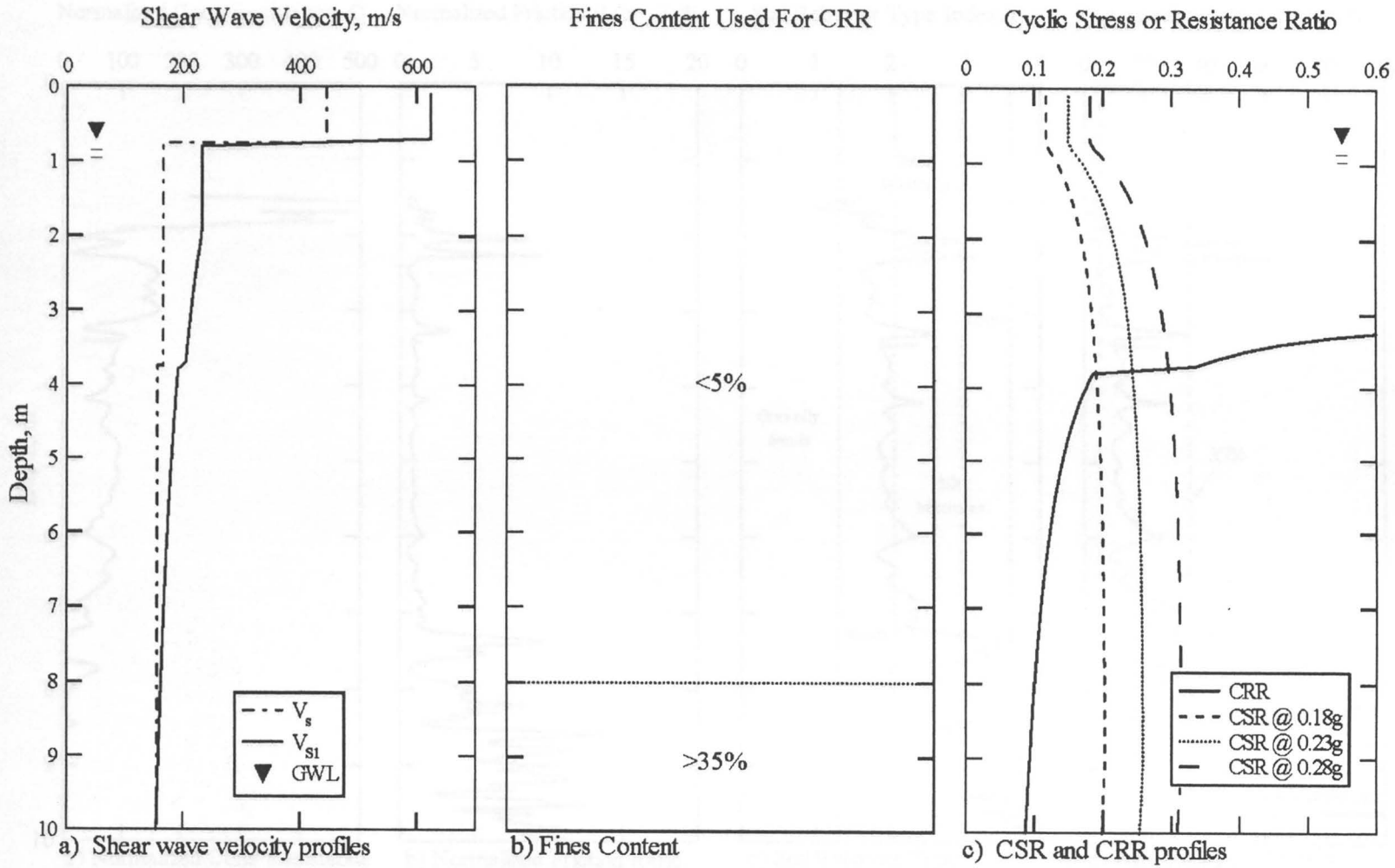

Figure 4.59 Graphs developed to delineate liquefiable soil using the simplified shear wave velocity procedure at Yalova Harbor, Yalova, Turkey.

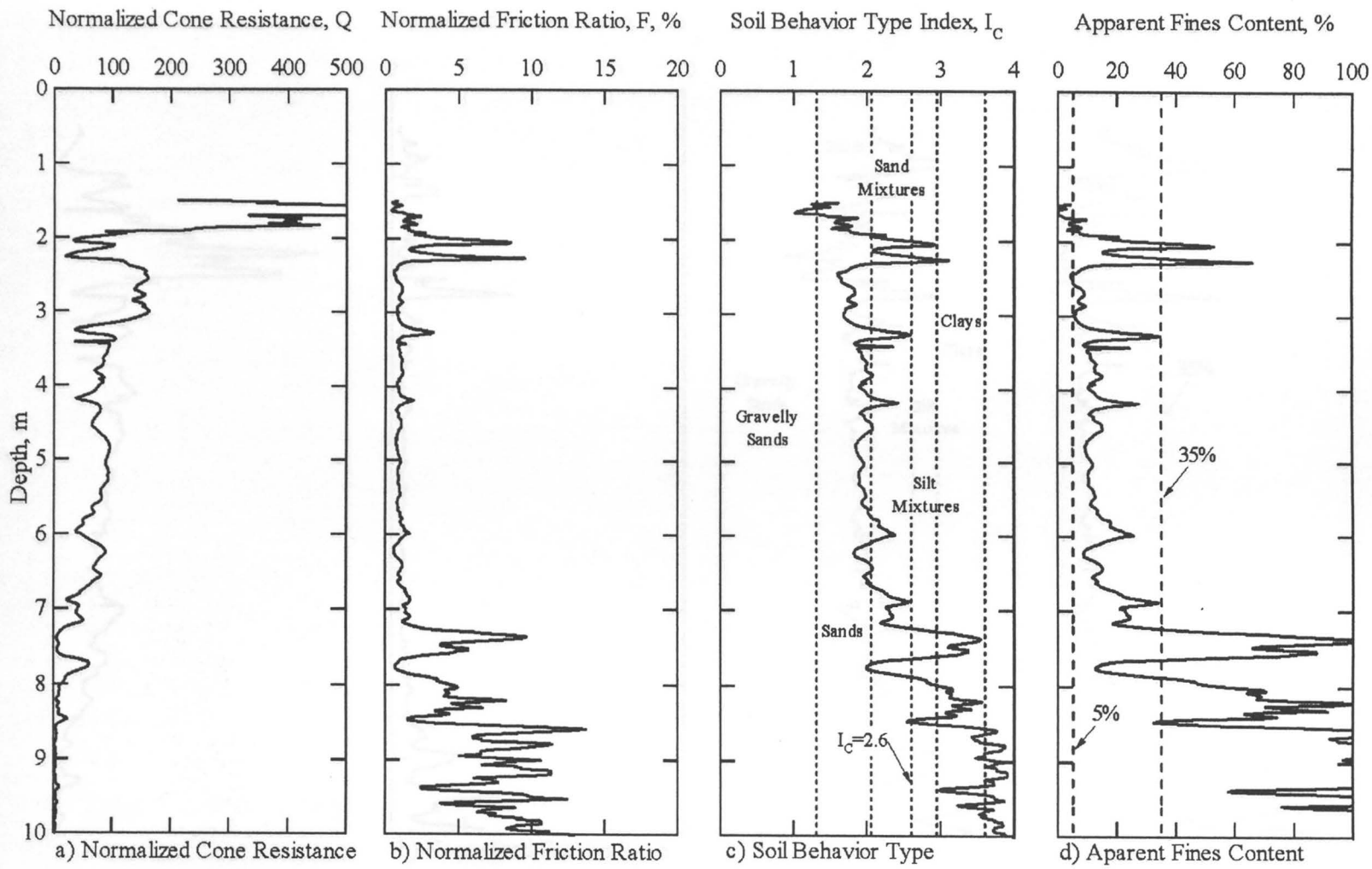

Figure 4.60 Graphs developed from CPT-YH1 to characterize the subsurface at Yalova Harbor, Yalova, Turkey (raw cone data from www.eerc.berkeley.edu/turkey/adapazari).

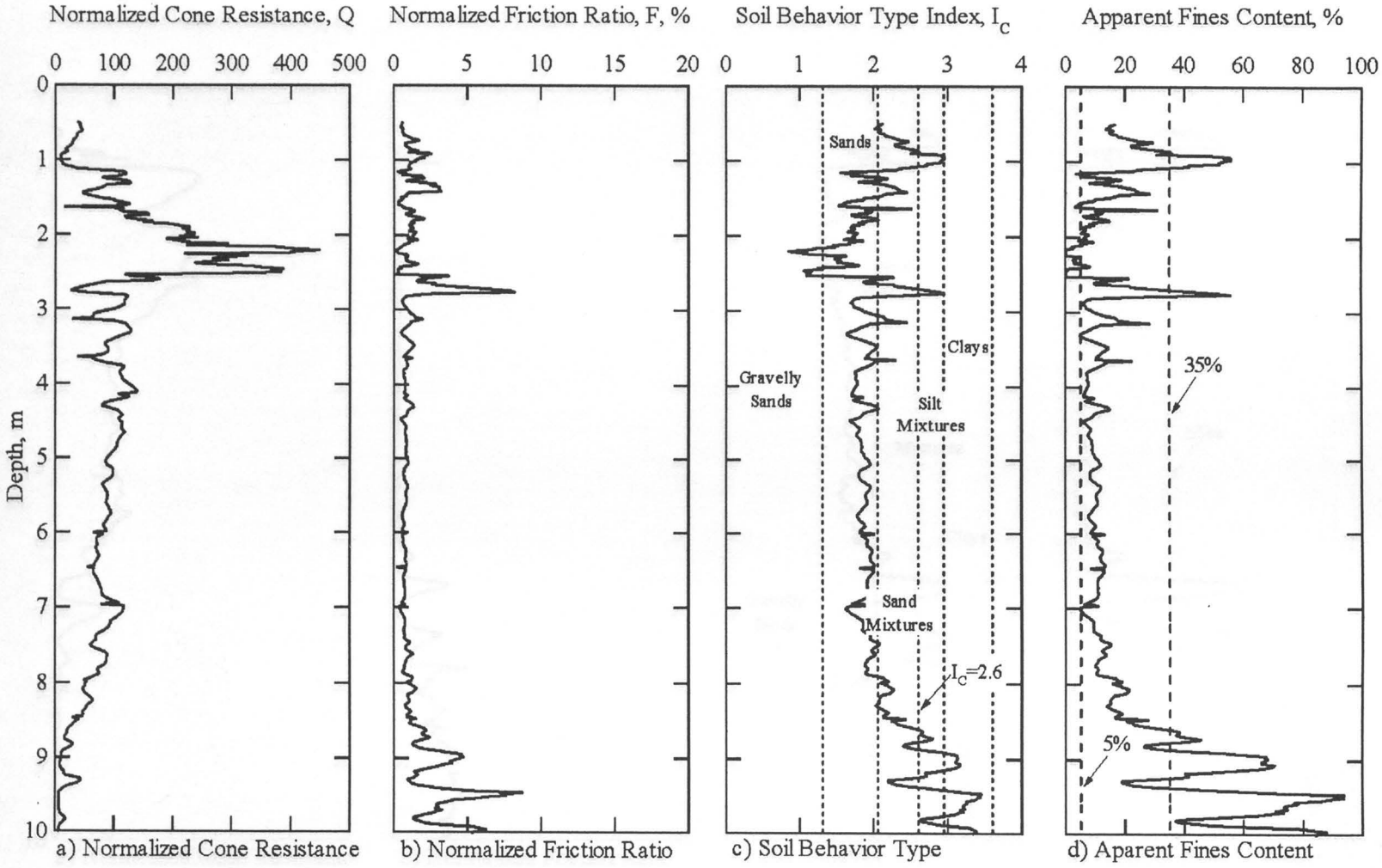

Figure 4.61 Graphs developed from CPT-YH2 to characterize the subsurface at Yalova Harbor, Yalova, Turkey (raw cone data from www.eerc.berkeley.edu/turkey/adapazari).

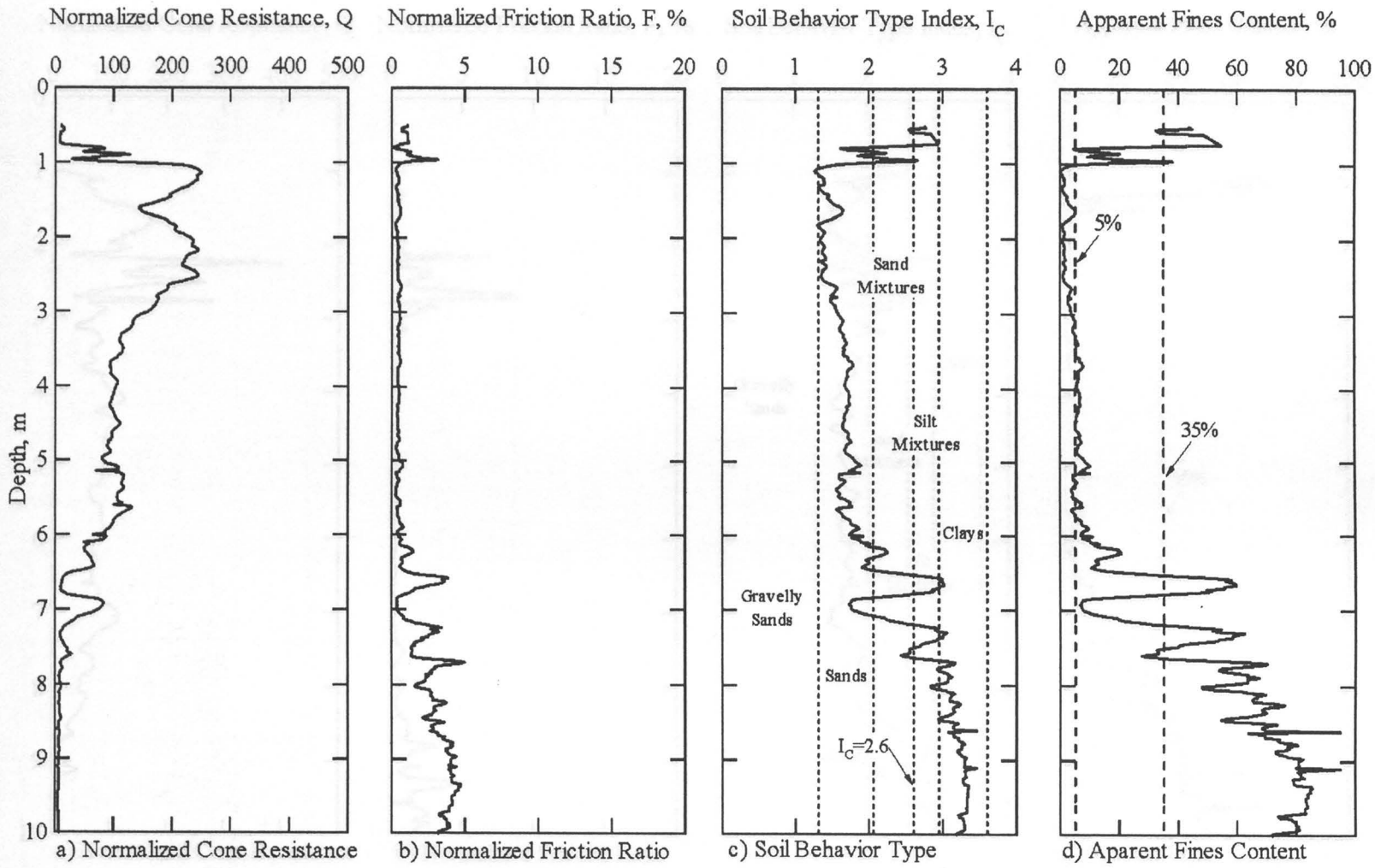

Figure 4.62 Graphs developed from CPT-YH3 to characterize the subsurface at Yalova Harbor, Yalova, Turkey (raw cone data from www.eerc.berkeley.edu/turkey/adapazari).

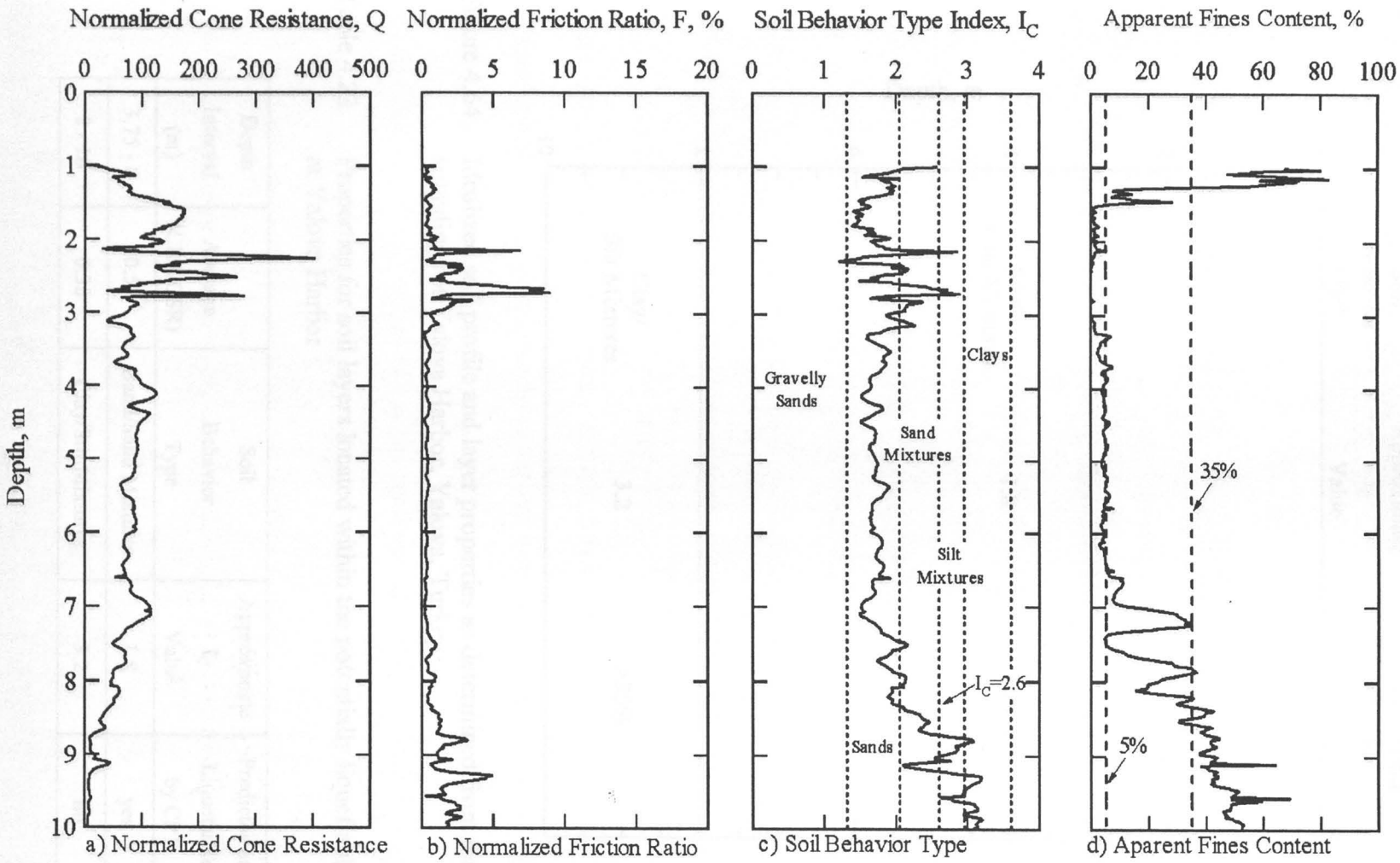

Figure 4.63 Graphs developed from CPT-YH4 to characterize the subsurface at Yalova Harbor, Yalova, Turkey (raw cone data from www.eerc.berkeley.edu/turkey/adapazari).

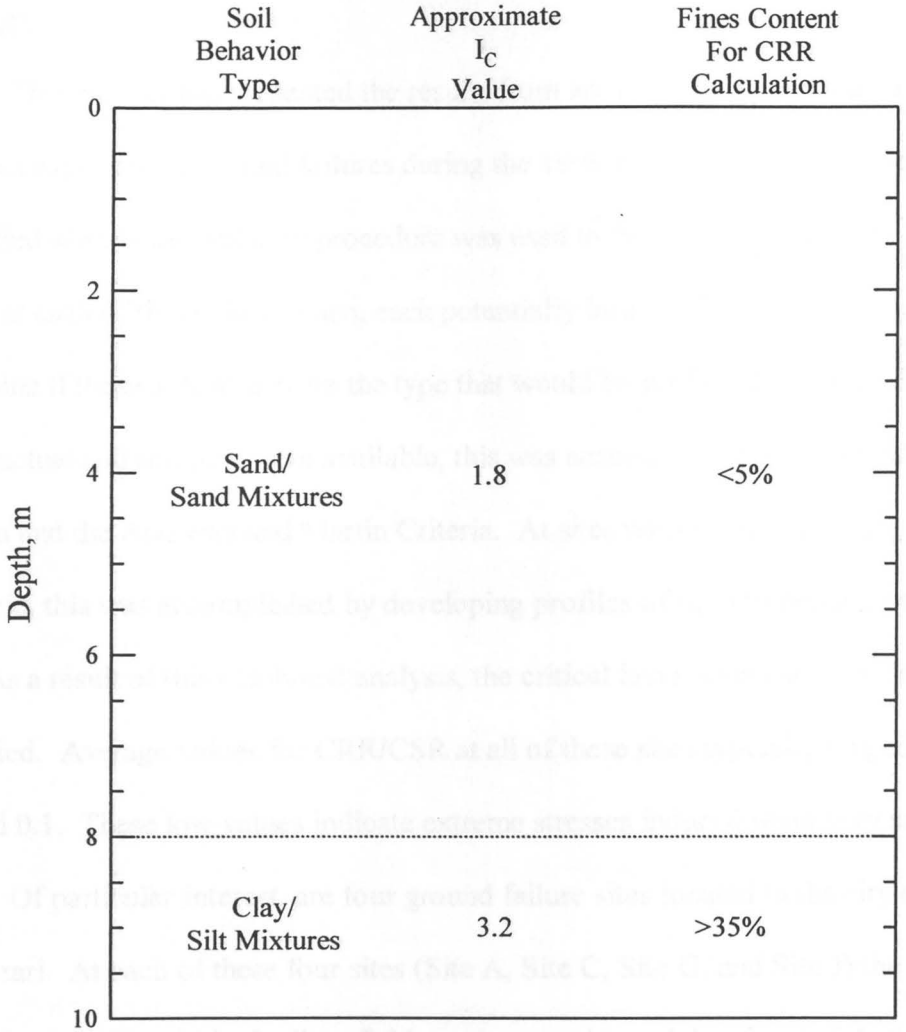

Figure 4.64 Idealized soil profile and layer properties as determined from four CPT soundings at Yalova Harbor, Yalova, Turkey.

Table 4.23 Properties for soil layers located within the potentially liquefiable region at Yalova Harbor

Depth Interval (m)	Average (CRR/CSR)	Soil Behavior Type	Approximate I_C Value	Predicted as Liquefiable by CPT
3.75 - 8	0.51	Sand/Sand Mixtures	1.8	yes
8 - 10	0.36	Clay/Silt Mixtures	3.2	no

Summary

This chapter has presented the results from an in-depth liquefaction analysis of 15 sites that experienced ground failures during the 1999 Kocaeli, Turkey earthquake. The simplified shear wave velocity procedure was used to delineate a potentially liquefiable region at each of these sites. Then, each potentially liquefiable region was evaluated to determine if these soft soils were the type that would be predicted as liquefiable. At sites where actual soil samples were available, this was accomplished by using the Chinese Criteria and the Andrews and Martin Criteria. At sites where only CPT data were available, this was accomplished by developing profiles of the soil behavior type index (I_C). As a result of this combined analysis, the critical layer/layers at each site were identified. Average values for CRR/CSR at all of these sites typically ranged between 0.3 and 0.1. These low values indicate extreme stresses induced upon very soft soils.

Of particular interest, are four ground failure sites located in the city of Adapazari. At each of these four sites (Site A, Site C, Site G, and Site J) the entire subsurface profile within the liquefiable region consists solely of materials that are classified as nonliquefiable according to the Chinese Criteria, and the Andrews and Martin Criteria. At each of these sites, the layer coming nearest to satisfy these criteria was chosen as the one most likely to have liquefied. In each instance, this layer appeared to be primarily made up of non-plastic silts having 2 μm clay contents ranging from 15 - 25%. It is strange for soils with clay contents this high to be considered as non-plastic.

CHAPTER 5

SUMMARY AND CONCLUSIONS

The 1999 Kocaeli, Turkey earthquake was one of the most damaging earthquakes in history, both in terms of life lost and property damaged. Soil liquefaction played a major role in this destruction. Intense research was initiated at many of these liquefaction sites in order to investigate the cause of each ground failure. The purpose of this work was to develop shear wave velocity profiles at sites where liquefaction occurred, and evaluate how well currently used shear wave velocity based liquefaction analysis methods predict ground failure.

Summary

This paper has presented shear wave velocity profiles for 15 sites liquefied by the 1999 Kocaeli, Turkey earthquake. These profiles were used in order to evaluate each liquefaction site by the simplified shear wave velocity procedure (Andrus et al., 2001). This procedure allowed for the identification of any potentially liquefiable regions within the subsurface at each site. Locating these layers at each site allowed for the separation of soils that were too stiff to liquefy from soils that were soft enough to liquefy.

However, soil stiffness alone does not control earthquake-induced soil liquefaction. The type of soil and its properties also control to a large extent the buildup of excess pore waster pressures. Therefore, in order to identify which soil layer/layers most likely liquefied at each site, detailed soil information was evaluated. This information was provided by a joint group of researchers who performed SPT and CPT

testing at these sites (www.eerc.berkeley.edu/turkey/adapazari). Analyzing this information allowed for the separation of liquefiable soils from nonliquefiable soils within each potentially liquefiable region. At sites where actual soil samples were available, this was accomplished by using the Chinese Criteria (Seed and Idriss, 1982) and the Andrews and Martin Criteria (Andrews and Martin, 2000). At sites where only CPT data were available, this was accomplished by developing profiles of soil behavior type index (I_C) (Robertson and Wride, 1998).

By combining these methods, the layer/layers most likely to have caused the liquefaction observed at each of these were identified. Granular soil layers were located within the liquefiable region at 11 of the liquefaction test sites. It is assumed that these layers were the ones responsible for the observed liquefaction. However, at four of the liquefaction sites, only soils predicted as not susceptible to liquefaction were encountered. In these cases, the layer coming closest to fulfilling the Chinese Criteria and the Andrews and Martin Criteria was chosen as the one most likely to have liquefied. At each of these four sites, this layer appeared to be primarily made up of non-plastic silts having 2 μm clay contents ranging from 15 - 25%.

Conclusions

The remainder of this chapter will review the conclusions derived from the liquefaction study at each test site. Then this information will be combined in order to evaluate the current state of practice for predicting liquefaction susceptibility.

Adapazari

The city of Adapazari, located approximately 7 km north of the fault rupture, suffered the highest degree of property damage and life loss of any city affected by the Kocaeli earthquake. The city experienced spectacular and extensive occurrences of soil liquefaction as hundreds of buildings settled, tilted, or translated excessively (EERI, 2000). Ten liquefaction sites from Adapazari were analyzed in this study. Of these 10 liquefaction sites, four were classified as not susceptible to liquefaction according to the current state of practice for liquefaction evaluation. These four sites were Site A, Site C, Site G, and Site J.

At Site A, the layer identified as most likely to have liquefied is a 1-meter thick layer of silt. It is extremely soft with an average CRR/CSR of 0.10. All of the soil samples within this layer were somewhat plastic; the average LL was approximately 34 and the average W_n/LL was 0.97. The average 5 μm clay content was 18% and the average 2 μm clay content was 14%. While predicted as not susceptible to liquefaction by both the Chinese Criteria and the Andrews and Martin Criteria, this layer only fails the Chinese Criteria due to a slightly high amount of clay-sized particles. However, it fails the Andrews and Martin Criteria due to both a high clay content and a high LL.

At Site C, the layer identified as most likely to have liquefied is an approximately 2-meter thick layer of silty sand and silt. It has a CRR/CSR of approximately 0.4. None of the soil samples within this layer were considered as plastic. The average 5 μm clay content was 20% and the average 2 μm clay content was 16%. Therefore, this layer is considered as not susceptible to liquefaction, according to the Chinese Criteria, only due to a high amount of clay-sized particles. Technically, since the layer is totally non-

plastic, the Andrews and Martin Criteria would classify this soil as "further studies required." However, since no guidance is given as to what those studies might be, the site is considered as not susceptible to liquefaction due solely to high clay-sized particle content.

At Site G, the layer identified as most likely to have liquefied is a 6-meter thick layer of silt. It has an average CRR/CSR of 0.20. While this layer was assigned a LL of 44.5, 10 of the 12 samples within it were classified as non-plastic. The average 5 μm clay content was 27% and the average 2 μm clay content was 24%. Therefore, this layer, like Sites A, and C, is considered as not susceptible to liquefaction only due to a high amount of clay-sized particles.

At Site J, the layer identified as most likely to have liquefied is an approximately 2-meter thick layer of silt. It has an average CRR/CSR of 0.25. While this layer was assigned a LL of approximately 39, 8 of the 12 samples within it were classified as non-plastic. The average 5 μm clay content was 28% and the average 2 μm clay content was 23%. Therefore, this layer, like Sites A, C, and J, is considered as not susceptible to liquefaction only due to a high amount of clay-sized particles.

Another site of interest in Adapazari is Site 1-24. This site was located along the banks of the Cark Canal, a likely site for liquefaction-induced lateral spreading. A nearly 3-meter thick layer of soft sand was identified here at a depth of approximately 6 meters. This sand layer was soft enough to liquefy with an average CRR/CSR of 0.24. However, no surface evidence of liquefaction was observed here.

At each of the other five liquefaction sites in Adapazari (Site B, Site D, Site 1-11, Site 1-41, and Site 1-42), sandy soil layers were identified within the potentially

liquefiable region. It was assumed that these layers were the ones responsible for the observed liquefaction. It must also be noted that soils similar to those described at Sites A, C, G, and J were also encountered at each of these five sites. However, since granular soils were also present within the potentially liquefiable regions, the observed liquefaction cannot be proved to have occurred in the silty soils with high clay-sized particle contents.

Hotel Sapanca

Hotel Sapanca is located on the southern shore of Lake Sapanca. Tectonic subsidence, liquefaction-induced settlement, and lateral spreading were all observed on hotel grounds during the Kocaeli earthquake. As a result of these events, the four-story hotel was carried partially into the lake. Lateral movements toward the lake were on the order of 2 meters and the hotel settled between 20 - 50 cm. These two phenomena, coupled with tectonic subsidence, resulted in movement of the shoreline inward by 30 - 50 meters (EERI, 2000).

Four SASW centerlines were used at this location in order to investigate the full extent of the on-shore portion of the lateral spread. These centerlines were spaced evenly along a line approximately 75 meters in length. Nearly all of the soil down to a depth of 15 meters is soft enough to liquefy. Values for CRR/CSR vary slightly with depth and centerline; however, most lie between 0.3 - 0.4. Cone data were used at this site to classify the subsurface material. The soil is sand/sand mixtures with an approximate I_C value of 1.7. These types of conditions indicate liquefaction susceptibility, and help to

explain the dramatic subsidence and lateral spreading that caused the hotel to be carried partially into the lake.

Izmit Bay

Numerous coastal failures occurred along the Marmara coast on the north, east, and south shores of Izmit Bay. These failures ranged from minor lateral spreading in the free field to catastrophic stability failures that carried buildings and people into the Bay. In addition to liquefaction-related failures, major coastal subsidence also occurred in the Golcuk area (EERI, 2000). Four liquefaction-induced lateral spread sites located in this region will be discussed below.

The largest and most devastating coastal stability failure occurred at Degirmendere Nose. Here, a large section of fill, along with a hotel and two restaurants, was carried into the bay. The cause of this enormous failure is not fully understood. Small lateral spread cracks were observed along the on-shore part of the failure behind a large head scarp. This study only identified a 1-meter thick layer, located between 8 - 9 meters in depth, that was soft enough to liquefy. This layer has an average CRR/CSR of 0.9. Cone data were used at this site to classify the subsurface material. The soil is sand/sand mixtures with an approximate I_C value of 1.7. It is probable that this layer did liquefy; however, it is likely that tectonic deformation also played a large role in the catastrophic failure at this site

At each of the other three liquefaction sites along Izmit Bay (Police Station, Soccer Field, and Yalova Harbor), layers of sand/sand mixtures were identified within the

potentially liquefiable region. It was assumed that these layers were the ones responsible for the liquefaction observed at these sites.

Current state of practice

It is well understood that granular soils, under the right conditions, can and do liquefy during earthquakes. However, the liquefaction of finer grained soils, such as silts and silt-clay mixtures, is more of a mystery to practicing engineers. Under the current state of practice, the governing "law" for evaluating these soils has been the Chinese Criteria (Seed and Idriss, 1982). More recently the Andrews and Martin Criteria (Andrews and Martin, 2000) have been developed as a refinement of the Chinese Criteria. Both of these criteria are based on Atterberg limits and grain size. Whether the authors intended it or not, the grain size part of these criteria has become a simple test used to separate "liquefiable" from "nonliquefiable" soils.

This study has shown that these criteria do not work for every case. Four of the 10 sites studied in the city of Adapazari, where liquefaction was observed, have been predicted as not susceptible to liquefaction. In each case, the layer identified as the one most likely to have liquefied is classified as a low-plasticity silt. These soil layers were either largely non-plastic, or slightly plastic with LL's less than 35. Therefore, the only basis for labeling them nonliquefiable is the fact that they all contained high amounts clay-sized particles (i.e. 15 - 25% finer than 2 μm).

This study has shown that soils should not be labeled as nonliquefiable just because they have high amounts of clay-sized particles. Particle size is an easy dividing line, but means nothing in and of itself. The properties of these small particles must also

be considered. Had only the LL part of these criteria been used, each soil layer would have properly been identified as liquefiable.

LITERATURE CITED

Andrews, D.C.A., and G.R. Martin. 2000. Criteria for liquefaction of silty soils. Twelfth World Conference on Earthquake Engineering, January 29-February 5, Auckland, New Zealand.

Andrus, R.D., and K.H. II Stokoe. 1997. Liquefaction resistance based on shear wave velocity. NCEER Workshop on Evaluation of Liquefaction Resistance of Soils, January 4-5 1996, Salt Lake City, UT, p. 89-128.

Andrus, R.D., and K.H. II Stokoe. 2000. Liquefaction resistance of soils from shear wave velocity. Journal of Geotechnical and Geoenvironmental Engineering, ASCE 126(11):1015-1025.

Andrus, R.D., K.H. II Stokoe, J.A. Bay, and R.M. Chung. 1998. Delineation of densified sand at Treasure Island by SASW testing, p. 459-464. In P.K. Robertson and P.W. Mayne (Eds.). Geotechnical site characterization. A.A. Balkema, Rotterdam, Netherlands.

Andrus, R.D., K.H. II Stokoe, and R.M. Chung. 1999. Draft guidelines for evaluating liquefaction resistance using shear wave velocity measurements and simplified procedures. NISTIR 6277, National Institute of Standards and Technology, Gaithersburg, Maryland, 121 p.

Andrus, R.D., K.H. II Stokoe, R.M. Chung, and C.H. Juang. 2001. Guidelines for evaluating liquefaction resistance using shear wave velocity measurements and simplified procedures. National Institute of Standards and Technology, Gaithersburg, Maryland. In press.

Atukorala, U., D. Wijewickreme, and N. McCammon. 2000. Some observations related to liquefaction susceptibility of silty soils. Twelfth World Conference on Earthquake Engineering, January 29-February 5, Auckland, New Zealand.

Brown, L.T, D.M. Boore, and K.H.II Stokoe. 2000. Comparison of shear wave velocity profiles from SASW and downhole seismic tests at a strong-motion site. Twelfth World Conference on Earthquake Engineering, January 29-February 5, Auckland, New Zealand.

Dobry, R., R.D. Ladd, F.Y. Yokel, R.M. Chung, and D. Powell. 1982. Prediction of pore water pressure buildup and liquefaction of sands during earthquakes by the cyclic strain method. NBS Building Science Series 138, National Bureau of Standards, Gaithersburg, Maryland, 152 p.

Earthquake Engineering Research Institute (EERI). 2000. 1999 Kocaeli, Turkey, Earthquake Reconnaissance Report, Earthquake Spectra: The Professional Journal of the Earthquake Engineering Research Institute, Supplement A to Volume 16, December 2000, 461 p.

Guo, T., and S. Prakash. 2000. Liquefaction of silt-clay mixtures. Twelfth World Conference on Earthquake Engineering, January 29-February 5, Auckland, New Zealand.

Joh, S.-H. 1992. User's Guide to WinSASW, a Program for Data Reduction and Analysis of SASW Measurements, The University of Texas at Austin. 287 p.

Kayabali, K. 1996. Soil liquefaction evaluation using shear wave velocity. Engineering Geology 44(4):121-127.

Kayen, R.E., J.K. Mitchell, R.B. Seed, A. Lodge, S. Nishio, and R. Coutinho. 1992. Evaluation of SPT-, CPT-, and shear wave-based methods for liquefaction potential assessment using loma prieta data. Fourth Japan-U.S. Workshop on Earthquake Resistant Design of Lifeline Facilities and Countermeasures for Soil Liquefaction, May 27-29,1992, Honolulu, Hawaii, p. 177-204.

Kramer, S.L. 1996. Geotechnical earthquake engineering. Prentice Hall, Upper Saddle River, New Jersey, 595 p.

Liao, S.S.C., and R.V. Whitman. 1986. Overburden correction factors for SPT in sands. Journal of Geotechnical Engineering, ASCE 112(3):373-377.

Lodge, A.L. 1994. Shear wave velocity measurements for subsurface characterization. Ph.D. dissertation. University of California, Berkeley, California. 243 p.

Nazarian, S., and K.H. II Stokoe. 1984. In situ shear wave velocities from spectral analysis of surface wave tests. Eighth World Conference on Earthquake Engineering, San Francisco, California, p. 31-38.

Rathjie, E. 2001. Professor at the University of Texas at Austin. Personal interview, May.

Robertson, P.K. 1990. Soil classification using CPT. Canadian Geotechnical Journal 27(1):151-158.

Robertson, P.K., and C.E. Wride. 1998. Evaluating cyclic liquefaction potential using the cone penetration test. Canadian Geotechnical Journal 35(3):442-459.

Robertson, P.K., D.J. Woeller, and W.D.L. Finn. 1992. Seismic cone penetration test for evaluation liquefaction potential under cyclic loading. Canadian Geotechnical Journal, Vol. 29, p. 686-695.

Sancio, R. 2001. Graduate student at the University of California. Personal interview, May.

Seed, H.B., and I.M. Idriss. 1971. Simplified procedure for evaluating soil liquefaction potential. Journal of the Soil Mechanics and Foundations Division, ASCE 97(SM9):1249-1273.

Seed, H.B., and I.M. Idriss. 1982. Ground motion and soil liquefaction during earthquakes. Earthquake Engineering Research Institute, Berkeley, California, 134 p.

Stokoe, K.H., II, S. Nazarian, G.J. Rix, I. Sanchez-Salinero, J.C. Sheu, and Y.J. Mok. 1988. In situ seismic testing of hard-to-sample soils by surface wave method, p. 264-289. In J.L. Von Thun (Ed.). Earthquake engineering and soil dynamics II—recent advances in ground-motion evaluation, Geotechnical Special Publications No. 20, ASCE.

Stokoe K.H., II, S.G. Wright, J.A. Bay, and J.M. Roesset. 1994. Characterization of geotechnical sites by SASW method, p. 1-24. In R.D. Woods (Ed.). Geophysical characterization of sites, IBH Oxford Press, New Delhi.

Tokimatsu, K., S. Kuwayama, and S. Tamura. 1991. Liquefaction potential evaluation based on Rayleigh wave investigation and its comparison with field behavior. Second International Conference on Recent Advances in Geotechnical Earthquake Engineering and Soil Dynamics, March 11-15, 1991, St. Louis, Missouri, University of Missouri at Rolla, p. 357-364.

Tokimatsu, K., and A. Uchida. 1990. Correlation between liquefaction resistance and shear wave velocity. Soils and Foundations, Japanese Society of Soil Mechanics and Foundation Engineering 30(2):33-42.

Yamamoto, A., H. Shinohara, and I. Furuta. 2000. Liquefaction potential using s-wave crosshole tomography. Twelfth World Conference on Earthquake Engineering, January 29-February 5, Auckland, New Zealand.

Yamamuro, J.A., and K.M. Covert. 2001. Monotonic and cyclic liquefaction of very loose sands with high silt content. Journal of Geotechnical and Geoenvironmental Engineering 127(4):314-324.

Youd, T.L., and I.M. Idriss. 1997. NCEER workshop on evaluation of liquefaction resistance of soils. National Center for Earthquake Engineering Research, Buffalo, New York, Technical Report no. NCEER-97-0022. 267 p.

Youd, T.L., and I.M. Idriss. 2001. Liquefaction resistance of soils: summary report from the 1996 NCEER and 1998 NCEER/NSF workshops on evaluation of liquefaction resistance of soils. Journal of Geotechnical and Geoenvironmental Engineering 127:297-313.

APPENDIX

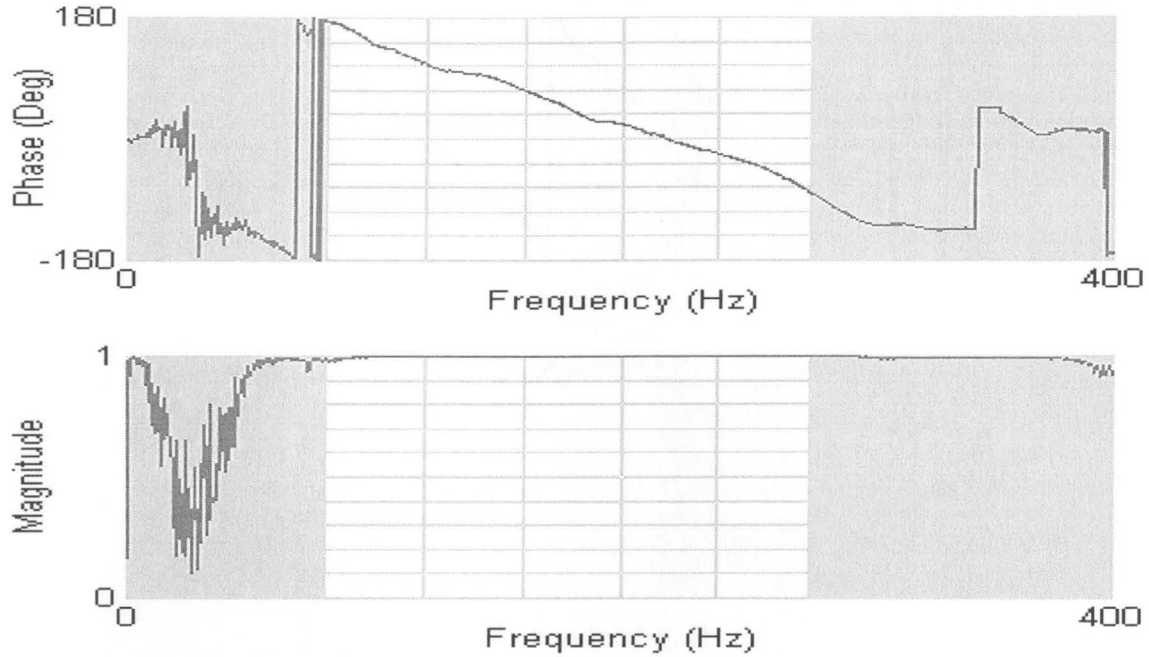

Figure A.1 Wrapped phase of the cross power spectrum (top), and corresponding coherence function (bottom), for the 1-meter spacing average profile measured at Site A, Aug. 15, 2000, Adapazari, Turkey.

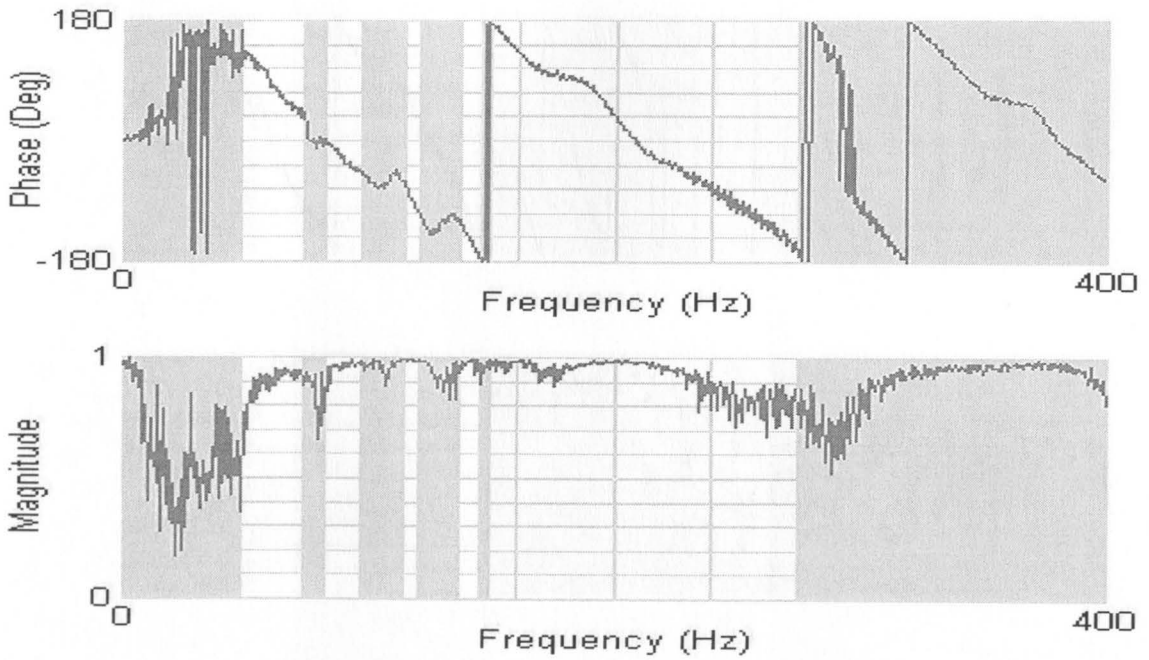

Figure A.2 Wrapped phase of the cross power spectrum (top), and corresponding coherence function (bottom), for the 2-meter spacing average profile measured at Site A.

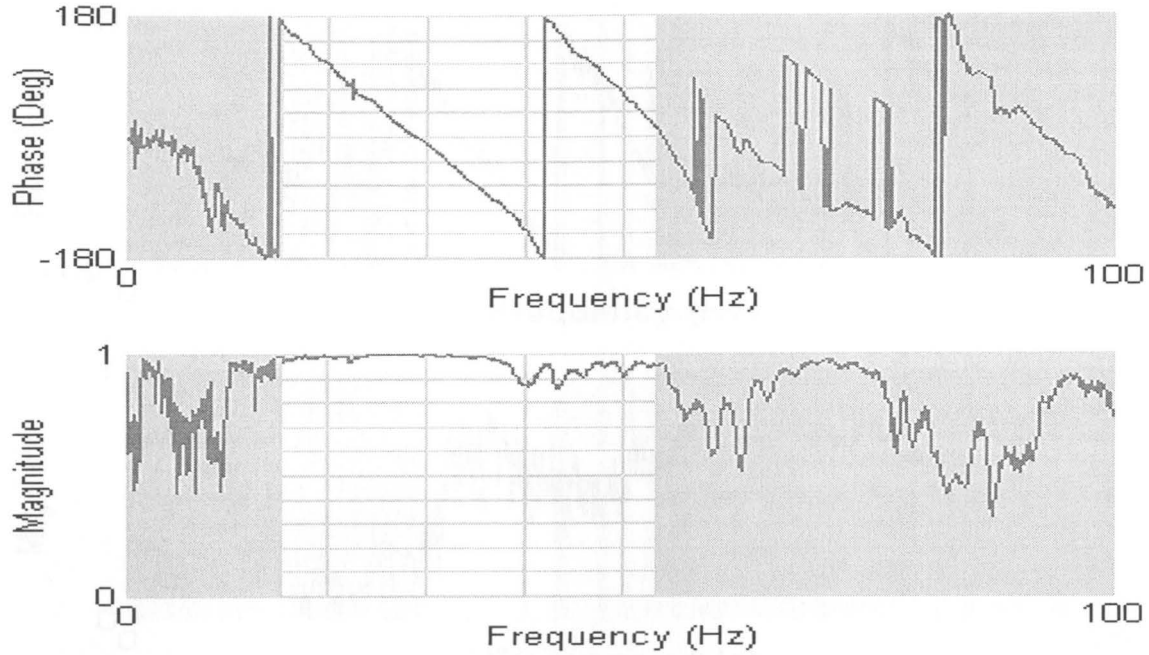

Figure A.3 Wrapped phase of the cross power spectrum (top), and corresponding coherence function (bottom), for the 4-meter spacing average profile measured at Site A.

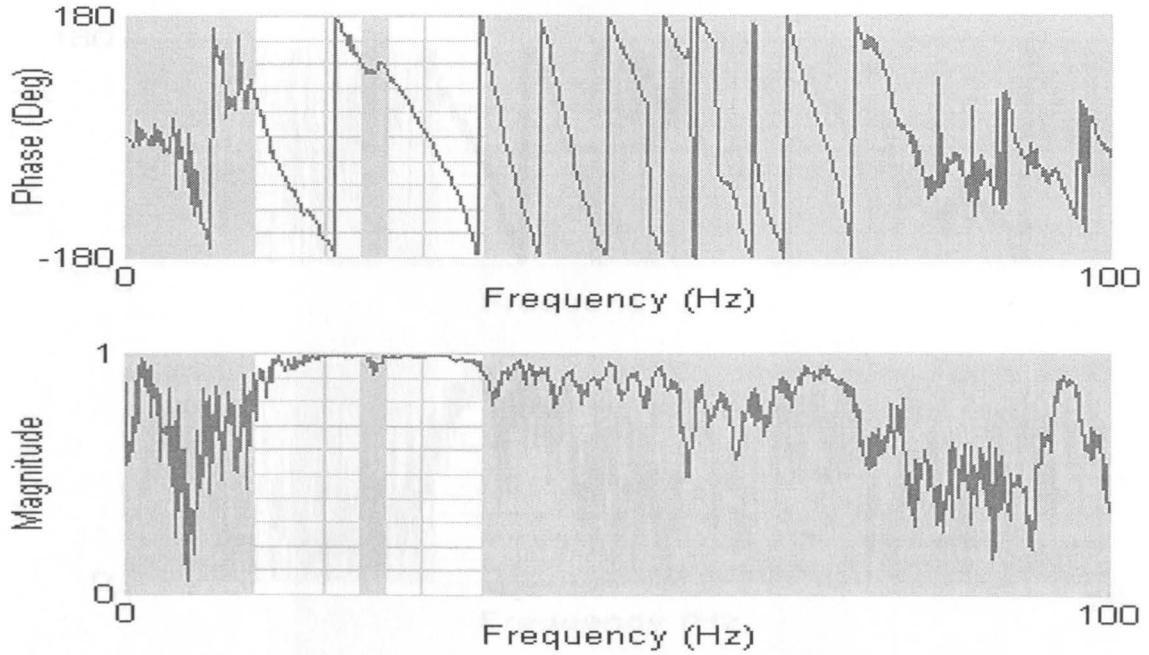

Figure A.4 Wrapped phase of the cross power spectrum (top), and corresponding coherence function (bottom), for the 8-meter spacing average profile measured at Site A.

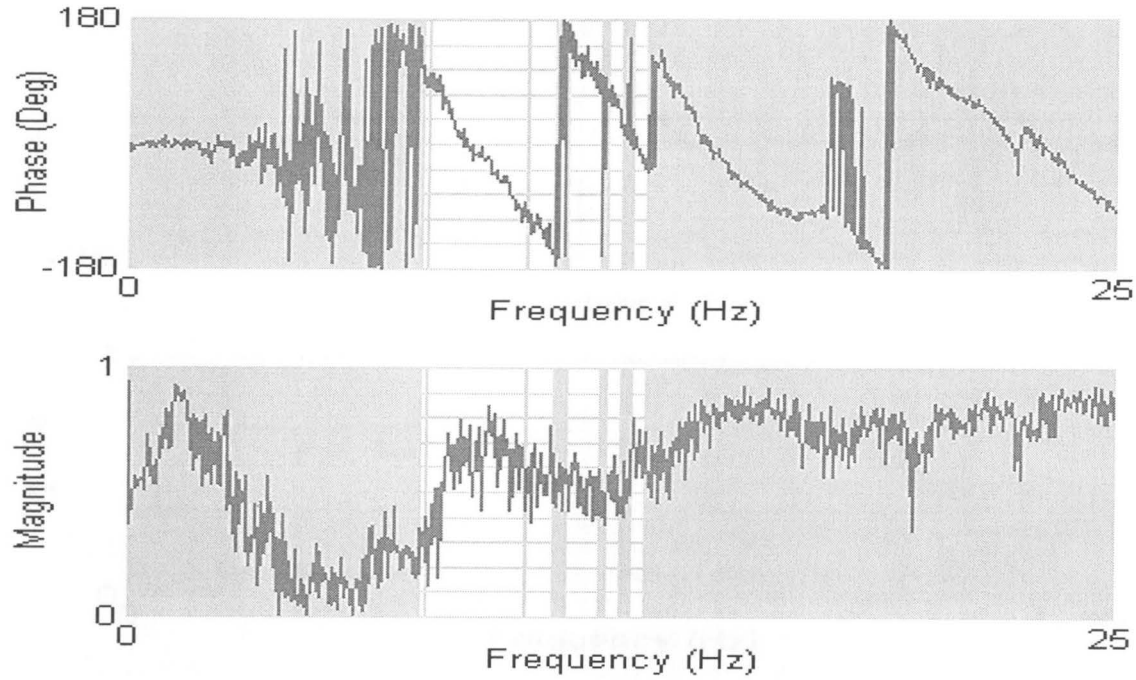

Figure A.5 Wrapped phase of the cross power spectrum (top), and corresponding coherence function (bottom), for the 16-meter spacing average profile measured at Site A.

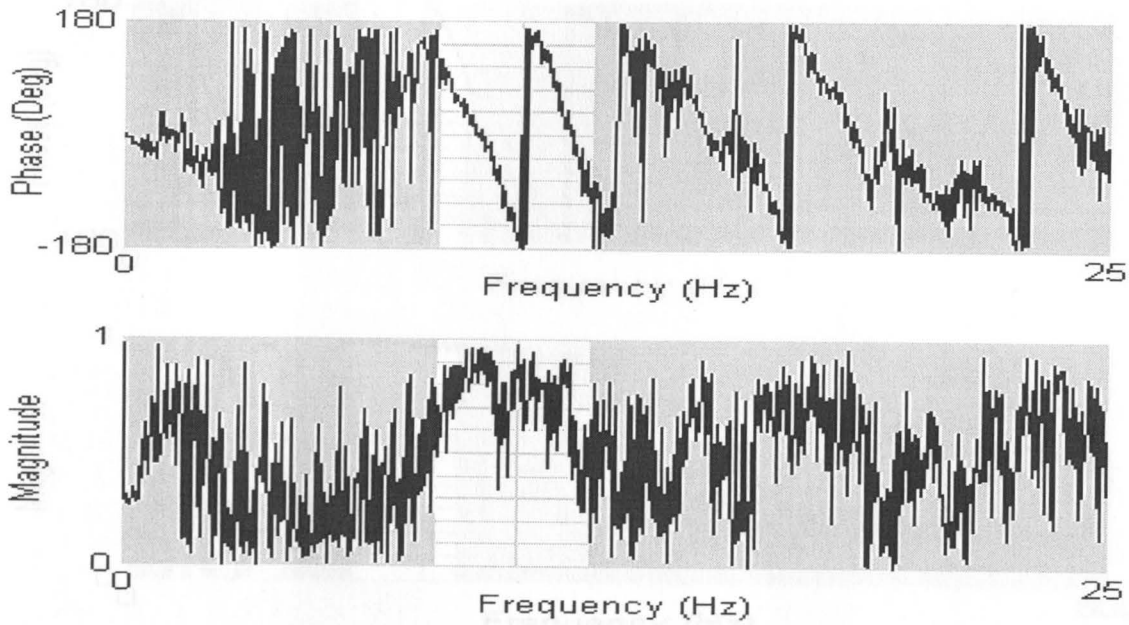

Figure A.6 Wrapped phase of the cross power spectrum (top), and corresponding coherence function (bottom), for the 32-meter spacing reverse profile measured at Site A.

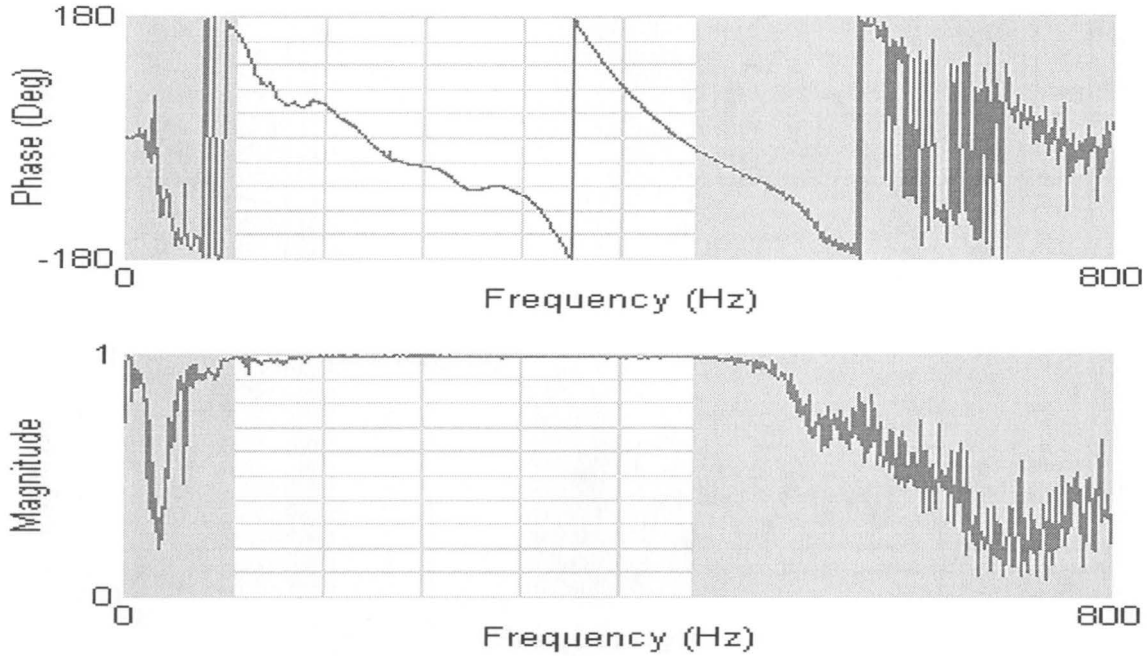

Figure A.7 Wrapped phase of the cross power spectrum (top), and corresponding coherence function (bottom), for the 1-meter spacing average profile measured at Site B, Aug. 16, 2000, Adapazari, Turkey.

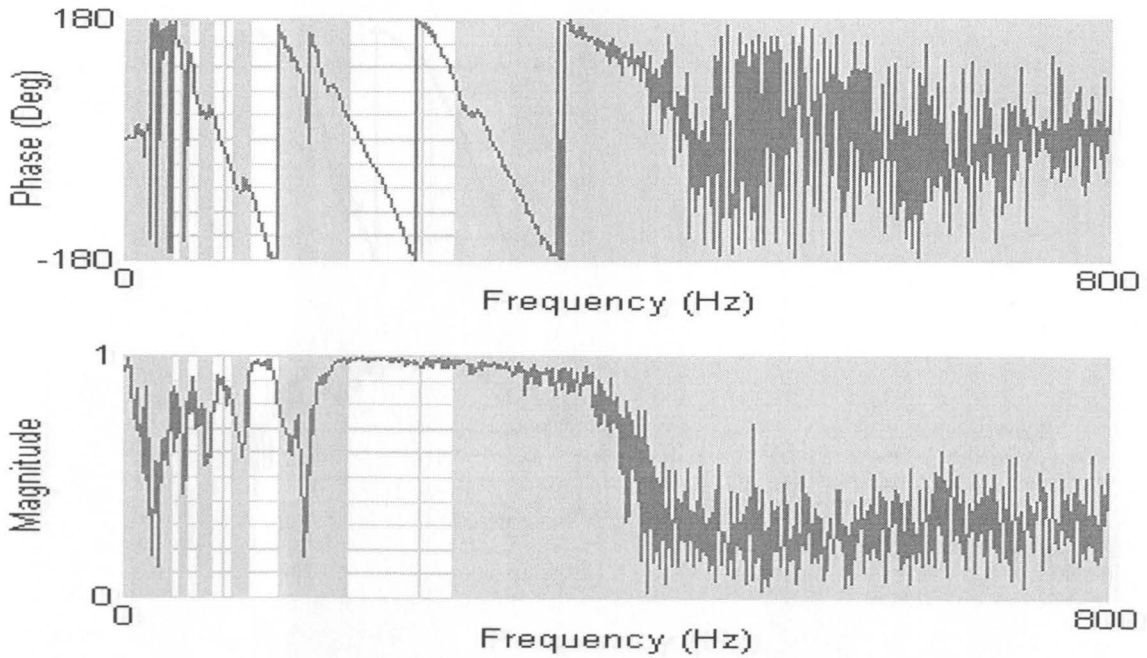

Figure A.8 Wrapped phase of the cross power spectrum (top), and corresponding coherence function (bottom), for the 2-meter spacing average profile measured at Site B.

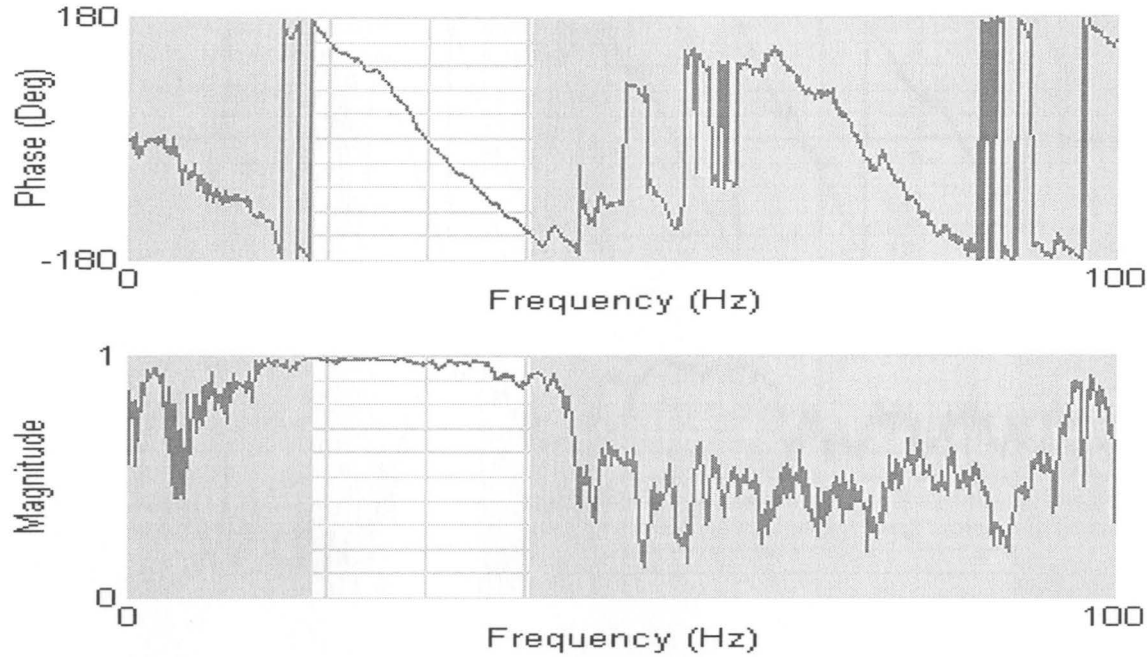

Figure A.9 Wrapped phase of the cross power spectrum (top), and corresponding coherence function (bottom), for the 4-meter spacing average profile measured at Site B.

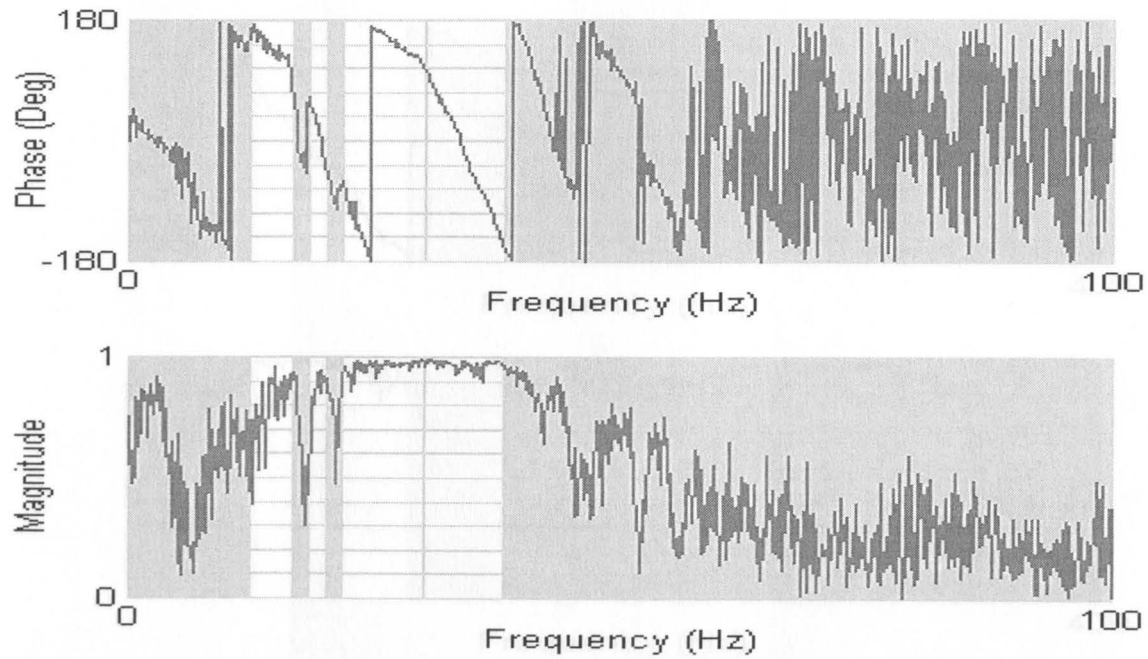

Figure A.10 Wrapped phase of the cross power spectrum (top), and corresponding coherence function (bottom), for the 8-meter spacing average profile measured at Site B.

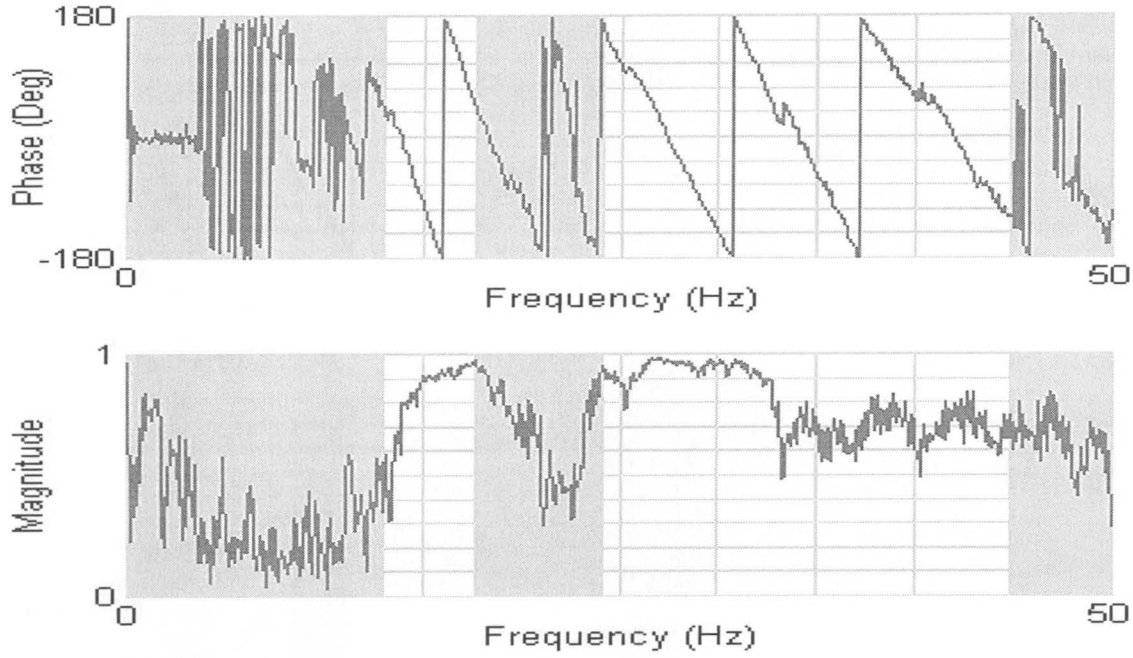

Figure A.11 Wrapped phase of the cross power spectrum (top), and corresponding coherence function (bottom), for the 16-meter spacing average profile measured at Site B.

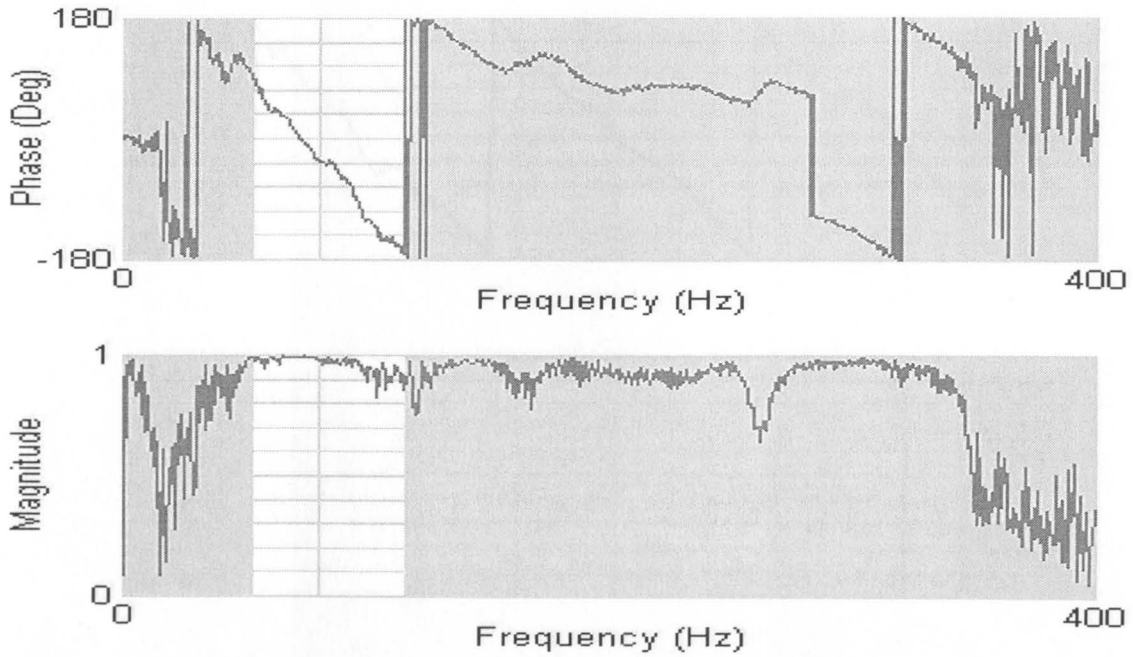

Figure A.12 Wrapped phase of the cross power spectrum (top), and corresponding coherence function (bottom), for the 1-meter spacing average profile measured at Site C North Centerline, Aug. 21, 2000, Adapazari, Turkey.

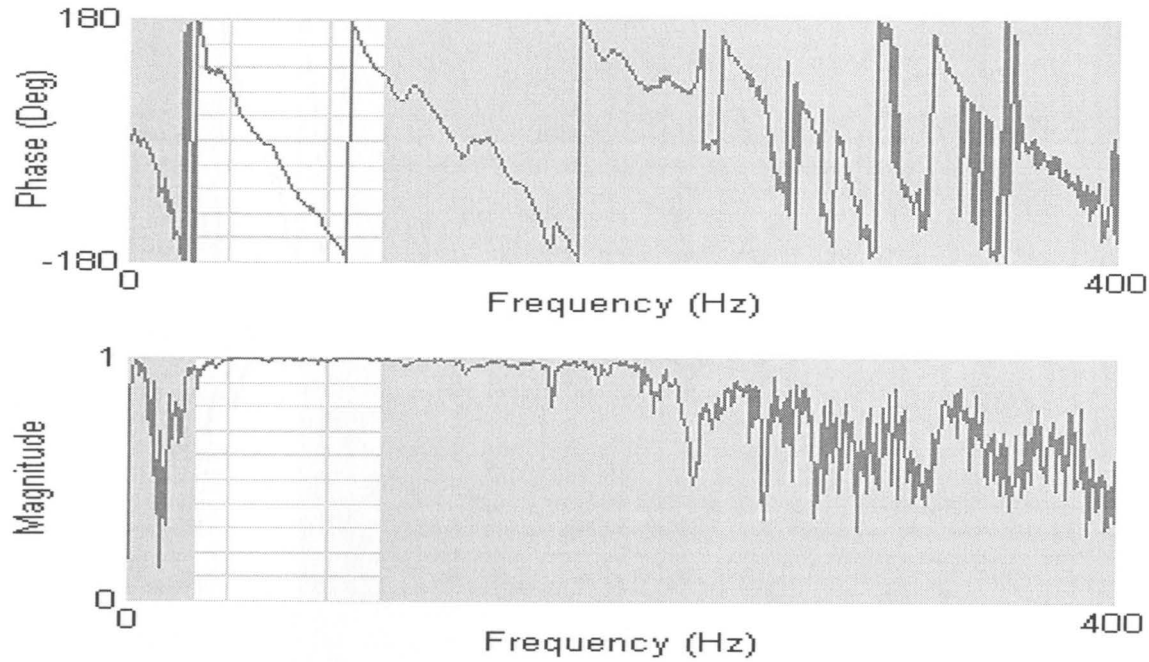

Figure A.13 Wrapped phase of the cross power spectrum (top), and corresponding coherence function (bottom), for the 2-meter spacing average profile measured at Site C North Centerline.

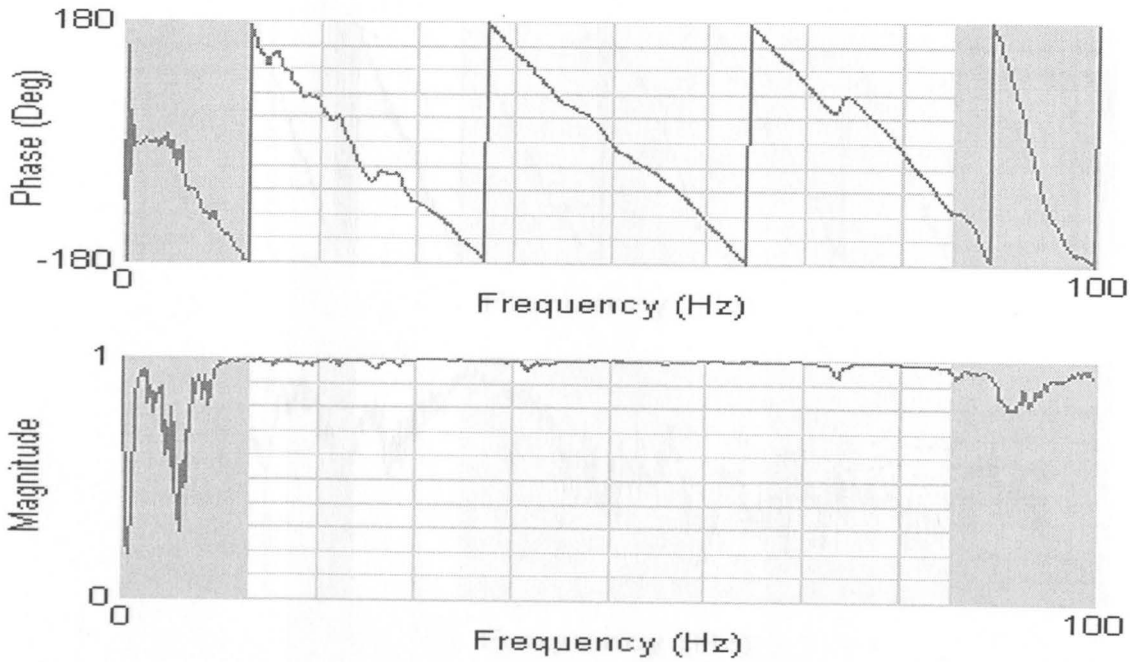

Figure A.14 Wrapped phase of the cross power spectrum (top), and corresponding coherence function (bottom), for the 4-meter spacing average profile measured at Site C North Centerline.

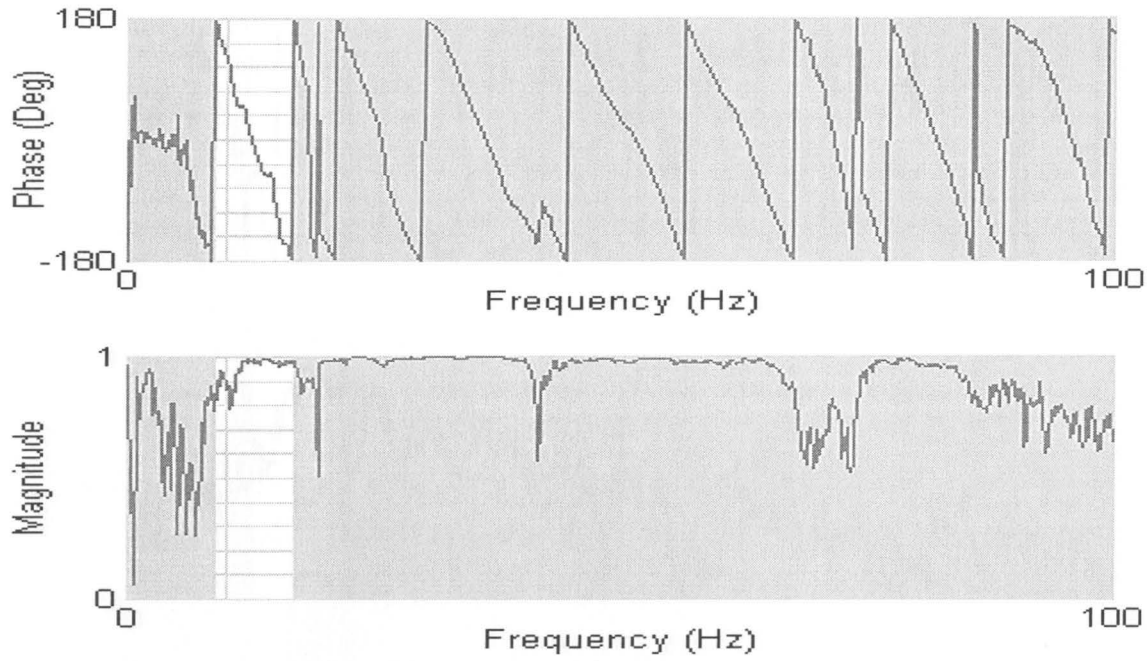

Figure A.15 Wrapped phase of the cross power spectrum (top), and corresponding coherence function (bottom), for the 8-meter spacing average profile measured at Site C North Centerline.

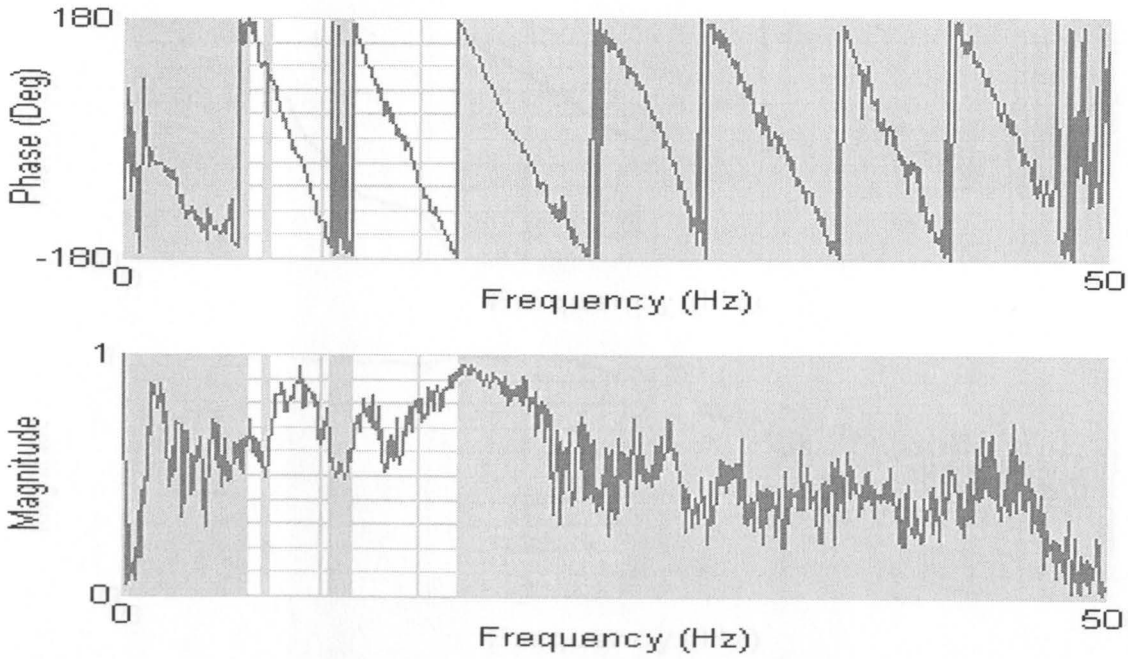

Figure A.16 Wrapped phase of the cross power spectrum (top), and corresponding coherence function (bottom), for the 16-meter spacing average profile measured at Site C North Centerline.

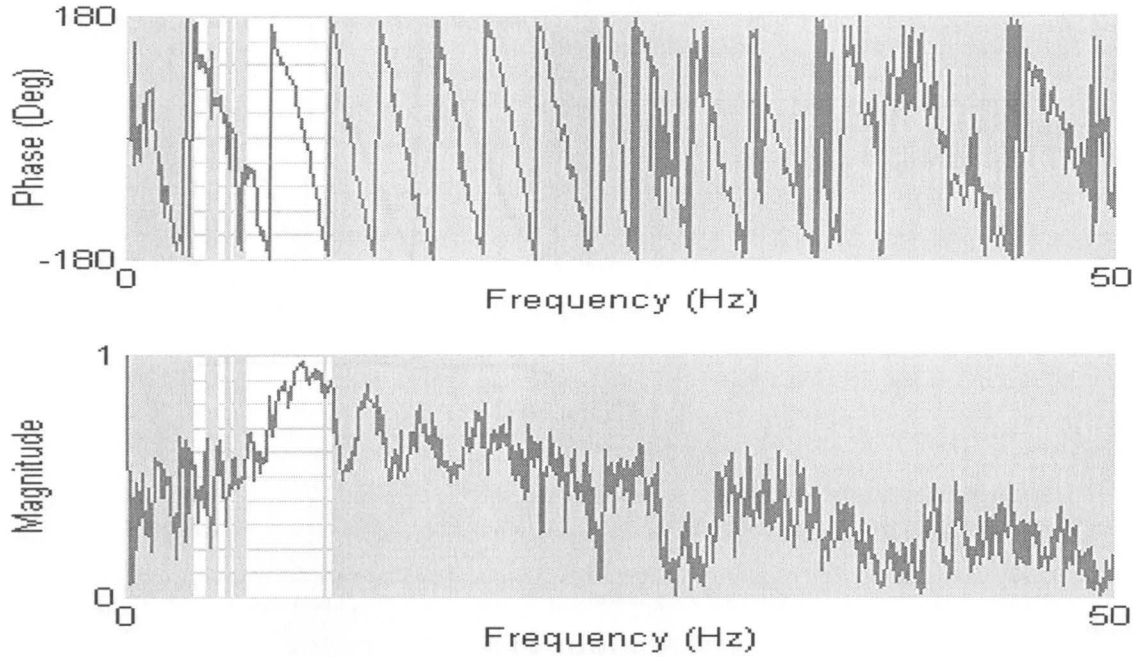

Figure A.17 Wrapped phase of the cross power spectrum (top), and corresponding coherence function (bottom), for the 32-meter spacing forward profile measured at Site C North Centerline.

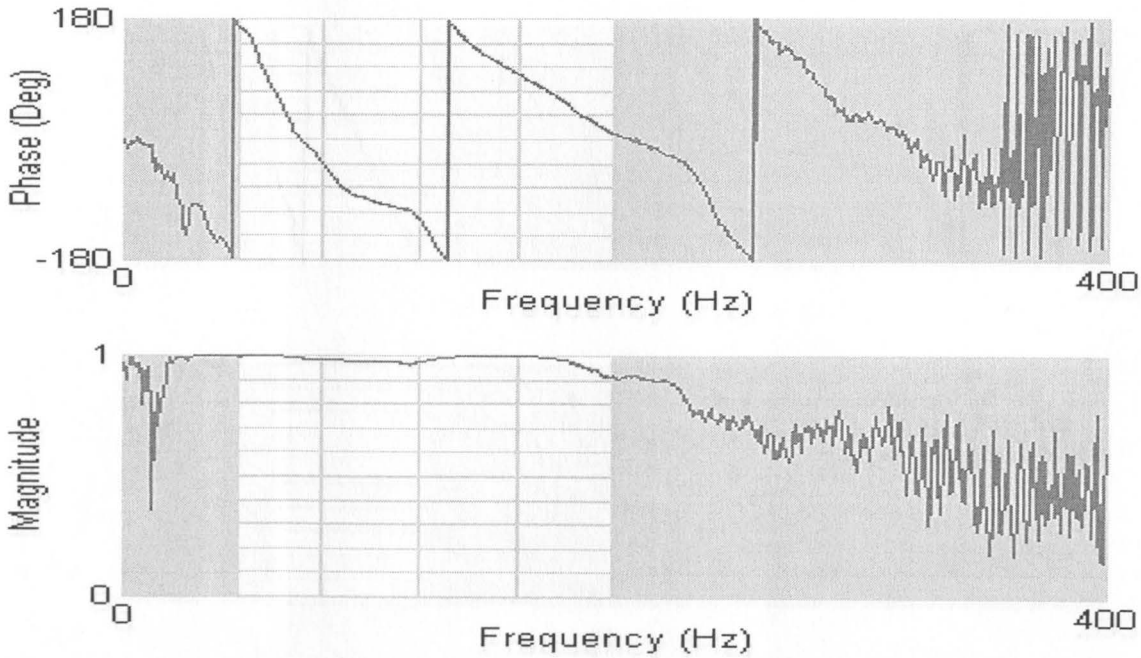

Figure A.18 Wrapped phase of the cross power spectrum (top), and corresponding coherence function (bottom), for the 1-meter spacing average profile measured at Site C South Centerline, Aug. 21, 2000, Adapazari, Turkey.

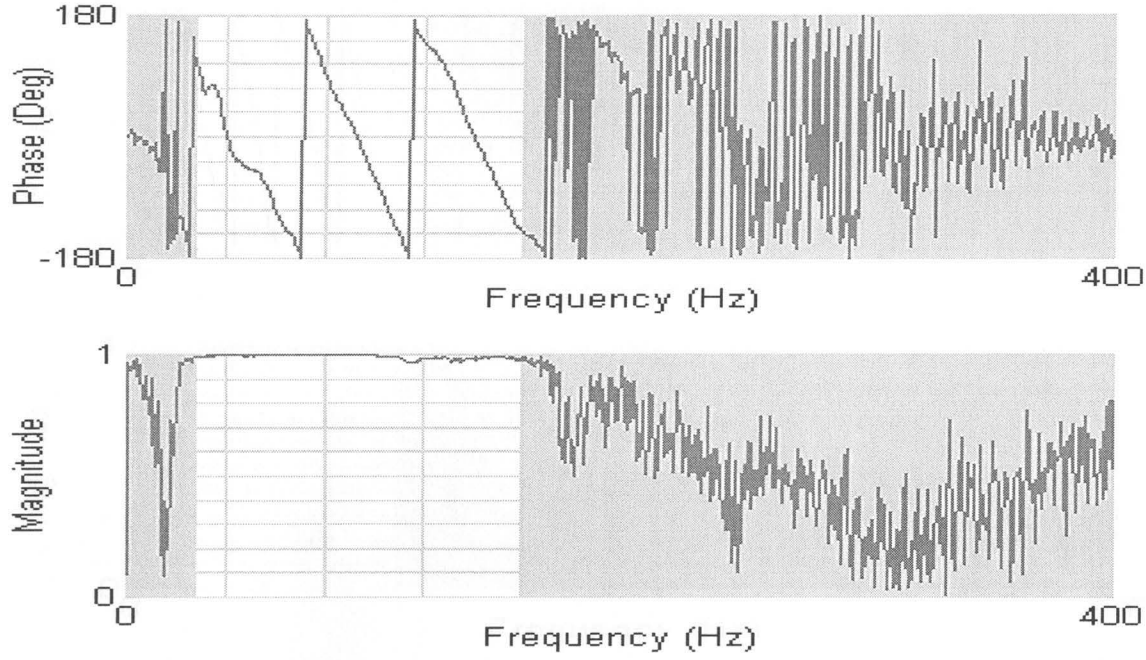

Figure A.19 Wrapped phase of the cross power spectrum (top), and corresponding coherence function (bottom), for the 2-meter spacing average profile measured at Site C South Centerline.

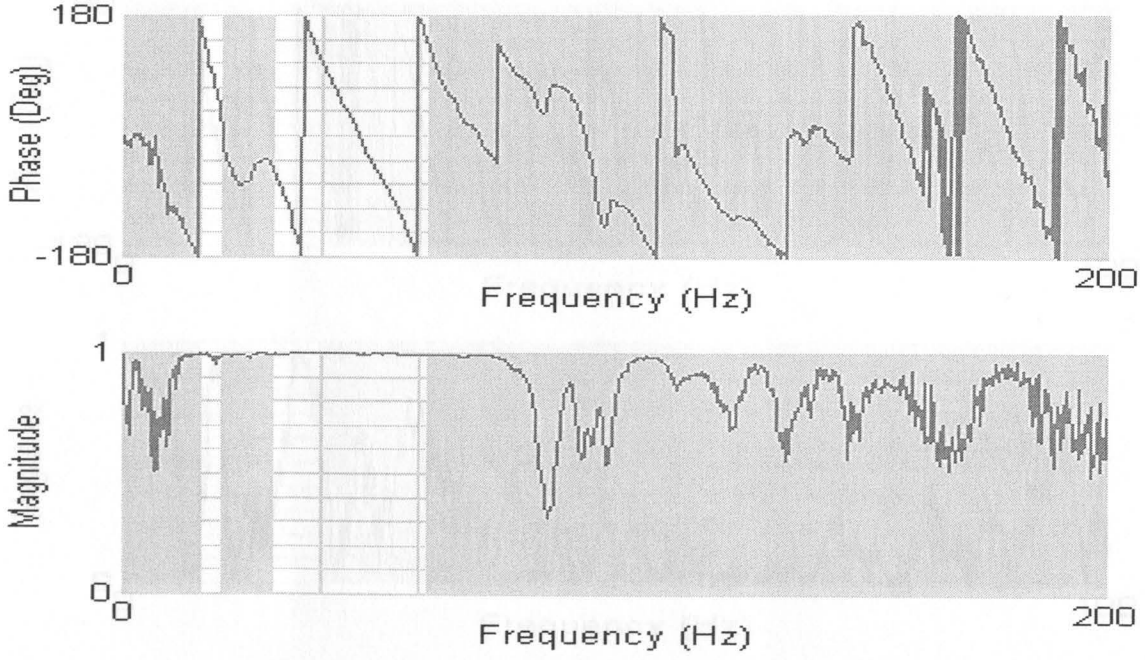

Figure A.20 Wrapped phase of the cross power spectrum (top), and corresponding coherence function (bottom), for the 4-meter spacing average profile measured at Site C South Centerline.

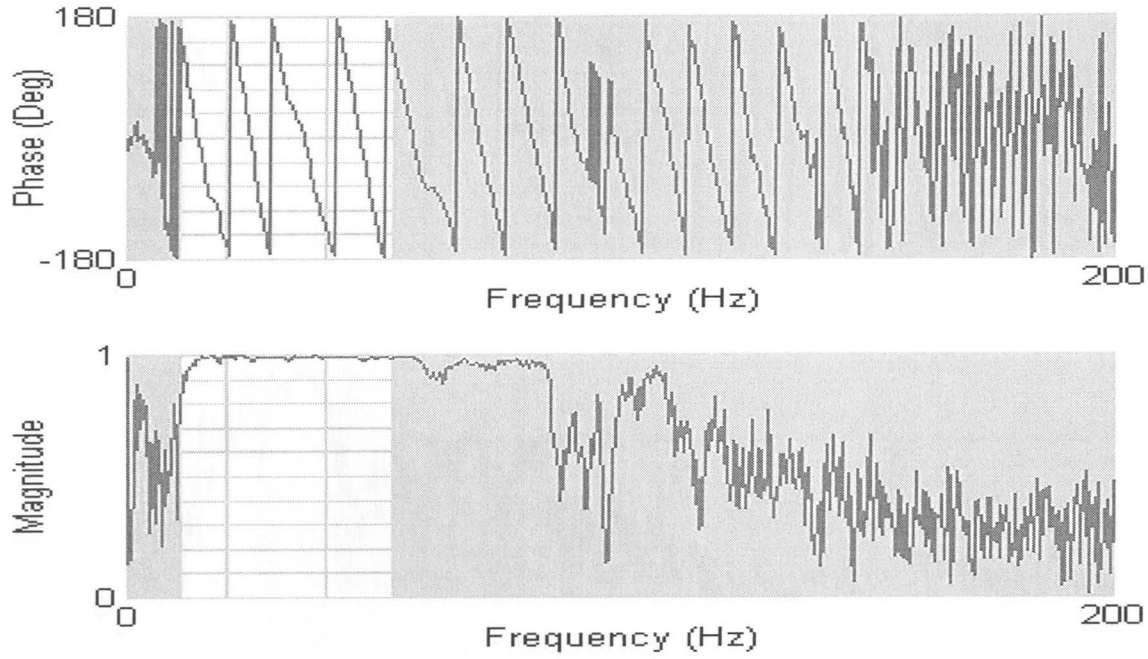

Figure A.21 Wrapped phase of the cross power spectrum (top), and corresponding coherence function (bottom), for the 8-meter spacing average profile measured at Site C South Centerline.

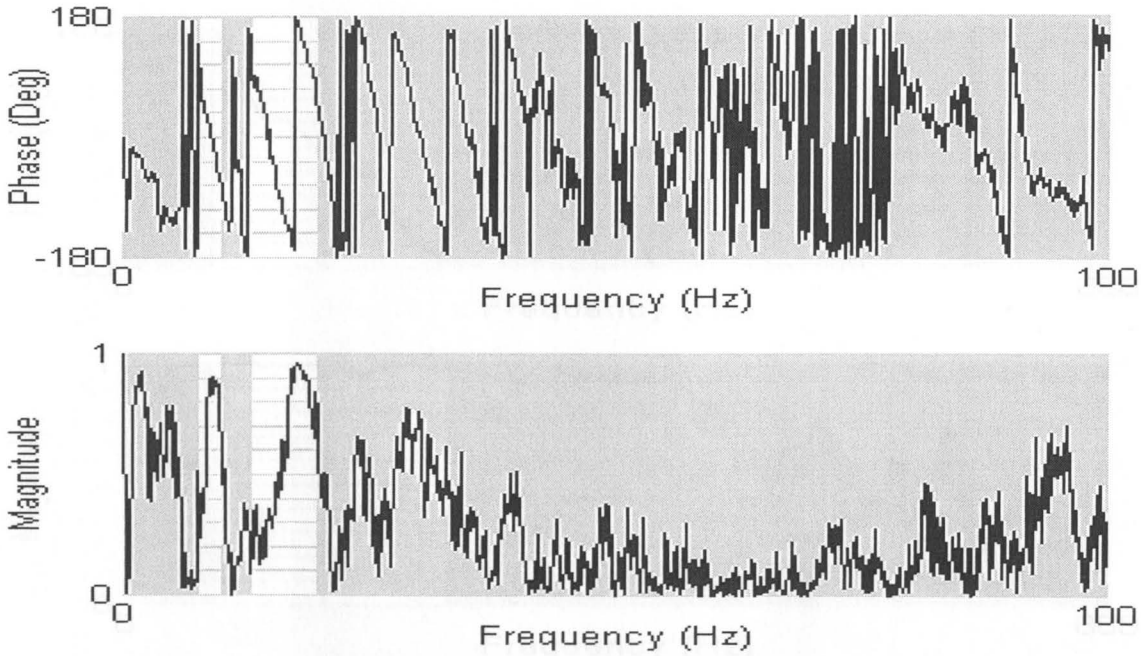

Figure A.22 Wrapped phase of the cross power spectrum (top), and corresponding coherence function (bottom), for the 16-meter spacing forward profile measured at Site C South Centerline.

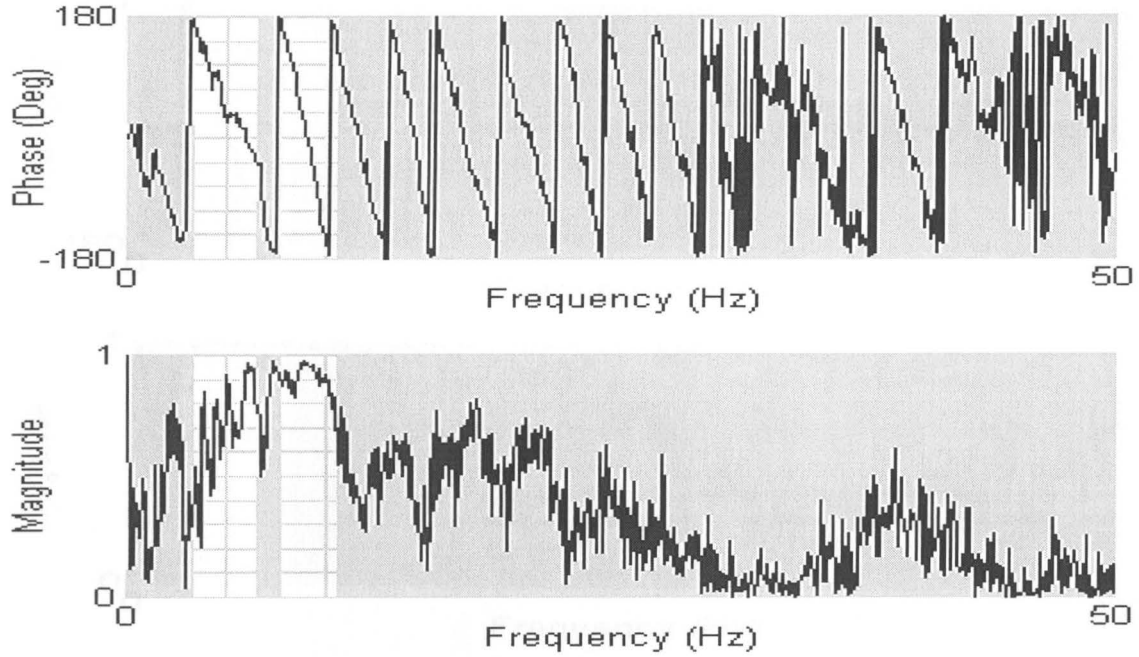

Figure A.23 Wrapped phase of the cross power spectrum (top), and corresponding coherence function (bottom), for the 32-meter spacing forward profile measured at Site C South Centerline.

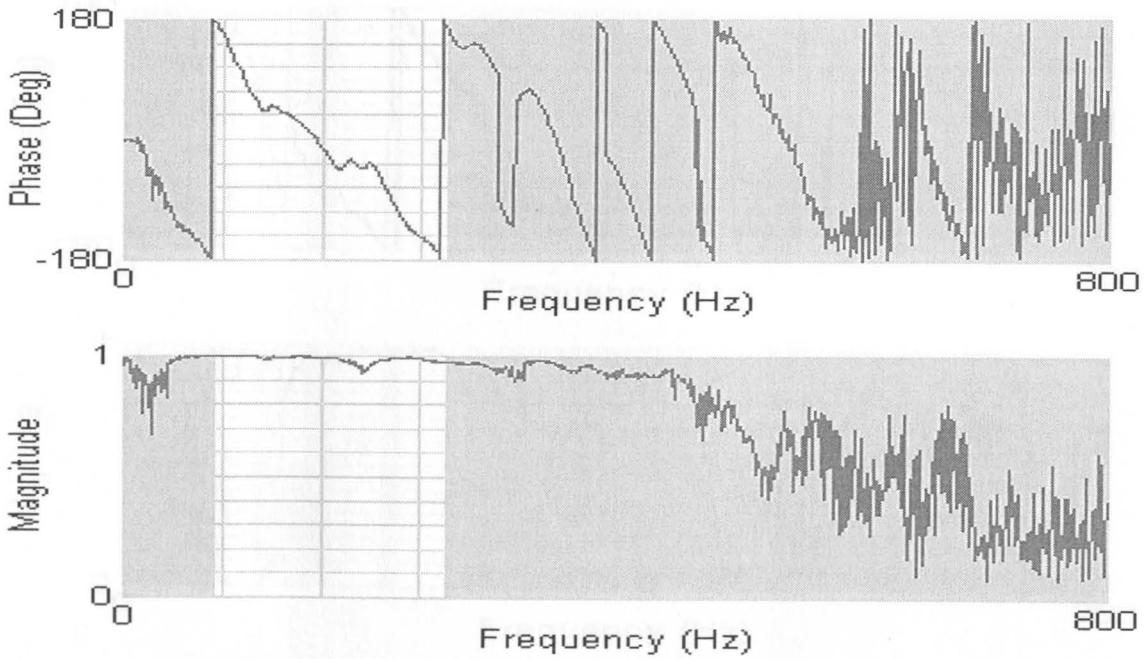

Figure A.24 Wrapped phase of the cross power spectrum (top), and corresponding coherence function (bottom), for the 1-meter spacing average profile measured at Site D, Aug. 17, 2000, Adapazari, Turkey.

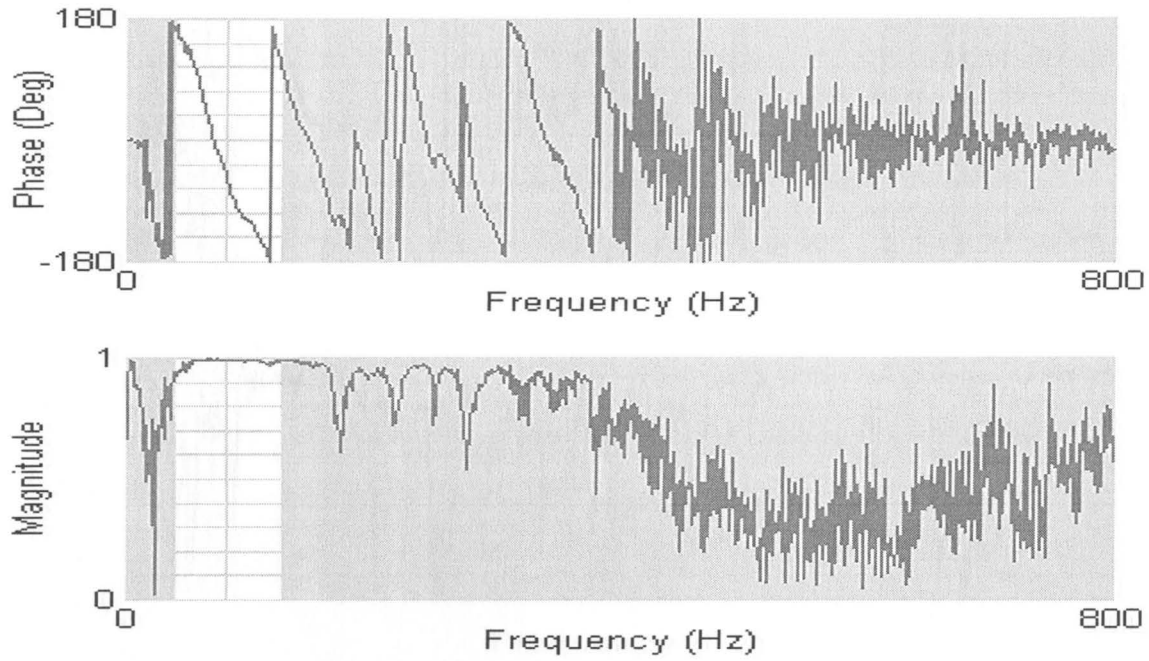

Figure A.25 Wrapped phase of the cross power spectrum (top), and corresponding coherence function (bottom), for the 2-meter spacing average profile measured at Site D.

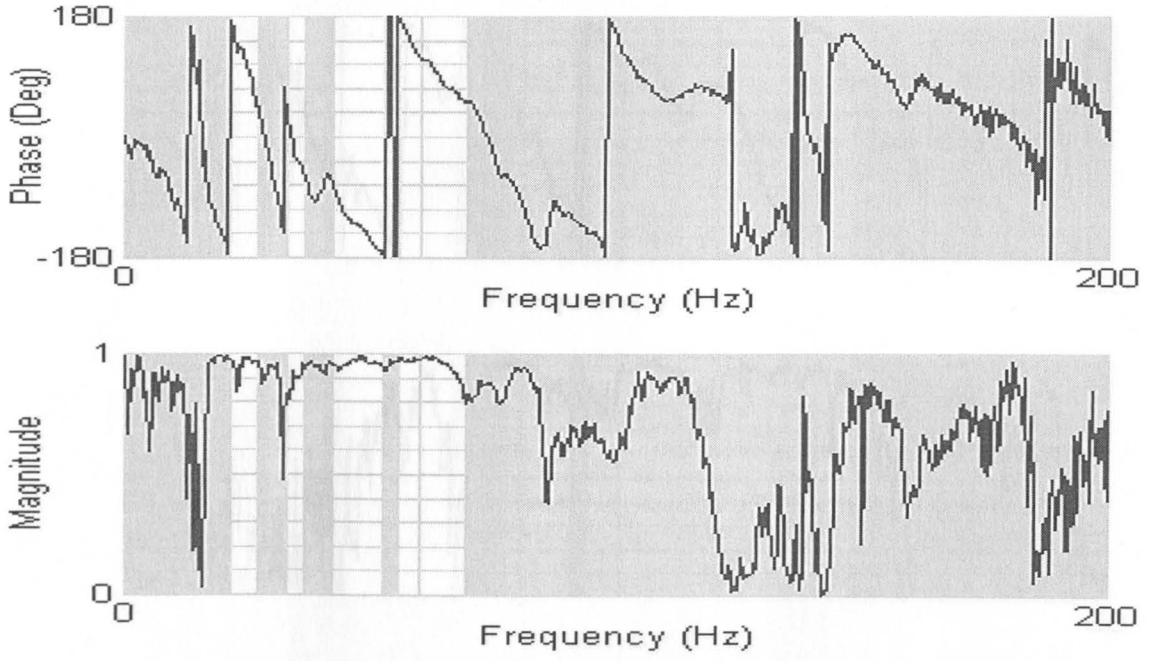

Figure A.26 Wrapped phase of the cross power spectrum (top), and corresponding coherence function (bottom), for the 4-meter spacing reverse profile measured at Site D.

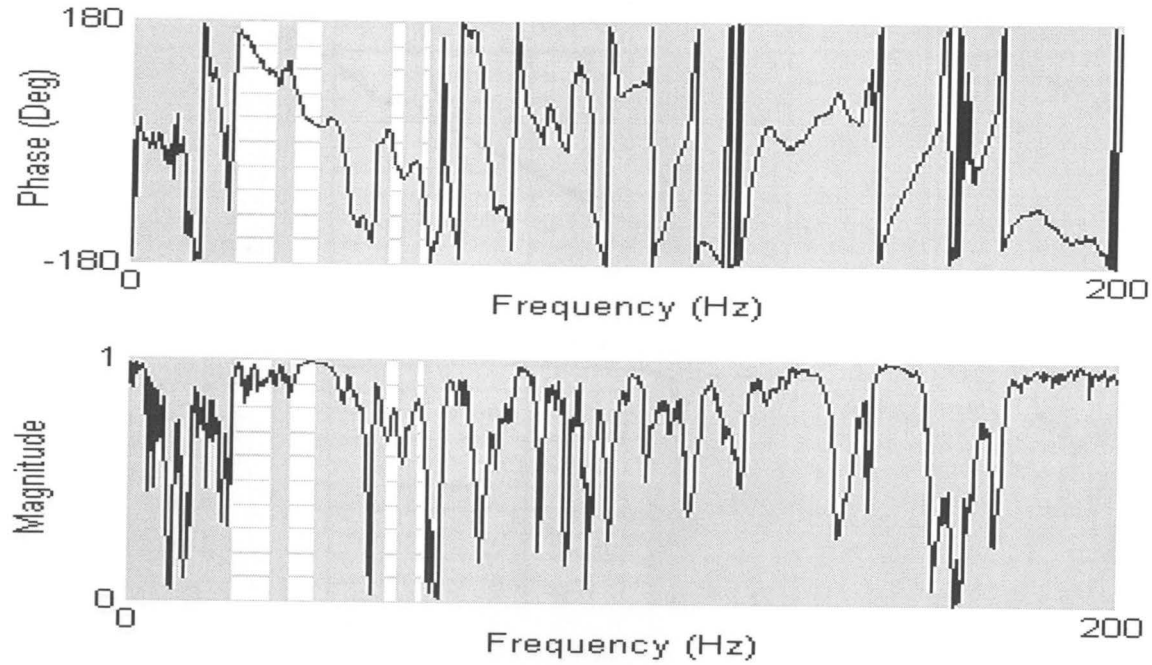

Figure A.27 Wrapped phase of the cross power spectrum (top), and corresponding coherence function (bottom), for the 8-meter spacing forward profile measured at Site D.

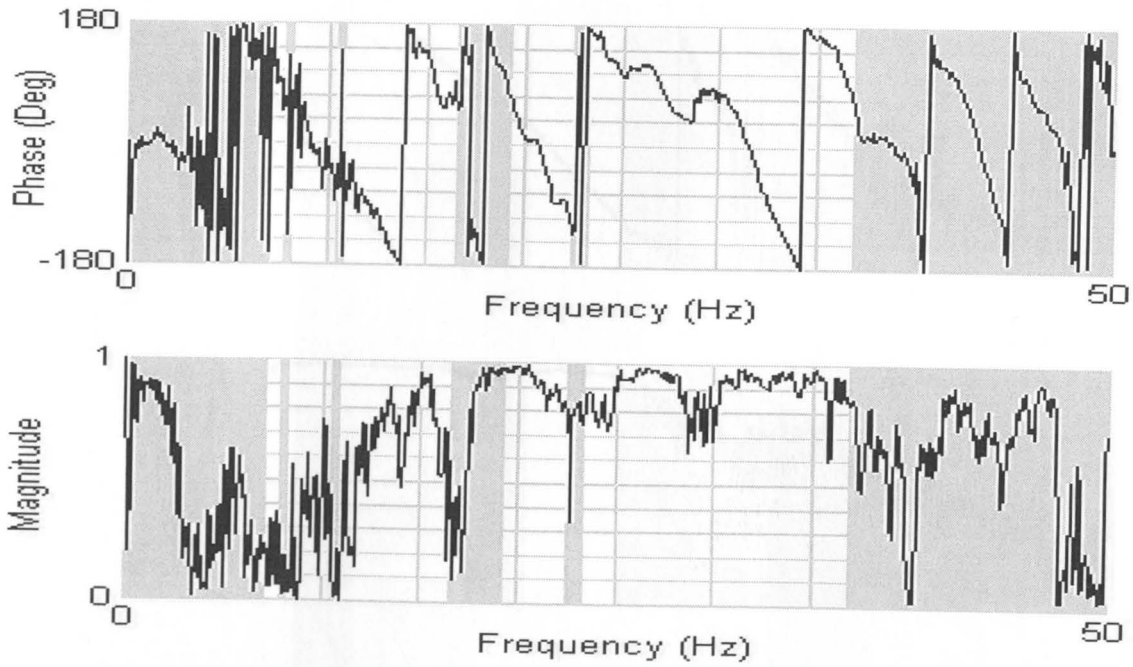

Figure A.28 Wrapped phase of the cross power spectrum (top), and corresponding coherence function (bottom), for the 16-meter spacing reverse profile measured at Site D.

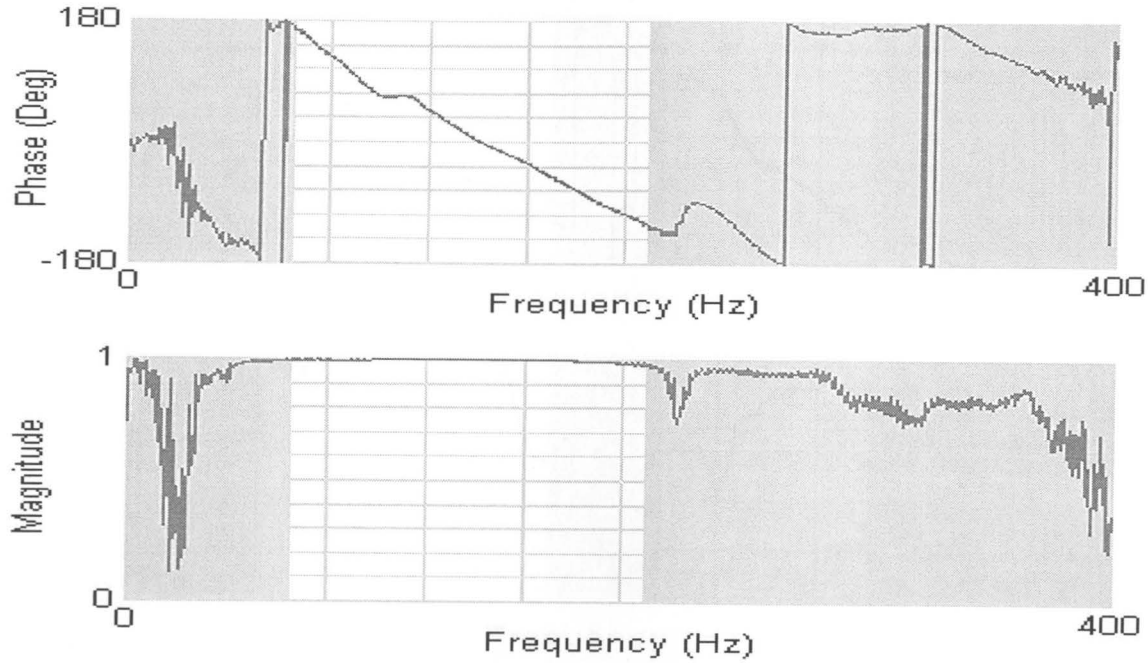

Figure A.29 Wrapped phase of the cross power spectrum (top), and corresponding coherence function (bottom), for the 1-meter spacing average profile measured at Site G, Aug. 16, 2000, Adapazari, Turkey.

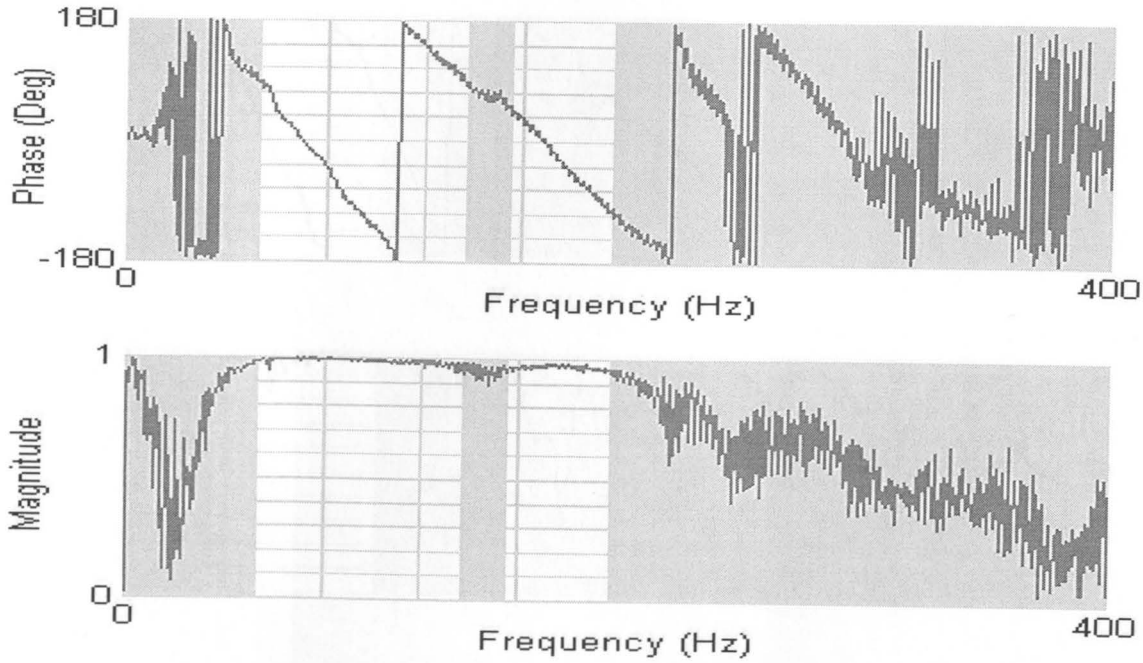

Figure A.30 Wrapped phase of the cross power spectrum (top), and corresponding coherence function (bottom), for the 2-meter spacing average profile measured at Site G.

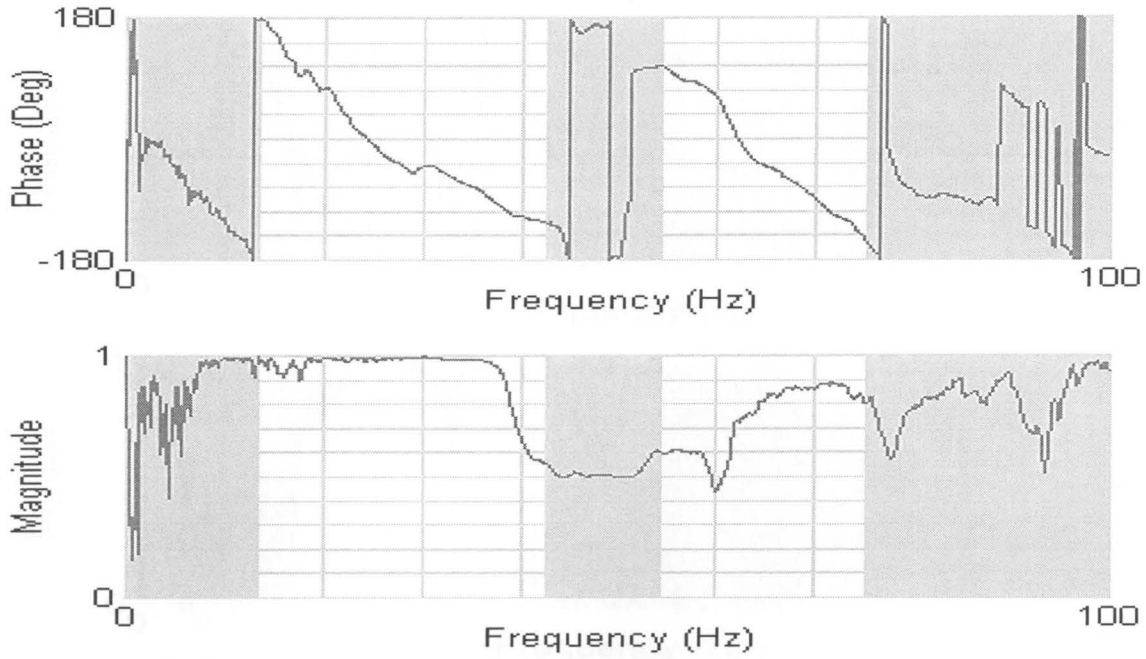

Figure A.31 Wrapped phase of the cross power spectrum (top), and corresponding coherence function (bottom), for the 4-meter spacing average profile measured at Site G.

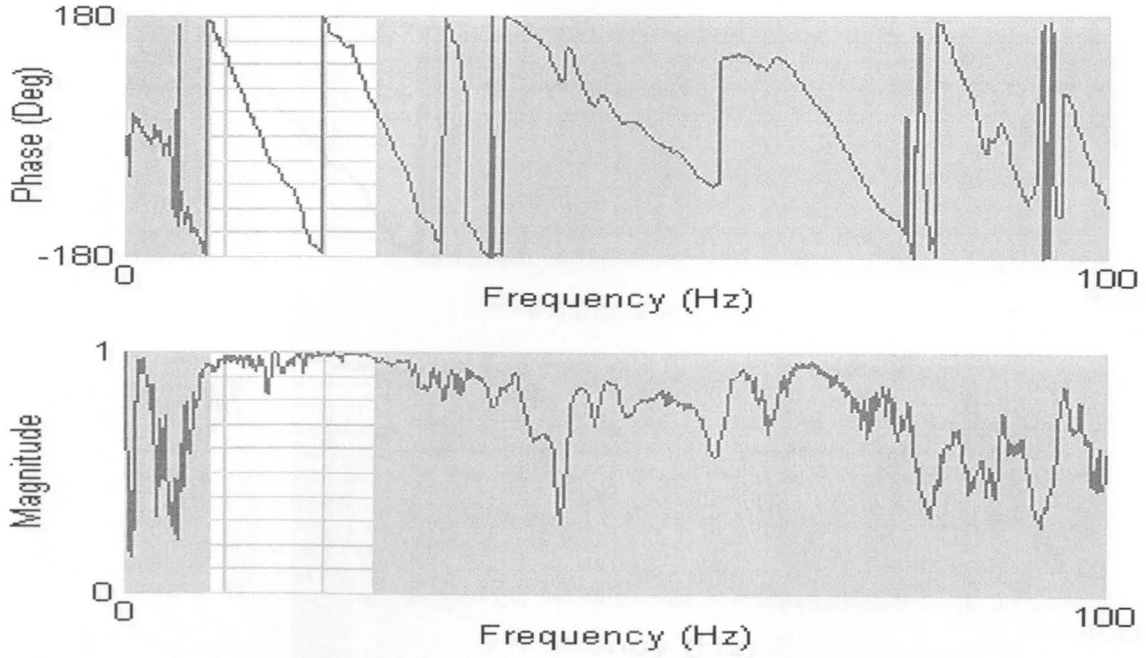

Figure A.32 Wrapped phase of the cross power spectrum (top), and corresponding coherence function (bottom), for the 8-meter spacing average profile measured at Site G.

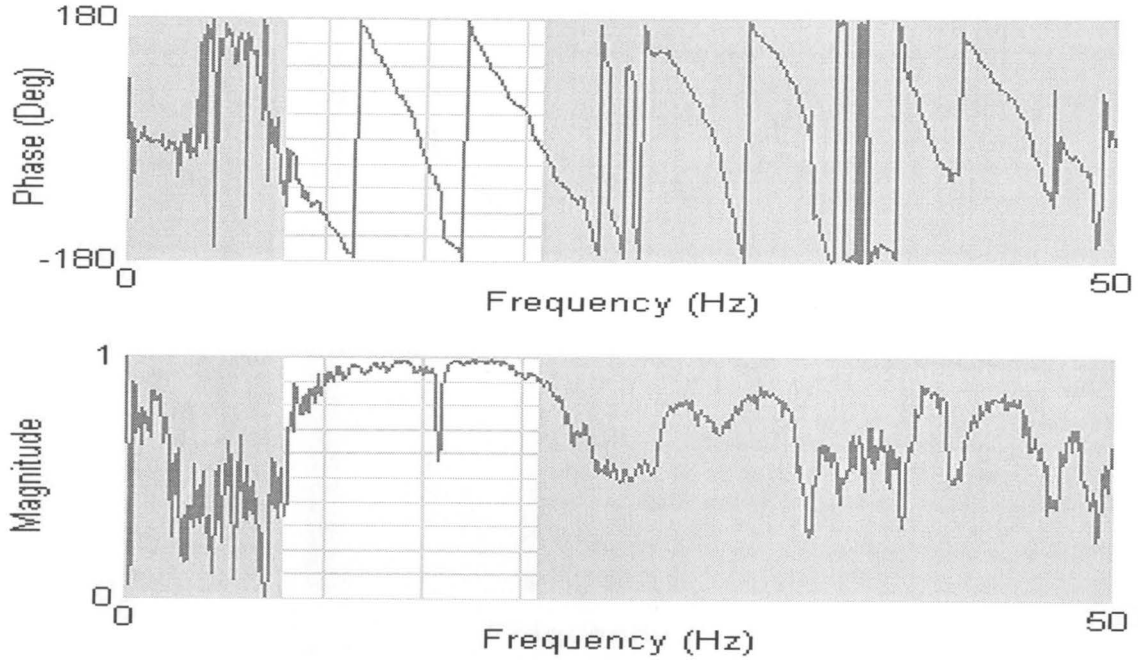

Figure A.33 Wrapped phase of the cross power spectrum (top), and corresponding coherence function (bottom), for the 16-meter spacing average profile measured at Site G.

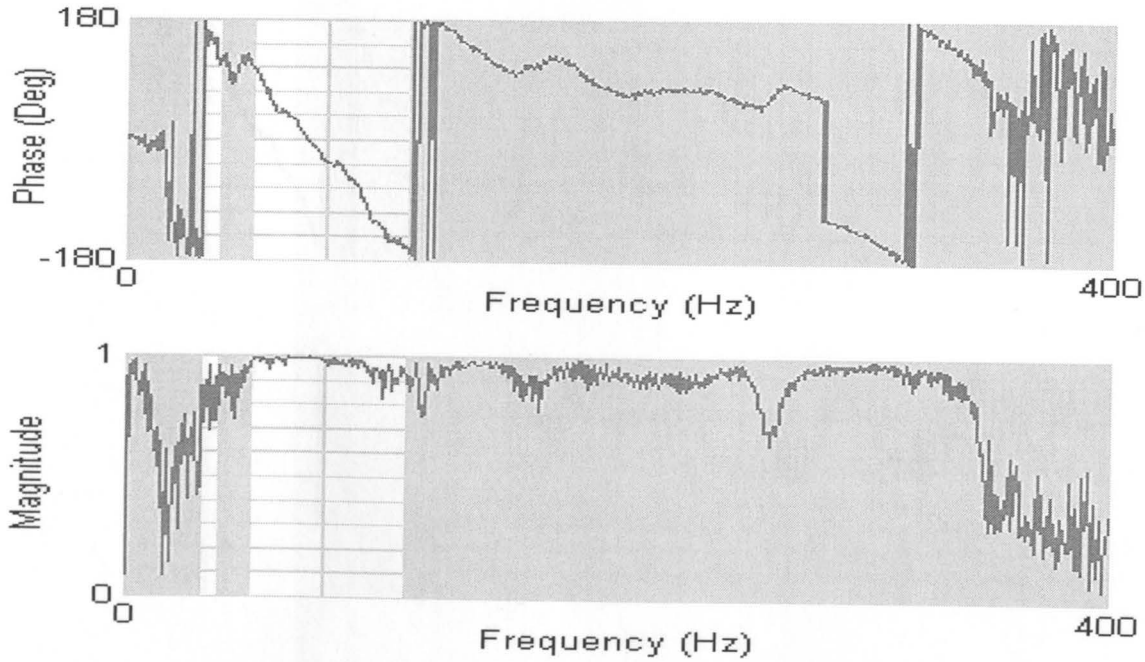

Figure A.34 Wrapped phase of the cross power spectrum (top), and corresponding coherence function (bottom), for the 2-meter spacing average profile measured at Site J, Aug. 21, 2000, Adapazari, Turkey.

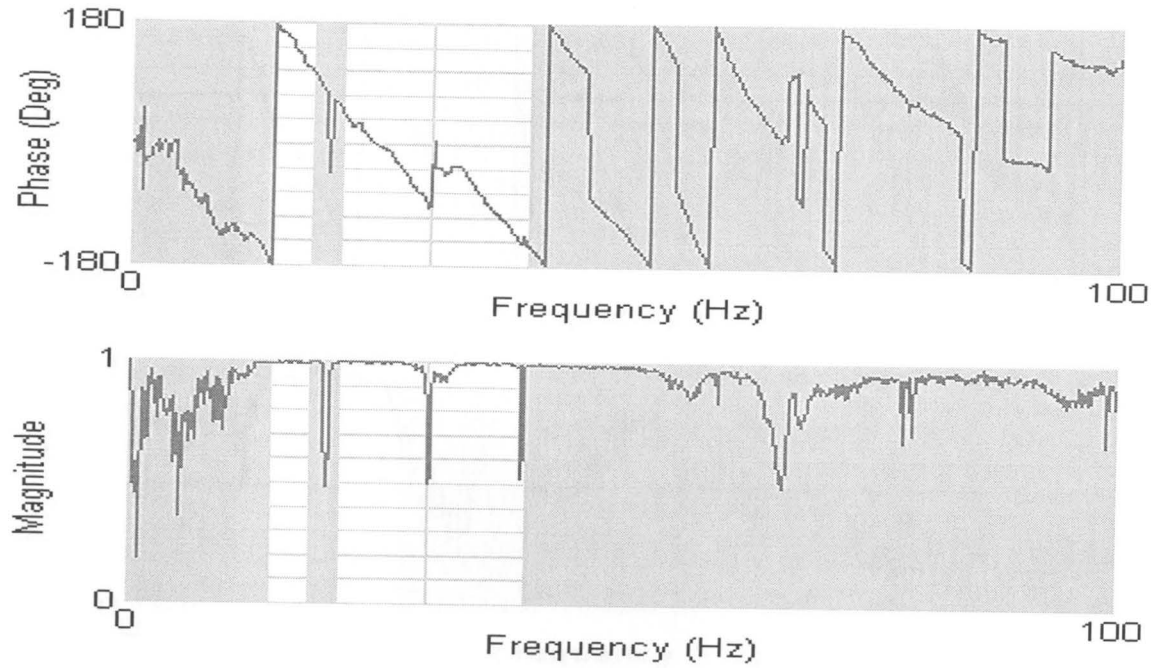

Figure A.35 Wrapped phase of the cross power spectrum (top), and corresponding coherence function (bottom), for the 4-meter spacing average profile measured at Site J.

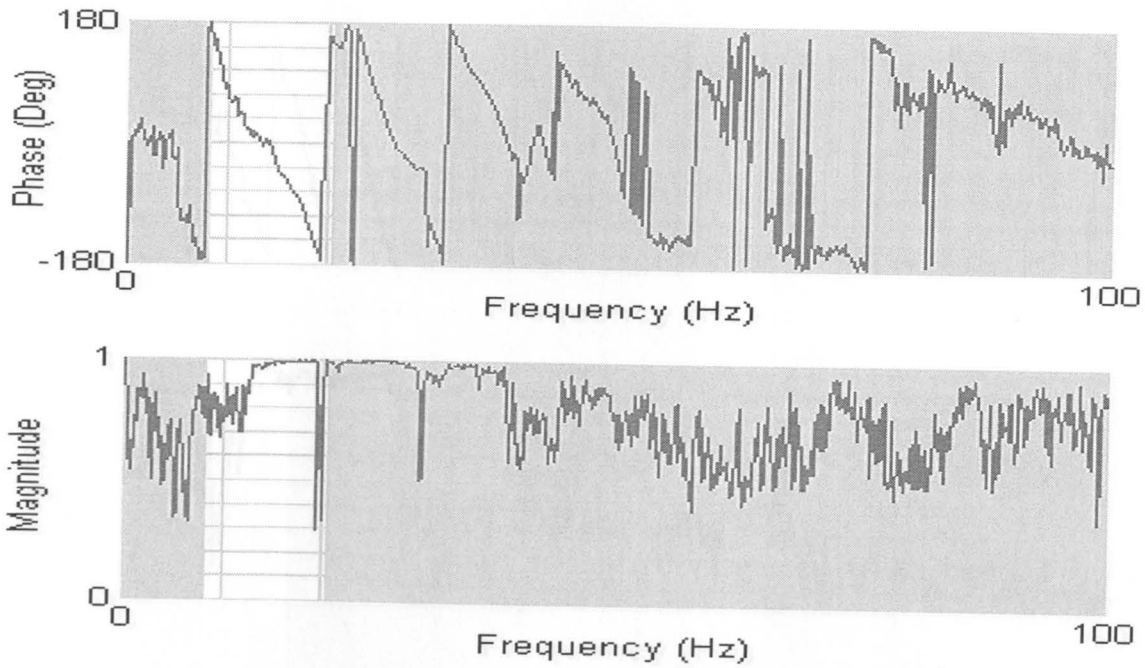

Figure A.36 Wrapped phase of the cross power spectrum (top), and corresponding coherence function (bottom), for the 8-meter spacing average profile measured at Site J.

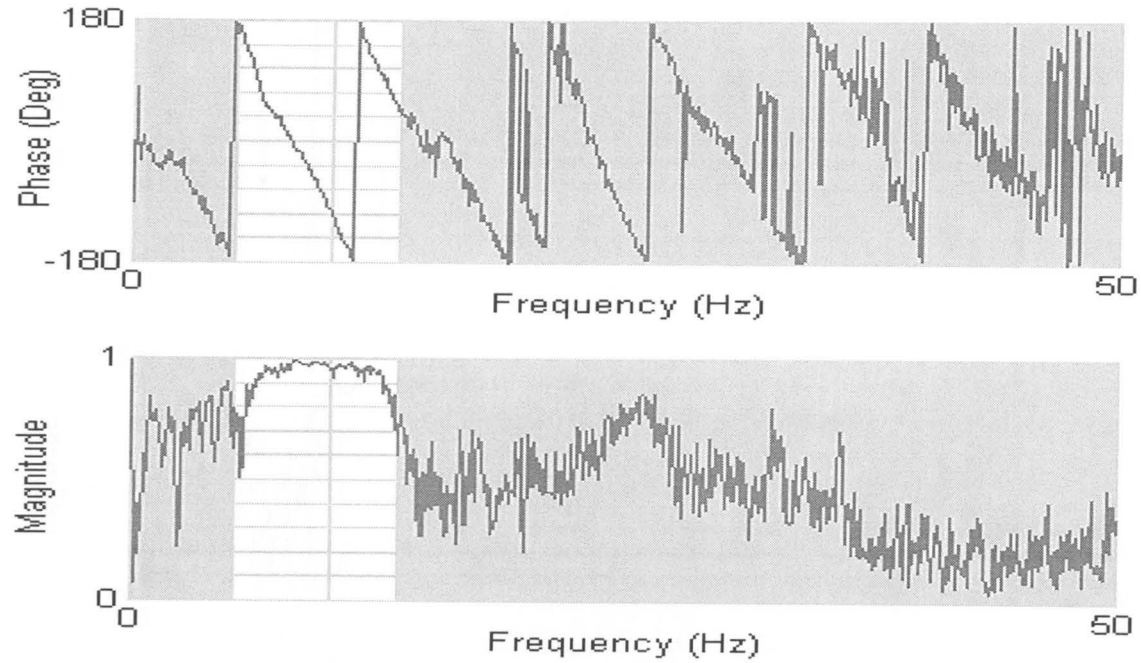

Figure A.37 Wrapped phase of the cross power spectrum (top), and corresponding coherence function (bottom), for the 16-meter spacing average profile measured at Site J.

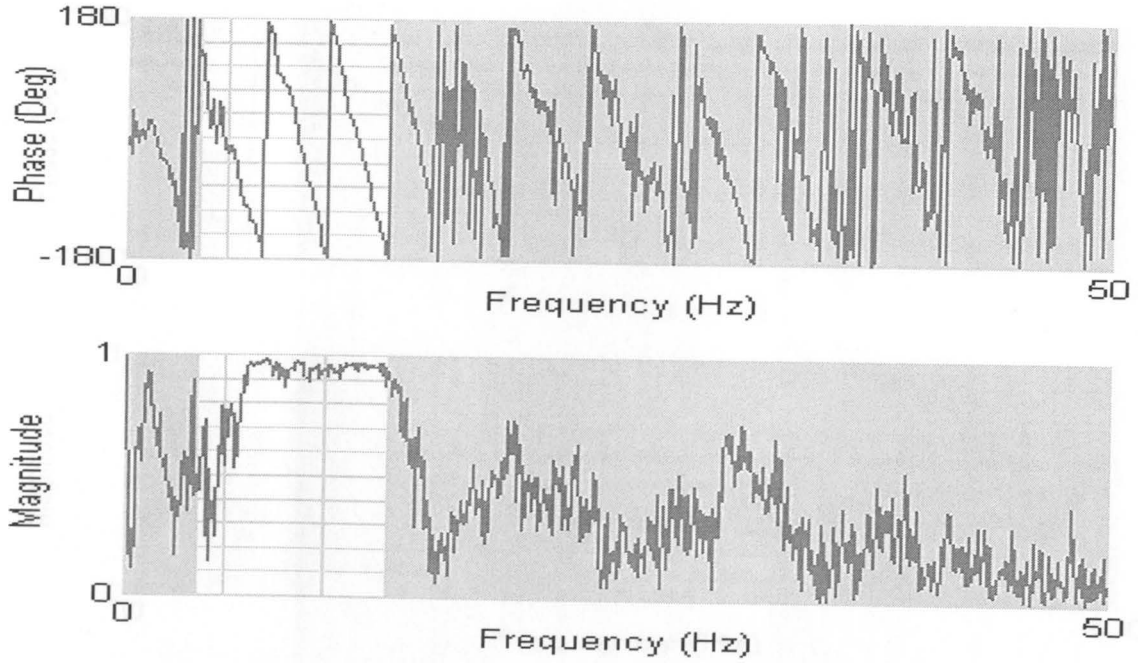

Figure A.38 Wrapped phase of the cross power spectrum (top), and corresponding coherence function (bottom), for the 32-meter spacing average profile measured at Site J.

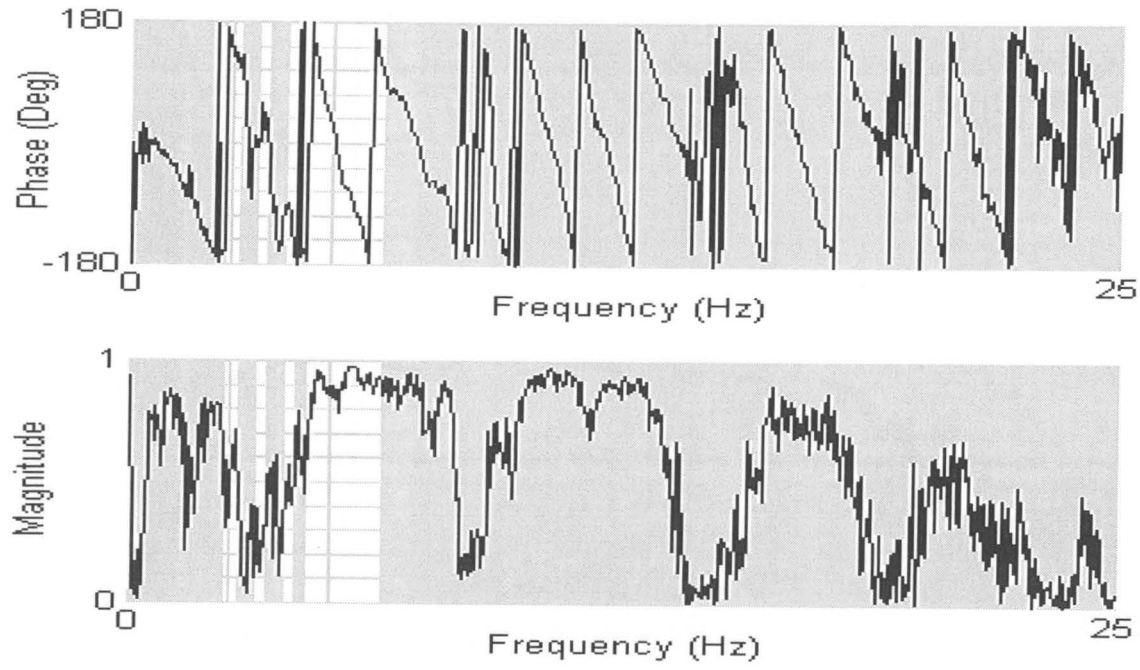

Figure A.39 Wrapped phase of the cross power spectrum (top), and corresponding coherence function (bottom), for the 64-meter spacing forward profile measured at Site J.

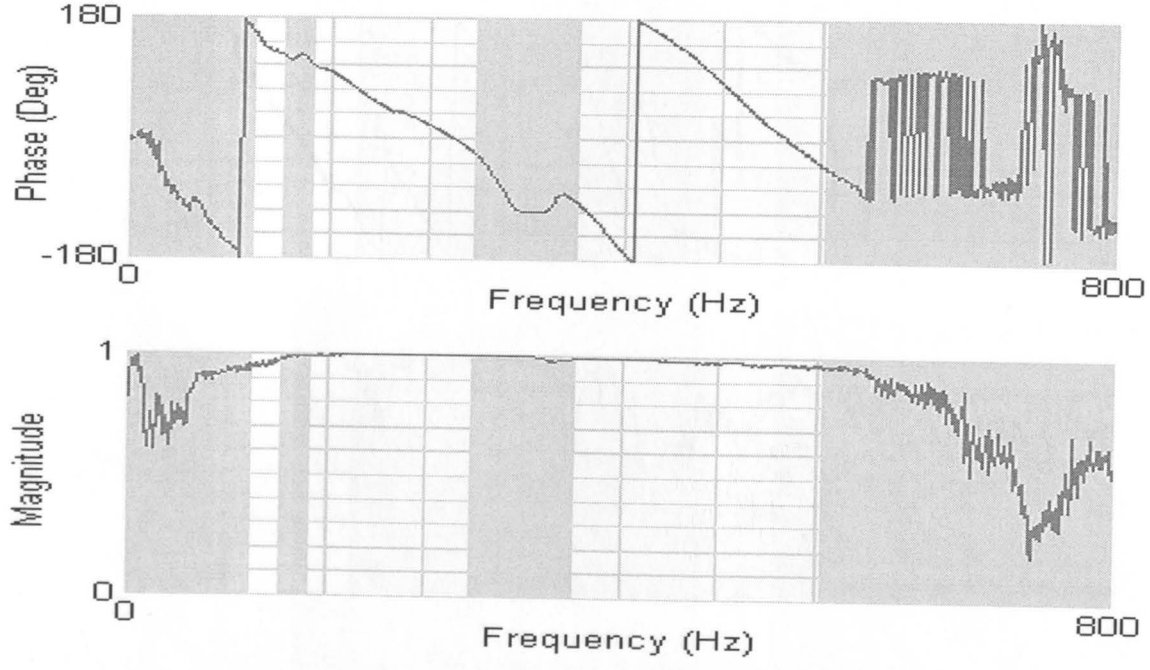

Figure A.40 Wrapped phase of the cross power spectrum (top), and corresponding coherence function (bottom), for the 1-meter spacing average profile measured at Site BYU 1-11, Aug. 15, 2000, Adapazari, Turkey.

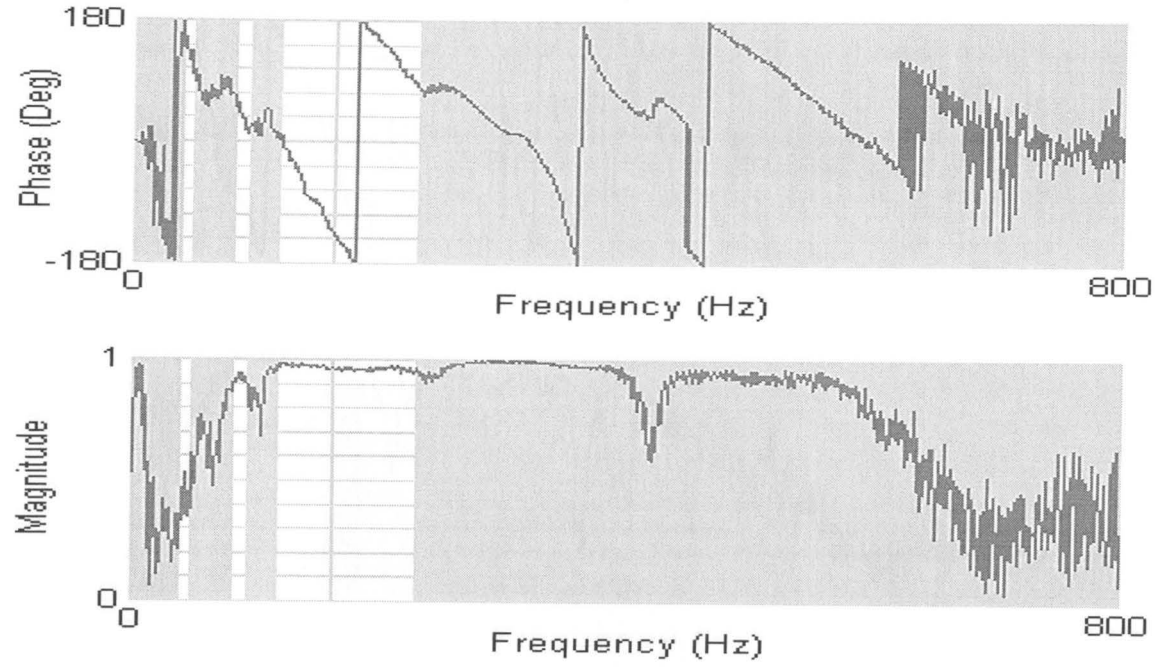

Figure A.41 Wrapped phase of the cross power spectrum (top), and corresponding coherence function (bottom), for the 2-meter spacing average profile measured at Site BYU 1-11.

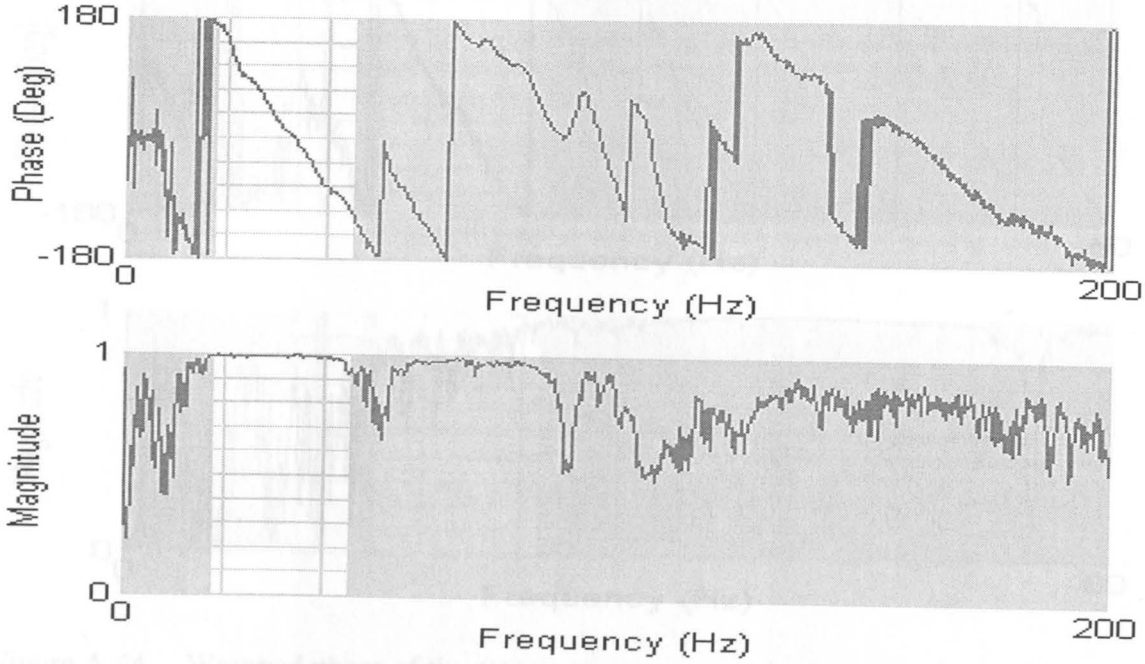

Figure A.42 Wrapped phase of the cross power spectrum (top), and corresponding coherence function (bottom), for the 4-meter spacing average profile measured at Site BYU 1-11.

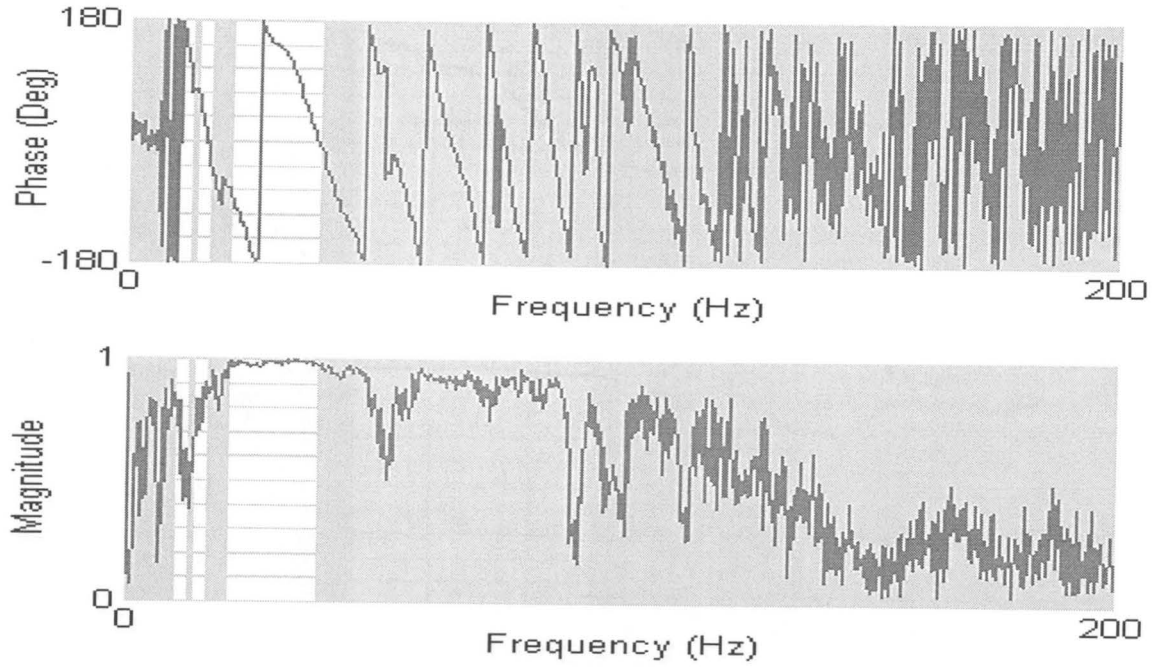

Figure A.43 Wrapped phase of the cross power spectrum (top), and corresponding coherence function (bottom), for the 8-meter spacing average profile measured at Site BYU 1-11.

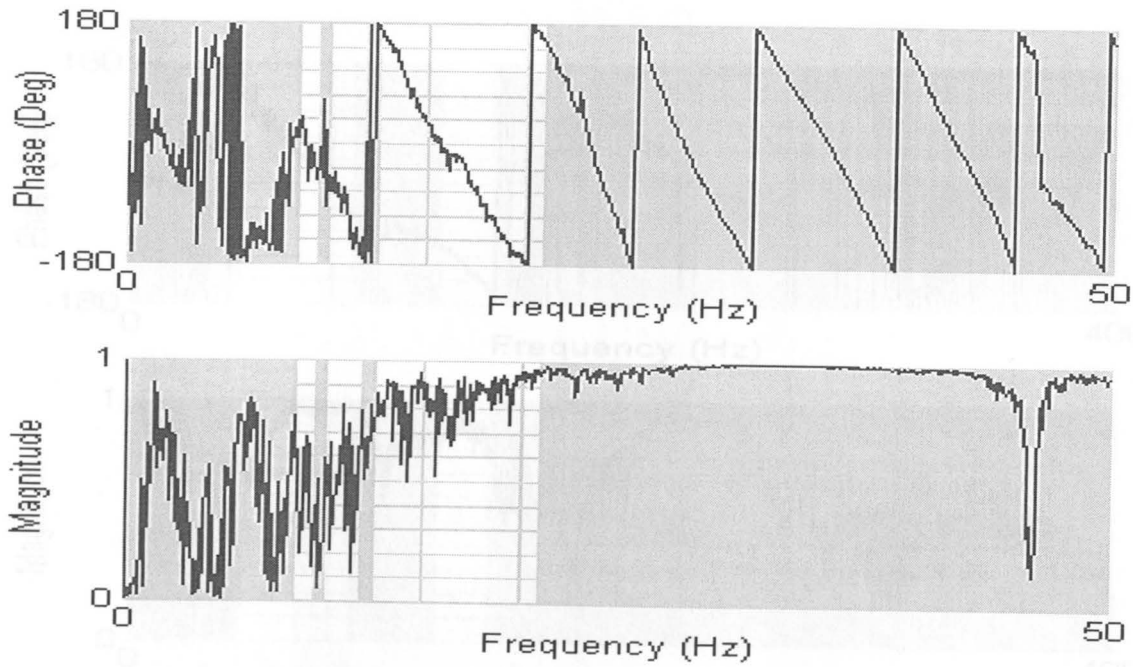

Figure A.44 Wrapped phase of the cross power spectrum (top), and corresponding coherence function (bottom), for the 16-meter spacing reverse profile measured at Site BYU 1-11.

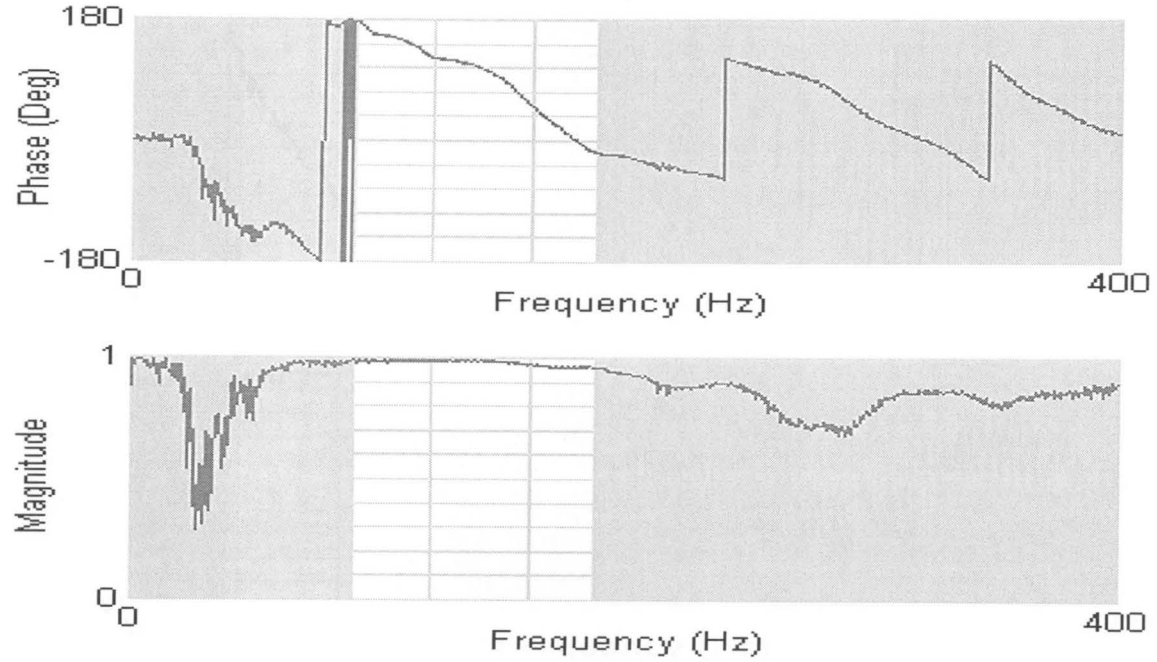

Figure A.45 Wrapped phase of the cross power spectrum (top), and corresponding coherence function (bottom), for the 1-meter spacing average profile measured at Site BYU 1-24, Aug. 15, 2000, Adapazari, Turkey.

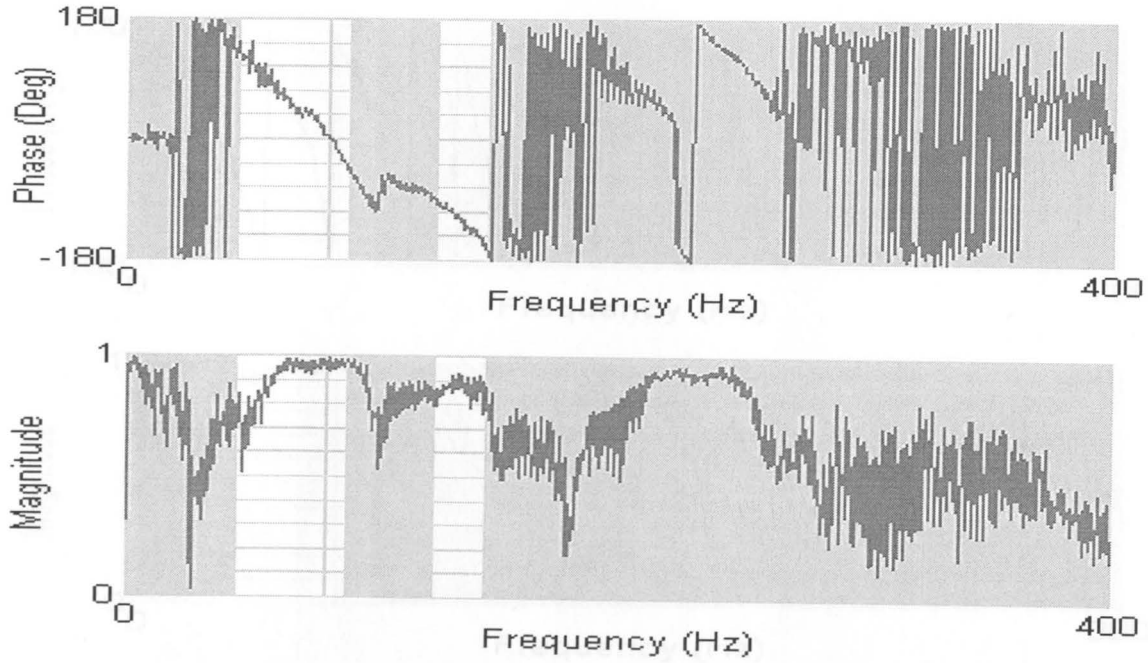

Figure A.46 Wrapped phase of the cross power spectrum (top), and corresponding coherence function (bottom), for the 2-meter spacing average profile measured at Site BYU 1-24.

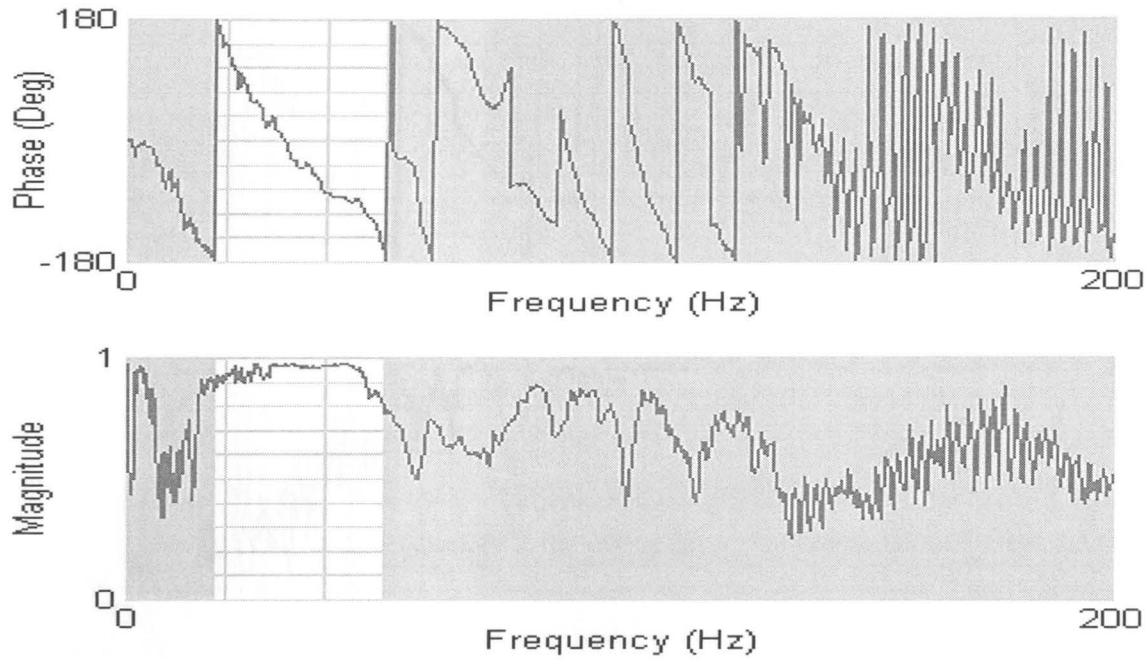

Figure A.47 Wrapped phase of the cross power spectrum (top), and corresponding coherence function (bottom), for the 4-meter spacing average profile measured at Site BYU 1-24.

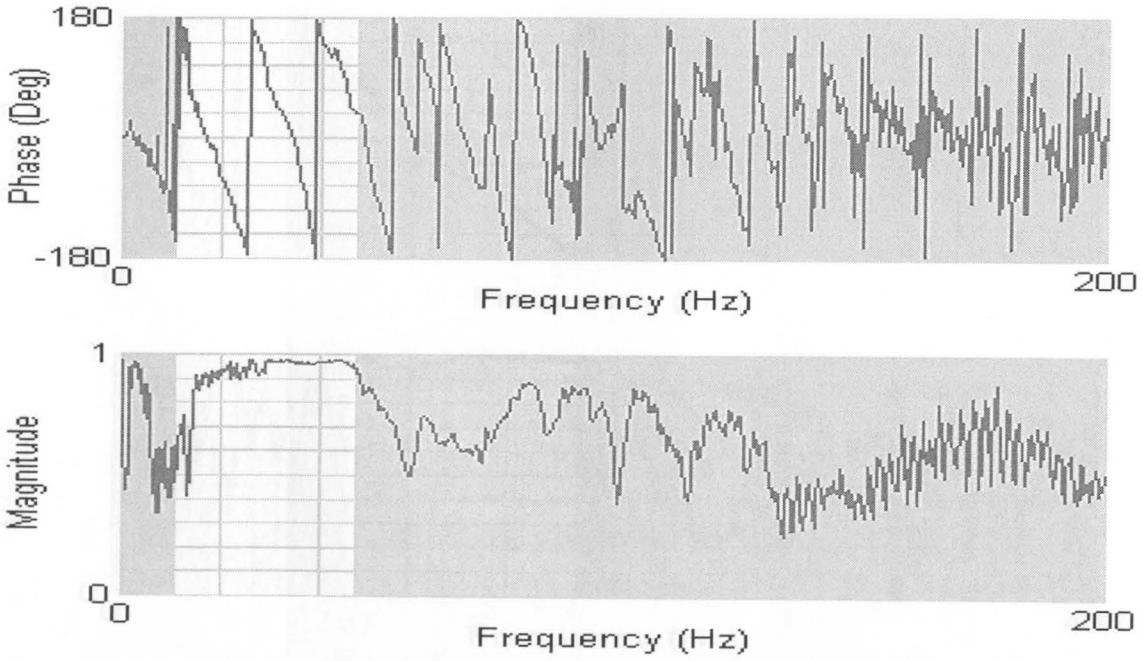

Figure A.48 Wrapped phase of the cross power spectrum (top), and corresponding coherence function (bottom), for the 8-meter spacing average profile measured at Site BYU 1-24.

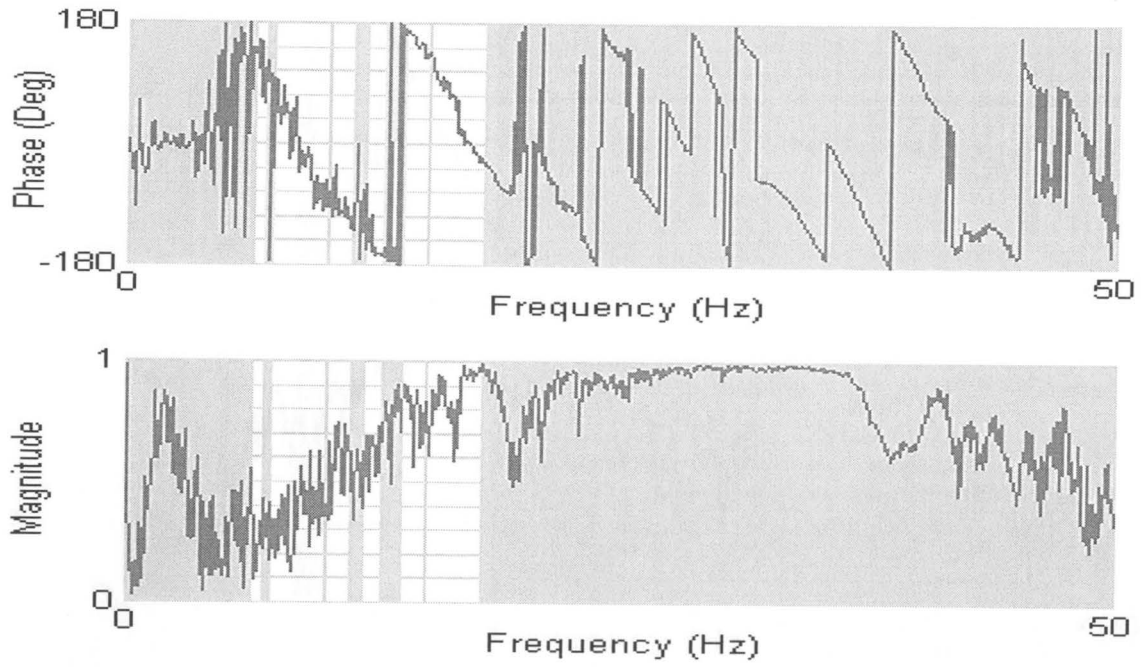

Figure A.49 Wrapped phase of the cross power spectrum (top), and corresponding coherence function (bottom), for the 16-meter spacing average profile measured at Site BYU 1-24.

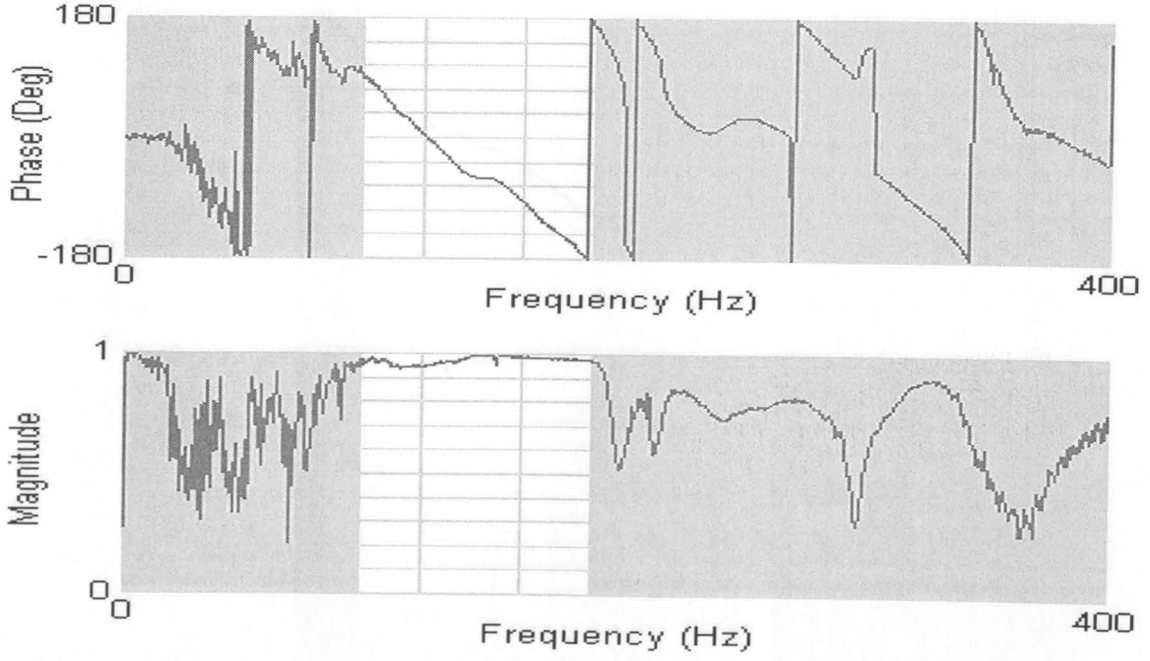

Figure A.50 Wrapped phase of the cross power spectrum (top), and corresponding coherence function (bottom), for the 1-meter spacing average profile measured at Site BYU 1-41, Aug. 17, 2000, Adapazari, Turkey.

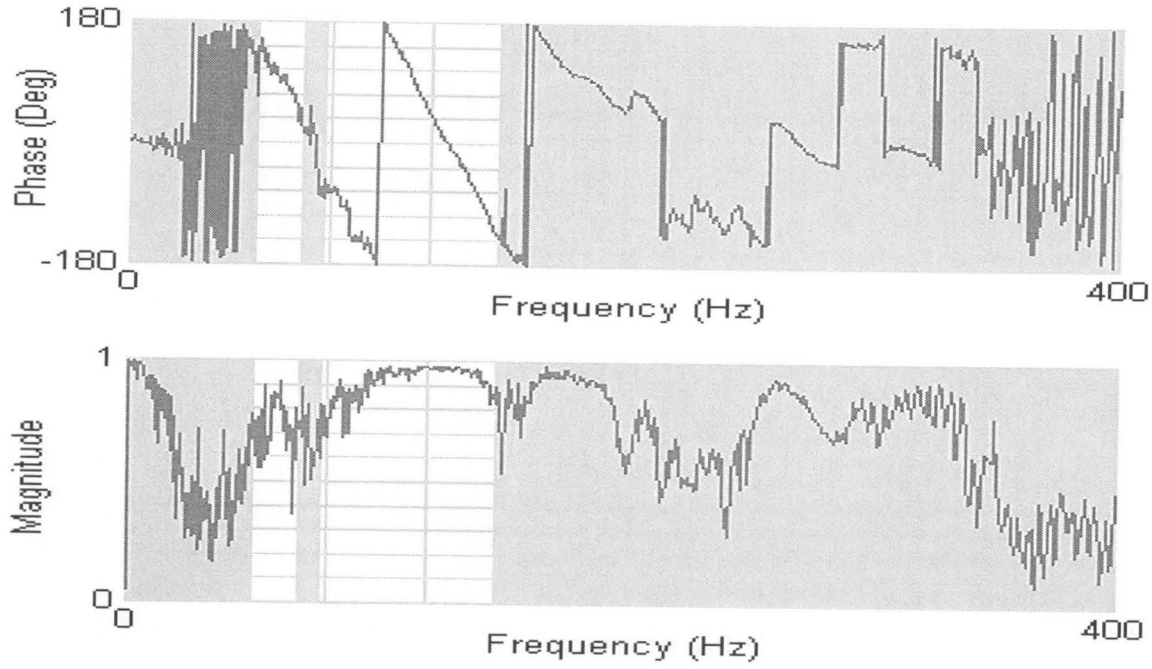

Figure A.51 Wrapped phase of the cross power spectrum (top), and corresponding coherence function (bottom), for the 2-meter spacing average profile measured at Site BYU 1-41.

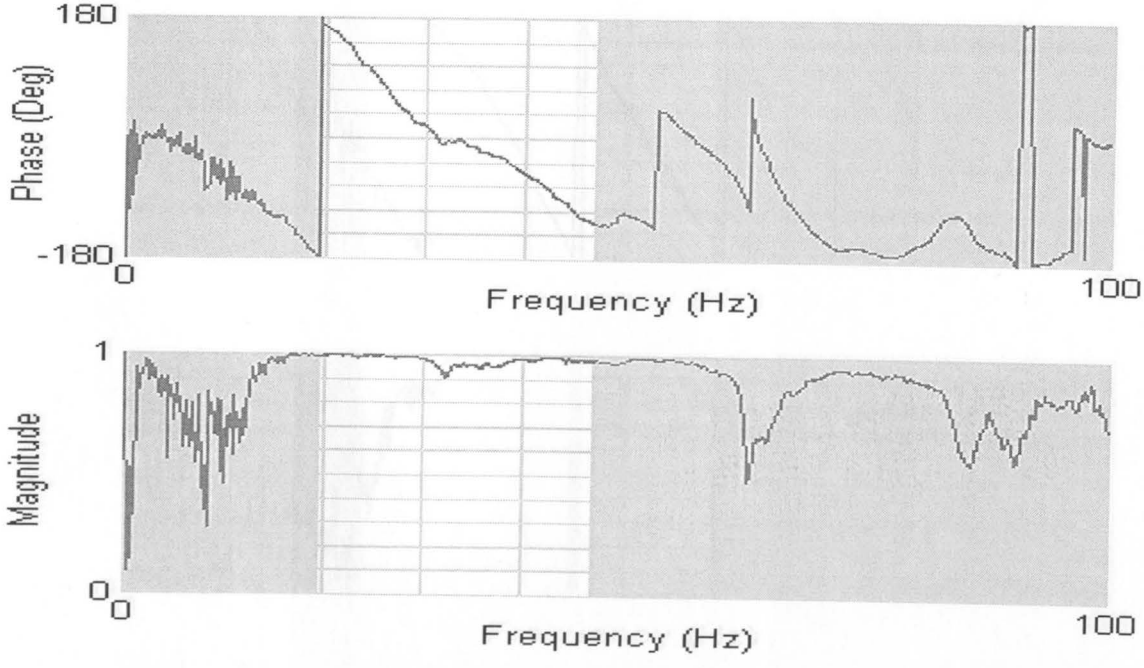

Figure A.52 Wrapped phase of the cross power spectrum (top), and corresponding coherence function (bottom), for the 4-meter spacing average profile measured at Site BYU 1-41.

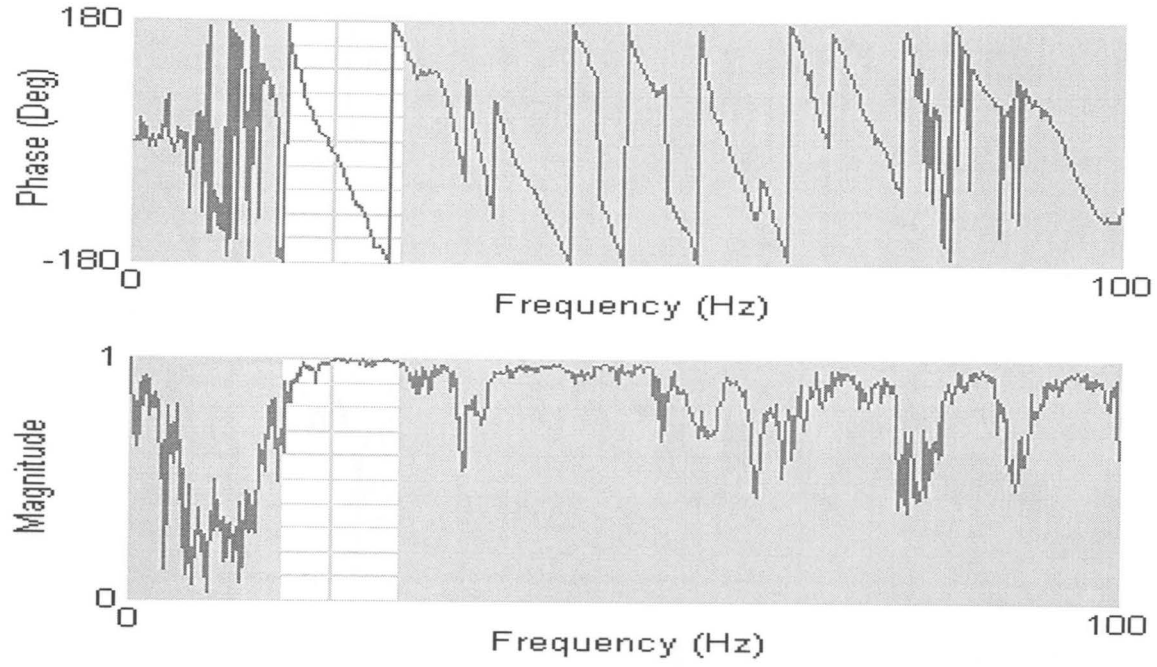

Figure A.53 Wrapped phase of the cross power spectrum (top), and corresponding coherence function (bottom), for the 8-meter spacing average profile measured at Site BYU 1-41.

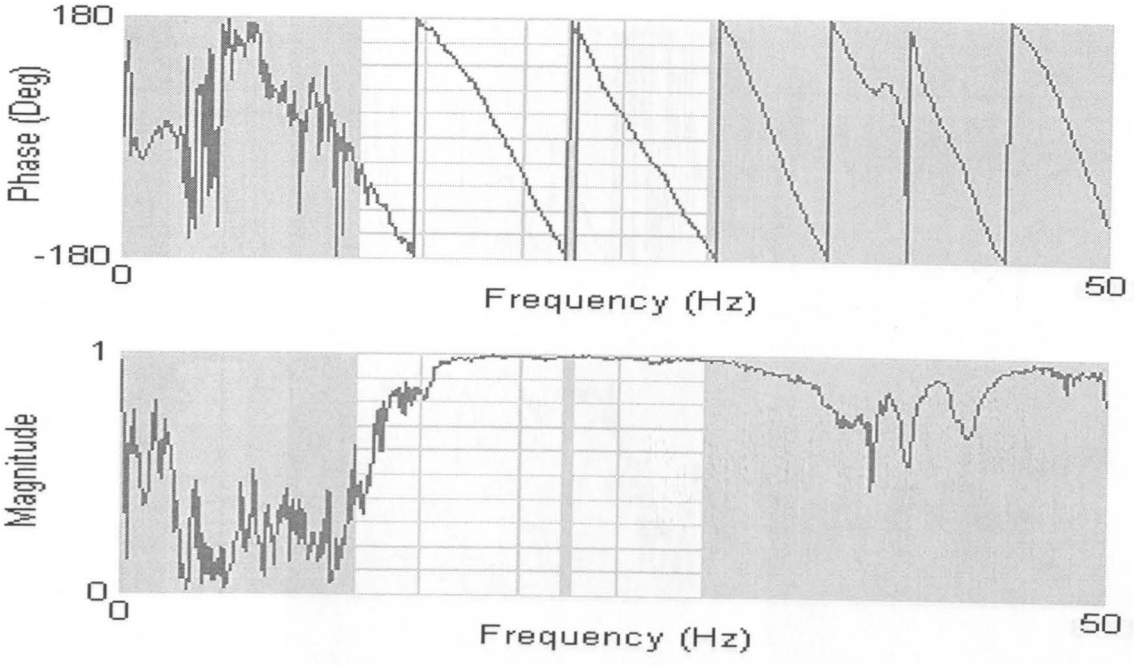

Figure A.54 Wrapped phase of the cross power spectrum (top), and corresponding coherence function (bottom), for the 16-meter spacing average profile measured at Site BYU 1-41.

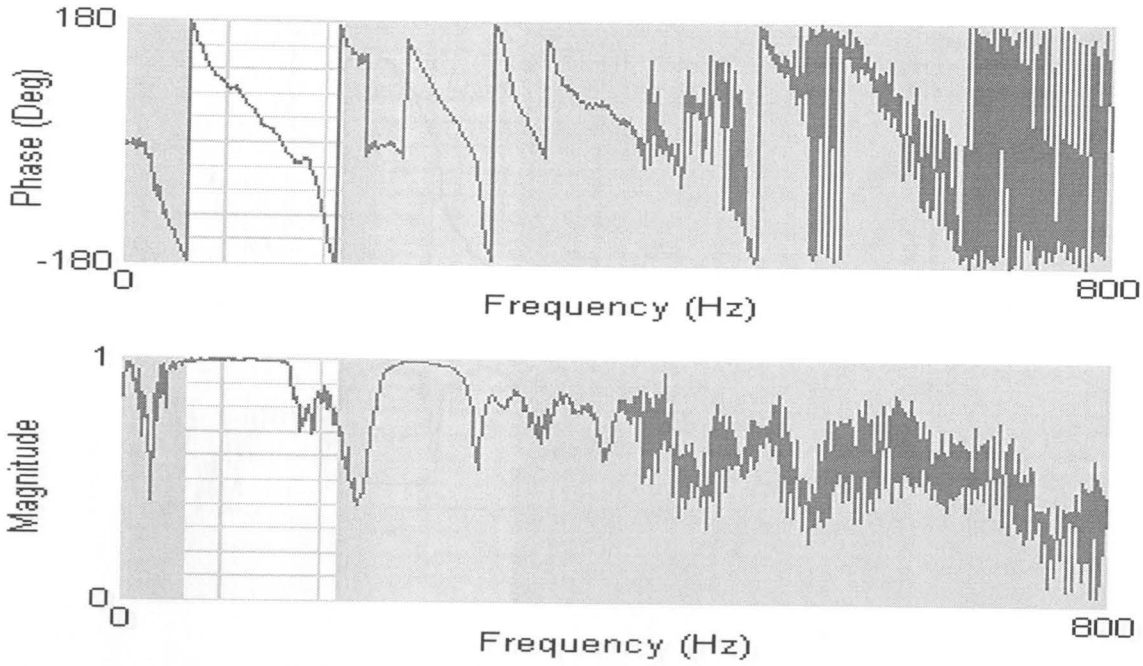

Figure A.55 Wrapped phase of the cross power spectrum (top), and corresponding coherence function (bottom), for the 1-meter spacing average profile measured at Site BYU 1-42, Aug. 17, 2000, Adapazari, Turkey.

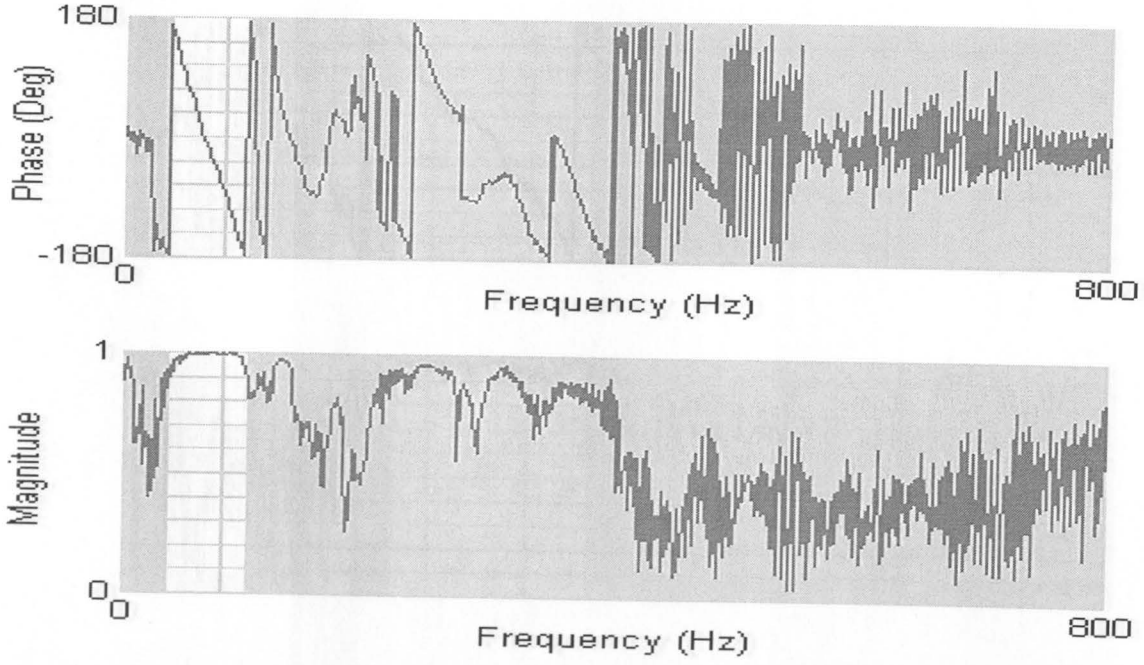

Figure A.56 Wrapped phase of the cross power spectrum (top), and corresponding coherence function (bottom), for the 2-meter spacing average profile measured at Site BYU 1-42.

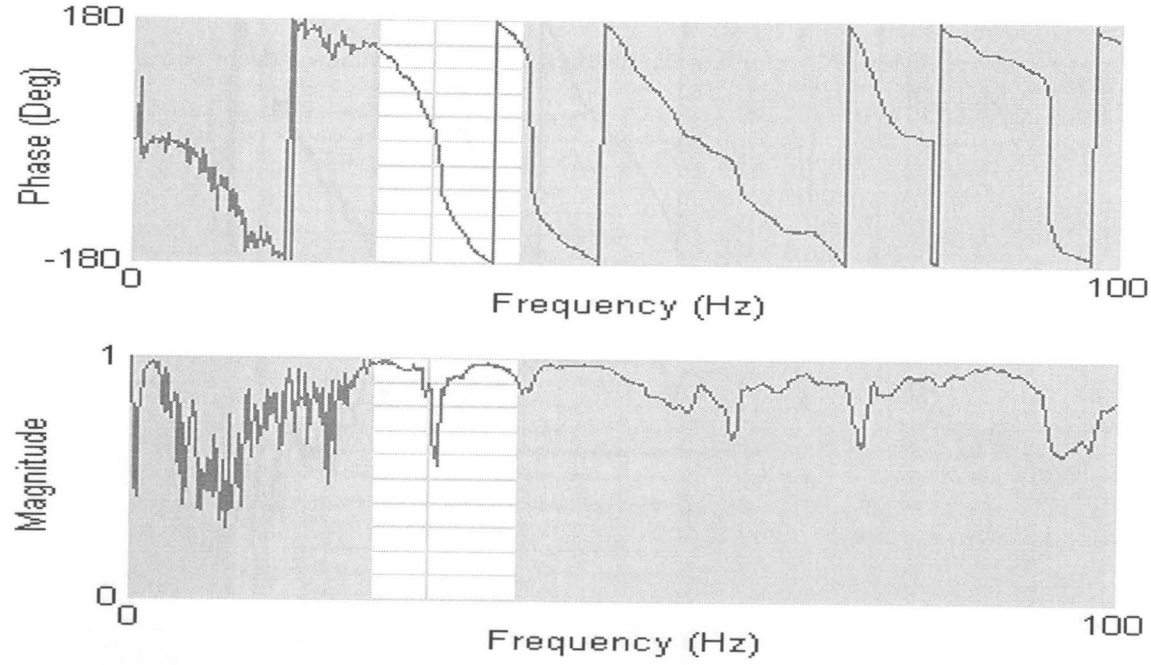

Figure A.57 Wrapped phase of the cross power spectrum (top), and corresponding coherence function (bottom), for the 4-meter spacing average profile measured at Site BYU 1-42.

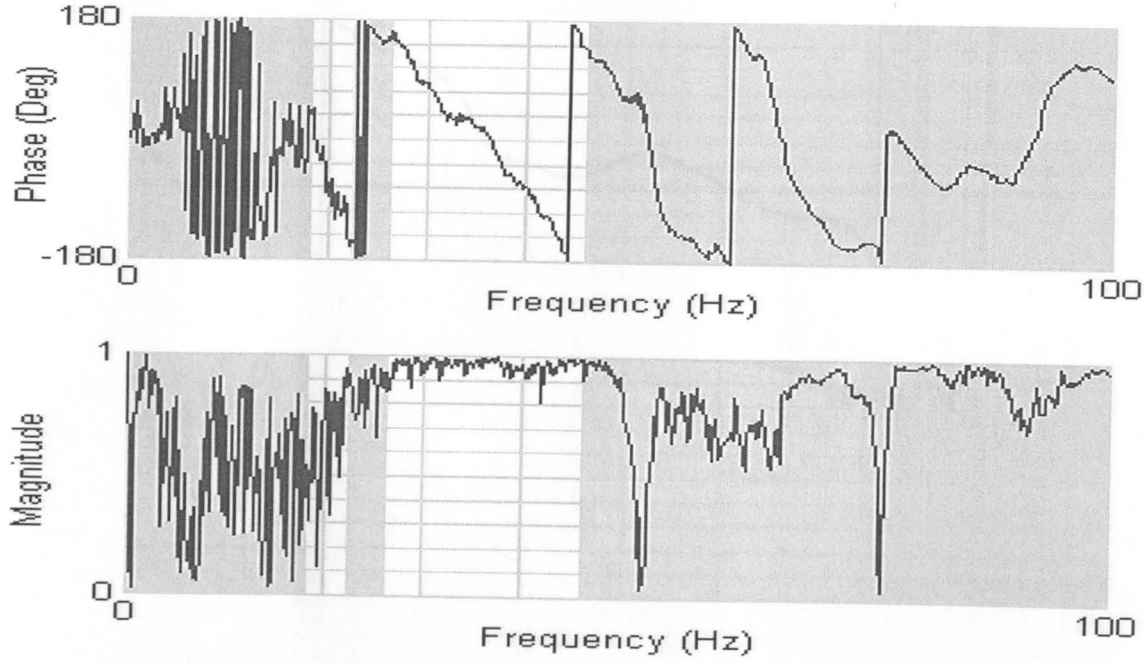

Figure A.58 Wrapped phase of the cross power spectrum (top), and corresponding coherence function (bottom), for the 8-meter spacing reverse profile measured at Site BYU 1-42.

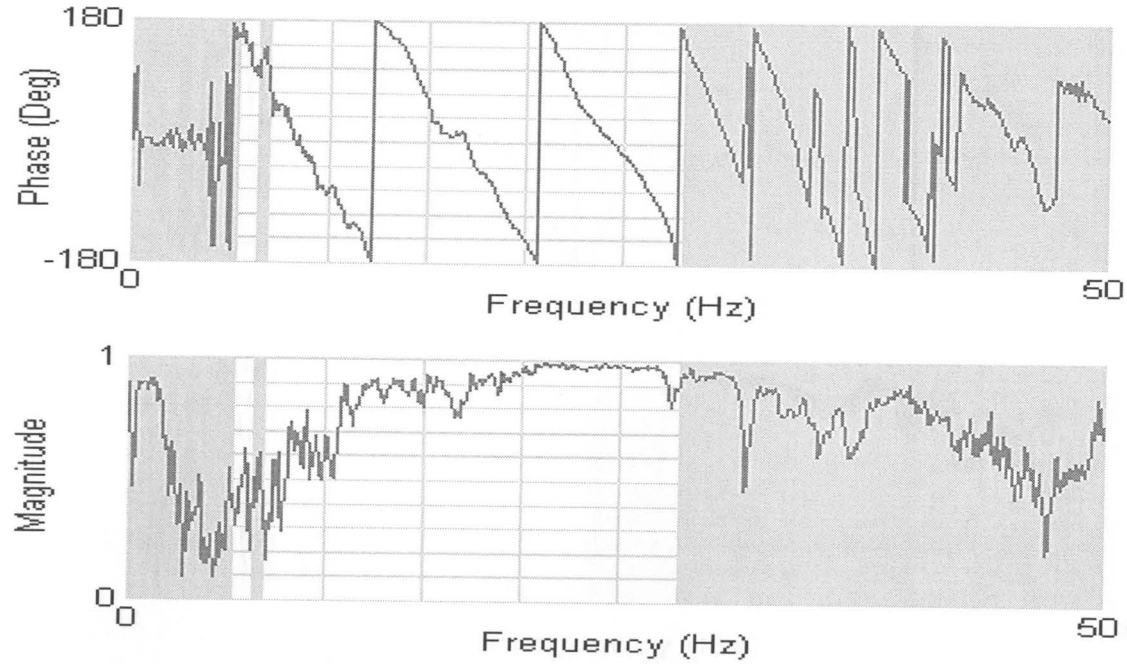

Figure A.59 Wrapped phase of the cross power spectrum (top), and corresponding coherence function (bottom), for the 16-meter spacing average profile measured at Site BYU 1-42.

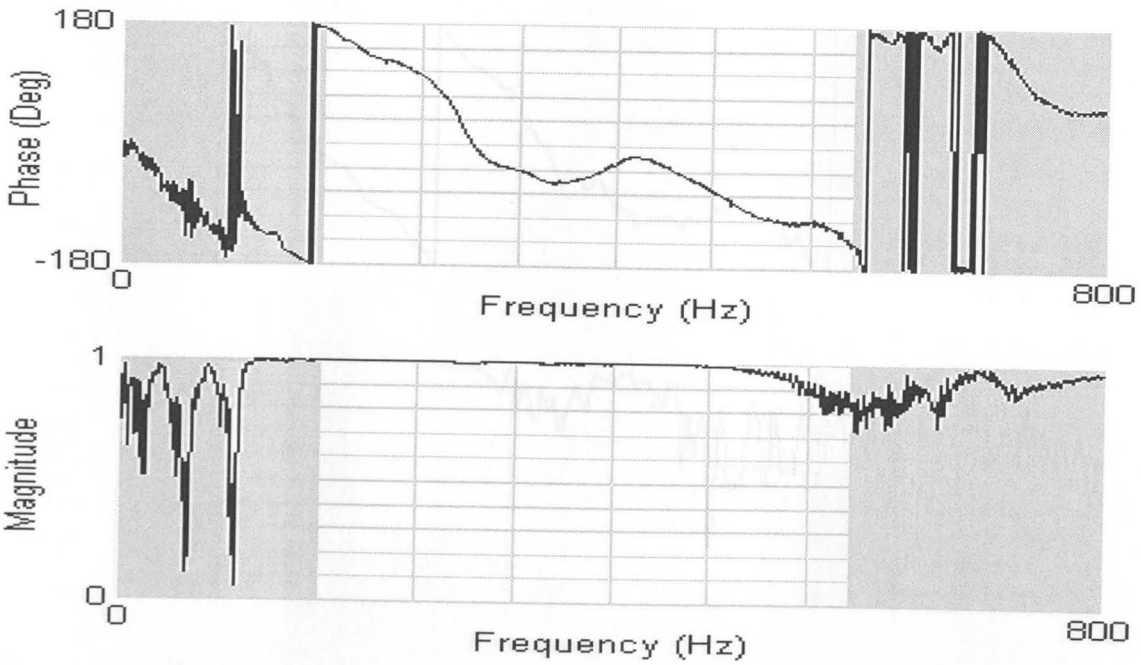

Figure A.60 Wrapped phase of the cross power spectrum (top), and corresponding coherence function (bottom), for the 1-meter spacing forward profile measured at Hotel Sapanca Centerline 1, Aug. 18, 2000, Sapanca, Turkey.

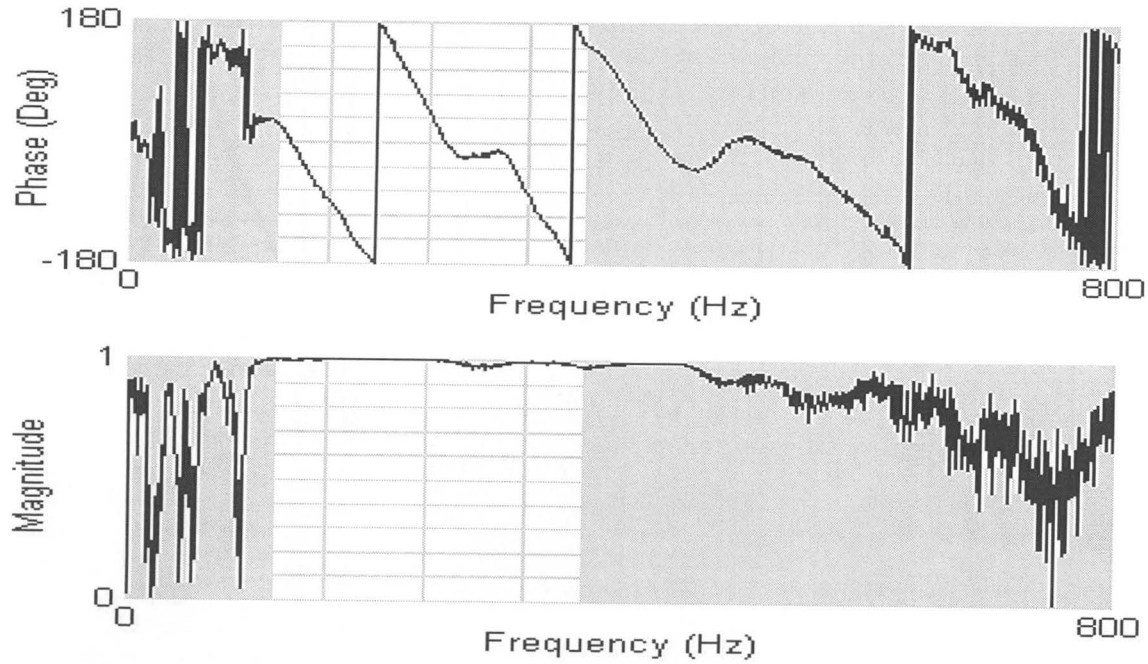

Figure A.61 Wrapped phase of the cross power spectrum (top), and corresponding coherence function (bottom), for the 2-meter spacing forward profile measured at Hotel Sapanca Centerline 1.

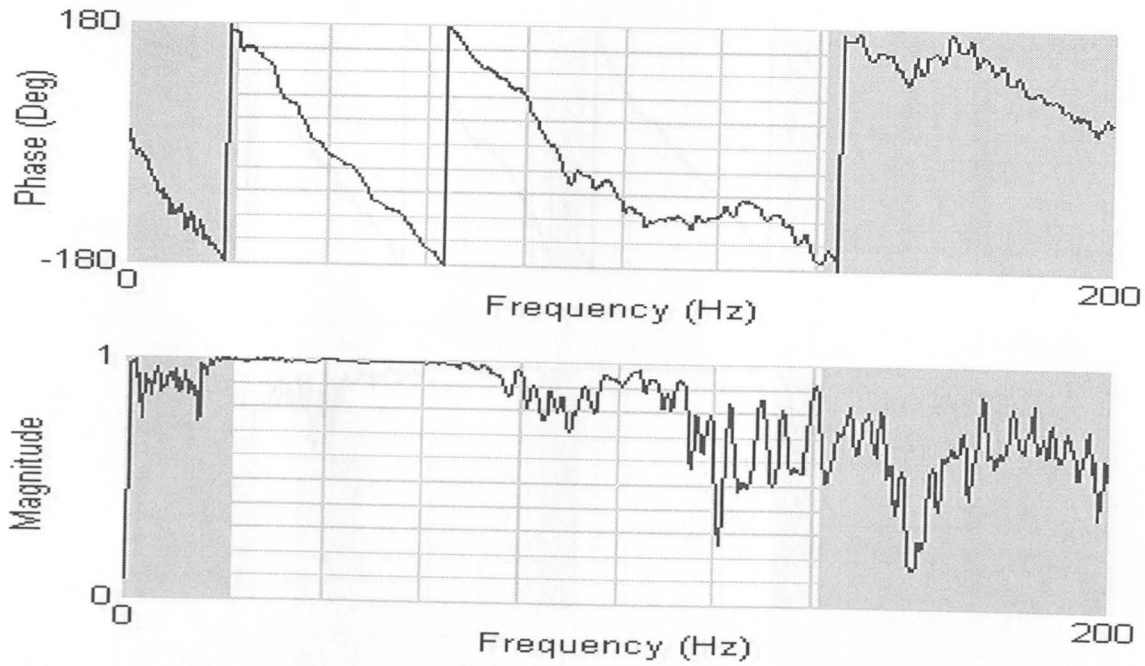

Figure A.62 Wrapped phase of the cross power spectrum (top), and corresponding coherence function (bottom), for the 4-meter spacing reverse profile measured at Hotel Sapanca Centerline 1.

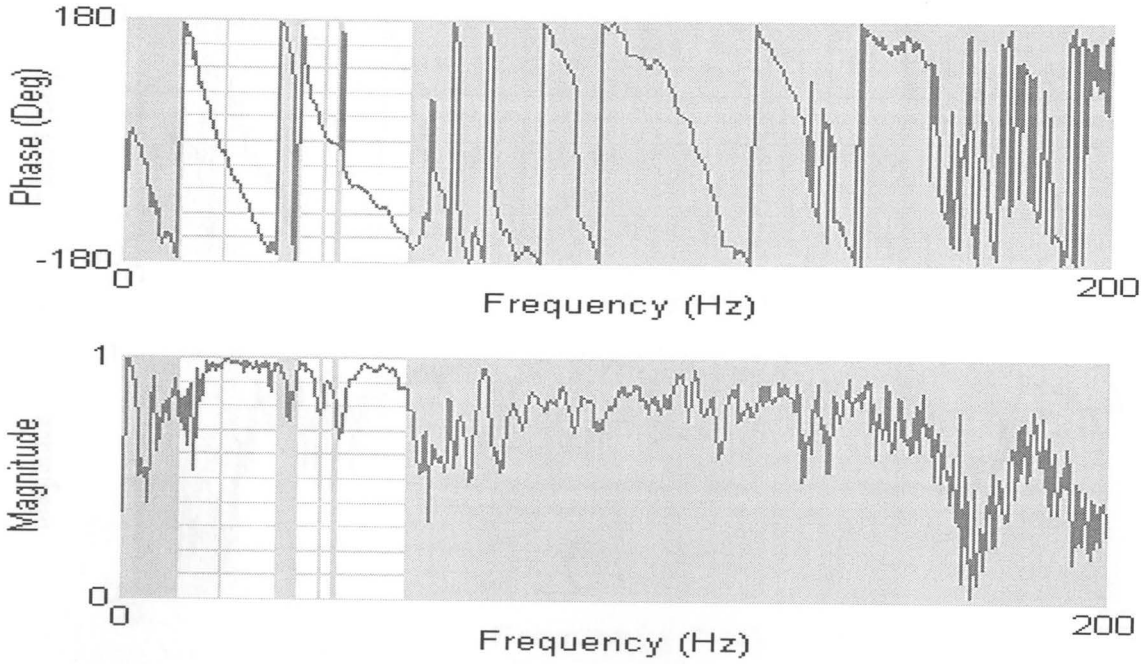

Figure A.63 Wrapped phase of the cross power spectrum (top), and corresponding coherence function (bottom), for the 8-meter spacing average profile measured at Hotel Sapanca Centerline 1.

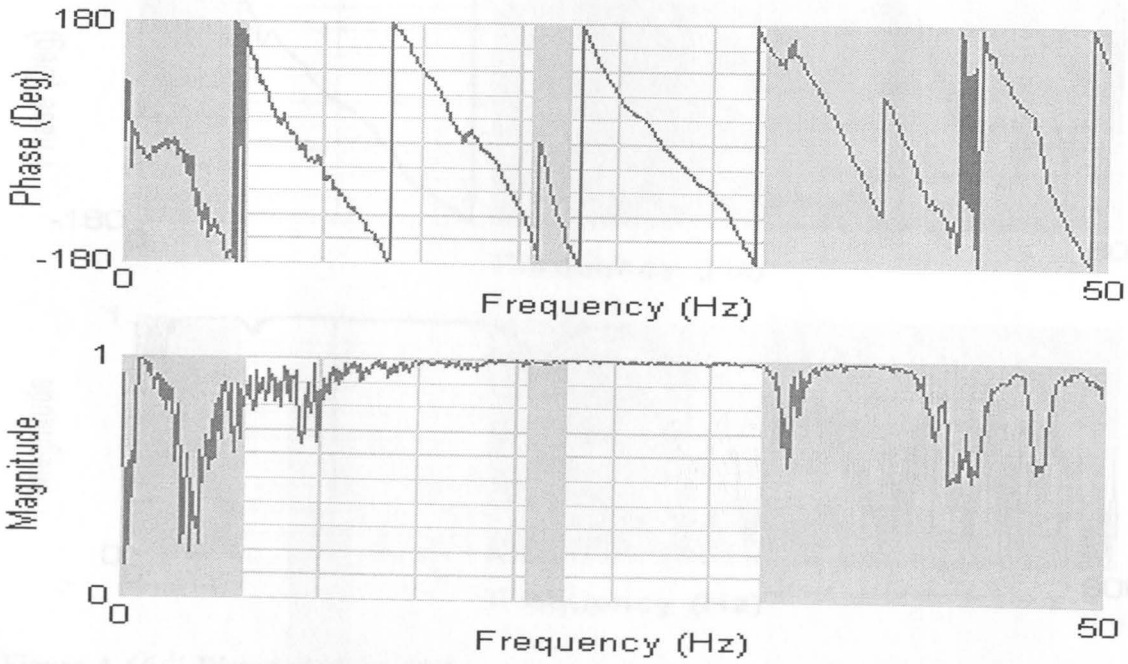

Figure A.64 Wrapped phase of the cross power spectrum (top), and corresponding coherence function (bottom), for the 16-meter spacing average profile measured at Hotel Sapanca Centerline 1.

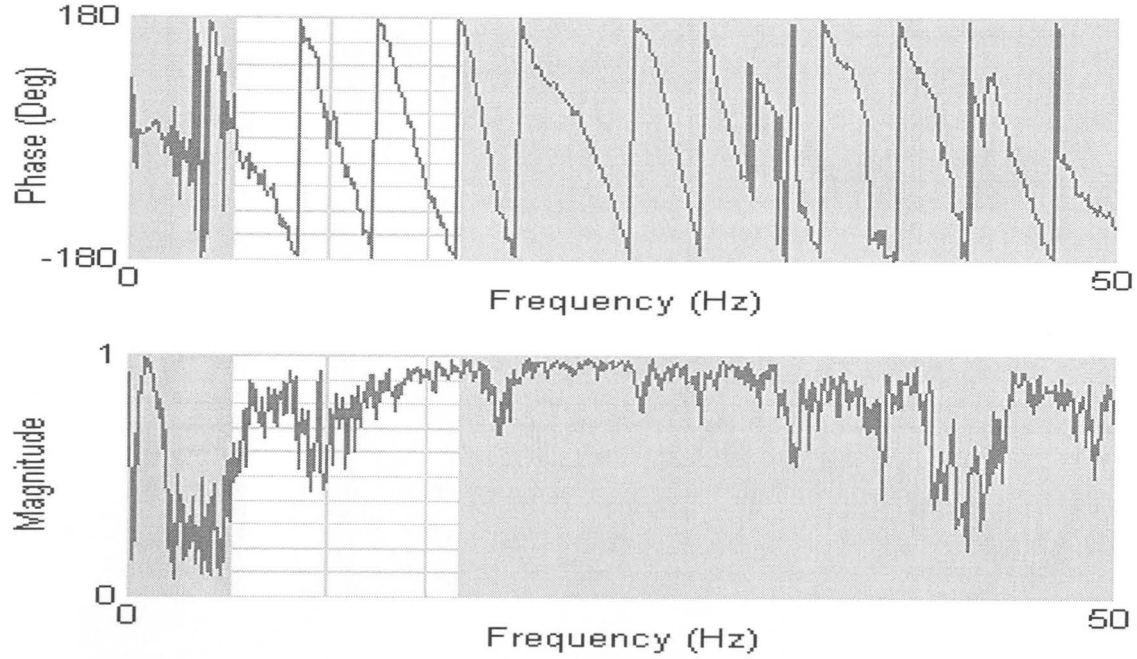

Figure A.65 Wrapped phase of the cross power spectrum (top), and corresponding coherence function (bottom), for the 32-meter spacing average profile measured at Hotel Sapanca Centerline 1.

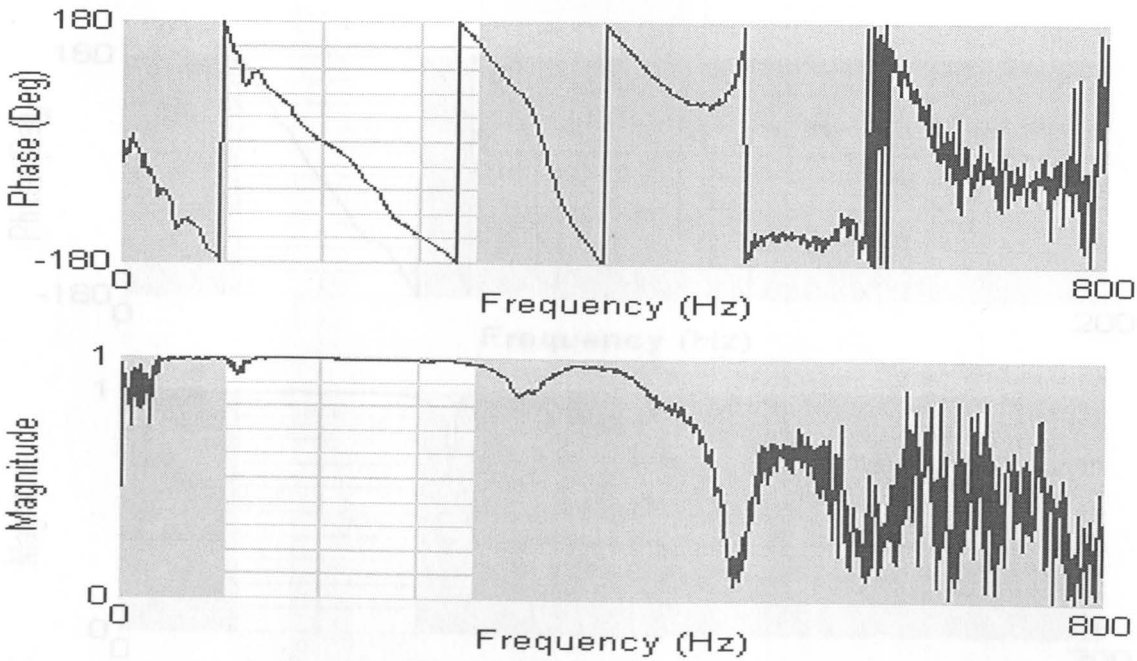

Figure A.66 Wrapped phase of the cross power spectrum (top), and corresponding coherence function (bottom), for the 1-meter spacing forward profile measured at Hotel Sapanca Centerline 2, Aug. 18, 2000, Sapanca, Turkey.

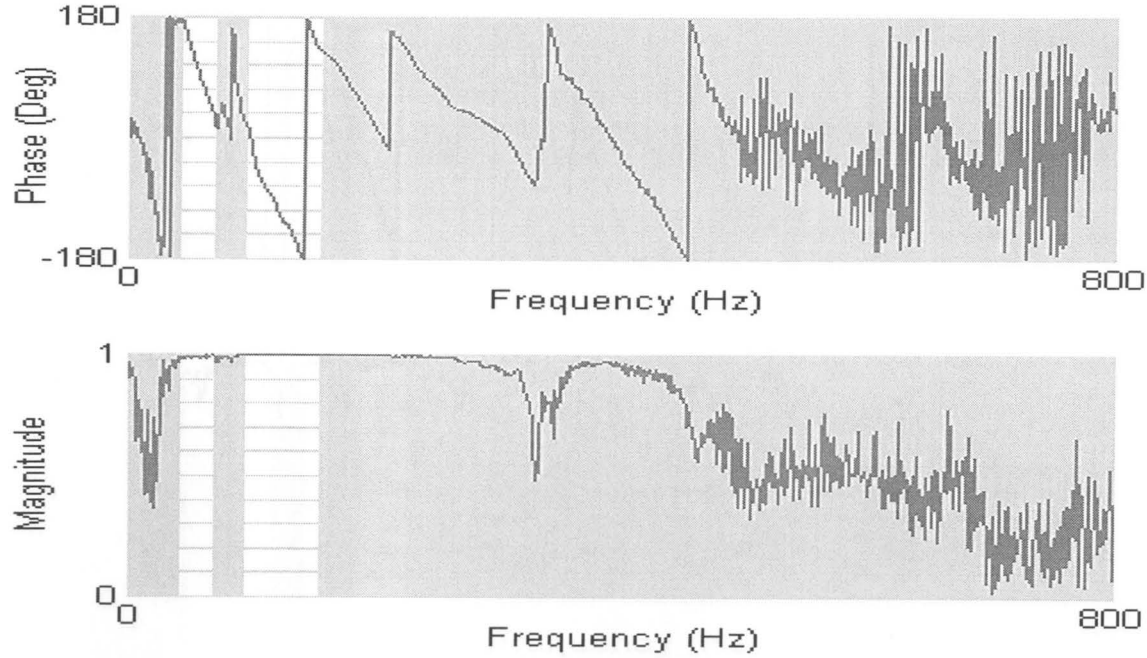

Figure A.67 Wrapped phase of the cross power spectrum (top), and corresponding coherence function (bottom), for the 2-meter spacing average profile measured at Hotel Sapanca Centerline 2.

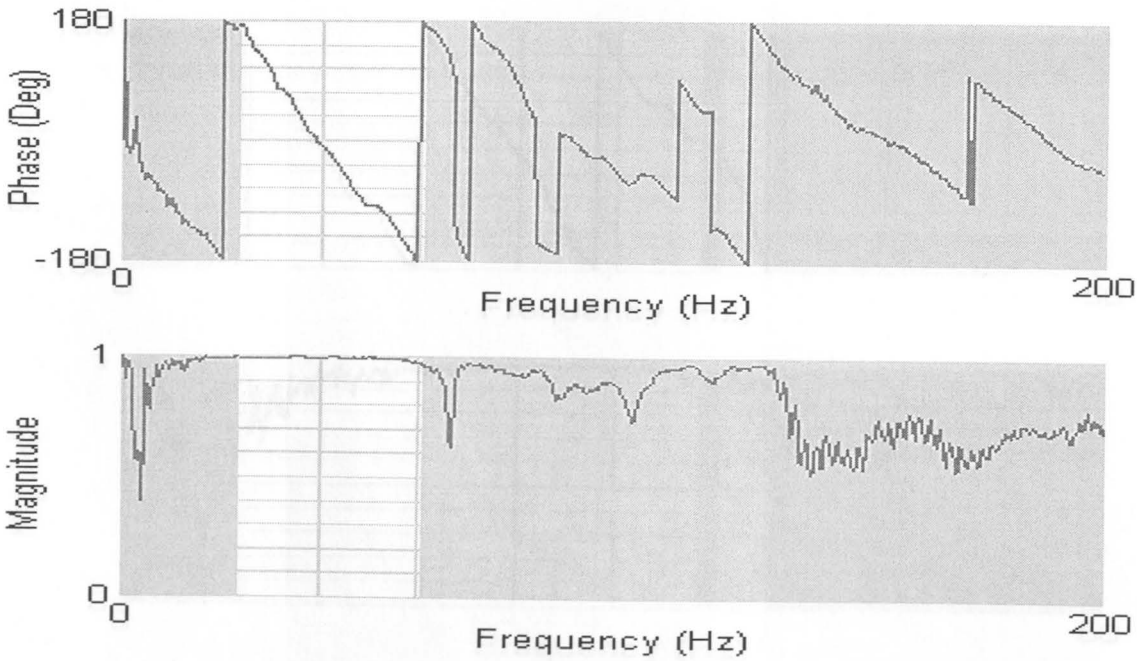

Figure A.68 Wrapped phase of the cross power spectrum (top), and corresponding coherence function (bottom), for the 4-meter spacing average profile measured at Hotel Sapanca Centerline 2.

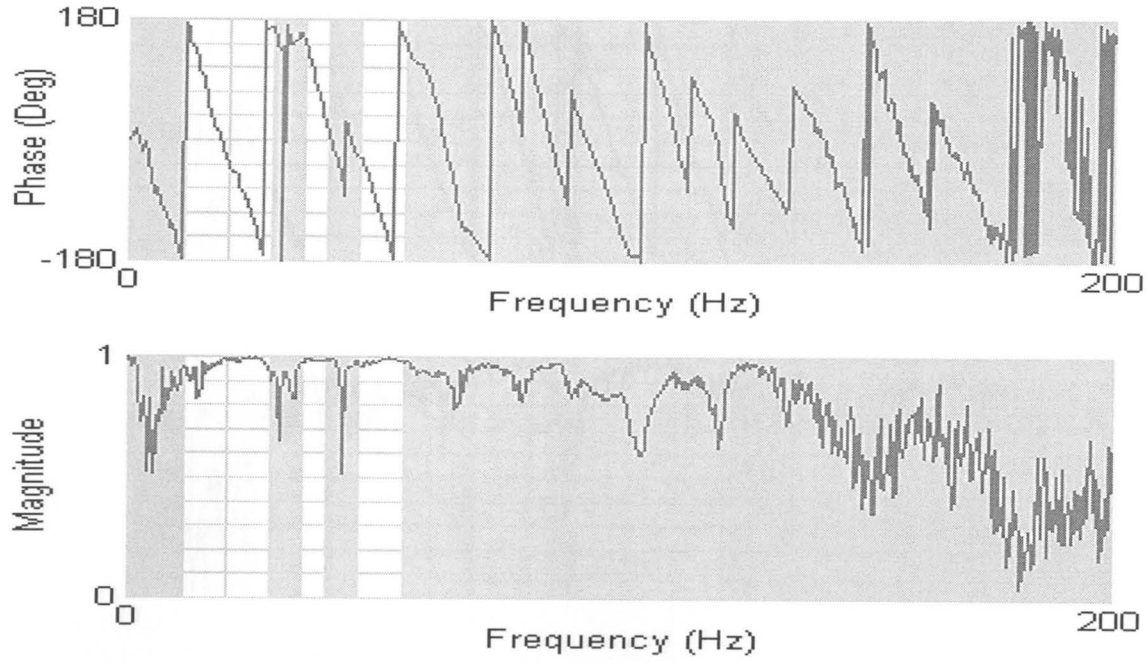

Figure A.69 Wrapped phase of the cross power spectrum (top), and corresponding coherence function (bottom), for the 8-meter spacing average profile measured at Hotel Sapanca Centerline 2.

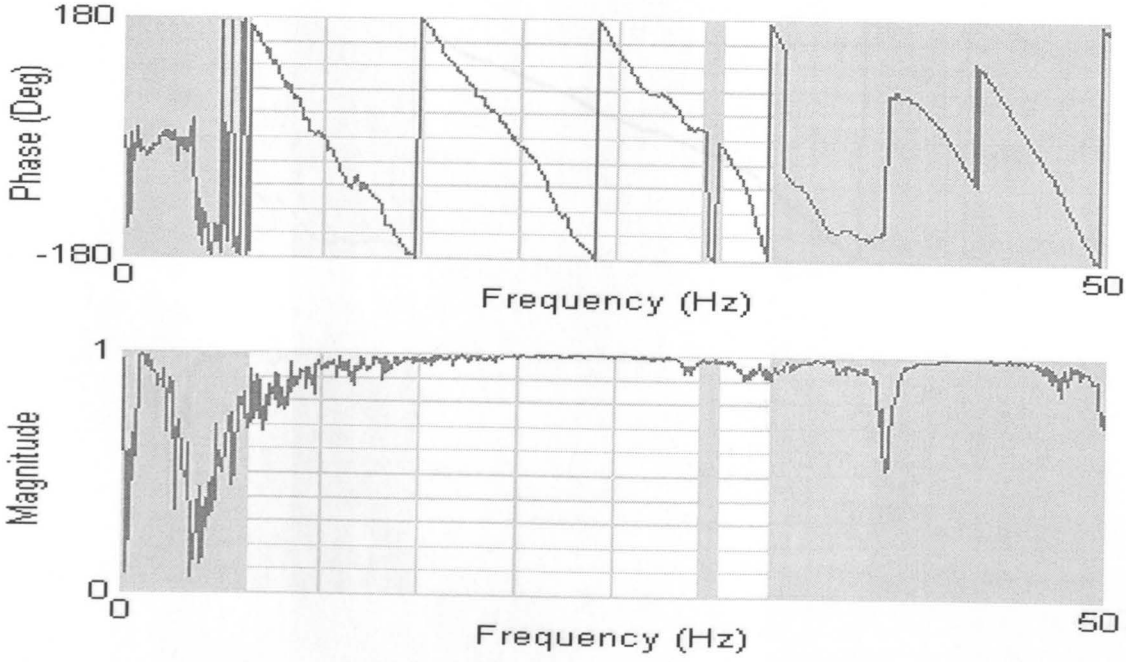

Figure A.70 Wrapped phase of the cross power spectrum (top), and corresponding coherence function (bottom), for the 16-meter spacing average profile measured at Hotel Sapanca Centerline 2.

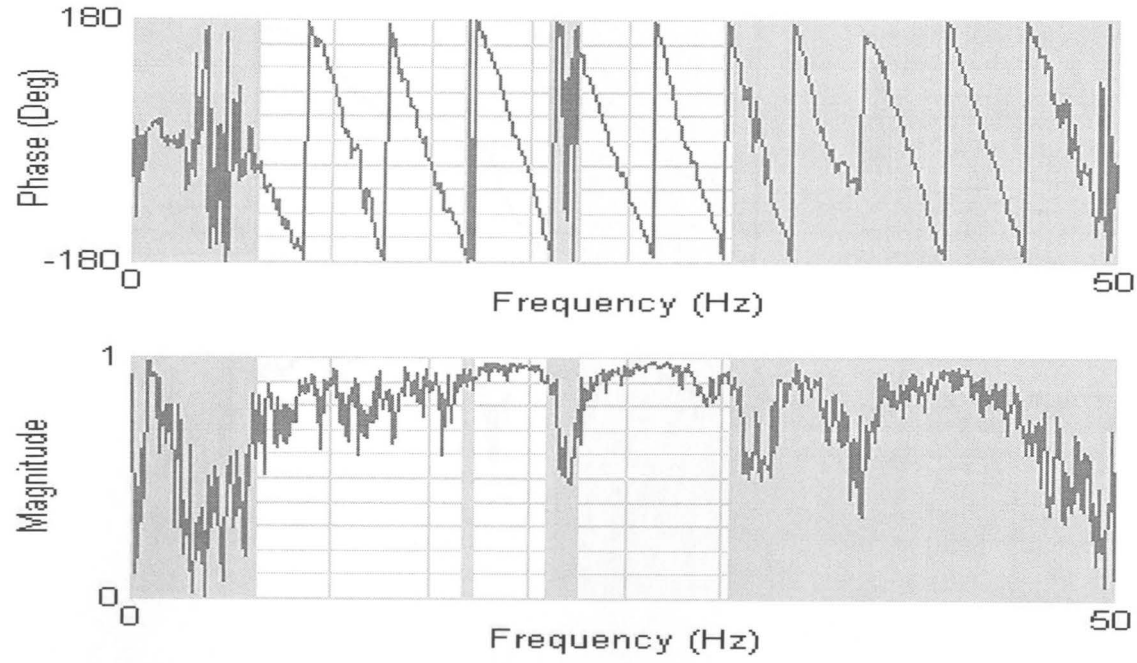

Figure A.71 Wrapped phase of the cross power spectrum (top), and corresponding coherence function (bottom), for the 32-meter spacing average profile measured at Hotel Sapanca Centerline 2.

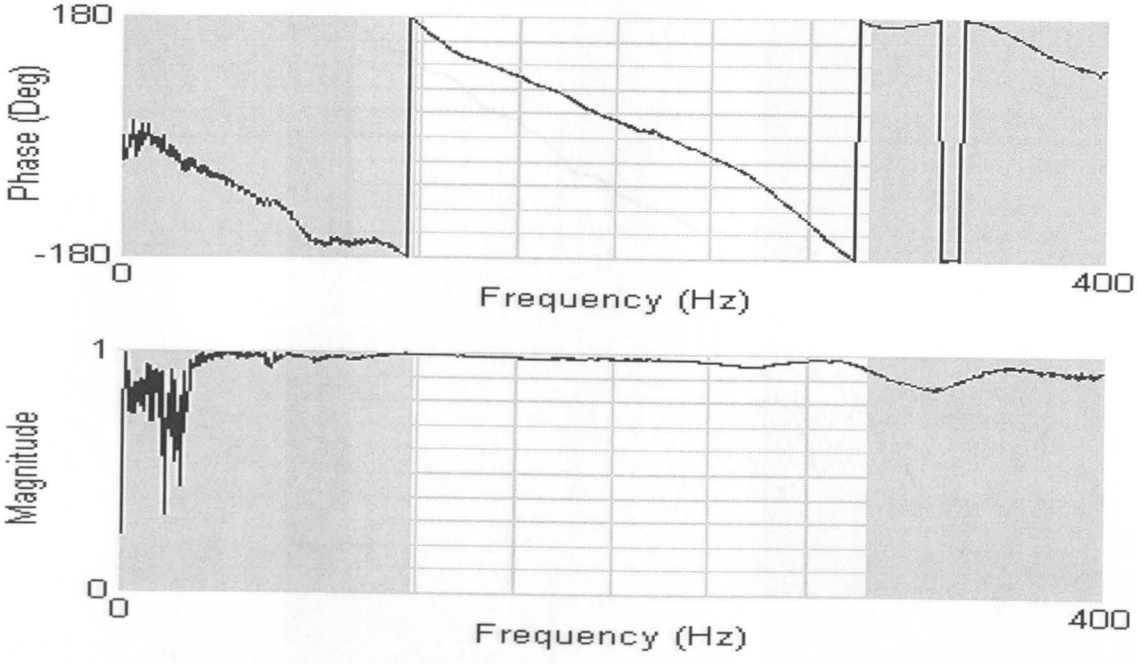

Figure A.72 Wrapped phase of the cross power spectrum (top), and corresponding coherence function (bottom), for the 1-meter spacing forward profile measured at Hotel Sapanca Centerline 3, Aug. 18, 2000, Sapanca, Turkey.

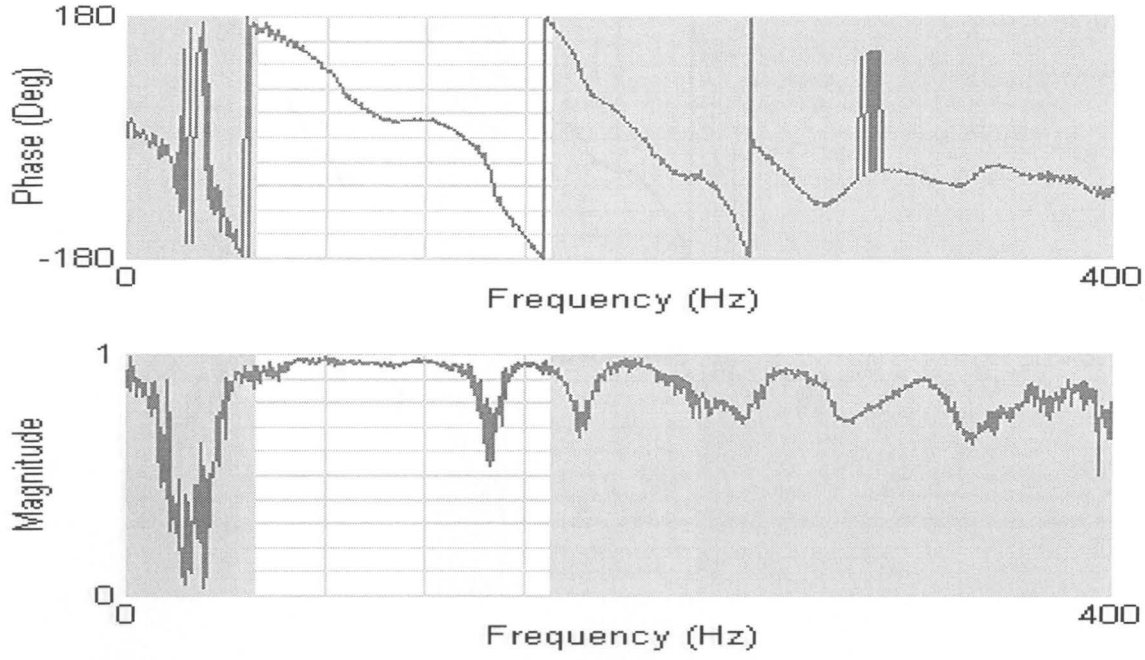

Figure A.73 Wrapped phase of the cross power spectrum (top), and corresponding coherence function (bottom), for the 2-meter spacing average profile measured at Hotel Sapanca Centerline 3.

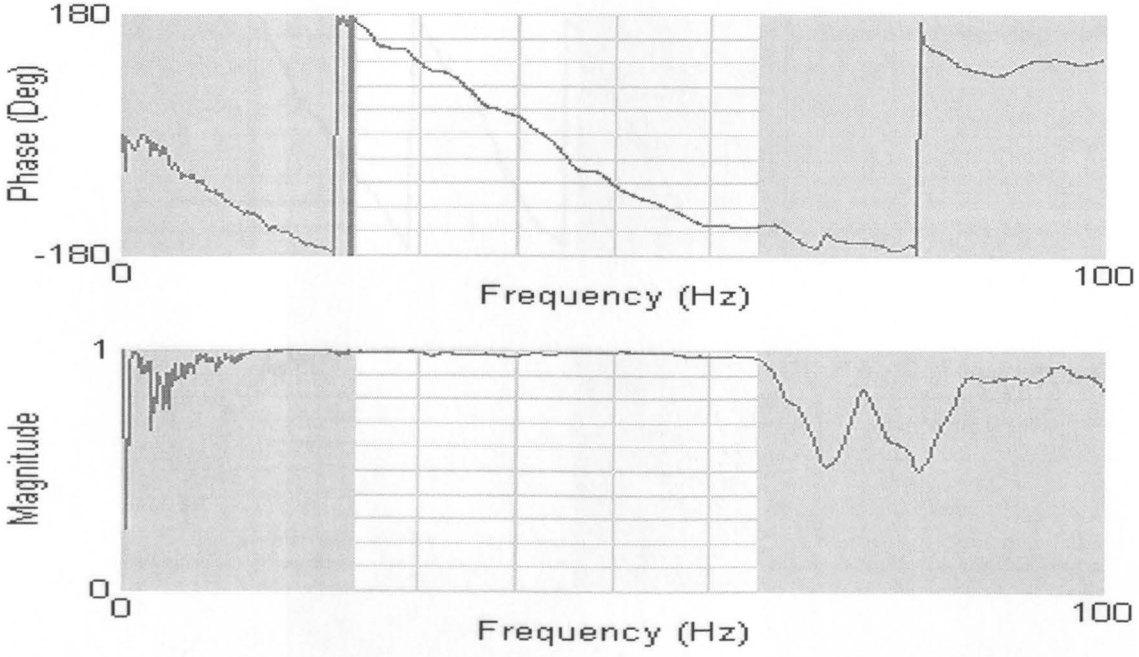

Figure A.74 Wrapped phase of the cross power spectrum (top), and corresponding coherence function (bottom), for the 4-meter spacing average profile measured at Hotel Sapanca Centerline 3.

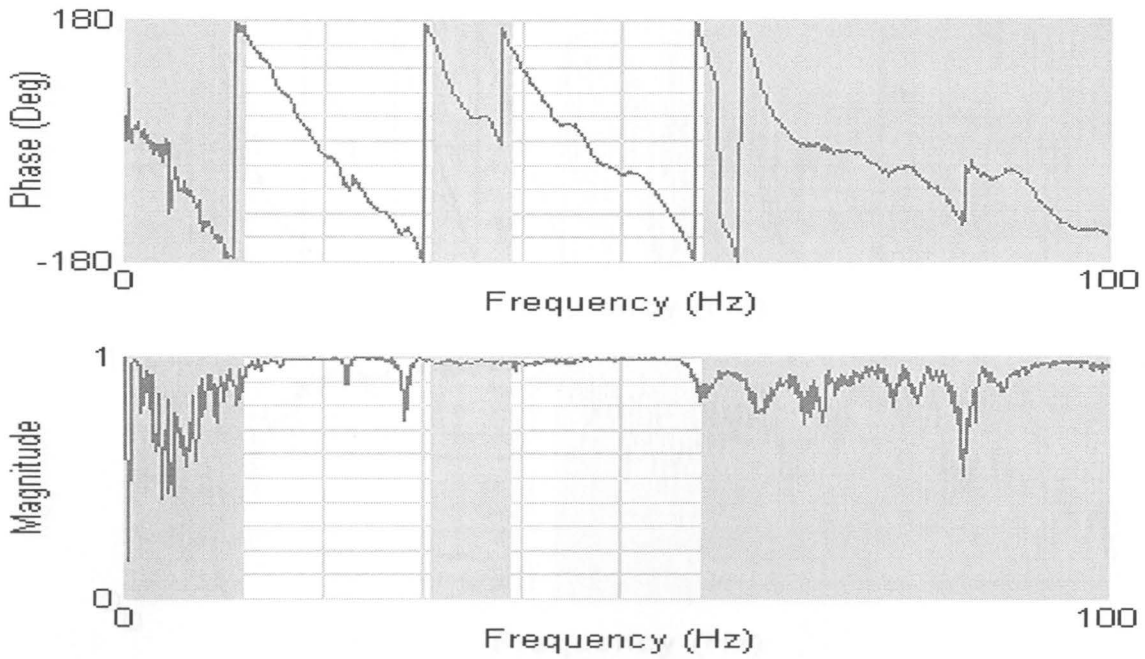

Figure A.75 Wrapped phase of the cross power spectrum (top), and corresponding coherence function (bottom), for the 8-meter spacing average profile measured at Hotel Sapanca Centerline 3.

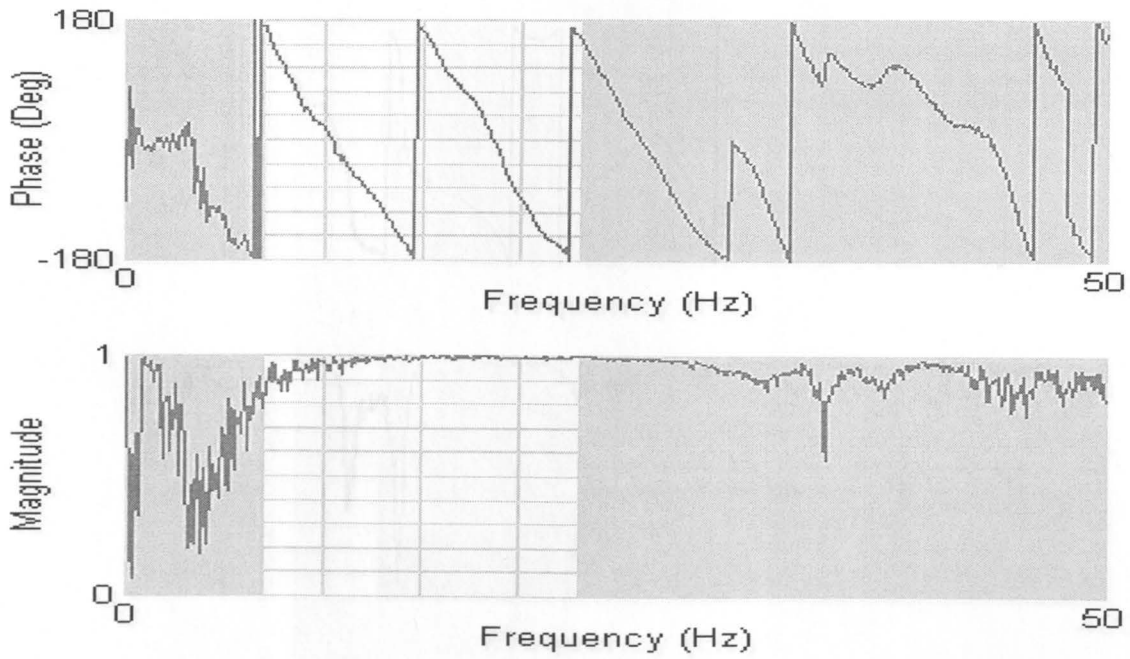

Figure A.76 Wrapped phase of the cross power spectrum (top), and corresponding coherence function (bottom), for the 16-meter spacing average profile measured at Hotel Sapanca Centerline 3.

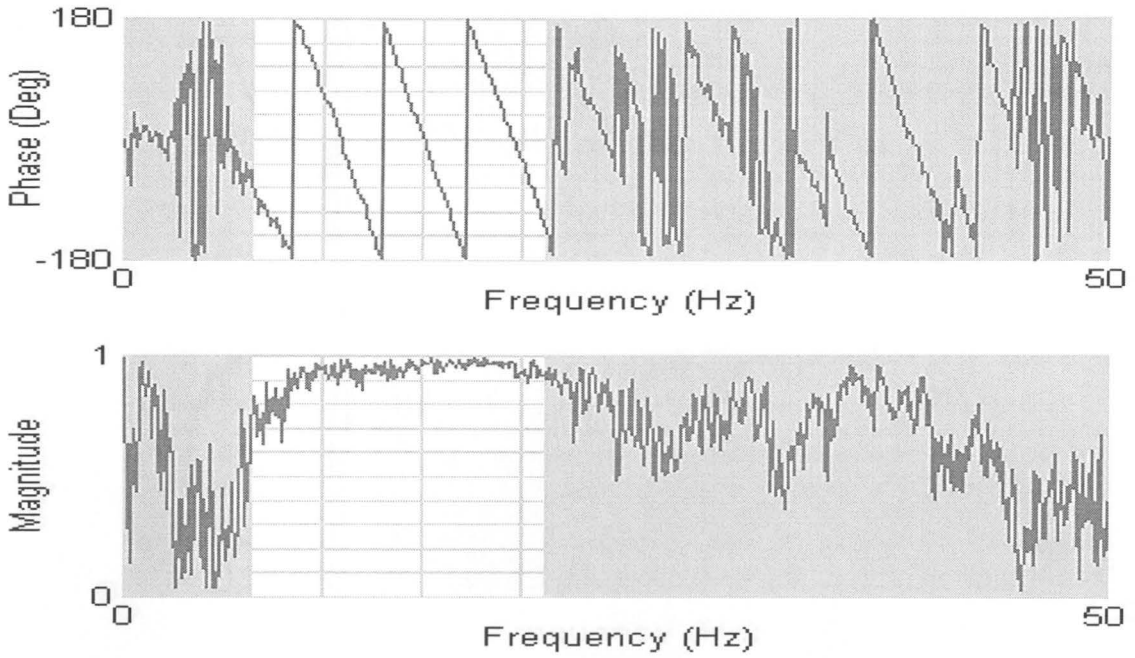

Figure A.77 Wrapped phase of the cross power spectrum (top), and corresponding coherence function (bottom), for the 32-meter spacing average profile measured at Hotel Sapanca Centerline 3.

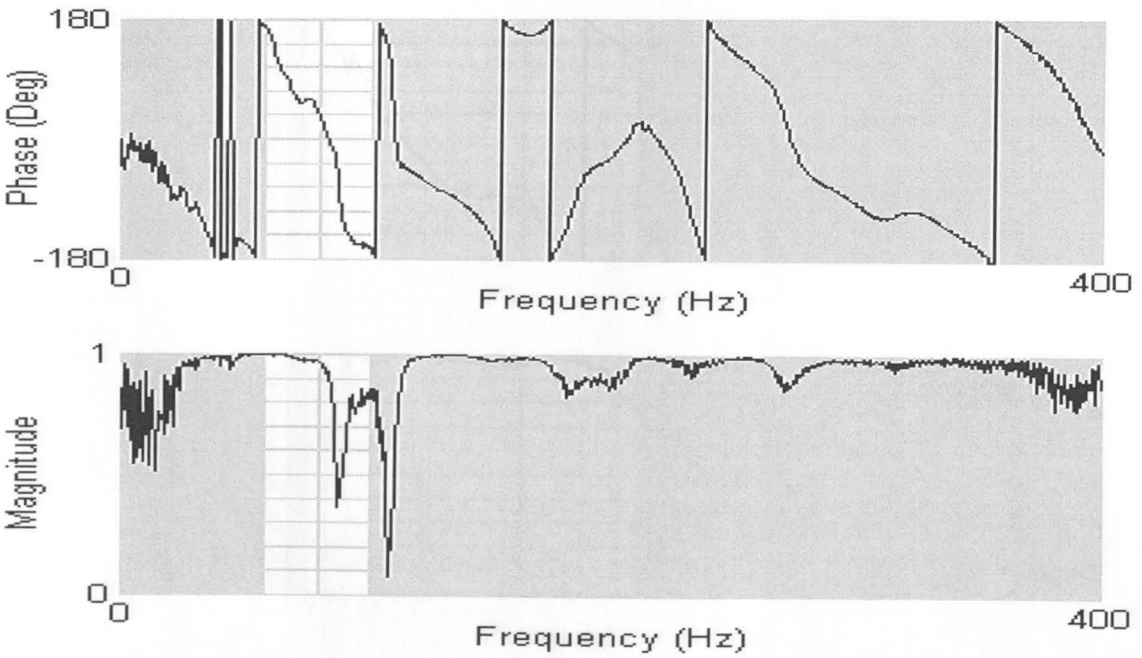

Figure A.78 Wrapped phase of the cross power spectrum (top), and corresponding coherence function (bottom), for the 1-meter spacing forward profile measured at Hotel Sapanca Centerline 4, Aug. 18, 2000, Sapanca, Turkey.

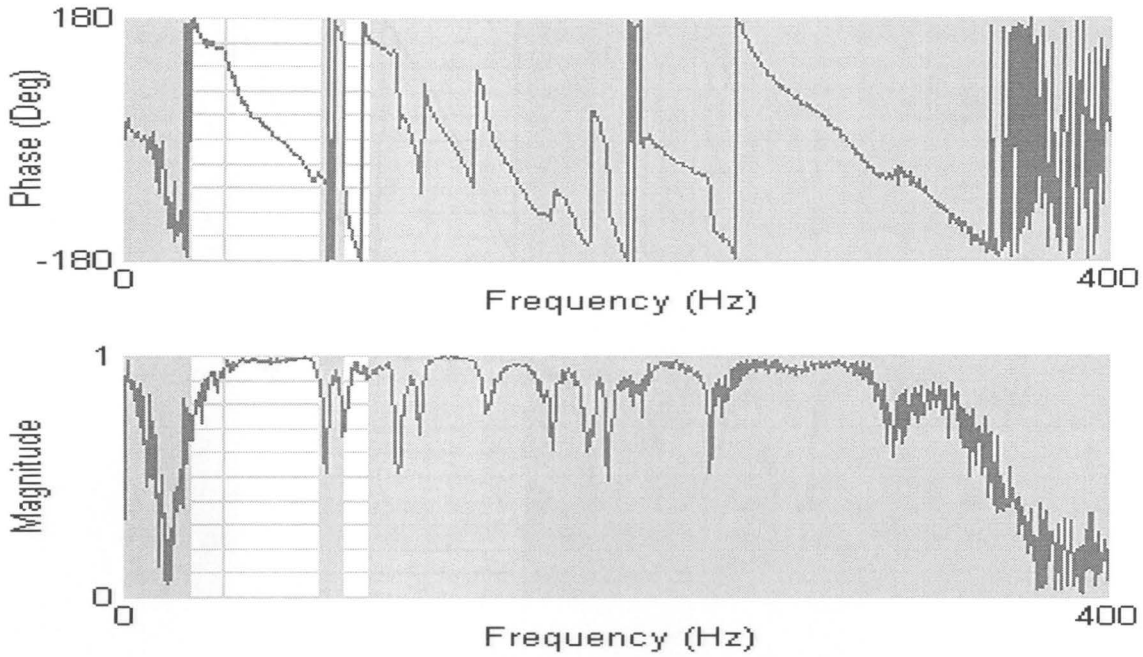

Figure A.79 Wrapped phase of the cross power spectrum (top), and corresponding coherence function (bottom), for the 2-meter spacing average profile measured at Hotel Sapanca Centerline 4.

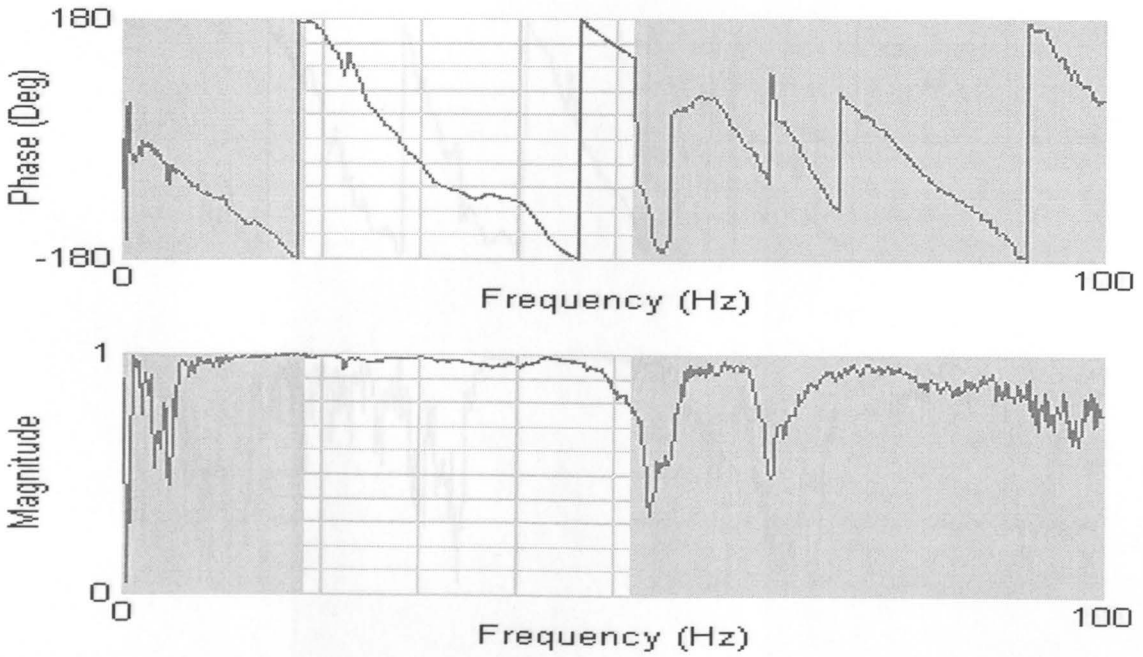

Figure A.80 Wrapped phase of the cross power spectrum (top), and corresponding coherence function (bottom), for the 4-meter spacing average profile measured at Hotel Sapanca Centerline 4.

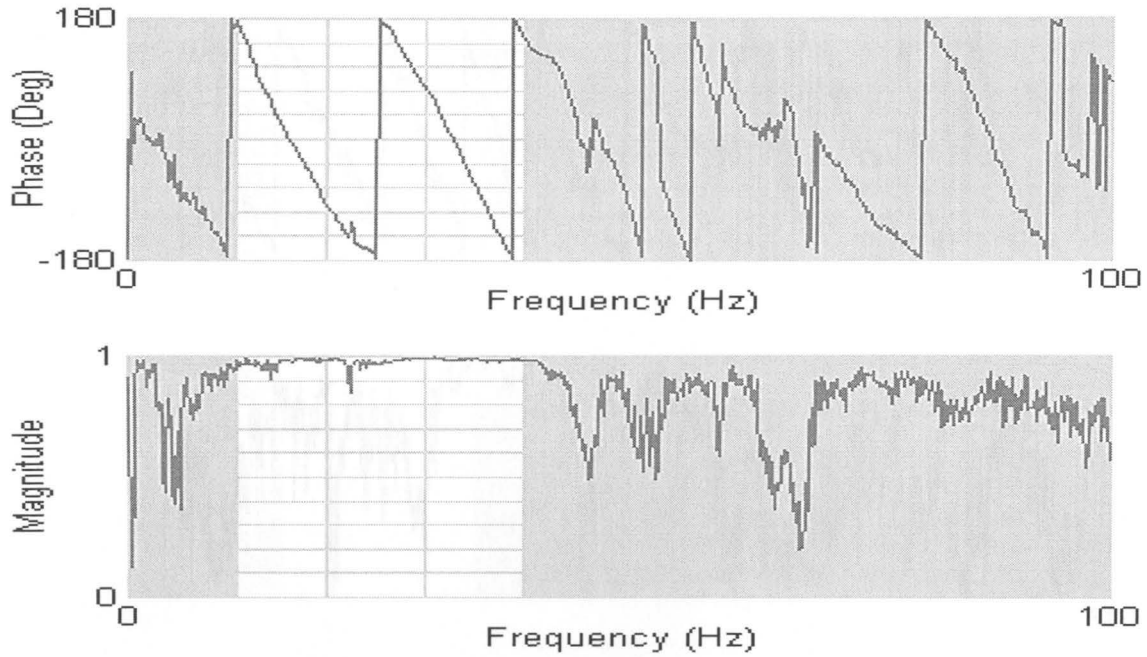

Figure A.81 Wrapped phase of the cross power spectrum (top), and corresponding coherence function (bottom), for the 8-meter spacing average profile measured at Hotel Sapanca Centerline 4.

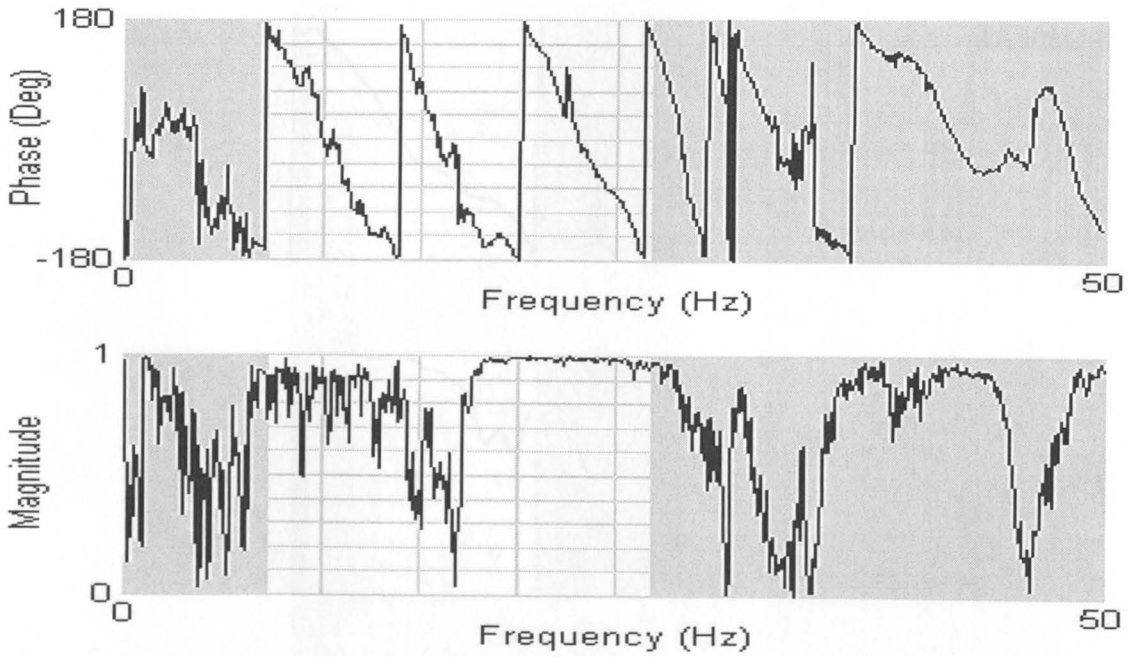

Figure A.82 Wrapped phase of the cross power spectrum (top), and corresponding coherence function (bottom), for the 16-meter spacing forward profile measured at Hotel Sapanca Centerline 4.

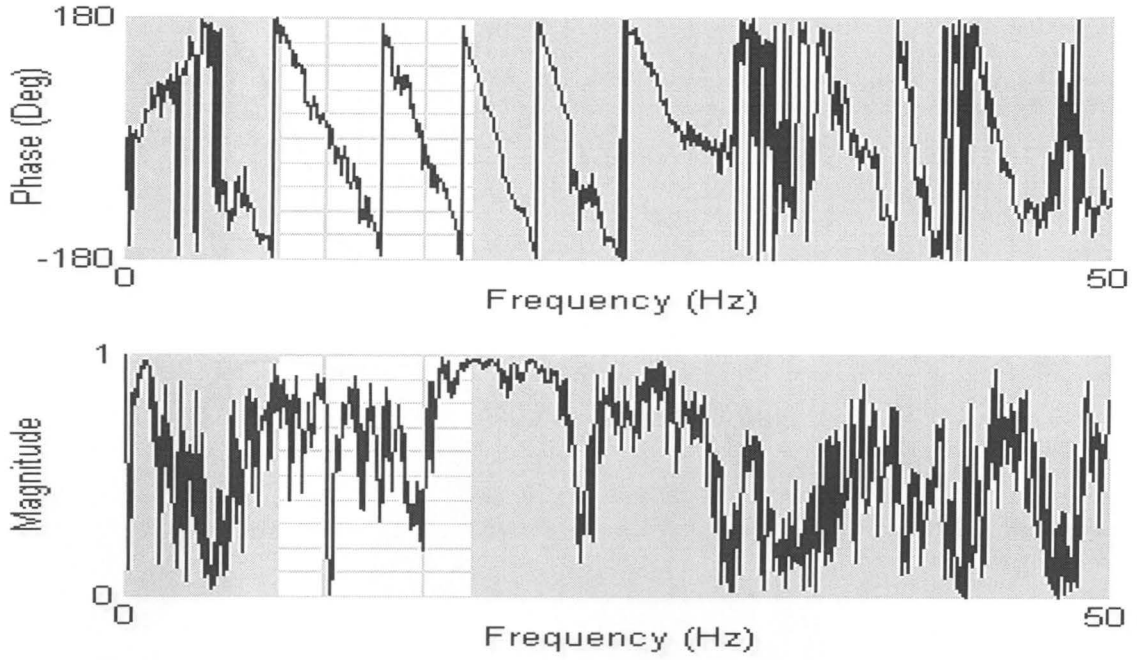

Figure A.83 Wrapped phase of the cross power spectrum (top), and corresponding coherence function (bottom), for the 32-meter spacing forward profile measured at Hotel Sapanca Centerline 4.

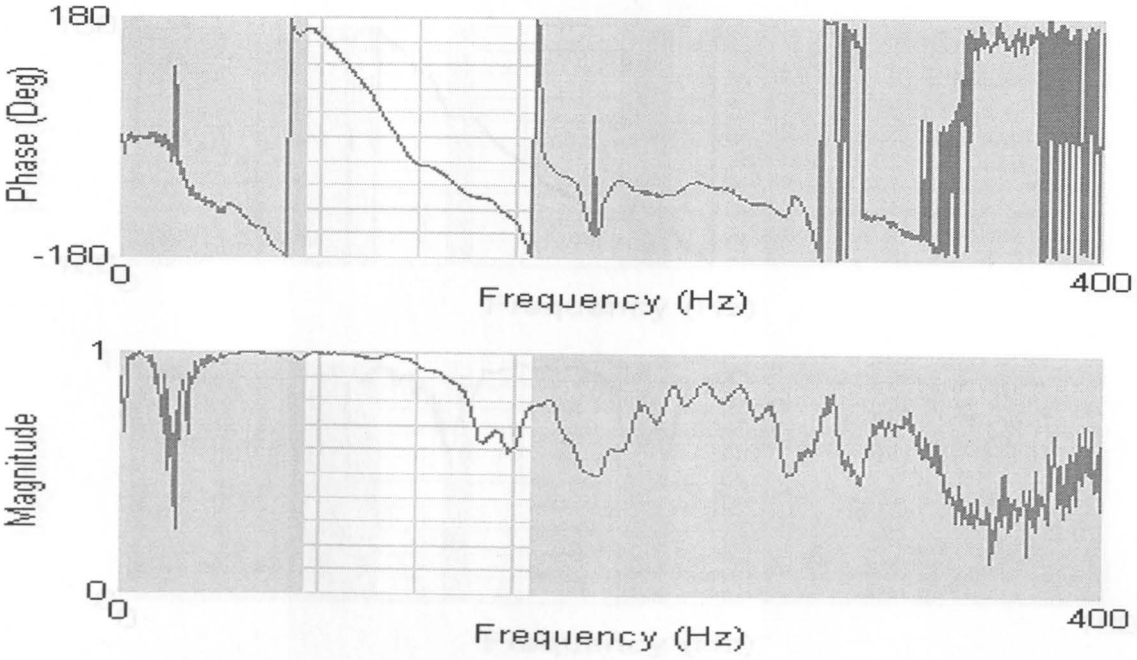

Figure A.84 Wrapped phase of the cross power spectrum (top), and corresponding coherence function (bottom), for the 1-meter spacing average profile measured at Degirmendere Nose, Aug. 23, 2000, Degirmendere, Turkey.

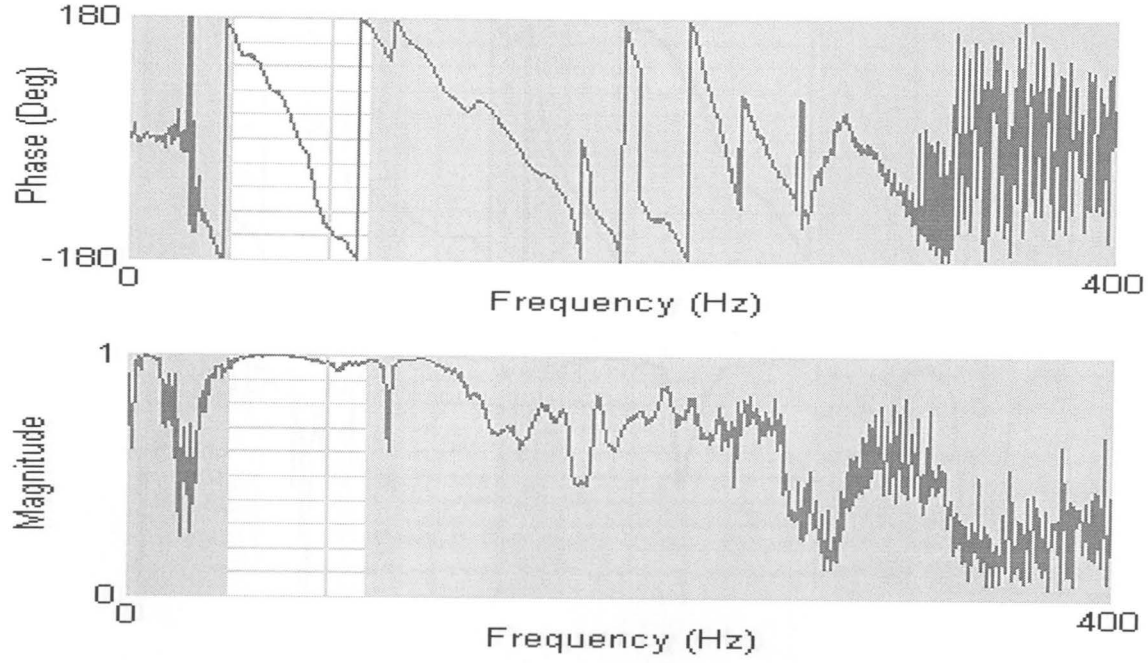

Figure A.85 Wrapped phase of the cross power spectrum (top), and corresponding coherence function (bottom), for the 2-meter spacing average profile measured at Degirmendere Nose.

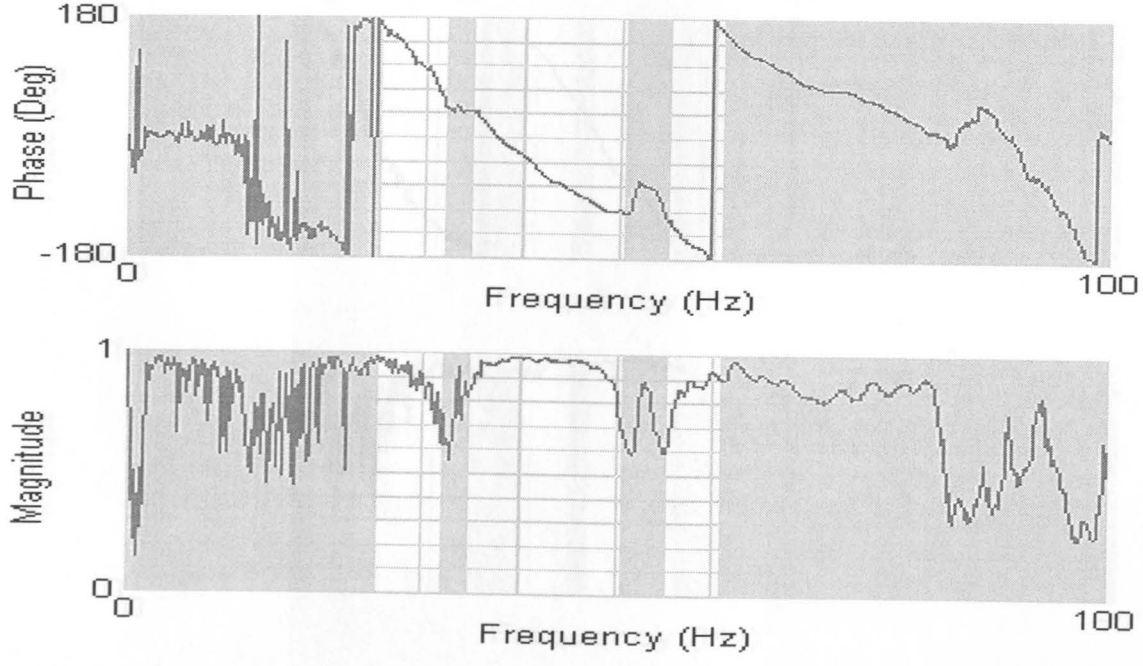

Figure A.86 Wrapped phase of the cross power spectrum (top), and corresponding coherence function (bottom), for the 4-meter spacing average profile measured at Degirmendere Nose.

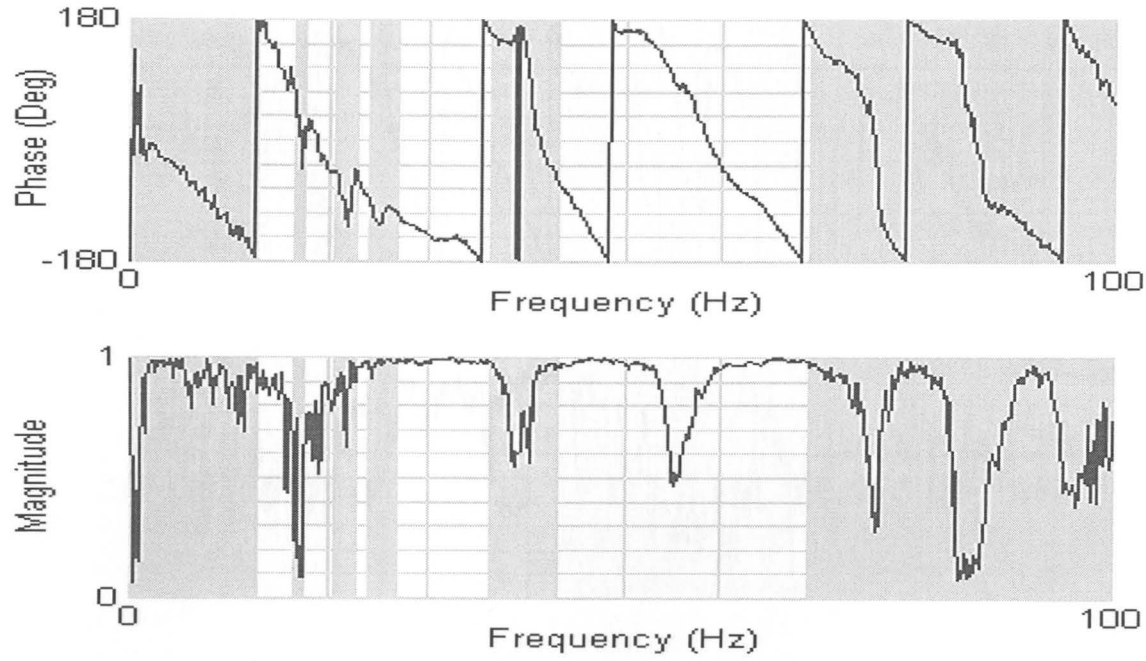

Figure A.87 Wrapped phase of the cross power spectrum (top), and corresponding coherence function (bottom), for the 8-meter spacing reverse profile measured at Degirmendere Nose.

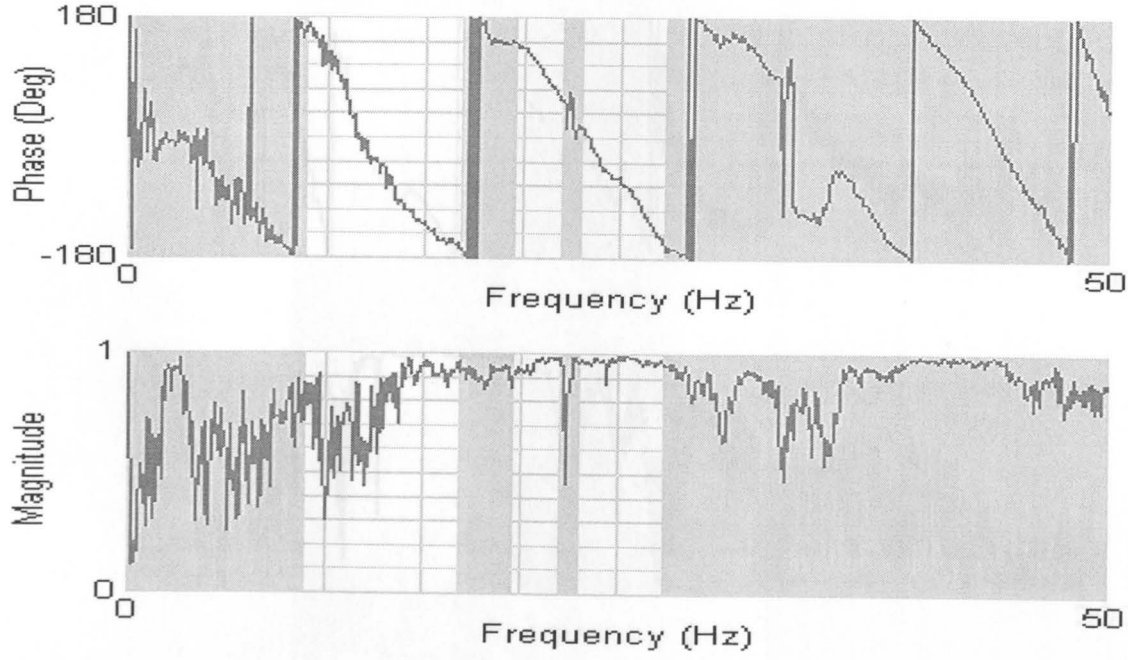

Figure A.88 Wrapped phase of the cross power spectrum (top), and corresponding coherence function (bottom), for the 16-meter spacing average profile measured at Degirmendere Nose.

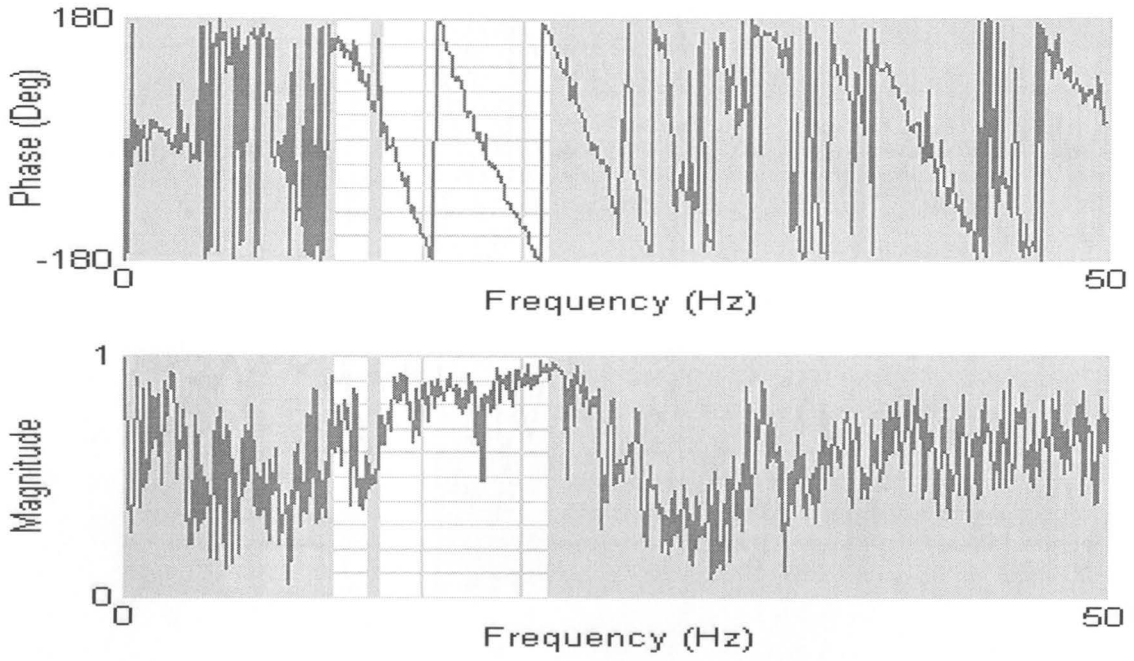

Figure A.89 Wrapped phase of the cross power spectrum (top), and corresponding coherence function (bottom), for the 32-meter spacing average profile measured at Degirmendere Nose.

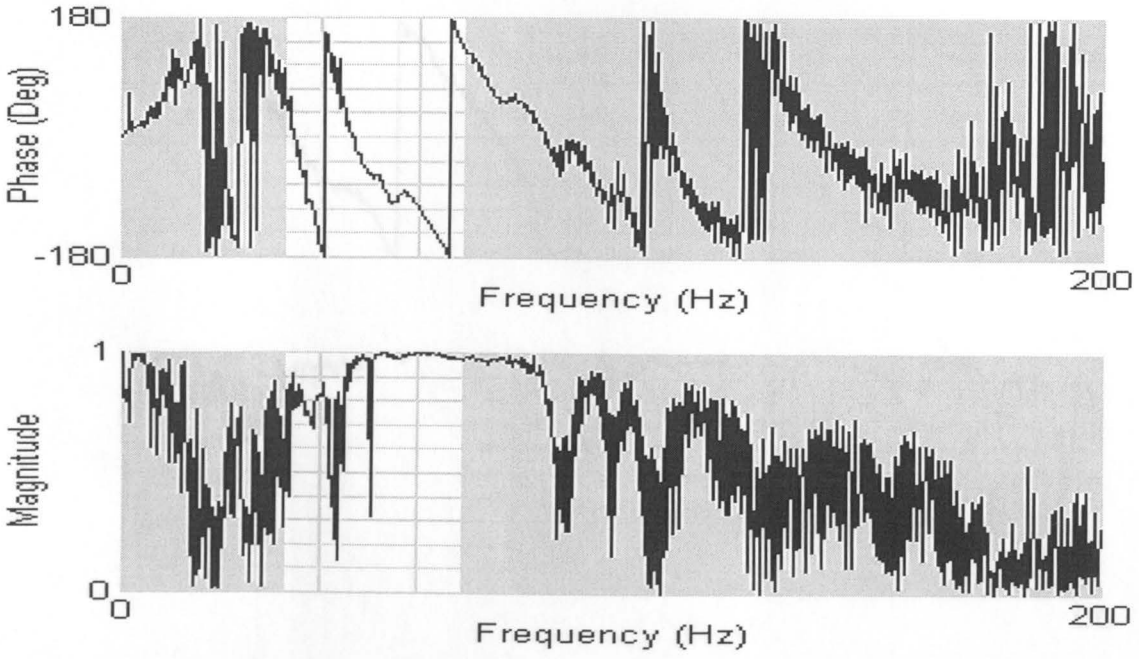

Figure A.90 Wrapped phase of the cross power spectrum (top), and corresponding coherence function (bottom), for the 3-meter spacing forward profile measured at Police Station, Aug. 23, 2000, Golcuk, Turkey.

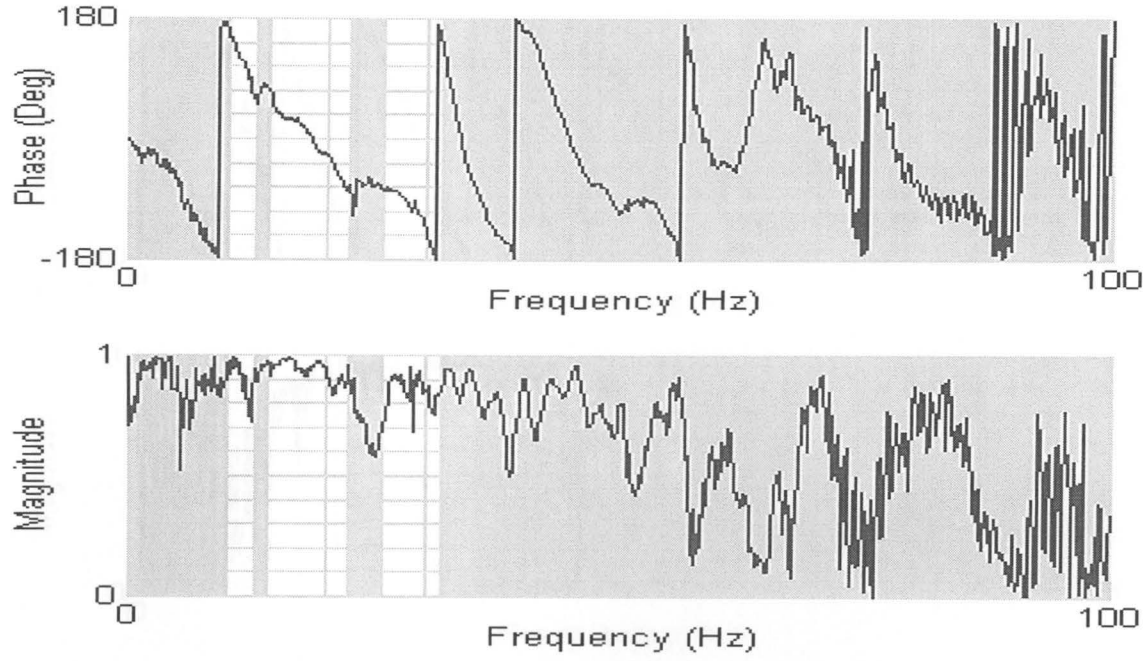

Figure A.91 Wrapped phase of the cross power spectrum (top), and corresponding coherence function (bottom), for the 6-meter spacing reverse profile measured at Police Station.

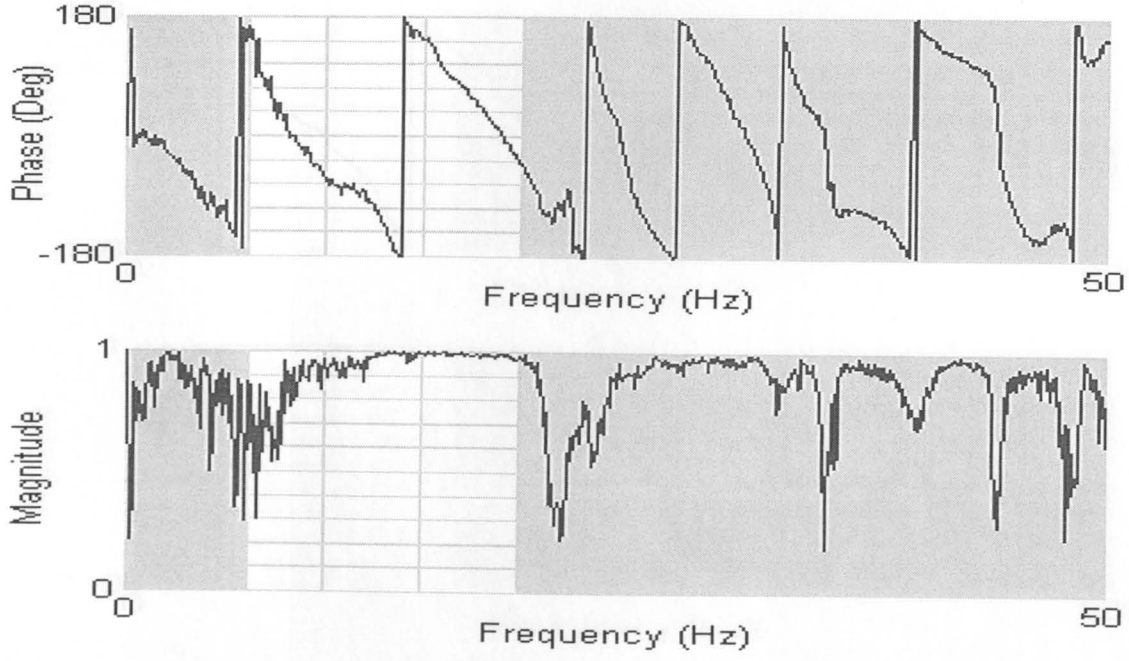

Figure A.92 Wrapped phase of the cross power spectrum (top), and corresponding coherence function (bottom), for the 12-meter spacing reverse profile measured at Police Station.

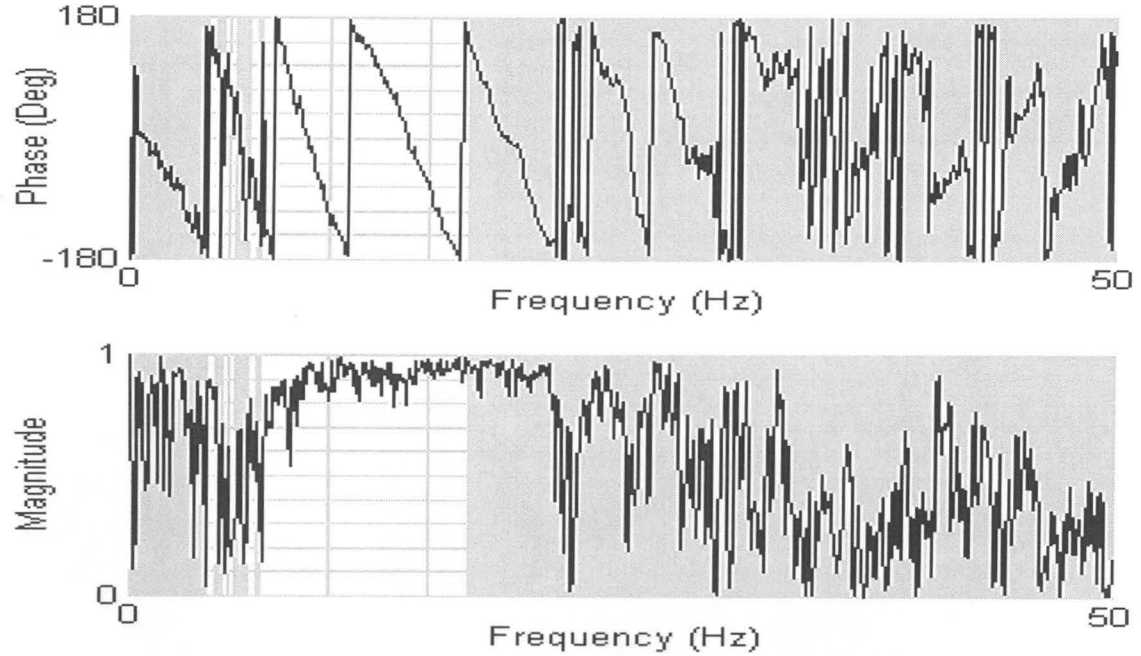

Figure A.93 Wrapped phase of the cross power spectrum (top), and corresponding coherence function (bottom), for the 24-meter spacing reverse profile measured at Police Station.

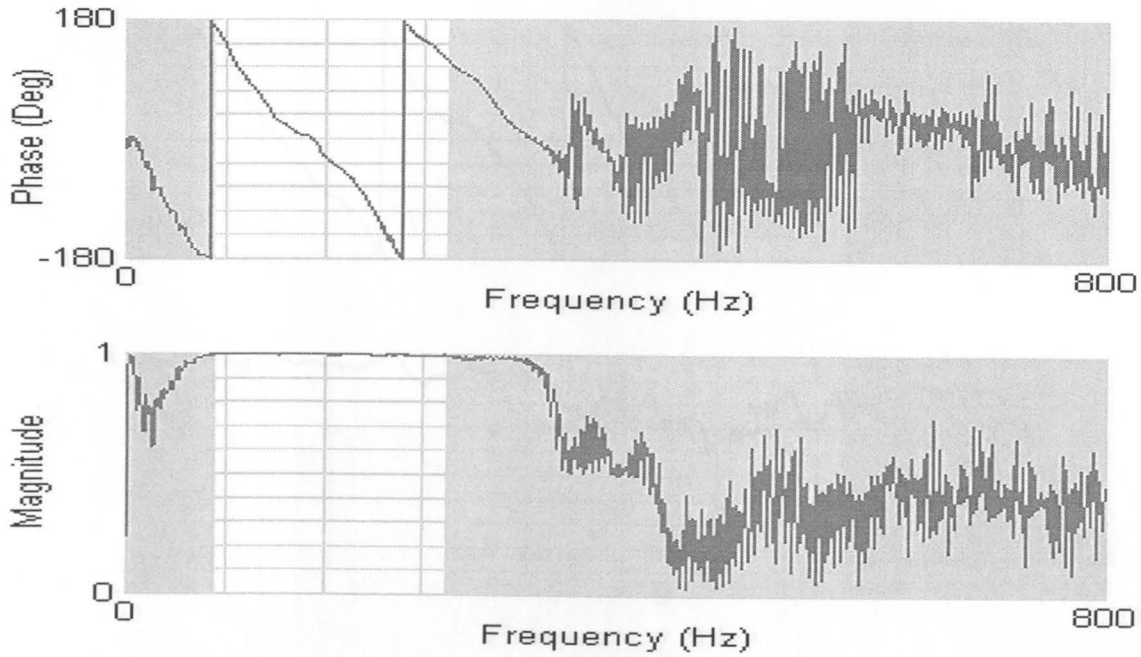

Figure A.94 Wrapped phase of the cross power spectrum (top), and corresponding coherence function (bottom), for the 1-meter spacing average profile measured at Soccer Field, Aug. 23, 2000, Golcuk, Turkey.

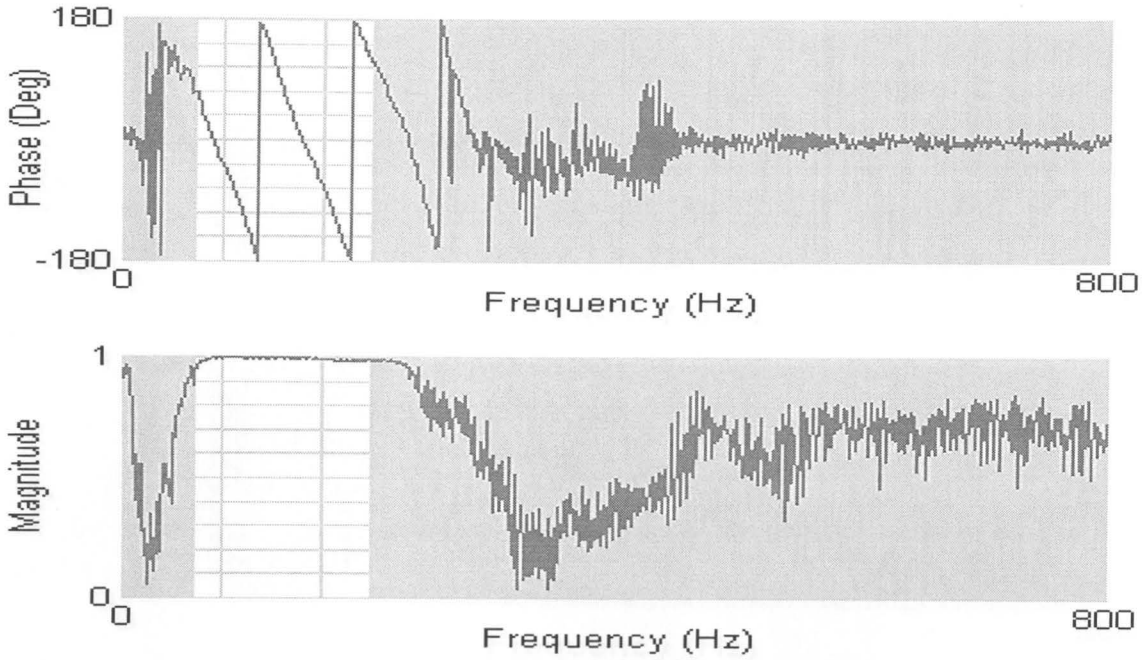

Figure A.95 Wrapped phase of the cross power spectrum (top), and corresponding coherence function (bottom), for the 2-meter spacing average profile measured at Soccer Field.

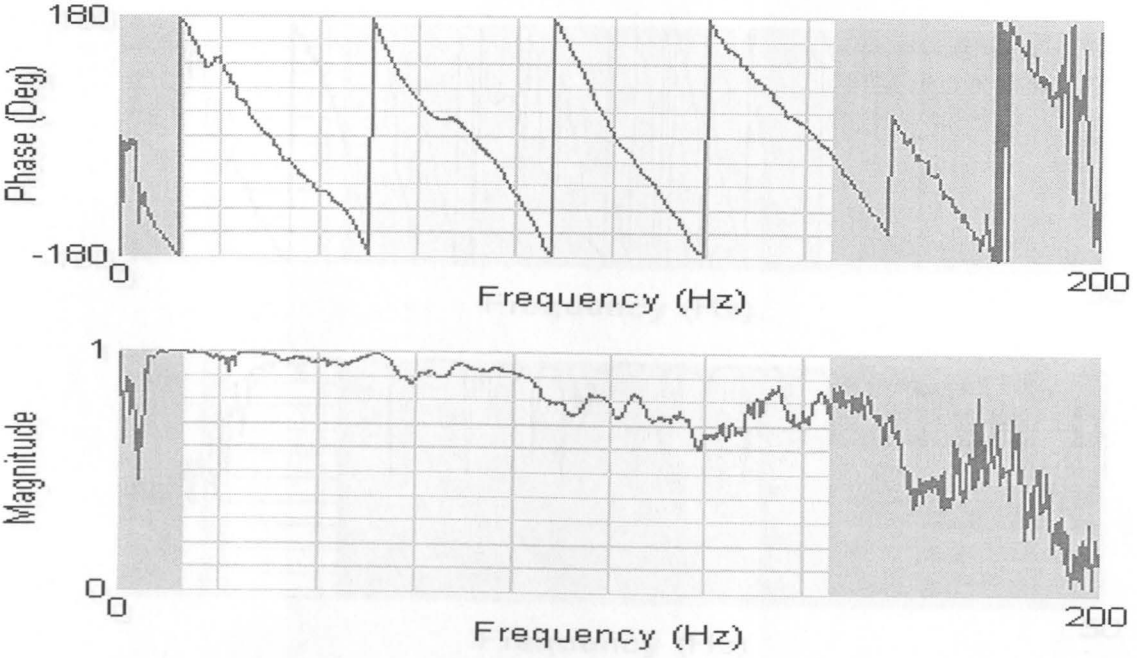

Figure A.96 Wrapped phase of the cross power spectrum (top), and corresponding coherence function (bottom), for the 4-meter spacing average profile measured at Soccer Field.

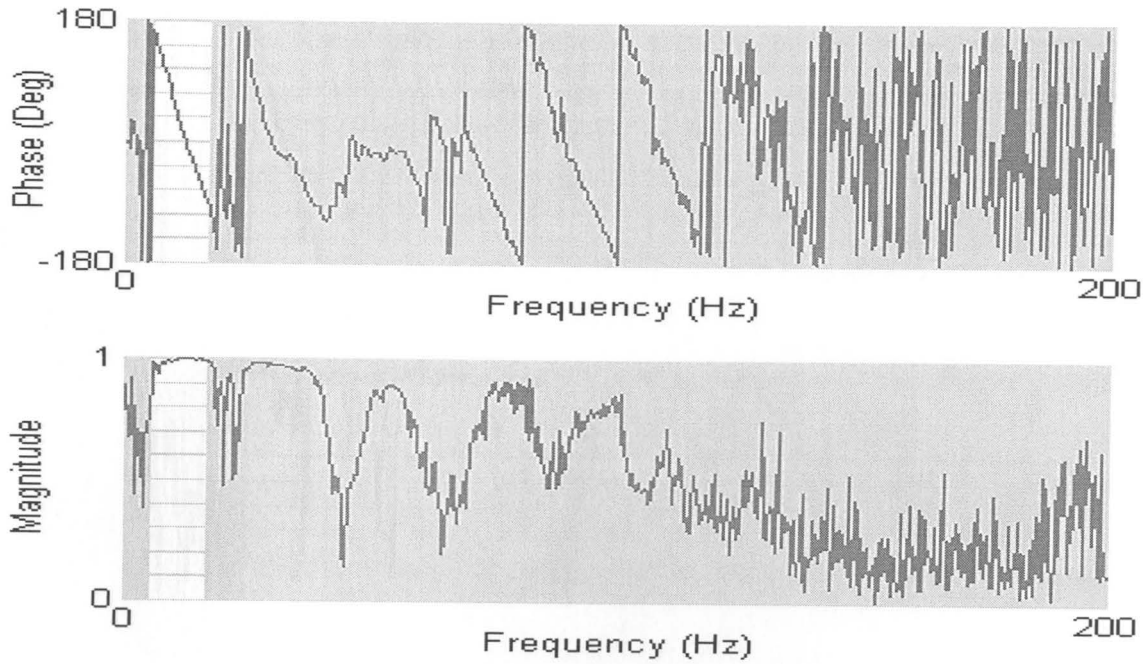

Figure A.97 Wrapped phase of the cross power spectrum (top), and corresponding coherence function (bottom), for the 8-meter spacing average profile measured at Soccer Field.

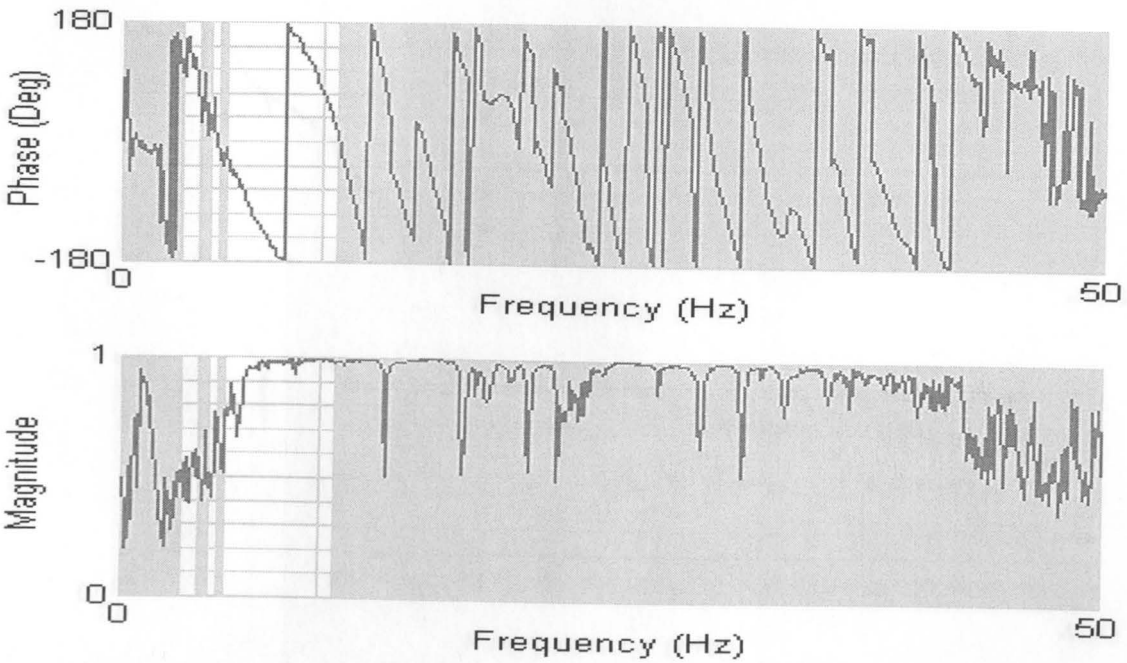

Figure A.98 Wrapped phase of the cross power spectrum (top), and corresponding coherence function (bottom), for the 16-meter spacing average profile measured at Soccer Field.

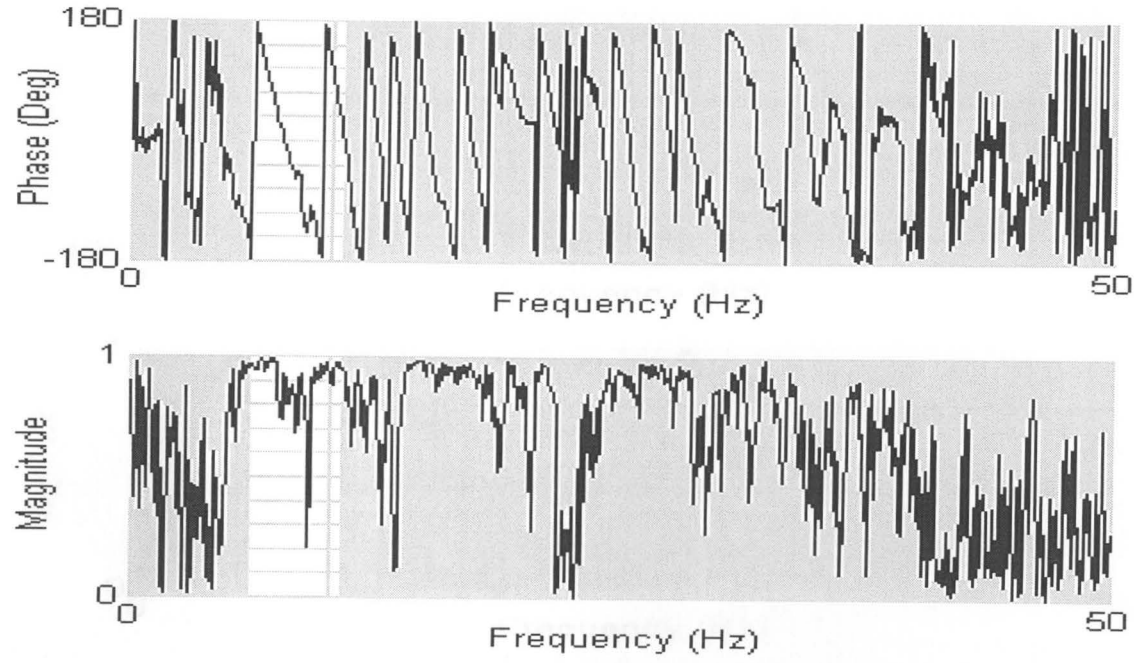

Figure A.99 Wrapped phase of the cross power spectrum (top), and corresponding coherence function (bottom), for the 32-meter spacing forward profile measured at Soccer Field.

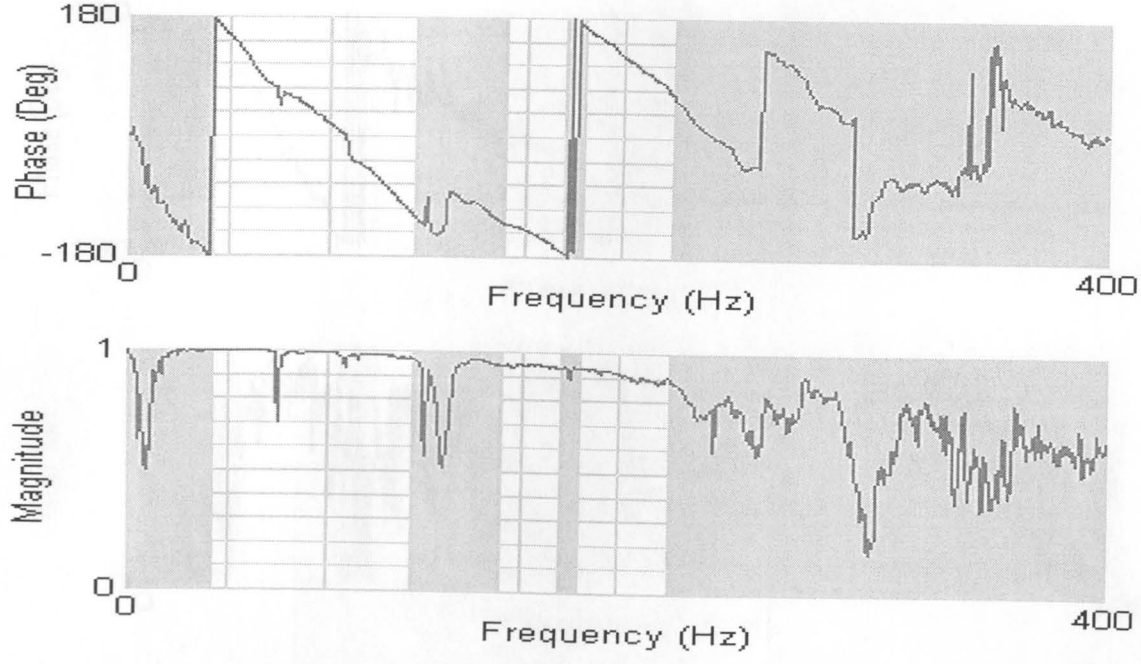

Figure A.100 Wrapped phase of the cross power spectrum (top), and corresponding coherence function (bottom), for the 3.05-meter spacing average profile measured at Yalova Harbor, Aug. 23, 2000, Yalova, Turkey.

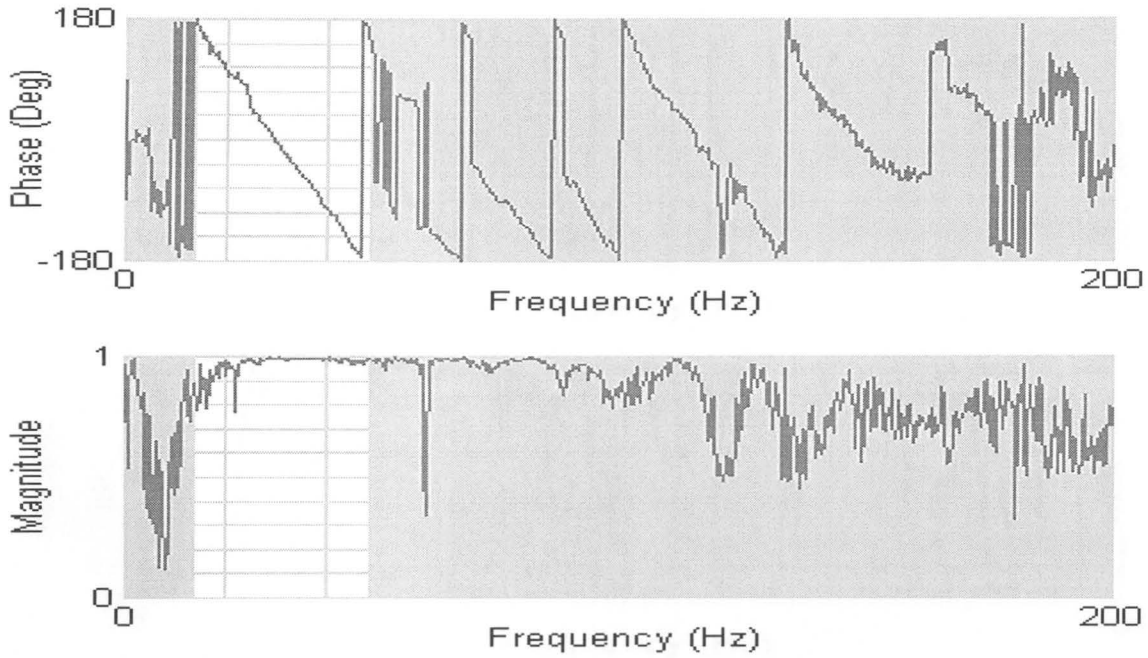

Figure A.101 Wrapped phase of the cross power spectrum (top), and corresponding coherence function (bottom), for the 6.1-meter spacing average profile measured at Yalova Harbor.

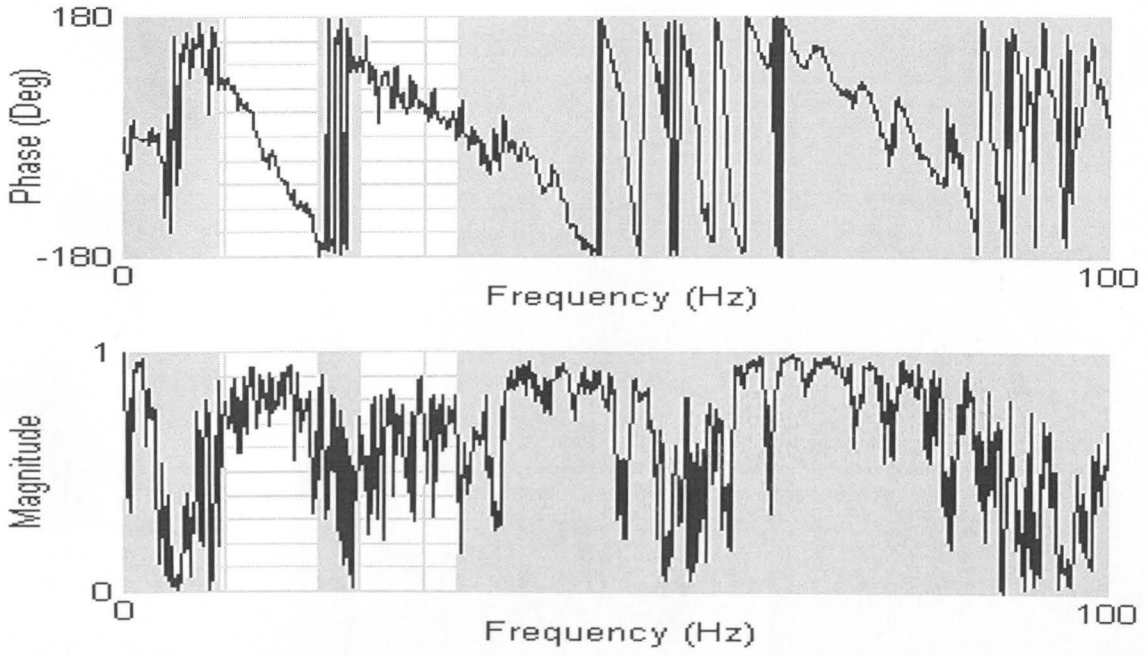

Figure A.102 Wrapped phase of the cross power spectrum (top), and corresponding coherence function (bottom), for the 12.2-meter spacing forward profile measured at Yalova Harbor.

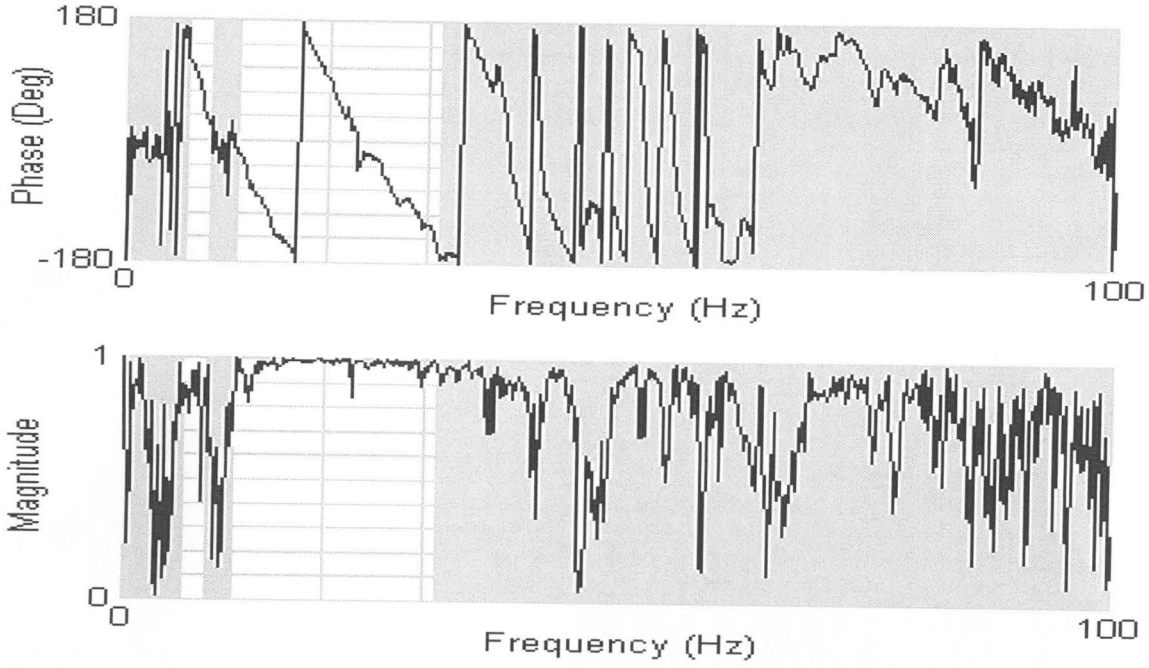

Figure A.103 Wrapped phase of the cross power spectrum (top), and corresponding coherence function (bottom), for the 15.2-meter spacing forward profile measured at Yalova Harbor.